

Modelling of Novel Photonic Devices Based on Micro-Structure Engineered for Space Division Multiplexing Optical Communication System

Rabiu Imam Sabitu

Thesis Submitted to the University of Nottingham,
Department of Electrical and Electronic Engineering,
For the Degree of Doctor of Philosophy
July 2019

Abstract

Standard single mode fibre has almost explored all degree of freedom, making it hard to accommodate considerable further enhancement in data carrying capacity in next generation optical networks. As a repercussion of the posing threat of a future capacity crunch, the consequential global effort to search for a viable alternative has been mobilised in recent years. The idea is to explore new fibre types, new photonic devices, and system, aiming to support much higher capacities by orthogonally combining multiple transmission paths over the same fibre, thereby upgrading or replacing the current optical communication system by the spatial dimension. The hope is to provide means of higher information stream per unit area to enable cost reduction and power saving benefits through the improved optical device integration and system interconnectivity.

This thesis presents a few novel types of researches in the area of optical photonic devices for space division multiplexing system. The research comprises the design of two different mode converter devices; one is based on the two multi-ring core fibre, and the other is based on a tilted fibre assisted by the dual arc waveguides; and modelling of two novel high dispersion fibres using LP-mode matrix method. The thesis also discusses high-speed mode division multiplexing transmission supporting four signal mode channels.

The design of the first converter device involves varying the lateral height and the distance that separates the two multi-ring core fibres, yielding a 94% coupling efficiency. The second converter device uses a multilayer core multimode fibre due to its low bending loss, high precession in mode confinement and ease of fabrication. The converter input was tilted at an optimised angle of 12^0 in order to align perfectly with the waveguides connected to the horizontal fibre having the same properties. Mode conversions of an LP_{11} to LP_{01}, LP_{02} to LP_{11}, and LP_{21} to LP_{01} were achieved with the conversion efficiency of 89.6%, 91.2% and 94.34% respectively.

Furthermore, a novel dispersions equalisation technique for multilayer core four-mode fibre using LP mode-matrix method is presented. Each of the core ring radii of the alternating centre-high and centre-low core index profile was optimised to a specific thickness value. The core ring radius was varied in each case to determine the optimised thickness for the dispersion equalisation. The optimised thickness of the centre high index core fibre denoted by R_1, R_2, and R_3 were found to be 4.25 μm, 2.6 μm and 2.3 μm respectively. Similarly, an optimised thickness of the centre low index core fibre, which was denoted by X_1, X_2, X_3 and X_4 was found to be 2.0 μm, 3.0 μm, 4.20 μm and 1.60 μm respectively. At 1.55 μm

wavelength, these values were used to model the two fibres to achieve an equalised modal dispersion.

Finally, performance analysis of high-speed mode division multiplexing transmission system was carried out. The binary non-return-to-zero and return-to-zero-on-off keying modulation at 10 Gb/s and 20 Gb/s bit rate were adopted using direct detection. The transmission distance was optimised by employing the dual port dual derive Mach Zehnder modulator. Expanding the proposed devices to accommodate more high order modes can enhance the bandwidth of a future spatial mode based-communication system.

Acknowledgments

Firstly, I would like to extend my profound thanks to my advisors Prof. Amin Malek Mohammadi, and Dr. Nafizah Khan. Prof. Amin's depth insights and systematic guidance always motivate me to put more efforts into the field of optical communications. It has been a great opportunity to work under his supervision, I have profited enormously from such opportunity by gaining a lot of experiences and advice he provided me. Prof. Amin has really been patient and helpful throughout the period of Ph.D. work.

My profound thanks go to Dr. Nafizah Khan for her tireless advice on how to improve this research work and for devoting much of her time to proofread the manuscripts. My acknowledgement also goes to the co-supervisor Dr. Gnanam for her contributions to see the work through. I would like to thank my internal examiner Dr. Mumtaj for sparing time and expressing her willingness in accessing and examining my research work. I'm extremely grateful to work with such helpful and hardworking advisors.

I also like to acknowledge my friend Dr. Nguyen Dong-Nhat for the contribution and valuable collaboration we had together most importantly on how to go about modeling optical transmission system.

I would also like to express my appreciations to the TetFund Nigeria through Kano University of Science and Technology (KUST), Wudil, and the University of Nottingham for the financial funding support provided for this research.

My profound and deepest appreciation, gratefulness and above all special thanks to my late father M. Imam Sabitu and my mother Hajiya Maryam Imam for their all-time support, guidance, advice, endless encouragement, and the continuous prayers right from childhood through B.Sc., M.Sc. degrees studies and to this final stage of my Ph.D. All the achievements would not have been demonstrated without their motivation and support.

My warmest appreciation goes to my brothers and sisters for their prayers and advice throughout the entire duration of the Ph.D.

This work is dedicated to my beloved life-partner Fatima M. Yusuf and her children for their love, understanding, and long-time patience. I could not access the level of support you have given me to see the work through.

Table of Contents

Abstract.....i

Acknowledgments.....iii

Table of Contents.....iv

List of Tables.....viii

List of Figures.....x

List of Abbreviations.....xv

List of Publications.....xix

Chapter 1Introduction.....1

1.1 Background 1

1.2 Problem Statement 8

1.3 Research Aims and Objectives 9

1.4 Scope of the Research 9

1.5 Contribution of the research 10

1.6 Software and Computer Aided Tools 11

1.7 Thesis Organisations..... 12

Chapter 2 Literature Review.....14

2.1 Overview 14

2.2 Mode Division Multiplexing (MDM) 14

2.2.1 Mode Conversion in MDM System 15

2.2.2 Mode Multiplexers in MDM System..... 18

2.2.3 Optical Amplifiers in MDM System 21

2.2.4 Uses of FMF in MDM 28

2.2.5 Challenges of FMF in MDM System 31

2.3 Spatial Division Multiplexing (SDM) 34

2.3.1 Multi-element Fibre (Fibre-Bundle) 36

2.3.2 Coupled and Uncoupled MCF..... 38

2.3.3 Coupled Multicore Fibres (C-MCFs) 39

2.4 Literature Review Summary 41

Chapter 3 Device Mathematical Model.....42
3.1 Introduction 42
3.2 FDTD Formulation 42
3.2.1 Two Dimensional (2D) FDTD Equations 42
3.2.2 Transverse Electric (TE) Wave 44
3.2.3 Light Source Model 47
3.2.4 Spectral Response Model 48
3.2.5 Power Model Based on the FDTD Method 49
3.2.6 Mode Converters Design Workflow 50
3.3 LP_{11}-LP_{01} MC Design Parameters 51
3.3.1 Multi-Ring Core Fibre (M-RCF) 51
3.3.2 Modeling of the M-RCF and CSIF converters 54
3.3.3 Design of MC-MMF 54
3.3.4 MC-MMF Parameter Evaluation 54
3.3.5 Principle and Model of the Arc Waveguide 58
3.4 High Dispersion Fibre Model 60
3.4.1 LP-MMM Model 61
3.4.2 Dispersion Model Using LP-MMM 61
3.4.3 Linearly Polarised Model (LP-Model) 64
3.5 Summary 65
Chapter 4 Mode Conversion for MDM System.....66
4.1 Introduction 66
4.2 LP_{11} to LP_{01} MC Using M-RCF and CSIF 66
4.2.1 Mode Orientation 69
4.2.2 Simulation Setup 71
4.3 Results and Discussions 73
4.4 Mode conversion Based on Tilts MC-MMF 91
4.4.1 Optimisation of the tilts input MC-FMF 91
4.4.2 Device Setup 94
4.4.3 Conversion Design and Analysis 94

4.5 Results and Discussions 96
4.6 Summary 104
Chapter 5 Novel High Dispersion Fibres for MDM System.....106
5.1 Introduction 106
5.1.1 Modal Dispersion Equalisation 107
5.2 Multilayer-Core Design Property 108
5.3 Optimisation of the Design Parameters 110
5.3.1 Inter-Modal Dispersion Optimisation 110
5.3.2 Modal dispersion Optimisation in the CH-ICF 111
5.3.3 Modal dispersion Optimisation in CL-ICF 114
5.3.4 CH-ICF and CL-ICF A_{eff} Optimisations 119
5.4 Summary 125
Chapter 6 High-Speed MDM Transmission.....126
6.1 Introduction 126
6.1.1 Optical Transmission System 127
6.2 System Theory 127
6.2.1 MDM System 127
6.2.2 Two-Mode Fibre 128
6.2.3 DP-DDMZ Modulator 130
6.2.4 Signal Pulse of NRZ and RZ Modulation format 131
6.3 Two Channels MDM System Model 132
6.4 Results and Discussions 135
6.4.1 NRZ and RZ MDM performance at 10 Gb/s 135
6.4.2 NRZ and RZ MDM performance at 20 Gb/s 139
6.4.3 MDM Optimisation Using DP-DDMZ at 10 Gb/s 140
6.4.4 Optimision Using DP-DDMZ at 20 Gb/s 142
6.5 Four Channels MDM System Model 147
6.5.1 MDM Transmission using MM-EDFA 148
6.5.2 4-Channel Transmission Performance at 10 Gb/s 154
6.5.1 Intermodal Nonlinearity 154

6.6 Summary 159

Chapter 7 General Conclusion and Future Work.....161

7.1 Conclusion and Summary 161

7.2 Future Work 164

Reference.....165

Appendix A.....183

List of Tables

Table 1-1-1: Global data centre (DC) traffic growth rate from 2016 to 2021 [15]. 4

Table 2-1: Recent progress in conversion device for MDM system. 17

Table 2-2: Summary of the recent technology in mode multiplexing for the MDM system. 19

Table 2-3: Recent progress in SDM/MDM optical amplifiers. 26

Table 3-1: Fibre design parameters for the outer rings. 54

Table 3-2 Summary of parameters of the arc waveguides, these parameters corresponds to that of the core layers in the tilted and horizontal fibres. 60

Table 4-1: Design parameters of the M-RCF and CSIF mode converters. 69

Table 4-2 Calculated power of the M-RCF and CSIF devices at 'h' value of 20.5 μm, for M-RCF and 22.2 μm for the CSIF-converter. The approximate output power of 94 % and 69 % for the M-RCF and CSIF converters were received at the fibre B output. 91

Table 4-3 Converter design parameters. 94

Table 5-1: Summary of the optical properties of the two fibres (CH-, CL- ICF at 1.55 μm). It includes A_{eff}, dispersion (Disp.) of the four LP modes, and the OPT. 124

Table 6-1: Summary of the LP_{01} / LP_{11} signal to noise ratio and the receive power penalty at a bit rate of 10 Gb/s and 20 Gb/s. In each case, the penalty is determine by evaluating the difference in power between the two modes. 137

Table 6-2: Performance optimisations at 10 Gb/s and 20 Gb/s bit rates, which includes all the optimised bias voltages (Vb1, Vb2), and their corresponding BER and Q-factors. The distance links were extended to 20 km, 22 km, and 23 km. Note that at 20 Gb/s bit rate, the distance can only be extended to 22 km. 146

Table 6-3: MM-EDFA Simulation parameters 148

Table 6-4: Fibre parameters at 1550 nm. 154

Table 6-5: Minimum and threshold power for the four LP modes at the BER of 10^{-9}. 157

Table 9-1: CH-FMF ring thickness R1 and measured dispersion of LP_{01}, LP_{11}, LP_{02} and LP_{21} 183

Table 9-2: CH-FMF ring thickness R2 and measured dispersion of LP_{01}, LP_{11}, LP_{02} and LP_{21} 184
Table 9-3: CH-FMF ring thickness R3 and measured dispersion of LP_{01}, LP_{11}, LP_{02} and LP_{21} 185
Table 9-4: CL-FMF ring thickness R1 and measured dispersion of LP_{01}, LP_{11}, LP_{02}, and LP_{21} 186
Table 9-5: CL-FMF ring thickness R2 and measured dispersion of LP_{01}, LP_{11}, LP_{02} and LP_{21} 187
Table 9-6: CL-FMF ring thickness R3 and measured dispersion of LP_{01}, LP_{11}, LP_{02} and LP_{21} 188
Table 9-7: CL-FMF ring thickness R4 and measured dispersion of LP_{01}, LP_{11}, LP_{02} and LP_{21} 189
Table 9-8: CH-FMF ring thickness R2 and measured effective index of LP_{01}, LP_{11}, LP_{02} and LP_{21} 190

List of Figures

Fig. 1-1: (a) Different techniques for channel multiplexing and modulation to increase optical communication system capacity (b) fibre types for an SDM communication system. 2

Fig. 1-2: Global mobile Forecasts 49 Exabyte per Month by the year 2021[12]. 3

Fig. 1-3: A spatial multiplexing metro transmission system with the essential space division multiplexing components [21]. 5

Fig. 1-4: A spatial multiplexing DC communication system [21]. 6

Fig. 1-5: SDM fibres: (a) fibre bundle (b) multicore fibre; and (c) multi-mode/ few-mode fibre 7

Fig. 1-6: The device design modelling and system analysis presented in the research work are highlighted. 11

Fig. 2-1: Illustration of the MDM communication system that employs MCs. .. 15

Fig. 2-2: (a) Schematic of a typical EDFA and (b) Basic amplification principle in Erbium-doped amplifier. 22

Fig. 2-3: (a) A cross-section of the multicore few-mode-EDFA (b) DMG average gain; Max. Noise figure (NF) for multicore few-mode-EDFA. 24

Fig. 2-4: Relative intensity noise (RIN) properties of the output light: (a) frequency (b) input optical power and (c) pump level dependency versus Noise [108]. 28

Fig. 2-5: Schematic of the basic concept of an MDM using FMF: (a) Constituted by an LP mode only, resulting in four-mode operation and (b) Both spatial and polarisation modes are included, which results in six-mode fibre operation. 29

Fig. 2-6: A diagram depicting an impulse response at a point of splicing [137]. 33

Fig. 2-7: Common SDM fibre and corresponding transmission systems: (a) uncouple multicore (b) few-mode fibre; (c) coupled multicore; and (d) example of a DSP complexity table suitable for a six-mode multimode fibre and a three-core two-mode FM-MCF. The symbol 'h' indicates complexity. In both cases, the solution results in an SDM factor of 6 and shows reduced complexity in the total MIMO calculation in the second case [26]. 35

Fig. 2-8: Different SDM transceivers: (a) Avago Minipod™ adopting 12-single mode ribbon [144] (b) multicore fibre photonic transceiver chip [145] (c) VCSCEL/PD (4×12), which interfaces a multimode fibre bundle opto-chip that support a 480Gbps transreceiver [146]. 36

Fig. 2-9: Cross-section of multi-element fibre fabrication: (a) demonstrate in core-pumping optical amplification (b) using the cladding-pumping technique (c) and (d) transporting fibre and (e) diagram depicting seven multi-element preforms on the draw tower[5][24]. 37
Fig 2-10: Diagram of a fabricated multi-elements type pluggable FI-FO device [151]..... 38
Fig. 2-11: (a) Cross-sectional diagram of the fabricated multi-step three-mode twelve-core uncoupled fibre consisting of a square-lattice configuration. The separations between two cores are denoted by odd, and even numbers respectively. Λ, T_c, represents core pitch, and the outer cladding thicknesses respectively, and D_c represents cladding [28] (b) Cross-section of 6-mode 19-core uncoupled fibres [153]. .. 39
Fig. 2-12: Cross-section and refractive index profile of the C-MCF with a radial line on a core centre [156]..... 40
Fig. 2-13 : Chapter summary 41
Fig. 3-1: Location of a transverse electric field (TE) in the computational layout. 45
Fig. 3-2: Total field technique for the input plane. 47
Fig. 3-3: Design workflow for the proposed different mode converters. 51
Fig. 3-4: (a) Schematic cut of the M-RCF; and (b) CSIF schematic as the light propagates along the fibre in 2D (xz-plane); MSC stands for the multi-step core. 52
Fig. 3-5: M-RCF core profile, comprising the central layer, three outer cores, and a cladding, each with different refractive index; a central core layer is having the highest refractive index value. 53
Fig. 3-6: Geometry of the two identical fibres that can support two modes separated by distance d between centres of the two fibres and a lateral displacement 'h'. 54
Fig. 3-7: Refractive index profiles of the four outer layers of the MC-MMF. 55
Fig. 3-8: A longitudinal cut of MC-MMF with M core layers. 56
Fig. 3-9: Pulse broadening (σ_M/σ_1) decrease with increase in the M core layers. 57
Fig. 3-10: Variation of the effective area with a change in the layer radius (r_3).58
Fig. 3-11: (a) Cut off of the core layers in the multistep arc waveguide; and (b) Layout of the arc bends in the simulation domain. 59
Fig. 3-12: (a) Connection of straight and bend (arc) fibres with core radius r, where R is the bending radius, n_{core} represents the refractive index of the core, and n_{clad} denotes that of the cladding, CV is the centre of

curvature and (b) Illustration of a bend round MC-MMF with radial core indices of n_1, n_2, n_3, and n_4. The refractive index n_5 is for the cladding. 60
Fig. 4-1: Illustration of the light coupling into the angled-cleaved CSIF 67
Fig. 4-2: Model of the proposed mode converter; CR is the coupling region; MST: multistep core. A similar model was used to simulate the CSIF with a single layer core. 67
Fig. 4-3: Two M-RCF (ring cores are not shown) each supporting two LP modes. An LP_{11} is excited at the input of fibre A and LP_{01} is collected in fibre B. 69
Fig. 4-4: The 2D-layout setting of the: (a) M-RCF (fiber A) to determine the effects of cleaving fibre end facet and (b) CSIF setup with a single layer core. 72
Fig. 4-5: The 2D simulation layout of: (a) M-RCF-converter and (b) CSIF-converter, each consists of fibre A and fibre B. An LP_{11} mode is launched at the input side of fibre A. 73
Fig. 4-6: Mode profiles of the CSIF at different cleaving angles. 74
Fig. 4-7: Mode excitation for LP_{01} and LP_{11} at angled-cleave 23°..... 75
Fig. 4-8: Mode excitation for LP_{01} and LP_{11} at angled-cleave 39°..... 76
Fig. 4-9: Mode excitation for LP_{01} and LP_{11} at angled-cleave 42°..... 76
Fig. 4-10: Mode excitation for LP_{01} and LP_{11} at angled-cleave 60°..... 77
Fig. 4-11: Mode excitation for LP_{01} and LP_{11} at angled-cleave 70°..... 77
Fig. 4-12: Mode excitation for LP_{01} and LP_{11} at angled-cleave 80°..... 78
Fig. 4-13: Mode excitation for LP_{01} and LP_{11} at angled-cleave 90°..... 78
Fig. 4-14: M-RCF-converter 3D-model, a similar diagram can be obtained for the CSIF-converter. 79
Fig. 4-15: (a) M-RCF-converter index distribution and (b) CSIF-converter index distribution during simulations. 80
Fig. 4-16: Plot of the M-RCF- and CSIF-converter Refracted angle versus incident cleaved-angles. The blue, red, and green markers illustrates the graphs of the LP_{01}, LP_{11a}, and LP_{11b} for the M-RCF-converter, respectively. Similarly, the magenta, black, and yellow, colour markers represents the mode excitations of the LP_{01}, LP_{11a}, and LP_{11b} for the CSIF-converter, respectively. 81
Fig. 4-17: Effect of "h" on CE (a) of the M-RCF (red curve) (b) CSIF (blue curve). The coupling point of the M-RCF and CSIF (red and blue circles) is 20.5 μm and 22.2 μm, respectively. 82

Fig. 4-18: Coupling length variation with the separation distance. The red curve is for the M-RCF and the blue curve for the CSIF converter. 83
Fig. 4-19: Mode profiles of the proposed mode converters (Fig 4-2) and simulated using the layout in Fig. 4-5: (a) M-RCF and (b) CSIF..... 84
Fig. 4-20: (a) Discrete Fourier transform field of the M-RCF mode converter and (b) Discrete Fourier transform field of the CSIF mode converter..... 86
Fig. 4-21: (a) LP_{01} mode amplitude of the M-RCF device (b) LP_{01} mode amplitude of the CSIF device..... 87
Fig. 4-22: LP_{01} mode purity of the injected model field as a function of wavelength. The red curve represents the M-RCF, and blue curve, the CSIF converter. 88
Fig. 4-23: LP_{01} mode purity as a function of the lateral height of the two converters. The red curve is for the M-RCF and blue curve for the CSIF device..... 89
Fig. 4-24: Converter wavelength dependence..... 90
Fig.4-25: 2D Simulation layout of the tilt fibre, the modes are excited from the left usinng input plane as the energy souce..... 92
Fig. 4-26: LP mode amplitudes decay at a 45°-tilted angle as it propagates along the fibre: (a) LP_{11} mode; (b) LP_{02} mode amplitude; and (c) LP_{21} mode. The lobes are gradually disappearing as the order of the modes get higher..... 93
Fig. 4-27: Mode amplitudes at 12°-tilted angle: (a) LP_{11} mode; (b) LP_{02} mode; and (c) LP_{21} mode..... 93
Fig. 4-28: Schematic of the proposed conversion device consists of three sections that include an input section (I-Section), conversion region (C_R), and the output section (O-Section)..... 95
Fig. 4-29: Effect of varying the layer offset as a function of IL. 96
Fig. 4-30: LP_{11} mode excitation at the input of the tilted fibre with the two lobes visibly seen at the input and the output. 97
Fig. 4-31: LP_{02} mode excitation at the input of the tilted fibre with the three lobes visible at the input and output..... 97
Fig. 4-32: LP_{21} mode excitation at the input of the tilted fibre with the four lobes visibly seen at the input and output..... 98
Fig. 4-33: Modes amplitude as a function of tilt angles. 99
Fig. 4-34: 3D layout of the device displayed during simulations. The components that constituted the device were well aligned to give the overall device architecture..... 99
Fig. 4-35: 2D Refractive index distribution of the proposed model..... 100

Fig. 4-36: LP_{11} to LP_{01} Mode conversion. An LP_{11} mode was excited at the input of the tilted fibre. After propagating through the bend, an LP_{01} mode is observed..... 101
Fig. 4-37: LP_{02} to LP_{11} Mode conversion. An LP_{02} mode was excited at the input of the tilted fibre. After propagating through the bend, an LP_{11} mode is observed at the output of the horizontal fibre. 102
Fig. 4-38: LP_{21} to LP_{01} Mode conversion, LP_{21} mode was excited at the input of the tilted fibre. After propagating through the bend, an LP_{01} mode is observed at the output of the horizontal fibre. 102
Fig. 4-39: Output absolute power of LP_{02} to LP_{11} and LP_{11} to LP_{01} mode conversions. 103
Fig. 5-1: (a) Cross section of the proposed CH-ICF. R1, R2, and R3 are the layer thicknesses and (b) Cross section of the CL-ICF with the X1, X2, X3, and X4 as the thickness of the rings. 109
Fig. 5-2: Simulated modal distributions and field intensity of the multilayer-core CH-ICF. 110
Fig. 5-3: The effect of R1 on the dispersion of the CH-ICF. 112
Fig. 5-4: Graph of R2 on versus dispersion CH-ICF. 113
Fig. 5-5: Graph of the effect of R3 on dispersion CH-ICF. 113
Fig. 5-6: Graph of change in X1 versus dispersion CL-ICF. 114
Fig. 5-7: (a) CL- profile of the LP_{01} mode confinement (b) CL- profile of the LP_{02} mode confinement (c) CL- profile of the LP_{21} mode confinement and (d) CL- profile of the LP_{02} mode confinement. 115
Fig. 5-8: Graph of change in thickness X2 against dispersion CL-ICF. 116
Fig. 5-9: Graph of the effect of varying thickness X3 on dispersion 116
Fig. 5-10: Graph of measured dispersions against change in the thickness (X4) CL-ICF. 117
Fig. 5-11: Dispersion against change in wavelength of LP_{01}, LP_{11}, LP_{02}, and LP_{21} of the CH-ICF at λ=1.55 μm. 118
Fig. 5-12: Dispersions against change in the wavelength of LP_{01}, LP_{11}, LP_{02}, and LP_{21} of the CL-ICF at λ=1.55 μm. 118
Fig. 5-13: Relation of the thickness of the low index region (R_2) of the CH-ICF and the A_{eff}. 119
Fig. 5-14: Relationship of the A_{eff} as a function of the thickness (X3) of the lower index region of the CL-ICF. 120
Fig. 5-15: Effective area of CH-ICF as a function of wavelength. 121
Fig. 5-16: Effective mode area of the CL-ICF as a function of wavelength 121
Fig. 5-17: Relation between the core-cladding index contrast (Δx) 122

Fig. 5-18: Relation between the cladding-low index contrast (Δy). 123
Fig. 6-1: Mode of operation of the MDM system. R_x: spatial receiver..... 128
Fig. 6-2: Section cut of a step index MMF. 129
Fig. 6-3: Spatial mode profile distributions and 2D intensities of the fibre signal modes: (a) LP_{01}, before multiplexing (b), LP_{11} before multiplexing (c) LP_{01}+LP_{11} (after multiplexing) (d) LP_{01} 3D intensity and profile distribution after separation using spatial de-multiplexers and (e) LP_{11} 3D intensity and profile distribution after demultiplexing. 130
Fig. 6-4: DP-DD-Modulator layout. 131
Fig. 6-5: Illustration of how optical signals of format NRZ are generated using an external modulator. 132
Fig. 6-6: Illustrations of how optical signals of format RZ are generated. 132
Fig. 6-7: Simulation setup of the proposed 2-mode channels MDM system: (a) Using a conventional modulator, S-T_{X1}: Spatial transmitter for the LP_{01}, S-T_{x2}: a spatial transmitter for the LP_{11} mode channel. Ideal mux: LP-mode spatial multiplexer. VOA: variable optical attenuator, STS: signal type selector. Pin = input power (b) MDM optimised transmission setup using DP-DD-MZ..... 133
Fig. 6-8: NRZ and RZ performance for various distance link at 10Gb/s..... 135
Fig. 6-9: Eye diagrams for NRZ-LP_{01} B2B, LP_{11}-B2B, LP_{01}-15 km, and LP_{11} -15 km. Similarly, for the RZ format LP_{01}-B2B, LP_{11}-B2B, LP_{01} -15 km and LP_{11} -15 km at BER of 10^{-9}..... 136
Fig. 6-10: BER as a function of the OSNR at 10 Gb/s; the results of the B2B, 5 km, 10 km, and 15 km for both the NRZ and RZ modulation formats are plotted. 137
Fig. 6-11: Effects of misalignment between the transmitter and receiver, which was observed on plotting the value of maximum Q-Factor (Max. Q-Factor) against photodetector active area width (X shift) at B2B and 15 km for both LP_{01} and LP_{11} using the NRZ and RZ at 10Gb/*s.*..... 138
Fig. 6-12: NRZ and RZ performance for various distance links at 20 Gb/s for the 2-mode channels. 139
Fig. 6-13: Eye diagrams of the NRZ modulation format (a) B2B LP_{01} (b) B2B LP_{11} (c) 15 km LP_{01}. (d) 15 km LP_{11}. With the Q-Factor of 5.82, 5.72 for the LP_{01}, $LP_{11,}$ B2B and 4.65, 4.58 for the LP_{01}, LP_{11} at 15 km were achieved at BER of 10^{-9} and 10^{-6} at 20 Gb/s bit rates, respectively. 140
Fig. 6-14: Eye opening of (a) LP_{01} NRZ and (b) LP_{11} NRZ (c) LP_{01} RZ (d) LP_{11} RZ over 20 km at 10 Gb/s..... 141

Fig. 6-15: MDM-Q factors over a 23 km distance link at the fixed receiver power of −13.75 dBm as a function of the Bias voltage Vb1..... 141
Fig. 6-16: Variation of MDM-Q factor bias voltage (Vb2) over a 23 km distance link at a bit rate of 10 Gb/s. 142
Fig. 6-17: MDM-Q factors over 22 km distance link at a fixed power of −29.75 dBm as a function of Bias voltage Vb1..... 143
Fig. 6-18: Variations of MDM-Q factor as a function of Bias voltage Vb2 at 20 Gb/s bit rate..... 144
Fig. 6-19: Optimised eye diagram at 10 Gb/s using NRZ and RZ modulation format over 20 km and 23 km distance links: (a) LP_{01}-NRZ over 20 km (b) LP_{11}-NRZ over 20 km (c) LP_{01}-NRZ over 23 km (d) LP_{11}-NRZ over 23 km (e) LP_{01}-RZ over 20 km (f) LP_{11}-RZ over 20 km (g) LP_{01}-RZ over 23 km and (h) LP_{11}-RZ over 23 km. 145
Fig. 6-20: Optimised eye diagram at 20 Gb/s using NRZ modulation format over 20 km and 22 km distance links: (a) LP01-NRZ-20 km (b) LP11-NRZ 20 km (c) LP01-NRZ- 22 km and (d) LP11-NRZ- 22 km. 145
Fig. 6-21: 4-Mode channel MDM transmission system setup (a) LP modes eye diagram at BER of 10^{-9}. (b) output field distribution of the four modes. 148
Fig. 6-22: (a) Doped intensity profile of the four pump non-degenerate modes (LP_{01}, LP_{11}, LP_{21}, and LP_{02}) (b) normalized intensity of the four spatial modes profile. 149
Fig. 6-23: BER Performance of the multimode EDFA with the variation in the EDFA core radius. 150
Fig. 6-24: Variation of the erbium-doped radius with the power distribution per mode channel..... 151
Fig. 6-25: Variation of MM-EDFA core radius with the power distribution per modes. 152
Fig. 6-26: Performance of the multimode EDFA in terms of BER as a function of the input power per spatial mode..... 153
Fig. 6-27: Performance of the multimode EDFA in terms launched 154
Fig. 6-28: Log (BER) for an MDM transmission over 40km of a four-mode fibre as a function of launch power. 156
Fig. 6-29: Comparison of the BER performance versus OSNR of the four signal modes at B2B and over 40km distance link. 157
Fig. 6-30: BER performance with the variation of the received optical power over the 5km, 15km, and 30km distance links. 158

Fig. 6-31: Eye diagrams of the LP_{01}, LP_{11}, LP_{21}, and LP_{02} at BER of 10^{-9} respectively. First row is for the B2B, and the second row is the eye diagrams over 40 km. 159
Fig. 6-32: Chapter summary 160

List of Abbreviations

AG	Average Gain
A_{eff}	Mode Effective Area
ASE	Amplified Spontaneous Emission
BF	Bessel Function
BER	Bit Error Rate
CAGR	Compound Annual Growth Rate
CE	Conversion Efficiency
CH	Centre High
CH-ICF	Centre High-Index Core Fibre
CL	Centre Low
CL-ICF	Centre Low-Index Core Fibre
C-MCF	Coupled-Multicore Fibre
CP	Coupling Point
CFLPG	Coiled- Fibre Long Period Grating
CeL	Centre Launching
CSIF	Conventional Step Index Fibre
CR	Cleaving Region
C_R	Coupling Region
CW	Continuous Wave
DAW	Dual Arc Waveguide
DB	Deflected Beam
DCN	Data Center Network
DD	Direct Detection
DP	Debye Potential
DFT	Discrete Fourier Transform
DMGD	Differential Mode Group Delay
DMG	Deferential Mode Gain
DMT	Discrete Multi-Tone
DP-DD-MZ	Dual Port Dual Derive Mach Zehnder Modulator
DP-QPSK	Dual Polarisation Quadrature Phase Shift Keying
DRA	Distributed Raman Amplifier
DSP	Digital Signal Processing
DT-MC	Double Fibre Taper-Based Mode Converter
EAD	Extra Annulus Doping
EDB	Electrical Duo-Binary
EDFA	Erbium-doped Fibre Amplifier

EM	Electromagnetic Field
ER	Extinction Ratio
FCC	Fibre Central Core
FDTD	Finite Difference Time Domain
FDM	Frequency Division Multiplexed
FFT	Fast Fourier Transform
FI/FO	Fan In/ Fan Out
FLT	Femtosecond Laser Techniques
FM	Field Model
FMF	Few-Mode Fibre
FOM	Figure-of-Merit
GD	Group Delay
GI	Graded Index
HOM	High Order Mode
$l_c L$	Fibre Length
IC-XT	Inter Core-Crosstalk
IEM	Intensity and Field Model
IL	Insertion Loss
IM	Intensity Model
IM-FWM	Intermodal-Four Wave Mixing
IM-XPM	Intermodal-Cross Phase Modulation
IoT	Internet of Thing
IPTV	Internet Protocol Television
LAN	Local Area Network
LP	Linearly Polarised
LP-MMM	Linearly Polarised-Mode Matric Method
LPFG	Long-Period Fibre Grating
LCOS	Liquid Crystal on Silicon
MAN	Metro Area Network
M-RCF	Multi-Ring Core Fibre
MC-MMF	Multistep Core Multimode Fibre
MCF	Multicore Fibre
MC-FM-EDFA	Multicore-Few Mode Erbium Doped Fibre Amplifier
MC	Mode Converter
MCP	Mode Coupling
MCVD	Modified Chemical Vapor Deposition
MD	Modal Dispersion
MDL	Mode Dependent Loss

MDM	Mode Division Multiplexing
MI-MMF	Measured Index-Multimode Fibre
MIMO	Multi Input Multi Output
MMF	Multimode Fibre
MMP	Multimode Photonic
MPLC	Multi-Plane Light Conversion
M-SBP	Mode-Selective Bidirectional Pumping
MSPL	Mode Selection Using Photonic Lantern
NF	Noise Figure
NM	Number of Modes
NRZ	Non-Return to Zero
O-ADM	Original to Any Desired Mode
OC	Outer Core
OFDM	Orthogonal Frequency Division Multiplexed
OI	Overlap Integral
OL	Observation Line
OPT	Optimised Thickness
OSA	Optical Semiconductor Amplifier
OSNR	Optical Signal to Noise Ratio
OOK	On-Off Keying
PAM	Pulse Amplitude Modulation
PDM	Polarisation Division Multiplex
PLC	Planar Lightwave Circuit
P_N	Power Needed
PP	Pump Power
PSP	Principle State Polarisation
P_{TH}	Threshold Power
Q-Factor	Quality Factor
RA	Raman Amplifier
RC-EDFA	Ring Core-Erbium Doped Amplifier
RCF	Ring Core Fibre
RIN	Relative Intensity Noise
ROADMs	Reconfigurable Optical Add/Drop Multiplexers
RUSS	Real Units of a Space Step
R_X	Receiver
RZ	Return to Zero
SBS	Stimulated Brillouin Scattering
S-D-MUX	Spatial Demultiplexers

SDM	Space Division Multiplexing
SLM	Spatial Light Modulator
SMF	Single Mode Fibre
SMF-B	Single Mode Fibre -Bundle
S-MUX	Spatial Multiplexer
SGF	Super-Gaussian Function
SOC	Second Outer Core
SRS	Stimulated Raman Scattering
SSM	Spatial Spectral Matching
TDM	Time Division Multiplex
TF/SF	Total Field/Scattered Field
TM	Transverse Magnetic
TMF	Two-Mode Fibre
TOC	Third Outer Core
T_X	Transmitter
ULA-SMF	Ultra-Low-Single Mode Fibre
U-MCF	Uncoupled Multicore Fibre
VCSEL	Vertical-Cavity Surface-Emitting Laser
VoD	Video on Demand
V_p	V-Parameter
WAN	Wide Area Network
WDM	Wavelength Division Multiplexing
WG	Waveguide
ZB	Zettabyte

List of Publications

1) **R. I. Sabitu** and A. Malekmohammadi, "Mode Conversion Based on Lateral Misalignment between Two Multi-Ring Core Fibres for MDM System," *J. Opt. Commun.*, pp. 1–10, Jan. 2019 (published).

2) **R. I. Sabitu**, N. Dong-Nhat, and A. Malekmohammadi, "High dispersion four-mode fibre for mode-division multiplexing systems," *Optik (Stuttg).*, vol. 181, pp. 1–12, Mar. 2019 (published)

3) **R. I. Sabitu**, Nafizah Goriman Khan and A. Malekmohammadi, "Recent Progress in Optical Devices for Mode Division Multiplex Transmission System," Opto-Electronics Rev., 2019 (accepted)

4) **R. I. Sabitu** and A. Malekmohammadi, "Mode Conversion Based on Tilted-Few-Mode Fibre Assisted by dual Arc Waveguide for Mode-Division Multiplexing System," *Optik (Stuttg).*, 2019 (under review)

5) **R. I. Sabitu** and A. Malekmohammadi, "All-Fiber Mode Converter Based on LP_{11} Coupled-Mode for Mode Division Multiplexing Systems," *Optic & Laser Technology.*, 2019 (revised)

6) **R. I. Sabitu** and A. Malekmohammadi, "NRZ / RZ-OOK over a 2-Channel Mode-Division Multiplexing for Interconnect and Metro Applications," IET Commuinication., 2019 (under review)

7) **R. I. Sabitu**, Nafizah Goriman Khan and A. Malekmohammadi, "40 Gb/s High Speed Mode Division Multiplexing Transmission Employing NRZ Modulation Format" *J. Opt. Commun.*, 2019 (under review)

Chapter 1 Introduction

1.1 Background

The impetus that necessitates the move towards the adoption of the space domain, as the next frontier in optical fibre network is the impending capacity crunch due to the single-mode fibre (SMF) having achieved its fundamental transmission limits of 100-Tb/s in the early 2010s [1]. This is further fuelled by Kerr nonlinearity [2], and the emergence of bandwidth-demanding systems and applications such as video-on-demand (VoD) and multimedia broadcasting [3][4][5]. In recent years, wavelength division multiplexing (WDM) [6] was able to meet the internet traffic demands as it has the capabilities to improve spectral bandwidth of an optical fibre communication network by 2-folds. Coherent detection is also considered as an alternative approach towards increasing capacity of an optical communication network where it enhances the signal-to-noise ratio (SNR) of fibre network channels beyond that of the direct detection [7]. Optical quadrature amplitude modulation (QAM) with coherent detection helps in enabling high spectral efficiency (SE) as data are transmitted using both the amplitude and phase of the carrier signals. The scaling in SNR can only be realised by maximising power, where channel capacity scales logarithmically as the signal power increases. Ultimately, increasing channel capacity by way of maximising power is not feasible to address the demands of the rapid traffic growth from both the technical and power consumption perspectives as the intrinsic nonlinearity nature of optical fibres limits the amount of signal powers.

The experimental capacities evaluation of the SMF over the last couple of decades comprises different multiplex schemes. These include time division multiplex (TDM), which consists of producing a series of time slots and allowing a single scalar quantity of the amplitude or phase to change within each time slots, hence the formation of symbols, which are transported in temporal succession at a given symbol rate. If each symbol represents one out of M possible level, for a pulse amplitude modulation (PAM), there will be $\log_2 M$ bits of data transported per symbol. Pulse shaping can be further implemented to compress the network spectral pulses subject to time-frequency constrains [8]. However, frequency division multiplex (FDM) is unsuitable for continuous signals, it requires extra guard time and synchronisation that transport multiple communication signals in parallel to a K-independent carrier frequency over the same medium such as on the existing shared-transporting medium of mobile wireless channels. Scalability of FDM is typically bounded by regulatory bandwidth constraints, while natural physical properties are added constraints when twisted-pair or fibre cables are

employed [9]. Polarisation division multiplex (PDM) via coherent detection optical network exploits the vector nature of electromagnetic waves to transmit two separate information streams simultaneously on a set of dual orthogonal polarisation. PDM increases transmission capacity by 2-fold compared to the non-polarised network. Fig. 1-1 (a) illustrates the exhausted physical domain and Fig. 1-1 (b) is the corresponding proposed space division multiplexing (SDM) fibres.

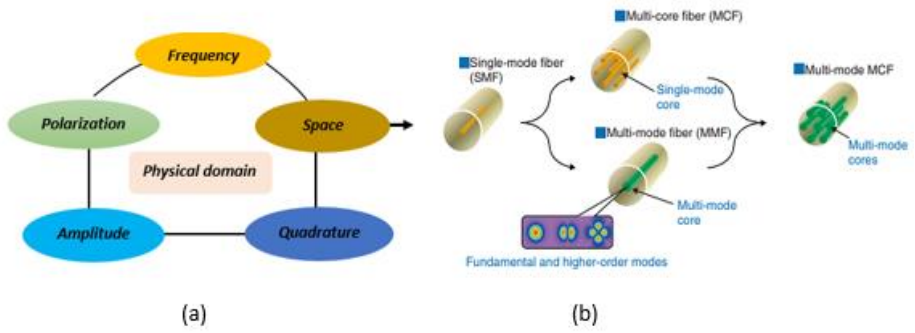


Fig. 1-1: (a) Different techniques for channel multiplexing and modulation to increase optical communication system capacity (b) fibre types for an SDM communication system.

The dual polarisation can be further enhanced by introducing correlations between symbols to give four-dimensional modulations that optimise network performance at the expenses of spectral efficiency [10]. It is important to mention that the significant difference between the TDM and wavelength division multiplexing (WDM) is the system requirements, where the former requires an increase in the electronic speed and optical transmitter and receiver, whilst the latter requires broadband optical amplifier and optical signal components. In addressing the earlier mentioned challenges and fulfilling the future requirements of high-capacity optical transmission systems, SDM appears to be a viable solution and has recently received a lot of research attention [2].

Furthermore, analysis of the metro system traffic growth carried out by the Bell Labs, Alcatel-Lucent [11], and the recent traffic growth projection given by the Cisco visual network index shows a manifold increase in data traffic. The metro area network (MAN) traffic increased by 560% in 2017, and the data traffic in mobile is expected to grow close to 49 Exabyte (EB) per month by the year 2021 [12]. This is a 7-fold increase over that of the year 2016. And the global mobile traffic is anticipated to rise at a compound annual growth rate (CAGR) of 47% from 2016 to 2021 as illustrated in Fig. 1-2.

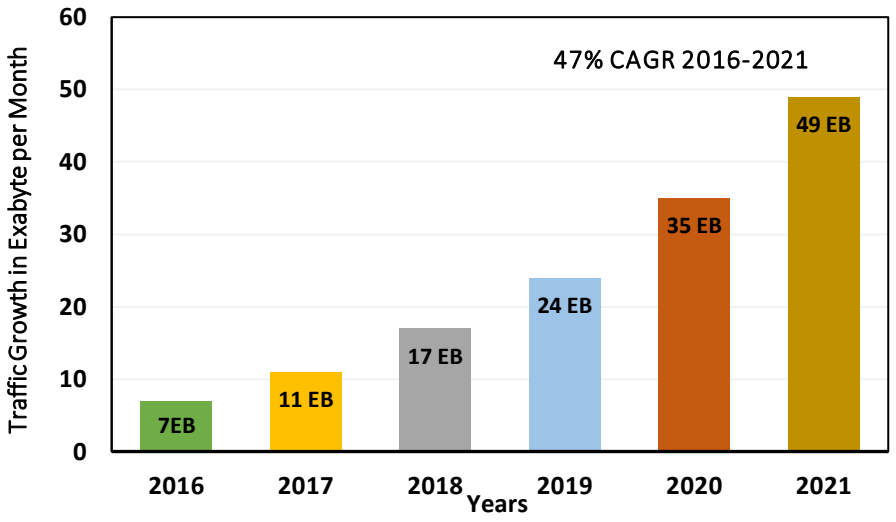


Fig. 1-2: Global mobile Forecasts 49 Exabyte per Month by the year 2021[12].

Metro network has grown double, which is more than the traffic stream into the backbone in the year 2017. This fast growth increase will undoubtedly need a network upgrade in MAN in the next three to five years [13].

Concurrently, the demand for data storage in data centres (DCs) has expanded. For example, every video streamed or downloaded has to be stored, and the same for social networking. This makes most of the information transmitted over access network travel back and forth between DCs and the users. State-of-the-art centres now operate at high-speed of 10 Gb/s or even faster, which favours transmission over optical fibre cables. Large DCs have quite a huge number of connections, with the average link distance of 100 m, which necessitates the use of multimode fibre (MMF) cables. To support higher bandwidth, an optical cable with the higher fibre counts was introduced. The early traffic growth projection of the worldwide internet and the wide area networks (WAN) is to increase by 3.3 zettabytes (ZB) each year by the year 2021 [14]. This amount of the expected yearly worldwide traffic increase has already hit 6.8 ZB in 2016 and expected to reach up to 20.6 ZB per year by the year 2021. The increase in the global data traffic signifies a 25% CAGR. Table 1-1 illustrates the details for global DC traffic growth rate between 2016 and 2021.

In view of the global rapid traffic demands, many types of research have considered a spatial domain as the only new technology (FMFs and MCFs) that can greatly alleviate the optical fibre capacity limit by adding additional spatial dimension. As discussed above, the metro communication systems are approaching their traffic growth limit, unless viewing from high data capacities such as Tb/s or

even Pb/s, which will inevitably require a new dimension to address the huge traffic growth.

Table 1-1: Global data centre (DC) traffic growth rate from 2016 to 2021 [15].

Classification or task							
	2016	2017	2018	2019	2020	2021	CAGR2016-2021
By Category (EB/ Year)							
DC to user	998	1,280	1,609	2,017	2,500	3,064	25.2%
DC to DC	679	976	1,347	1,746	2,245	2,796	32.7%
Within DC	5,143	6,831	8,601	10,362	12,371	14,695	23.4%
By segment (EB/Year)							
Consumer	4,501	6,152	8,052	10,054	12,401	15,107	27.4%
Business	2,319	2,391	3,505	4,070	4,716	5,449	18.6%
By Type (EB/year)							
Cloud DC	5,991	8,190	10,606	13,127	16,086	19,509	26.6%
Traditional DC	826	897	952	997	1,030	1,046	4.8%
Total (EB/Year)							
Total DC	6,819	9,087	11,557	14,124	17,116	20,555	24.7%

Other factors such as cost-effectiveness, characterisation by interoperability, and most importantly flexibility in reaction to a system failure must be taken into consideration. Spatial domain as a new technology could only be the available dimension that can cope with most of these issues [16]. As illustrated in Fig. 1-3, transition from SMF technology to the SDM would require S-Mux/S-deMux. Although remarkable progress has been achieved in terms of SDM amplifier solution for MCF, FMF and other spatial approaches [17], a lot is still expected to be done in order to come up with a viable solution. On the other hand components such as switches, spatial reconfigurable optical add/drop multiplexers (ROADM) proto-types were already printed for capacity multiplicity enhancement, with both the WDM and spatial signal channels [18-20].

It is worth mentioning that ROADMs are often considered the integral component of metro communications. This is because they serve as the major interconnection nodes between transmission network linking cities, DCs, etc. Therefore, it is absolutely necessary to have an SDM prototype implementation for the next generation multidimensional transmissions. Thus, one of the transition obstacles from the existing network to the new spatial multiplexing approach is that the metro network is typically a brownfield.

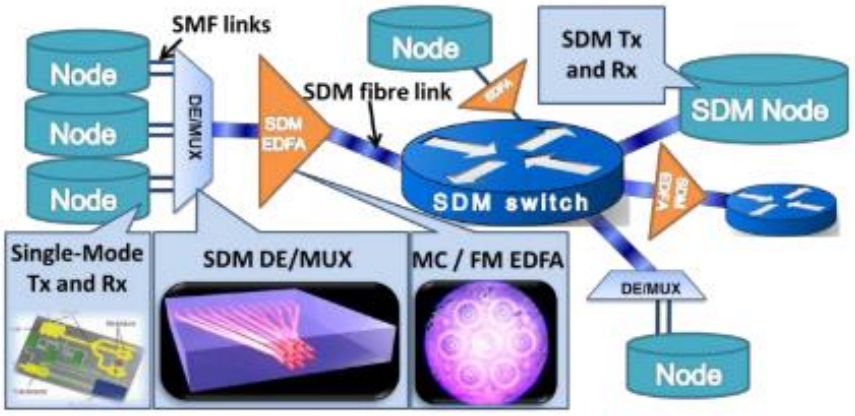


Fig. 1-3: A spatial multiplexing metro transmission system with the essential space division multiplexing components [21].

Furthermore, SDM technologies that include spatial amplifiers, ROADMs, S-Mux/S-deMux are inversely compatible with the existing multi-elements fibres. Lastly, an SDM accommodates resilience and failure recovery function due to the fact that it consists of multiple spatial channels. If for one reason or the other a particular channel fails, an adjacent one can substitute it immediately.

Similarly for a future data centre network (DCN) that demands capacity above 100 Gb/s consisting of 10×10 G, or 1 Tb/s (32×25 G) [22] will absolutely require a novel modulation technique that can consist of TDM-SDM-WDM plus a DSP. This combination may not be cost-effective, and its maintenance will be expensive as well.

As illustrated in Fig. 1-4, a single SDM fibre (multicore or FMF) can address these challenges, giving the same capacity with better spectral efficiency or even higher [21]. A recent investigation based on all-optical upgradable intra-data centre network employing SDM [23] shows that this can be achieved at no additional expenses.

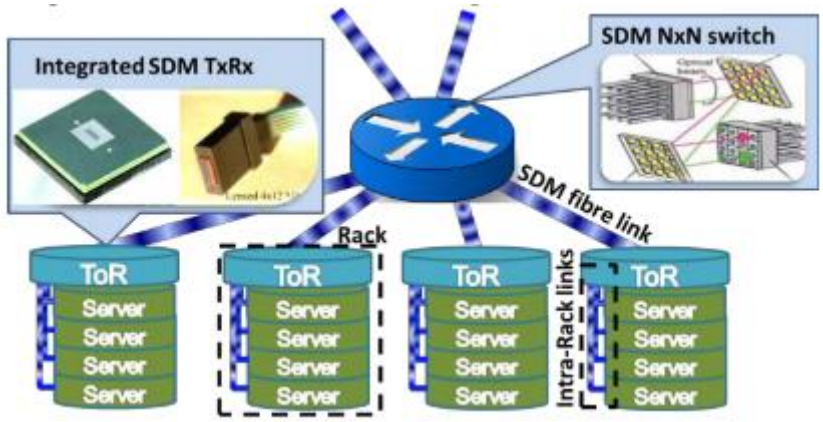


Fig. 1-4: A spatial multiplexing DC communication system [21].

A hybrid of the multi-element fibre and TDM was experimentally achieved. It is worth noting that spatially integrated devices like transmitters (Txs)/receivers (Rxs), converters that facilitate through coupling with spatial optical fibres, minimise valuable space and resources within the DC racks, which leads to an increase in energy efficiency [11]. A key feature to be considered in an optical system is the low level of power consumption; this might be realised if only SDM network is employed, compared to using a combined WDM-SDM hybrid. In addition, employing a low-cost/power VCSELs with a grey interface in the distinct mode channels of the SDM fibre can contribute to achieving higher capacity and energy efficiency.

The concept of an SDM allows minimisation of the network cost per bit for data capacity enhancement. Cost savings can effectively be improved by implementing device integration, which includes integrating multiple Txs, Rxs, and optical amplifiers such as erbium-doped amplifiers (EDFA) in a single circuit with the aid of switches. Different proposal to achieve multiple spatial signal channels has been studied. Fig. 1-5 illustrates the three basic SDM fibres: fibre bundle; multicore fibre (MCF); and multi-mode/ few-mode fiber (FMF).

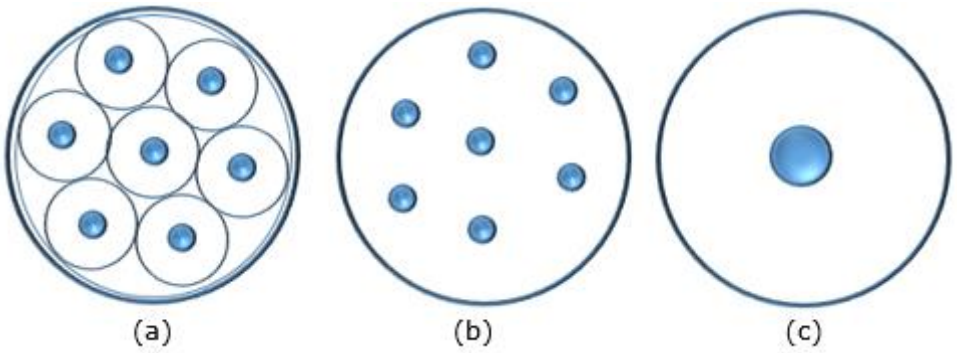


Fig. 1-5: SDM fibres: (a) fibre bundle (b) multicore fibre; and (c) multi-mode/ few-mode fibre

The least complex is to utilise fibre bundle (fibre ribbon/multi-element fibre) as the fibre management is similar to the multiple SMF systems. Hence, it can accommodate a smooth transition during system upgrade by adopting the existing components [24]. MCF is another interesting SDM fibre where individual fibre cores are incorporated in a common glass cladding. Among the superior features are: the optical path length of neighboring cores of MCF suffers less temperature instability, and MCFs can adopt a simpler system architecture as the local oscillator (pilot tone) can be transmitted and shared on the MCFs [25]. Also, weakly-coupled MCFs provide a more straightforward and promising approach as it targets minimum crosstalk in the adjacent cores so that multiple-input-multiple-output (MIMO) digital signals processing is not required for signal recovery. FMF uses mode orthogonality to constitute multiple signal channels [26]. Here, eliminating mode coupling is a major concern, compelling the use of MIMO and DSP. There are also strongly-coupled MCFs, which are in some manner similar to FMF but has the additional advantage of reduced differential mode group delay (DMGD) [27]. It is also plausible to combine MCF with FMF of a common cladding [28]. The highly achieved spatial mode signal multiplicities demonstrated to date adopted fibres of this configuration, which comprises 3-modes × 36-core FM-MCF, and 6-mode ×19-core MCF [29].

The above-mentioned technologies that employ SDM domain by adopting MCF or MMF/FMF are independent technologies that require different approaches. Combining them in an appropriate way can open up a new path of possibility in realising a dense optical communication that employs SDM signal channel higher than 30 to 100 in wavelength division multiplexing (WDM) system [30][31]. Detail reviews on the MDM, MCF and multi-element fibres are presented in Chapter 2.

1.2 Problem Statement

Due to the required optical signal to noise ratio (OSNR) on the SMF and adoption of conventional amplification technique, the use of higher order modulation formats is limited to short haul communication [32]. For a data rate of about 400 Gb/s or beyond, a new low loss fibre with the large effective area (A_{eff}) and low modal dispersion (MD) are required to extend the distance. Nonetheless, using FlexiGrid to improve the system spectral efficiency over SMF increases the capacity by only 20%. Several possibilities were adopted for enhancing transmission capacity, for example, a modulation that adopts different amplitude levels, two orthogonal subcarriers [33], and polarisation frequency [34] used in WDM. Hence, the only untapped dimension is space. The new approach of employing SDM has indicated significant potentials, but these potentials can only be exploited if certain challenges are addressed. The most prominent challenge in MCFs is the crosstalk between the adjacent cores, which can be explained as the leaking of optical signal power between the cores. Thus, research addressing the interference caused by the transfer of power in the MCF [35][8] is ongoing. It was shown that crosstalk minimisation can be achieved by employing a step index fibre with a trench-assisted core [36] or using a fibre-bend [37], and can also be mitigated by introducing enough space between the fibre cores. It was also reported that using the bi-directional signal in the cores to avoid lengthy co-propagation can successfully minimise interference [38]. For the MMF/FMF based SDM system, the major obstacles arise when a large number of mode channels are involved. These include the MD [39][40], mode coupling (MCP) [41], and differential mode group delay (DMGD) ([42]), making it extremely difficult for long distance communication. In addressing this issue, large MIMO digital signal processing can be employed on the receiver side. It is crucial to note that MIMO complexity scales up with an increase in the number of modes. Recently, a 22.3 km transmission that includes spatial and polarisation with 30×30 MIMO-DSP was reported [43]. Employing MMF/FMF for MDM system or a vortex fibre for orbital angular multiplexing in long-haul communication is extremely difficult. This can be justified from the previous investigations [44-46], in which both the optical signal and their corresponding OSNR are affected largely by MDL, DMGD, and MD even with the implementation of a complex MIMO DSP.

Other challenging issues with the SDM approach are components integration, compatibility with existing infrastructures, and cost implication for modification. Still, more investigations would be required to access the benefits and at the same time establish its merits when compared with the various network so far used. An

important step toward an SDM realisation would include the standardisation of the transporting medium to engage more research towards fibre deployment. Moreover, a large bandwidth provided by the SDM fibres can largely contribute to the component's integration (Txs/Rxs, S-Mux/S-deMux, EDFA, MCs, and so forth). Scalability in both routing and switching in the SDM network provides great potentials as predominant drivers to the next level of research in this field.

For the backbone and metro systems, new spatial or MM-EDFA amplifiers, particularly those operating based on a cladding pump [47], can be companionable with existing SMF-based system structure to improve integrations. Hence, cutting down in resources, for example using a single MM-EDFA can contribute significantly to power savings. Evident issues related to power and gain balancing still require intensive studies [21].

1.3 Research Aims and Objectives

The research aims to model novel optical devices, specifically MCs and high dispersion optical fibres and investigate a high-speed MDM transmission network that can support four modes (non-degenerative signal mode) channels. The research mainly focuses on the MDM-based device and transmission over MMF/FMF.

The objectives of this research are:

i) To design a novel conversion device with low loss coupling power, this device precisely expected to convert LP_{11} to LP_{01} mode channel

ii) To design a novel mode converter (MC) device using a dual arc waveguide (DAW) to convert three mode channels

iii) To present a mathematical model based on a finite difference time domain (FDTD) for modelling the proposed MCs

iv) To present a mathematical formulation based on the LP-mode matrix method (LP-MMM) for the modelling of two high dispersion fibres

v) To design two novel high dispersion fibres: a high dispersion four-mode fibre with the centre high (CH) refractive index profile, and another one with the centre low (CL) refractive index profile core.

vi) To investigate the transmission performance of a high-speed MDM system adopting NRZ/RZ-OOK using DD approach.

1.4 Scope of the Research

An SDM transmission system comprises multi-element, multi-core, and multi-mode or few-mode communication-based network. The research work is explicitly

proposed for the MDM-based transmission applications and combines different approaches as listed below:

i) Modelling of the MDM photonic device (MCs) for communications based on the MDM transmission network
ii) Optimisation through parametric variations to design models of novel high dispersion fibres and
iii) Numerical investigation of system performance of high-speed MDM transmission network based on the NRZ-RZ-OOK modulation format using DD.

The research work is restricted to consider four distinct modes to represent the channels rather than going down to each degenerate. This is because they are costly and complicated to de-multiplex at the receiving part of the network system. Specifically, the study focuses on the LP_{01}, LP_{11}, $LP_{21,}$ and LP_{02} only. The degenerative modes under each spatial mode are considered as one spatial mode.

1.5 Contribution of the research

MDM communication photonic devices are numerically modelled and studied in this thesis. Hence, each of the contributions below is based on MDM applications:

i) Review of the basic concepts and investigation of the state-of-the-art of the optical devices that incorporate many aspects of the SDM-based communication system. This includes optical MCs, multiplexers, MM-EDFA, and different fibres for the SDM communication system.
ii) Modelling of the MC devices that were achieved based on the finite difference time domain (FDTD) method, which includes:
    a) MC based on the lateral misalignments between two identical multi ring cores (M-RCF).
    b) Modelling of an MDM MC based on a tilted MC-MMF assisted by the DAW. The proposed device can be employed in both multiplexing and demultiplexing due to the expected multi-conversion behaviour.
iii) Demonstration of the new fibres with the equalised MD for the MDM transmission. In this case, two novel high dispersion fibres are modelled:
    a) A high dispersion fibre with the CH refractive index profile, and
    b) A high dispersion fibre with the CL refractive index profile

Both the two fibres demonstrate dispersion equalisation of the four spatial non-degenerate mode channels.

Fig. 1-6 illustrates the flow chart describing different components investigated in the research work.

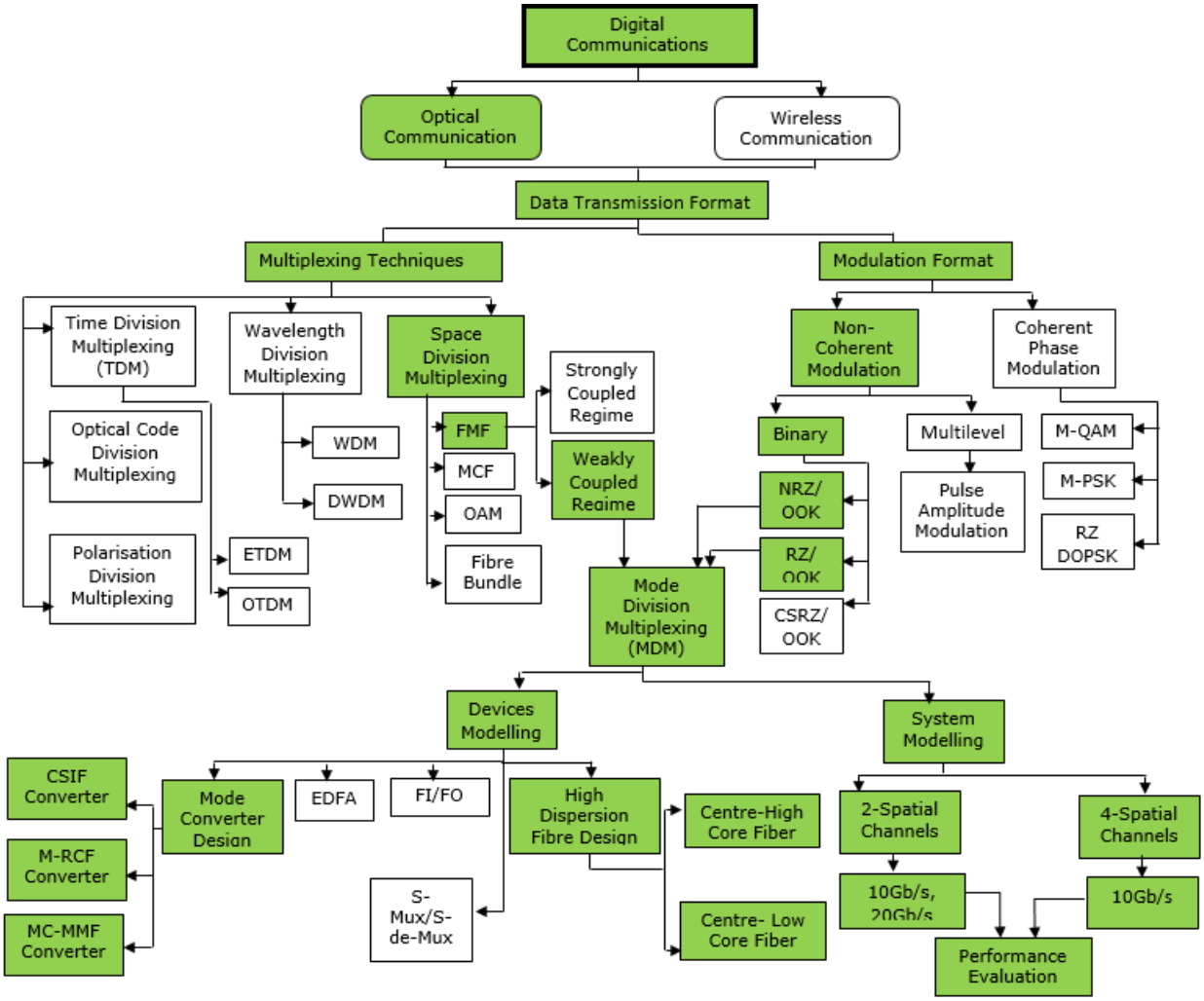


Fig. 1-6: The device design modelling and system analysis presented in the research work are highlighted.

1.6 Software and Computer Aided Tools

The simulation tools used to carry out the research work are:

1) OptiFDTD 12.0
2) OptiFibre and
3) Optisystem 15.20 communication package.

1.7 Thesis Organisations

This section describes the layout of the thesis. The thesis Chapters are:

Chapter 2: Literature review incorporates a review of the SDM system. This includes recent progress in MCs and S-Mux/S-deMux. The chapter also reports on recent finding in the optical amplifiers, fan-in-fan-out (FI/FO) devices. It provides a comprehensive review of the challenges in the optical fibres such as DMGD, MCP, mode dependent loss (MDL). Furthermore, different SDM approaches such as MCF, MMF/FMF, and the fibre-bundles are also discussed.

Chapter 3: Mathematical model presents the mathematical formulation employed for modelling of the devices. Two-dimensional (2D) FDTD equations, TE wave equations, light source model, spectral response model, and power models were presented. Likewise, the mathematical model based on LP-MMM for the MD parameter optimisation is reported.

Chapter 4: Mode Conversion presents modelling and investigations of the MCs. The first converter comprises two identical M-RCF fibres where the effects of cleaving the fibre output at a different angle were examined. The effects were used to model a converter by laterally misaligning the second fibre of the same properties to determine the best position to couple the power. Furthermore, the second mode converter was designed by optimising a tilt angle at the MC-MMF input. This converter, unlike the first device, converts up to three higher order mode channels.

Chapter 5: High Dispersion Fibres discusses two novel high dispersion fibres were modelled by employing LP-MMM. This method was adopted because of its accuracy in calculating dispersion. The optimisation was accomplished by shifting the core layer thicknesses (core-ring radius) to a specified optimised thickness (OPT) value, these values would coincide with that used to optimise the A_{eff}. The goal here is to match the dispersion of the individual modes to a specific reference value of 17ps/(km.nm); this is because most of the practical glassy fibre operates around this value. Additionally, equalising the dispersion close to this value can allow a mode signal to transmit and receive without using the complicated MIMO-DSP module for the dispersion equalisation. The A_{eff} of the modes were evaluated in a similar manner. It is important to mention that the OPT values in the two cases must be the same; this is to avoid conflict between the two parameters (MD and A_{eff}).

Chapter 6: MDM System model demonstrates the transmission system model supporting two and four nondegenerate spatial modes. An LP_{01} and LP_{11} transmission performance of high-speed MDM system adopting NRZ/RZ-OOK using DD were examined. It was found that replacing the conventional modulator with

the DP-DD-MZ modulator can extend the transmission distance. The effects of misalignment between the transmitter and receiver for the two modes (LP_{01} and LP_{11}) were also discussed. Correspondingly, the performance of a transmission system supporting four non-degenerative spatial modes at 10 Gb/s was explored. The analysis here adopts the NRZ modulation format to evaluate the system performance in terms of the minimum power needed (P_N) and the nonlinear threshold power (P_{TH}) at a bit error rate (BER) of 10^{-9}. The receiver sensitivity, an OSNR, and the maximum transmission distance were examined.

Chapter 7: Conclusions and Future Works presents a summary of the key findings and the general conclusions of the research work. Finally, an outlook for future research was highlighted in this chapter. All the optimised table of values obtained during the ring thickness optimisation are contained therein Appendix A.

Chapter 2 Literature Review

2.1 Overview

The adoption of space domain as the next frontier for optical communication has received considerable attention in the last few years. Optical devices are the integral parts of an MDM transmission. Therefore, conducting an intensive review on such devices is paramount to the successful realisation of the overall system. This chapter presents a review of the recent advances in the inline components of an MDM system, consisting of MCs, S-Mux/S-deMux, optical amplifiers, and FMFs. Also presented are different mode conversion and multiplexing schemes. Recent techniques of minimising differential mode gain (DMG) in the optical amplifiers are also reviewed. The review covers other types of amplification schemes and their current standing in the MDM system. This includes optical semiconductor amplifier (OSA) and Raman amplifier (RA). Finally, the chapter also highlights the role of FMF, MCF, and their relationship with FI/FO devices.

The successful deployment of an MDM communication system relies solely on the successful development of novel optical components such as converters, FMF, S-Mux, optical amplifiers and so forth [48][49]. In addition, FMFs for MDM poses various challenges such as large DMGD, MCP effect, MD, and bending loss. Crosstalk (XT) and MDL also require careful design, fibre modeling, and overall system level control.

2.2 Mode Division Multiplexing (MDM)

An MDM transmission system (Fig. 2-1) is made up of spatial mode dependent optical components, which may include spatial laser source (S-CW Laser) that directly generates higher order modes, S-Mux/S-deMux for spatially combining/separating signal mode channels, and MC for the conversion between an LP_{01} mode and higher order modes channels. At the input transmission side, an S-CW Laser that can generate distinct LP modes are required, and S-Mux is employed to combine the distinct modes into an MMF/FMF. If the S-CW Laser can only produce an LP_{01} mode, MCs are required to convert the LP_{01} to higher order modes. Correspondingly at the receiver side, an S-D-Mux is required for spatial separation of the modes plus a conversion device to convert the distinct higher order modes back to an LP_{01} for detection.

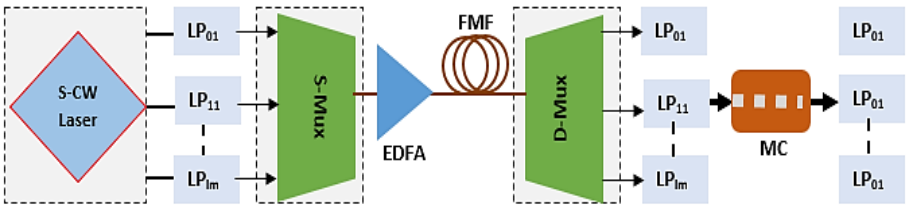


Fig. 2-1: Illustration of the MDM communication system that employs MCs.

2.2.1 Mode Conversion in MDM System

An MC is one of the critical optical devices used for multiplexing in the MDM communication system and can be realised using various types of mode conversion techniques such as phase plate, a spatial light modulator (SLM), spot, planar Lightwave circuit (PLC), fibre coupler, and photonic lantern. Some of the mentioned types can achieve selective LP mode excitation, which is an important aspect of MDM, in which separate signal channels are combined using distinct excitation modes. Most of the available mode conversion techniques concentrate on conversion between the fundamental (LP_{01}) mode and higher order LP modes. Conversion of higher order LP modes was reported in [50], where a PLC-type mode rotator was designed and fabricated for the conversion of an LP_{11a} (LP_{11b}) mode to LP_{11b} (LP_{11a}) mode [22]. Perturbation of an incident field propagating in an optical fibre can induce mode coupling where modes are converted as it tranverse the structure. For example, cleaving a fibre at an angle can influence coupling between mode degenerates [51].

MC/(de)multiplexing using liquid crystal on silicon (LCOS) [52] was realised by utilising SLM. On exciting the device with an LP_{01} mode, the power loss of the (de)multiplexer is around 16 dB, which was increased to 25 dB when employing the masks for an LP_{11} conversion. The additional multiplexing losses were contributed from mode conversion. Furthermore, the use of a phase plate technique was demonstrated [53] with a beam splitter, mirror, phase plate, and lenses aiding the mode multiplexing by means of conversion with coupling loss in the LP_{01}, $LP_{01a,}$ and LP_{01b} of 9.6 dB, 9 dB, and 7.8 dB, respectively. Thus, the mode multiplexer/converter demonstrates mode selectivity of greater than 28 dB.

Free space optics mode conversion approach is insensitive to polarisation and broadband but has higher insertion loss (IL) and is usually bulky. An all-fibre MC based on long period fibre grating (LPFG) written in the FMF is reviewed [54]. An LP_{01} to high order mode conversion (LP_{11}, LP_{21}, and LP_{02} modes) was demonstrated using a single LPFG. The conversion efficiency (CE) of 99% was realised at 1553 nm wavelength. Inter-modal crosstalk on system capacity performance can be

minimised using dynamic routing, spectrum and mode assignment (MC-CA-RSMA) algorithm over SDM-EONs [55]. Here the converter was not only implemented and positioned at each node for flexibility in the conversion but is capable of converting up to twelve spatial modes. The algorithm adopted can highly mitigate crosstalk that influences system-blocking performance when compared to other algorithms. General purpose converter capable of converting virtually any given mode to any desired mode in FMF/MMF for spatial mode application was reported [56]. This was achieved using a phase-only SLM by programming it to a binary phase filter using the SA algorithm. The work precisely demonstrates conversion within LP_{01}, two degenerates of LP_{11} ($LP_{11}a$, $LP_{11}b$), LP_{02}; two degenerates of LP_{21} ($LP_{21}a$, $LP_{21}b$), and two degenerates of LP_{12} (LP_{12a}, LP_{12b}) with more than 80% correlation coefficient and selectivity of over 12 dB was achieved. In addition, MC contributes to the interferometric composition, wavelength filtering, and loss compensation in the MDM system. Finally, the overall applications of MCs contribute greatly to the success of mode multiplexing and amplification in the MDM system. Table 2-1 summarises the recent advancement in MCs and shows that most of the recently reported work concentrates on the conversion of an LP_{01} to the higher order modes. The conversion approach with minimum IL (0.2-0.5 dB) reported here is the mechanical mode converter [57], which employs periodic structure using the grating period (PSG). The all-fiber-doubly tapered converter demonstrates higher conversion efficiency (CE) between 97-99% [58].

The following abbreviations were used in Table 2-1: converter model types (Conv. Type), mode conversion involved (M-Conv.), techniques applied (Method), insertion loss (IL) and extinction ratio (ER). In addition, operating wavelength (OP-WL), and applications (Appl.) of each of the converters are highlighted. Other abbreviations used in the table are centre launching (CeL), femtosecond laser techniques (FLT), a periodic structure using the grating period and bipyramid combined structure (BCS). Also, the remaining abbreviation used includes ultra-compact mode converter (U-CMC), double fibre taper-based mode converter (DT-MC), 1.6°-tilted FM-FBG (FM-FBG), and spatial spectral matching (SSM), higher order mode (HOM) and original to any desired mode (O-ADM).

Table 2-1: Recent progress in conversion device for MDM system.

S/N	Conv. Types	Method	M- Conv.	IL(dB)	ER (dB)	CE (%)	OP-WL	Appl.	Ref
1	Mode-selective couplers	CeL	LP_{01} SMF to LP_{01} MMF	1.7-2.1	Not reported	62-71%	C-band	WDM	[59]
2	integrated MC	FLT	LP_{01} to LP_{02}	<1	Not reported	>80%	C-band	MDM	[60]
3	Mechanical MC	PSGP	LP_{01} to LP_{11}	0.2-0.5	Not reported	89 %	Not reported	MDM	[57]
4	All fiber MC	BCS	LP_{01} to LP_{02}	0.5	12	89%	C-band	MDM	[61]
5	Perturbed waveguide	U-CMC	LP_{01} to LP_{lm}	0.5	>13	Not reported	C-band	MDM	[62]
6	All-fiber-doubly tapered MC	DF-MC	LP_{01} to LP_{02}	Not reported	19-30	97-99%	O-, S-, C-Band	WDM/MDM	[58]
7	Reflective MC	FM-FBG	LP_{01} to LP11	Not reported	Not reported	99.5%	C-band	MDM	[63]

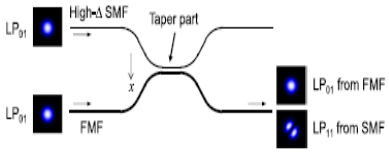
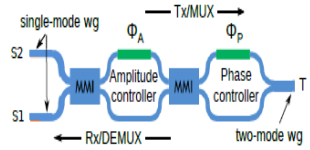
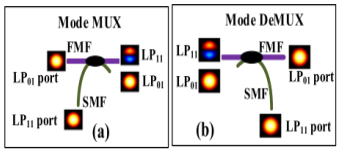
2.2.2 Mode Multiplexers in MDM System

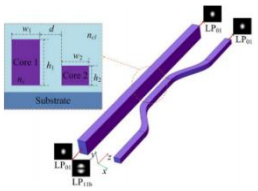
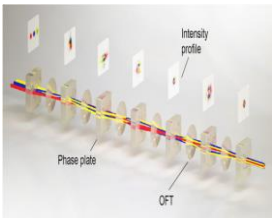
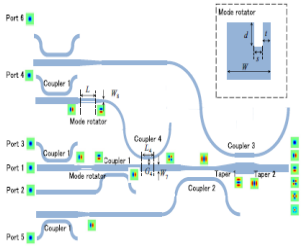
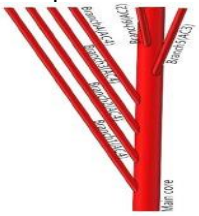
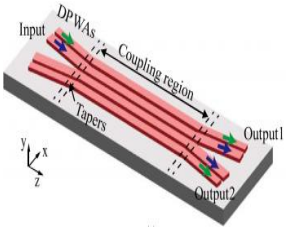
One of the vital devices in an MDM network is the S-Mux, which combines K spatial modes into an FMF. S-deMux operates in the inverse way in which it separates the combined modes back to K spatial signal modes. Different strategies are employed to control the spatial modes of the FMF/MMF. For example, by exciting the fibre input with set of orthogonally combined eigenmodes [2]. Thus, the mode channels are strongly coupled. This brings complexity in demultiplexing and requires full modal diversity and using complicated DSP. Another option may include using fibre and optical components that employ weakly coupled (uncoupled) spatial modes, reducing the DSP complexity to jointly detect the degenerate mode groups [64]. Regardless of the two approaches chosen, there must be a mode-selective S-deMux. The uncoupled approach requires a reduced modal cross talk generated by the S-deMux, so that mode selectivity ensures low MDL. This gives room to compensate the DMGD [65], which drastically reduced DSP complexity during transmission. Other essential issues for S-deMux are IL and the bandwidth to be large enough for compatibility with the WDM. Mode selectivity in multiplexers has been proposed using different techniques. The currently used mode multiplexers in the MDM network is designed based on the free space components such as SLM [52], and phase plate [66]. These are relatively large, with a high cost of productions, and above all demonstrates high IL. Phase plate converters [67] are widely adopted because of their simplicity, at the expenses of high IL. Using mode-selective photonic lantern (MSPL) as an alternative with the distinct input SMF can minimise the IL [65]. However, achieving mode selectivity still remains a concerning issue due to the complication in the fibre modeling. A 10-mode S-deMux demonstrating higher mode-selectivity, using MPLC, with a reduced IL over the full C-band and L-band was reported [68]. It demonstrates average crosstalk of -26 dB, mode selectivity of 26 dB, and higher CE (low IL less than 4 dB when coupled to the MMF) and very low MDL (average MDL 1.2 dB).

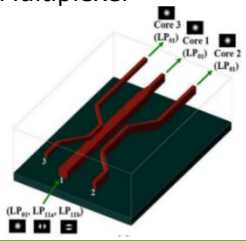
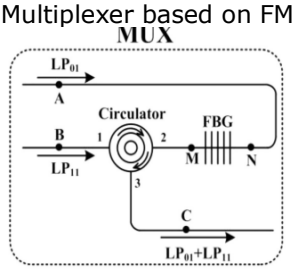
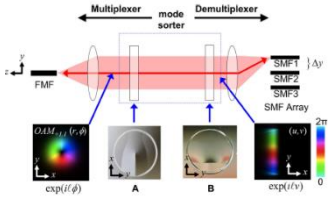
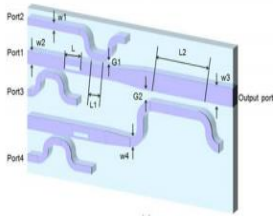
Moreover, all fibre MDM multiplexers, which includes LPFBG [69], mode selective coupler [70], adiabatically tapered fibre multiplexer [71], photonic lantern [72], and PLC [73] are compact, cheap to produce, and demonstrate low IL with high CE. The photonic lantern has the ability of multiplexing many modes with low loss at the expenses of fabrication difficulty. LPFBG multiplexers are small in size and demonstrate low IL, with the narrow operating bandwidth. In opposed to the LPFBG multiplexers, selective mode couplers have the larger working bandwidth, minimum loss, and can be fabricated easily. All fibre selective mode (de)multiplexer for weakly coupled application is reported [74]. Based on the selective mode coupling, a composition of SMF and FMFs were used with the LP_{01}

mode in the SMF coupled to an FMF supporting high order modes. It was achieved by adopting cascaded couplers with the distinct matched-effective indices and by so doing a pair of 6-mode (de) multiplexer was fabricated. The performance of the device was evaluated experimentally by transmitting 6-mode using the DP-QPSK modulation. An OSNR penalty of 3 dB while using partial 6×6 MIMO equaliser was achieved. On replacing it with the full 12×12 MIMO, the OSNR penalty was lowered to less than 1 dB. Recently, a novel three mode scrambling-type multiplexer [75] was reported with a less wavelength dependence, and low ER. Nevertheless, the design is still superior over the conventional S-Mux that works based on the asymmetric directional coupler, especially in terms of scalability to accommodate higher number of modes and fabrication tolerance. This multiplexer was made by cascading a y-branch waveguide with the rotator on silica planar circuit. Table 2-2 presents a summary of the recent technology reported in mode multiplexing for an MDM system; under each device, a brief of the basic finding is highlighted. These include XT, IL, MCP, and ER.

Table 2-2: Summary of the recent technology in mode multiplexing for the MDM system.

Device Technology	**Device Properties**				
	XT (dB)	**IL (dB)**	**MCP(dB)**	**ER(dB)**	**Ref.**
Few/single mode Fibre coupler 	<−20	−2.2 to 1.5	<−20	Not reported	[74]
Integrated mode (de)multiplexer 	-20	<2	Not reported	14.5 to 16.3	[76]
All-fiber mode MUX 	-22 to -20	0.3 (LP_{01}) 1.8 (LP_{11})	Not reported	15	[77]

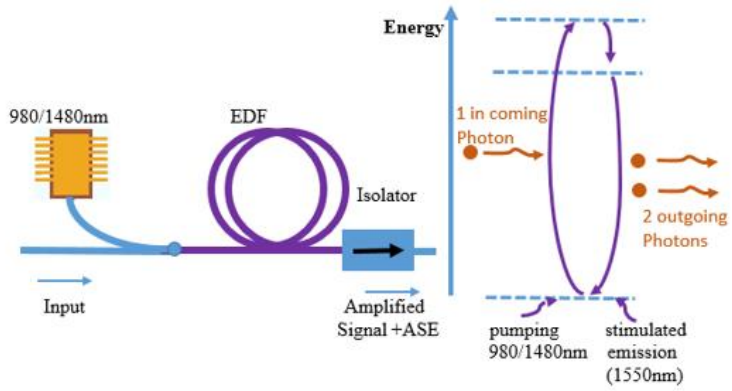
Device Technology	Device Properties				
	XT (dB)	**IL (dB)**	**MCP(dB)**	**ER(dB)**	**Ref.**
DC-based mode (de)multiplexer 	< −55 (LP_{01})	9.6 (LP_{01}) to 12.8 (LP_{11b})	0.95	Not reported	[78]
3-mode MUX based on MPL 	-26	<4	Not reported	Not reported	[79]
Six mode Mux PLC coupler 	-23 to -16	1.3	Not reported	>15	[73]
Mode wide bandwidth (de) multiplexer 	< −20	< − 0.05	Not reported	Not reported	[80]
2 × 2 dual-mode 3 dB coupler 	14	0.25 (average)	< 1	Not reported	[81]

Device Technology	Device Properties				
	XT (dB)	IL (dB)	MCP(dB)	ER(dB)	Ref.
Compact 3D Waveguide Mode Multiplexer 	−23.2 to −14.6	1.7 to 6.4	10	Not reported	[82]
Multiplexer based on FM- FBG 	> -20	4	Not reported	Not reported	[69]
OAM mode sorter 	Not reported	– 9	< 1.5	Not reported	[83]
PLC-Based 4M-(de) multiplexer 	Not reported	<3.5	<1	> 20 (S,L), >15 (C)	[84]

2.2.3 Optical Amplifiers in MDM System

The most recent and crucial optical amplification technique is the EDFA. This technology has the advantage of avoiding optical signal conversion into an electrical signal before it undergoes reconversion again into an optical one. Unlike other conventional optical amplification schemes, it has the advantage of reduced system complexity and power consumption. Fig. 2-2 (a-b) shows the schematic and mode of operation of an EDFA. It consists of an optical fibre doped with Erbium ions. The input signal is coupled into the fibre with the help of a pump signal at a wavelength of 980 nm or 1480 nm. Signal pumping can be injected from both or either side into the Erbium-doped fibre (EDF). This results in co- or contra-

propagating pump signal (Fig 2-2). Within the EDFA, the photons of the input signal at a wavelength of around 1550 nm can force the erbium ions to go back to the initial lower energy state and hence generating replicas of the signal photons by a process called stimulated emission [85]. In some cases, the Erbium ions can fall back to their initial energy level without experiencing any stimulation by signal photons, which referred in the literature as spontaneous emission. The produced photons is amplified by the same mechanism as in the initial photons.



(a) (b)

Fig. 2-2: (a) Schematic of a typical EDFA and (b) Basic amplification principle in Erbium-doped amplifier.

This process describes the amplified spontaneous emission (ASE) [86] and considered as the main source of noise generation in optical amplifiers. The noise figure (NF), is a quantity of an amplifier due to generated ASE and quantified by analysing the physical process inside the amplifier.

Optical amplifiers are crucial to the successful deployment of large data capacity within an MDM system. MDM fibre amplifier design to support many spatial mode channels can be engaged to extend transmission to a longer distance (long haul communications) and improve bandwidth in the SDM system. However, there are certain issues with the Erbium-doped amplifiers in FMF. One of which is getting an adequate amplification gain at less differential mode gain (DMG) between the entire transporting mode channels for the overall performance of the MDM network. This is because the translation of the DMG to excessive MDL can lead to system outage [87]. In reducing DMG in MM-amplifiers, it is crucial to limit the overlapping integrals of the distinct modes which serve as a measure to minimise the overlapping between the excited ion, and signal mode intensity profile.

Different techniques can be used to reduce DMG. For example, it can be achieved through adaptive equalisation or reconfigurable mode gain. This can be

achieved in two different approaches. One of which is to put a control measure for the modal content of the pump (core or cladding). Here, the distinct pump mode powers are excited to a few-mode-EDF with parallel mode signals. The differential gains can be reduced by varying the pump power to the desired value. Some theoretical explorations have adopted using this approach, in which the gain of an MM-EDFA can be controlled by turning the mode contents of the pump. It has been achieved by varying the power and input orientation, which allows a dependent gain to be tuned over a given dynamic range [88]. In addition, using SLM was also proposed as a technique to equalise the differential gain by adjusting the pump modes power [89]. Varying the powers of the separate amplified modal signals was achieved by placing an SLM immediately after the amplifier to equalise the differential gain. Using higher-order mode pumping to minimise the differential gain has also been investigated experimentally. A 2-mode group amplifier (LP_{01} and two degenerates of LP_{11}) was demonstrated by adopting a step-index fibre consisting of a doped profile core region [90]. Furthermore, an investigation of all-fibre type MM-EDFA and control DMG using LPG was reported [91]. It was demonstrated that the DMG can be altered between the range of -7 dB to 5 dB. The differential gain control was achieved by adjusting the LP_{01} to LP_{11} pump mode-ratio.

The second technique that minimises DMG is by controlling the doping level of the Erbium ions to the modes power distribution by, for example, the ring dope ions. An investigation of the 4-mode amplifier has been demonstrated [92], which involve the use of a fibre design constituted by two sections of distinct-doping levels. It demonstrates a low gain of less than 1 dB in the 4-mode EDFA that uses simple pumping configuration by adopting the LP_{01p} and LP_{41p} as the pump modes. Moreover, a five-mode amplifier using a ring-doped profile has achieved a gain greater than 13 dB at DMG of less than 5.7 dB [93]. Similarly, a 6-mode EDFA with circular ring-structured profiles was initially used on Er^{3+}-doped for the gain equalisation that employs a conventional fibre fabrication procedure [94]. Nevertheless, gain equalisation through this technique is difficult to realise experimentally. Thus, a new approach based on a 'pixelated' Er^{3+}-doped core was implemented to achieve gain beyond the initial limit. In addition, a six-spatial mode optical amplifier with a reconfigurable DMG control was demonstrated using a bi-directional pumping technique in association with the Erbium doped amplifier [95]. A specially tailored doped-profile leads to achieving a gain greater than 20 dB for the LP-modes, demonstrating DMG of less than 2 dB. The photonic lantern was used to achieve mode selective amplification in a large mode area cladding-pumped Yb-doped fibre [96]. This reported signal gains of around 19 dB and

output power greater than 1 W. In another report, a gain control six-mode EDFA was demonstrated by adopting MSPL for the pump light control. The device shows the ability to amplify the six modes separately with DMG value of less than 1 dB and a signal gain of around 16.17 dB [97]. An DMG can be reduced using ring-core EDFA (RC-EDFA) as reported in [98], a ring core and conventional step index EDFA are compared in terms of DMG. It was found that the RC-EDFA demonstrates lower DMG of 1.6 dB and 1.8 dB for LP_{01} and LP_{11}, respectively. While a 9.2 dB and 6.1 dB are respectively determined for the LP_{01} and LP_{11} using a conventional step-index EDFA.

Multicore EDFA (MC-EDFA) is also considered as a key element for the integration of MCF SDM-based network. A cladding pump approach was reported for an SDM-EDFA to realise 18 channels (comprising 6-core by three-modes) [99], which utilises a common pump diode that exhibits similar complexity of a single mode EDFA (SM-EDFA). The amplification delivered a total power of greater than 20 dBm per core and NF of less than 7 dB over the C-band. This SDM-EDFA can combine SDM-WDM over parallel MMF span. In addition, a core with the multi-ring index profile adapted to MC-FM-EDFA was reported. Fig. 2-3(a) depicts a cross-section of the fabricated MC-FM-EDF [100], which consists of 7-cores, all laid close to each other in hexagonal form. The core pitch of 40.3 μm housed by a cladding of 153 μm in diameter was employed. The core in each of the FMF supported 2 modes (LP_{01} and LP_{11}), cutting-off the LP_{21} mode at 1470 nm wavelength.

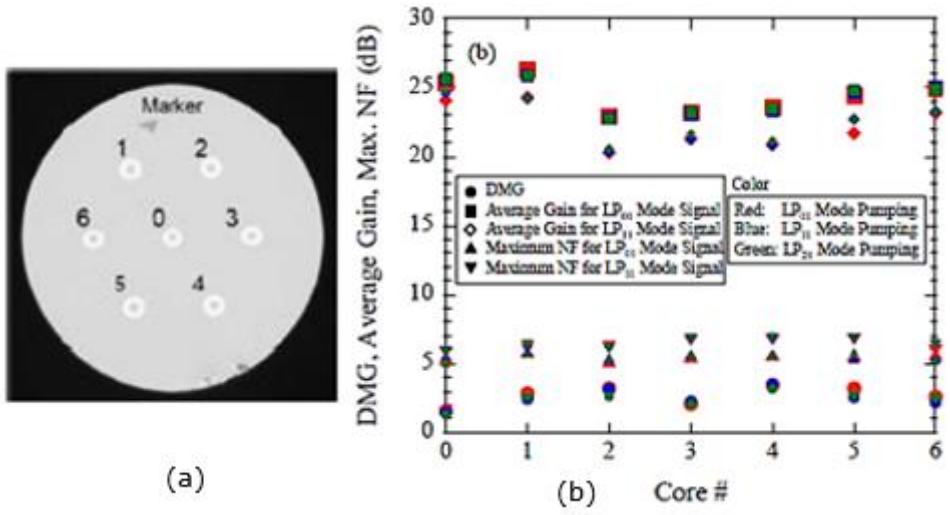


Fig. 2-3: (a) A cross-section of the multicore few-mode-EDFA (b) DMG average gain; Max. Noise figure (NF) for multicore few-mode-EDFA.

The MC-FM-EDFA connection was made to a WDM coupler modules (using free-space coupling), which comprises of optical isolators and changeable binary phase plates to pump the light to achieve mode conversion [101] with the help of FI/FO device. As reported in [101] both the gain and the noise characteristics of the MC-FM-EDFA are calculated core by core. The amplification gain and the NF values are shown in Fig. 2-4(b) [100]. Table 2-3 summarises the recent progress in SDM/MDM-EDFA technology. It includes the method applied in the amplification process, the NM involved, and the average gain (AG) obtained. Also included in table 2-3 are the DMG, NF, and the pump power (PP). Other abbreviation used in the table includes nondominated sorting genetic algorithms (NSGA-II), intensity and field model (IFM), intensity model (IM), Field model (FM). Cladding-pump (CP), few-mode distributed Raman amplifier (FM-DRA), and ring-core erbium-doped fiber (RC-EDFA). Also, overlap integral (OI), mode-selective bidirectional pumping (M-SBP), extra annulus doping (EAD) and semiconductor optical amplifiers (SOA) are used.

Table 2-3: Recent progress in SDM/MDM optical amplifiers.

Opt. Amp	Method	NMs	AG(dB)	DMG (dB)	NF (dB)	PP (mW)	Ref.
FM-EDFA	NSGA-II	12 (7-group)	22.2	3.3	Not reported	300	[102]
6-modes FM-EDFA	IFM	6	17.1	7.1-15(IM) 0.3-0.8(FM)	Not reported	600 (300 for each vector mode)	[103]
RC-MC-FM-EDFA	CP	18	>20	Not reported	<7	15×10^3 (6-cores × 3 modes)	[99]
FM-DRA	SOA	2	15.46	< 0.4	1.2 (LP_{01}) 1.1 (LP_{11})	30-260	[104]
Elliptical-core FMEDF	Not reported	5	17.5	7	4.3-15.1 (all modes)	100	[105]
RC-EDF	OI	2	17	1	<5.2 (LP_{01}) <5.8 (LP_{11})	Not reported	[101]
FM-EDFA	EAD	22 (6-group)	>20	< 0.9	Not reported	≥220	[36]
6M-EDFA	M-SBF	6	>20	<4 (all modes)	Not reported	338.8	[95]
FM-EDFA	CP	6	>20	~3	6-7	1300-3100	[106]
TM-TDFA	CP	2 (group)	17-18.3	Not reported	7-8	3200	[107]

Besides EDFA, another type of optical amplifiers can be employed to enhance performance in an MDM system. For example, semiconductor optical amplifiers (SOAs) such as the one reported in [108], and RAs [109] can be engaged for the MDM communication. The SOAs are not frequently used today in the long-haul communication because of their drawbacks such as high noise, polarisation dependence, and nonlinear effect or fast gain response.

Fig. 2-4 (a-c) compares the relative intensity noise, relative noise frequency, input output power, EDFA pump power and SOA deriving currents [108]. The SOA indicates a greater noise level than EDFA, which is because of higher involvement in ASE, higher optical absorption, and higher instability in the electron density injected. However, the OSA has a peculiar feature that helps in reducing the RIN of the light at the output below the input intensity level under some conditions. The line-width spectrum is very difficult to increase in the case of both SOAs and the EDFAs in linear operation. The noise effect in SOA was reported in [110] and is caused due to the counter phase fluctuation in the electron density, which was associated with optical power [111]. This is not observed in the case of EDFA, because it has less instability in atomic density [112]. However, a four-mode OSA was recently demonstrated, which aimed to suppress equalise gain issue in EDFA for an MDM, and has demonstrated the potential of providing an equalised-gain for multiple input signal mode channels without introducing additional complexity, and economically more affordable than EDFA [113]. Moreover, RAs are hardly used in the current commercial system because of their complexities and requires high pumping power. One of the advantages of RA over EDFA and SOA is that it gives room for achieving distributed amplification [104], which in turn reduces noise generation. Therefore, combining EDFA and RA technologies can allow extending transmission distance more than adopting only EDFA.

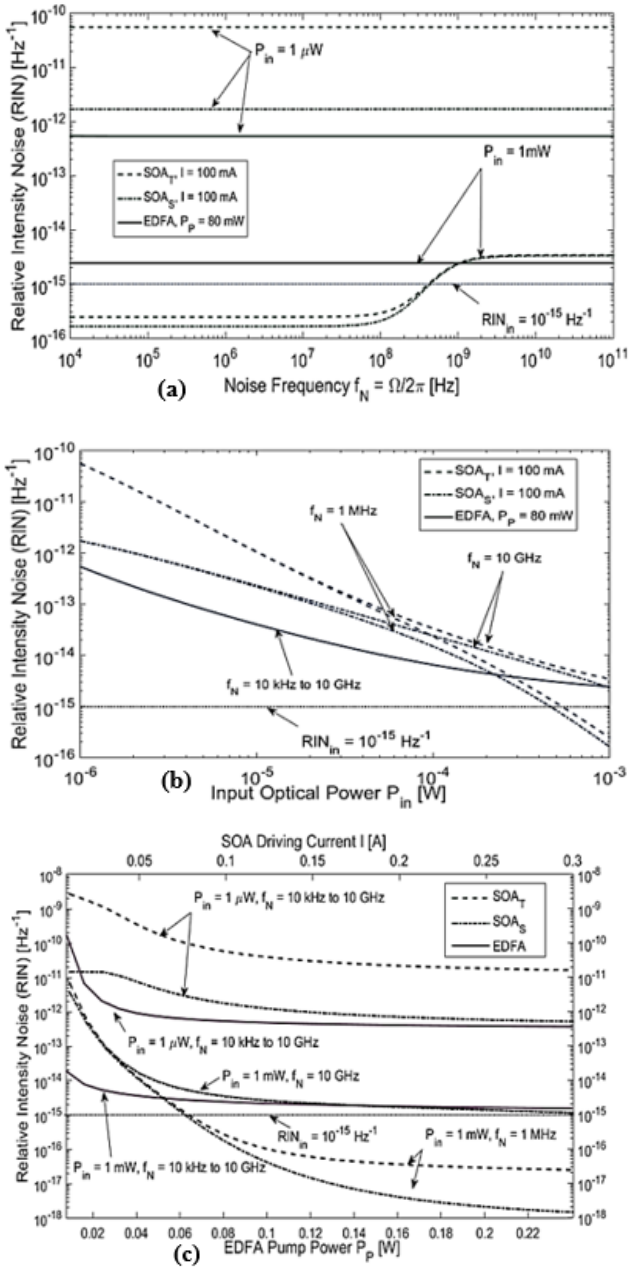


Fig. 2-4: Relative intensity noise (RIN) properties of the output light: (a) frequency (b) input optical power and (c) pump level dependency versus Noise [108].

2.2.4 Uses of FMF in MDM

The concept of using FMF for MDM is to restrict the number of spatial modes propagation in a fibre to avoid MD. This is because the higher the number of propagating modes the more severe the MD and the less bandwidth available [26]. Significant progress has been made to minimise the MD. For example, recently two novel high dispersion fibres with equalised MDs were reported [114]. Spatial

modes transmitted through a single core and modes in an FMF are assumed orthogonal with respect to each other. Theoretically, each of the independent signal channels can be modulated onto each spatial mode, transport them through the same fibre and retrieve the signal at the output with minimum or no loss of information [115]. The data capacity per fibre is multiplied proportionally to the number of spatial modes transported by such fibres. This is in analogy to MCFs where the increase in system capacity is multiplied by the number of cores or number of fibres itself [30].

Fig. 2-5 depicts the basic of the most commonly adopted approaches in MDM, it consists of two techniques, one uses linearly polarised modes as the independent channels (Fig 2-5a), and the other includes each degenerate as a separate signal channel (Fig 2-5b).

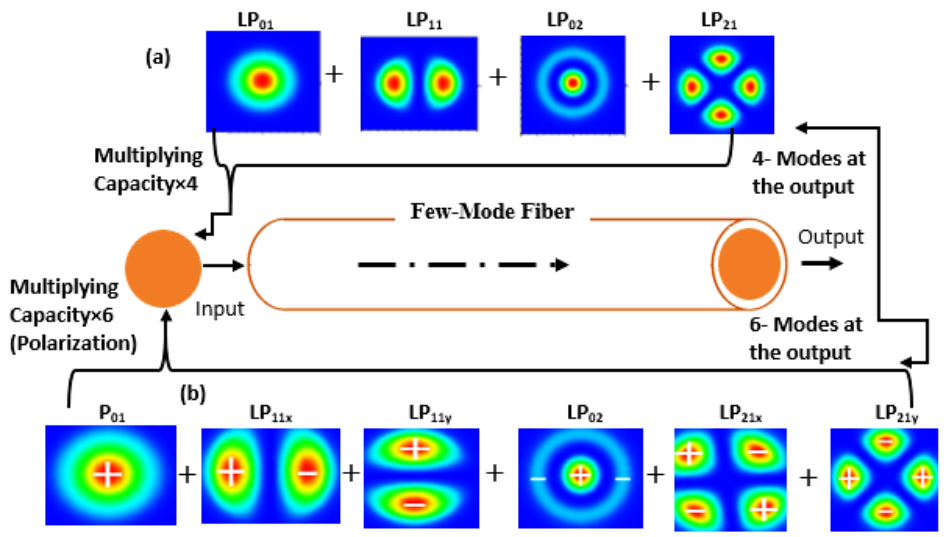


Fig. 2-5: Schematic of the basic concept of an MDM using FMF: (a) Constituted by an LP mode only, resulting in four-mode operation and (b) Both spatial and polarisation modes are included, which results in six-mode fibre operation.

Fig. 2-5 (a) is restricted to using four distinctive modes (LP_{01}, LP_{11}, $LP_{21,}$ and LP_{02}) each representing a signal channel rather than going down to each degenerate, this is easier to deal with during mode (de) multiplexing. In Fig 2-5 (b), the degenerate modes (LP_{01}, LP_{11x}, LP_{11y}, LP_{21x}, $LP_{21y,}$ and LP_{02}) under each spatial mode is considered as one channel, this adds more capacity to the system. X-pol and Y-pol are costlier and more complicated to de-multiplex at the receiving part of

the network. It is difficult to perform PDM for SDM network. The technicality of the implementation is challenging for both experiment and numerical investigation.

2.2.4.1 Strong and Weakly Coupled Approach in FMF

FMFs have so far demonstrated higher potentials compared to their counter MCF. The main challenge is reducing the DMGD and MCP among propagating modes. Two approaches are now under intensive research: weakly and strongly coupled approaches.

Weakly–coupled approach [116][117] targets at reducing coupling effect between the propagating modes so that each LP mode can separately serve as an independent channel and can be detected separately using simple MIMO technique irrespective of the number of LP modes involved. To achieve this, the FMF must be carefully designed in such a way that MCP is drastically mitigated to an acceptable level. Compatibility of the step index fibre (SI-fibre) with existing SSMF technology makes it promising and proven to be the most effective to utilise under weakly coupled regime [118]. It is worth mentioning that such approach contributes very high DMGD. However, looking at the simplicity it offers in design and manufacturing processes, it is considered as a good alternative. To design an FMF under this regime, the highest normalised frequency value is chosen, which allows N number of modes to propagate in the fibre, cutting off the next remaining high order modes. The core index is optimised after knowing the value of V-parameter (V_p). The core diameter is obtained from the V_p relation, which is given by:

$$V_p = 2\pi a/\lambda.\,(n_{cr}^2 - n_{cl}^2)^{1/2} \qquad \text{Eq (2.1)}$$

where *a* is the core radius, n_{cr} is the core index, n_{cl}, the cladding index, and λ represents the operating wavelength. Setting the index spacing $\{\triangle n_{eff}\} > 1.0\times10^{-3}$ for any two adjacent LP modes can reduce coupling effect [119-120]. Bending losses must be reduced to a minimum value (at a radius 32mm) to ensure robustness for all LP modes within the intended value of V_p. A_{eff} is expected to be >100μm² to suppress intra-model non-linearity along the fibre [118].

The strongly coupled approach aims at mitigating the DMGD so that the LP modes are simultaneously detected using complex MIMO technique [121-122]. In this approach, the coupling is not viewed as an issue, but the fibre requires a careful design strategy to minimise DMGD. A fibre with the graded index profile (GI profile) is prepared for high-bandwidth FMF targeting low DMGD. Such type of fibres is capable of demonstrating DMGD of as low as 0.1 ps/m at a wavelength of 850 nm with the expectation of high bending losses [123]. This configuration is nevertheless well adopted to strongly coupled fibre for MDM systems [124][125], for which the DMGD has to be drastically reduced. The same modeling procedure

as in the weakly coupled fibre can be adopted for the V_p selection. In addition, the exponent value that predicts the index shape may slightly differ from 2 to reduce DMGD [124]. The optimisation became more difficult as the number of transporting modes increases, most especially when good mode robustness (low bending loss per turn at a specified bending radius at 1550 nm) is targeted. DMGD can increase to a value higher than 0.1ps/m as the mode count in the propagating fibre is greater than or equal to four. However, it was reported that introducing a trenched cladding can minimise the bending sensitivity [126], and help improve a trade-off in DMGD and the bending losses [127]. It has been reported that DMGDs of below 0.025 ps/m was achieved for trench-assisted GI supporting six-LP-modes [128]. This fibre design has a sensitivity to small profile variations, which occurs while manufacturing. A better way to minimise DMGD is to adopt DMGD-compensation technique for FMF links [129]. This approach was implemented long ago in MMFs and seems to work perfectly well with FMF [130].

2.2.5 Challenges of FMF in MDM System

2.2.5.1 Distributed Mode Coupling

As discussed in section 2.2.4.1 under the weakly coupled regime, it is significantly important for the FMF to have minimum MCP between the supporting modes. This reduces crosstalk between the multiplexed data streams (channels) [126]. The guided modes in an ideal fibre must satisfy orthogonality and hence, energy remains uncoupled among the transporting modes. This orthogonality can suffer breakage in a real fibre due to the imperfections, which include inhomogeneity in the fibre index or deformations in core size and non-circularly core shape. These effects can give rise to energy coupling between the modes. In addition, imperfections in the channel path or coupling points can cause excessive power exchange among the optical modes. As demonstrated in some reports [131-132], such issue can be dealt with by implementing MIMO signal processing, but for the sake of understanding of the rationale behind FMF characteristics, one must have a proper view of the potential and effects of MCP. Note that MCP between degenerates (modes with the identical phase constants) is stronger, which means a substantial amount of optical power would be transferred between the modes within a close distance (very small distance) [133]. In the case of other modes with reasonable differences in propagation constant e.g. between LP_{11} and LP_{01}, the coupling can be much weaker. Thus, the optical signal may cover up to tens of kilometers without significant coupling among the modes. Theoretically, for imperfect optical waveguides, the energy will couple between modes when the perturbations have a longitudinal frequency component, which could be introduced

from the difference in longitudinal propagation constants {Δβ} of the modes. The strength of coupling between two modes is a function of Δβ [134-135]. It was also reported that the coupling between modes of adjacent mode groups is given by:

$$\mathrm{MCP} = (\Delta\beta)^{-(4+2q)} \qquad \text{Eq (2.2)}$$

where *q* characterises the power spectrum of the changes and typically carry values between 0 and 2, depending on the nature of the external perturbations. Thus, the best way to reduce MCP is to increase the value of Δβ between the modes.

2.2.5.2 Differential Group Delay (DGD)

Modes group velocities that carry independent MDM data stream are different. Thus, pulses can be launched simultaneously into the various modes of the optical fibre, which propagate and arrive at the receiver at different times. MCP and DMGD may both be present and could lead to crosstalk that spread across multiple bit periods. The MIMO signal processing components that suppress signal channel crosstalk become complex due to the accumulated DGD between the individual modes and the crosstalk induces over many bit periods [136]. The DGD is expressed as

$$\mathrm{DGD} = \frac{\left(\mathrm{n}_{\mathrm{eff}}^{\mathrm{lm}} - \mathrm{n}_{\mathrm{eff}}^{\mathrm{l'm'}}\right)}{\mathrm{c}} \qquad \text{Eq (2.3)}$$

where n_{eff} is the effective index, l, m, are the azimuthal and radial number respectively, c is the velocity of light. This effect would be more severe for a long haul SDM transmission [115]; hence, it is crucial to develop means to minimise the DGD. It is also extremely challenging to reduce both the DGD and MCP simultaneously.

2.2.5.3 DMGD Accumulation with Transmission Distance

DMGD accumulation is proportional to the transmission distance, as well as to the magnitude of Δβ. Mode coupling effect depends on the issues related to fibre deployment. Moreover, cabling and splicing effects need to be considered thoroughly. Cabling stress increases the distributed MCP by inducing some additional source of perturbations in the fibre. Additionally, splices and connectors also bring some discrete MCP [137]. Even by taking into account small and random MCP, it can be proven that the DGD grows linearly with increasing length [138]. When a short signal pulse is launched simultaneously in each mode, the variation in arrival times of the pulse is given as a function of the fibre length, L [139]:

$$\langle (T - \langle T \rangle)^2{}_{av} \rangle = \frac{DMGD^2 l_c L}{4}\left[1 - \frac{l_c}{2L}(1 - e^{-(2L/l_c)})\right] \qquad \text{Eq (2.4)}$$

where l_c represents correlation length, T is the time-of-flight through the fibre length. Note that from Eq (2.4), the spread in signal arrival time normally scale up with the product of square root of the correlation length and the fibre length ($l_c L$). This scaling law can similarly be adopted for any guides irrespective of the number of modes involved [140][141].

2.2.5.4 Measurement of Impulse Response

The method of launching light pulse at the same time in the various modes has been in practice for a long time. DGD in FMFs is relatively large to quantify by a mere comparison of the difference in arrival time of the light pulses that were launched simultaneously into different modes. It is the same approach that has been adopted in DGD measurement in MMF [142]. The difference in arrival time of the modes at the end of fibre allows determination of the DGD. To determine the sign of the DGD, it is crucial to figure out which mode corresponds to which pulse at the receiver. This can be achieved by demultiplexing the mode at the receiving end or by varying its launching properties (relative power in the two modes). Fig 2-6 shows an example of an impulse response schematic splicing at a point, on two-mode fibre (TMF), which adopts an overfilled launch condition. The LP_{01} was converted to LP_{11} mode at the splicing point. The additional pulses (coupling pulses) are caused by coupling initiated at a splicing point.

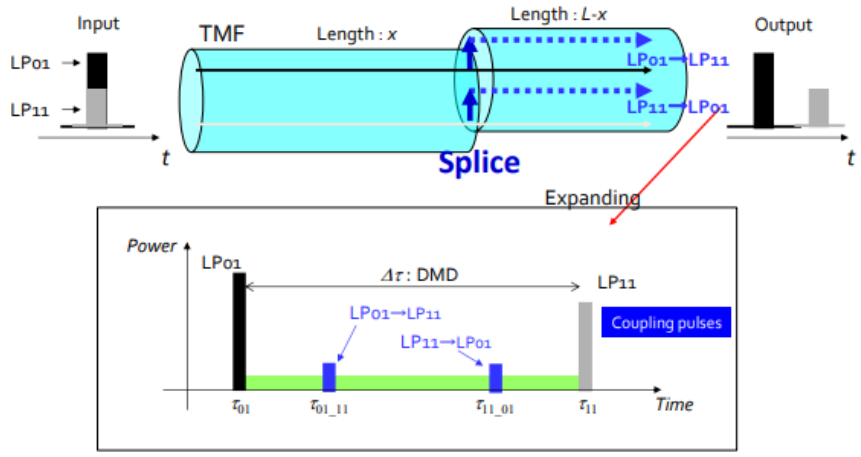


Fig. 2-6: A diagram depicting an impulse response at a point of splicing [137].

2.2.5.5 Differential Mode Attenuation (DMA)

One of the key issues in FMF transmissions is the attenuation of individual mode as it propagates along the fibre length. The major challenge is the fact that MIMO processing technique is unable to compensate for DMA effects. It has been reported in [143] that the signal degradation does not depend on the DMA over the entire end-to-end optical link. For example, a 20 dB DMA results in a loss of system capacity of approximately 20%. This 20 dB is equivalent to 0.02 dB/km of DMA for a 1000 km link, 0.05 dB/ km for a 400 km link, 0.1 dB/km for a 200 km link, and 0.2 dB/km over a 100 km link. Hence, it is inevitable to device a means of limiting DMA to a lower value to support backbone signal propagation over traditional distances. An indirect way of assessing DMA effects is by optimising channel performance, which can be done by optimising the power launch into each mode, the difference in the required power between modes is due to DMA [26].

2.3 Spatial Division Multiplexing (SDM)

A practical SDM system realisation can be comprehensively understood by clear identification of the four main approaches illustrated in Fig. 2-7 (a-d). The key difference is based on the employed fibre category, which determines the type of system to deal with. It is crucial to have unanimity between the individual spatial signal channels to minimise the required space needed of the SDM system.

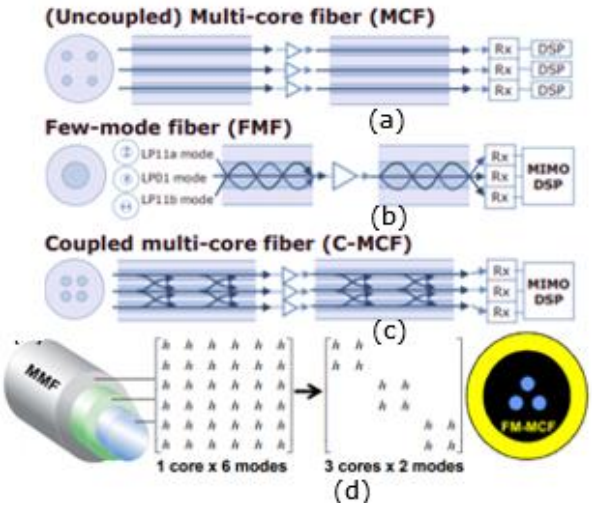


Fig. 2-7: Common SDM fibre and corresponding transmission systems: (a) uncouple multicore (b) few-mode fibre; (c) coupled multicore, and (d) example of a DSP complexity table suitable for a six-mode multimode fibre and a three-core two-mode FM-MCF. The symbol 'h' indicates complexity. In both cases, the solution results in an SDM factor of 6 and shows reduced complexity in the total MIMO calculation in the second case [26].

This can reduce the overall cost of both system operation and deployment. The unanimity anticipated across the system includes the entire fibre length, optical amplifiers, and transceivers as illustrated in Fig. 2-8 (a-c). Another important issue is reducing performance-limiting interactions in spatial channels and transmitting signals. Considering the mentioned criteria, each of the proposed approaches has specific potentials and challenges in MIMO complexity (Fig. 2-7d). In the following section, each of the four approaches would briefly be reviewed.

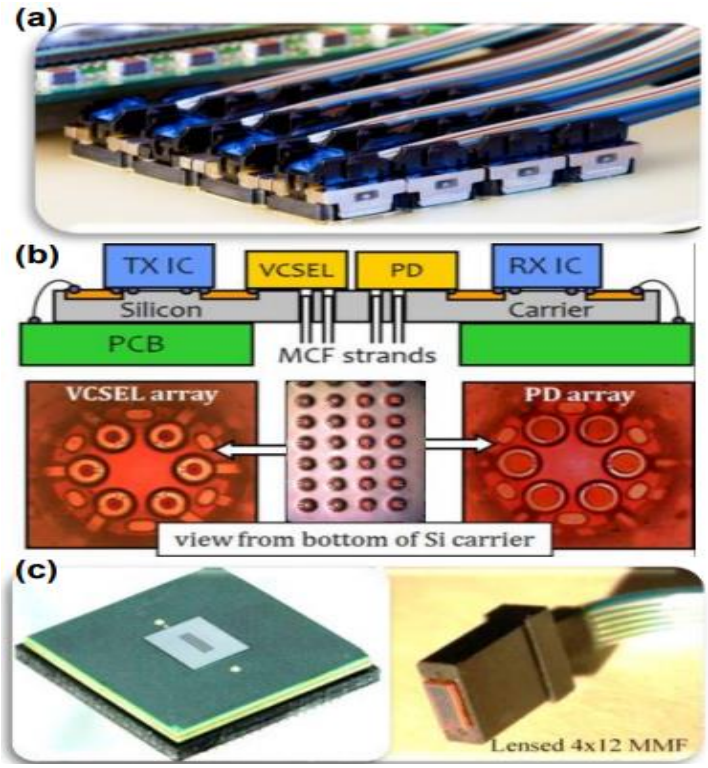


Fig. 2-8: Different SDM transceivers: (a) Avago Minipod™ adopting 12-single mode ribbon [144] (b) multicore fibre photonic transceiver chip [145] (c) VCSCEL/PD (4×12), which interfaces a multimode fibre bundle opto-chip that support a 480Gbps transreceiver [146].

2.3.1 Multi-element Fibre (Fibre-Bundle)

The data, capacity over a conventional SMF has become insufficient to match the demands of the current optical systems. One of the approaches considered to increase communication bandwidth is to deploy multiple numbers of SMF in parallel. Theoretically, this approach is visualised as one form of the SDM [21]. Unlike in multiple packed coaxial copper cables, optical fibres demonstrate no crosstalk between the associated fibres in a bundle when putting them as multiple elements. Deploying a single mode fibre-bundle (SMF-B) demonstrates no additional propagation impairments compared to SMF-based network [21]. The first demonstration of SMF-B was reported using core-pumped spatial amplifier [5], a 3-SMF-B and 7-SMF-B with no crosstalk was demonstrated. Fig. 2-9 (a) shows the schematic cross-section of the 7-SMF-B core-pumped fibre. The major drawback with this approach is the higher cost of production because of using a single diode assigned to each core. The cladding-pump that implements a single common pump diode was developed.

The launching into the cladding pump was achieved using a delivery fibre element that finally coupled the pumping light to the fibre element. Fig. 2-9 (c) and Fig. 2-9 (d) illustrates the extension of the SMF-B in the fabrication of the passive MDM fibre for data propagation. Also showing in Fig. 2-9 (e) is an extract of the 7-SMF-B assembled preform on the draw tower.

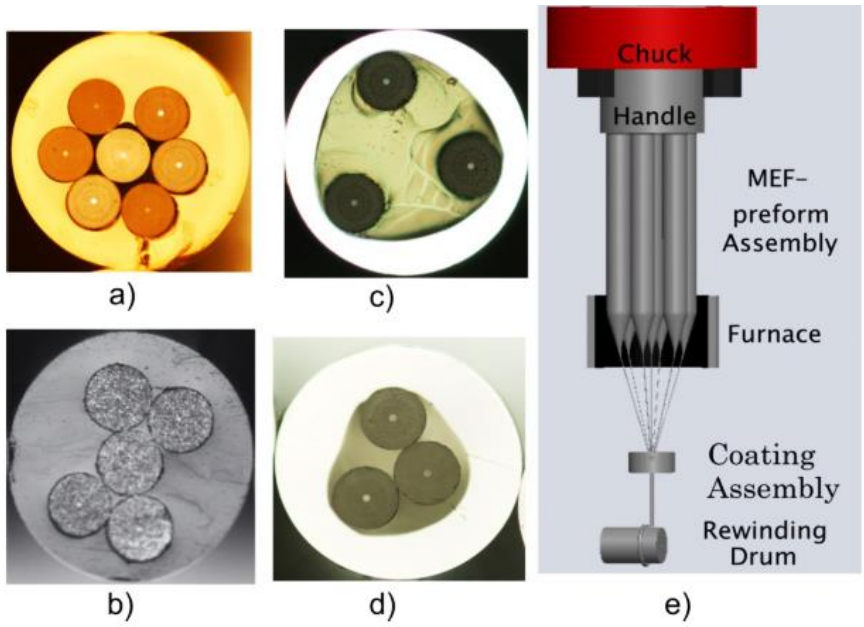


Fig. 2-9: Cross-section of multi-element fibre fabrication: (a) demonstrate in core-pumping optical amplification (b) using the cladding-pumping technique (c) and (d) transporting fibre and (e) diagram depicting seven multi-element preforms on the draw tower[5][24].

Another key issue for realising fibre bundle is the connecting devices such as FI/FO component. It aligns and couples each of the single core (de)multiplexer coupling individual FM with the parallel SMFs. The requirement is either to combine FI/FO device to a few mode-multicore fibres (FM-MC) and arrange them in an array of mode (de)multiplexers for the individual FMF or integrate them in a similar way as in FI/FO integrated photonic lantern, with fabrication achieved using ultra-fast laser inscription [147]. The model of the FI/FO so far reported mainly targeted single mode multicore fibres, including multi-element type [148], a fused taper [149], and the one applicable to a free space optics [150]. Recently, FI-FO device with improved alignment aimed to achieve low loss, low MDL (less than 2 dB) at connection terminals was reported [151]. The report described in detail the design processes and fabrication procedure of the FI/FO device, which can be a good

candidate in the fibre bundle for FM-MCFs. As shown in Fig. 2-10, the configuration of this device comprises two ferrules and split sleeve. A cladding of 246 μm was used, and the FM-MCF insertion was made to couple into the micro-holes, which fit into the ferrules. In addition, the single core FMFs was made to fit the hexagonal micro-hole of the ferrule.

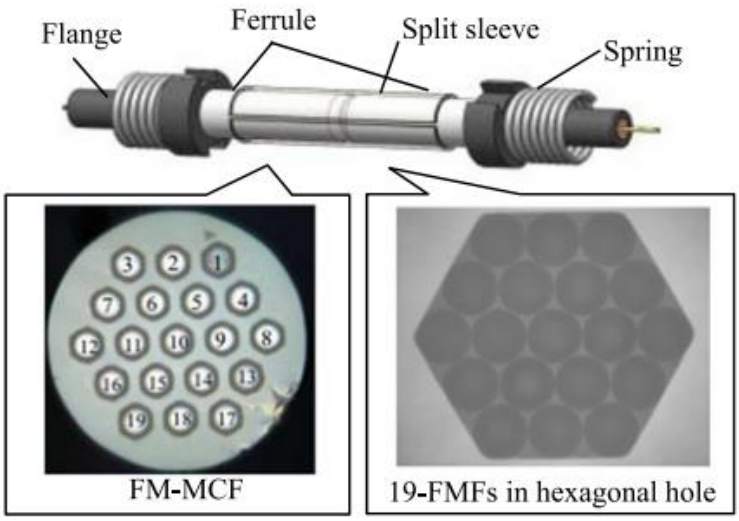
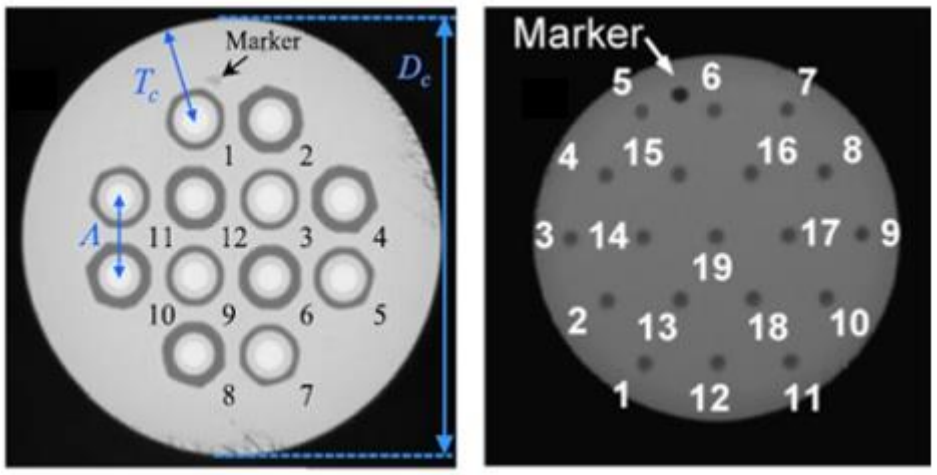


Fig 2-10: Diagram of a fabricated multi-elements type pluggable FI-FO device [151].

Single fibre bundle technology can be considered a candidate to burst data capacity through SDM implementation in optical fibre communication. It provides a crosstalk free platform between the spatial mode channels and can splice using conventional splicing procedure.

2.3.2 Coupled and Uncoupled MCF

The uncoupled approach adopts transmission of independent signals through distinct cores of the same or similar fibres. The promising advantage of this approach is that it demonstrates no significant crosstalk. This is realised through employing high integration in the inline fibre. Although crosstalk is not much anticipated, the cores must have enough separation distance from each other [150]. As shown in Fig. 2-11 (a-b), a different approach can be employed to design uncoupled-multi core fibre (U-MCF), for example, design an MCF with heterogeneous core arrangement consisting of two distinct cores to reduce inter-core crosstalk (IC-XT) using the multistep index as reported in [152]. Adopting this core profile reduces and control DMGD without trade-off to intermodal crosstalk.



(a) (b)

Fig. 2-11: (a) Cross-sectional diagram of the fabricated multi-step three-mode twelve-core uncoupled fibre consisting of a square-lattice configuration. The separations between two cores are denoted by odd, and even numbers respectively. Λ, T_c, represents core pitch, and the outer cladding thicknesses respectively, and D_c represents cladding [28] (b) Cross-section of 6-mode 19-core uncoupled fibres [153].

Furthermore, a square lattice structure permits the inclusion of twelve cores in the cladding of 230 μm diameter. This fibre demonstrates inter core-crosstalk (IC-XT) and low DMGD. Moreover, homogeneous core fibres can be employed for the U-MCF. Recently, an ultra-dense SDM optical transmission over six-mode nineteen-core fibres (6-mode-19-core fibre) was achieved [153]. The cross-section of the fibre is shown in Fig. 2-11 (b). Here, the fabrication of the six-mode, 19-CF was processed in such a way to minimise crosstalk between the associated cores, as well as the MCP, which results in a large cladding with a diameter greater than 300 μm and the index contrast (Δ) greater than 1%. A system of 4.5 THz bandwidth capacity at C-band, (19×114×2.05 pbit/s) was demonstrated [153]. This experimental demonstration is the highest recently reported aggregate spectral efficiency of 456 bit/s/Hz.

2.3.3 Coupled Multicore Fibres (C-MCFs)

The core adopted to C-MCFs is closer to one another compared to that in U-MCFs. The cores closeness initiates coupling between the signal mode channels propagating through the multicores. Due to the formation of supermodes, C-MCFs imposes minimum constraints in terms of fibre design and productions. This is at

the expanses of complex MIMO-DSP at the receiver for decoupling the supermodes. Quite reasonable progress has been reported on the experiment using supermodes to achieve transmission. For example, a distance of 1200 km and 4200 km [154-155] was achieved, and the work was presented during the post-deadline conference (ECOC2011, OFC2012). The modulation at 20 GBound was implemented and the supermodes were successfully decoupled by employing a 6×6 MIMO including two polarisations in each mode. Recently, a C-MCF consisting of four-core that demonstrate low MD ($3.14\pm0.17 ps/\sqrt{km}$) operating in the C-band is realised [156]. The design recorded ultra-low mode attenuation (0.158 dB/km), these are the lowest reported dispersion and attenuation in the optical fibre that utilises couple multicore approach. It was achieved based on employing the index profile of ultra-low-pure silica core single mode fibre shown in Fig. 2-12 with a larger A_{eff} of 112 μm^2.

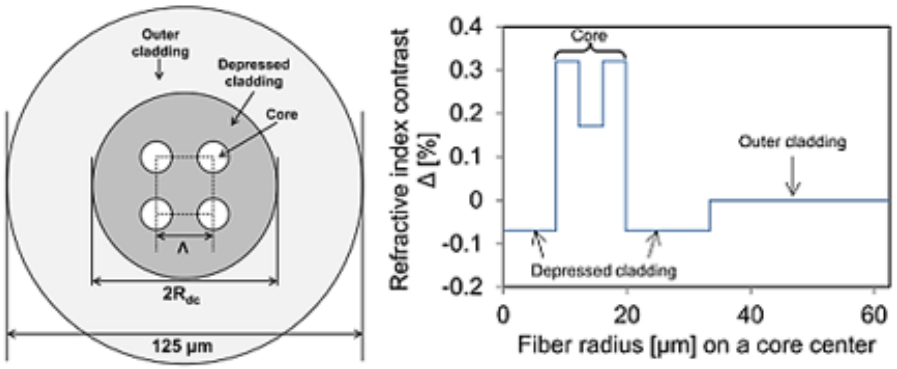


Fig. 2-12: Cross-section and refractive index profile of the C-MCF with a radial line on a core centre [156].

A recent comparison between the commercially available ultra-low losses SMF (ULA-SMF) [157] and a four-core C-MCF [158] that are virtually of the same core configuration was carried out. The two fibres employed are of the same length of 110 km using the same optical equipment. The result indicates that the four-core C-MCF can demonstrate a 0.7 Q-factor higher than that of the ULA-SMF. The maximum launch power targeted a distance range between 500 km and 10,000 km using both QPSK and 16-QAM. This was determined using a combination of the WDM-SDM on 30 Gbaud and a 33.33 GHz channel spacing (15-WDM channels); a 1115200 bit/s/Hz record of spectral efficiency distance product was achieved for the SDM transmission [158].

2.4 Literature Review Summary

A review was presented on the recent achievements in the optical fibre devices, which are paramount to the successful realisation of an SDM system. Different mode conversion techniques were discussed, and it has shown that more effort is needed for the higher order mode conversions as most of the recently reported work centred on LP_{01} mode conversion. Moreover, the recent finding in different mode multiplexed schemes were discussed, including the one exhibiting the highest demonstrated LP-mode selectivity in a ten-mode multiplexer with the average crosstalk of -26 dB, reporting higher coupling efficiency (low IL less than 4 dB when coupled to the MMF) and very low MDL (average 1.2 dB), over the entire C and L band. In addition, the recent advancement of various schemes to minimising DMG in FM-EDFAs and MC-FM-EDFAs is being studied. It also highlights the advantages of RAs over EDFA and SOA, which includes achieving distributed amplification and reducing noise generation. Combining the two technologies EDFA and RA allows extending transmission distance than adopting only EDFA. Finally, recent work on the SDM system was reviewed. It is crucial to have unanimity between the individual spatial signal channels to minimise the required space needed of an SDM system. This can reduce the overall cost for both system operation and deployment. Fig. 2-13 illustrates the chapter summary.

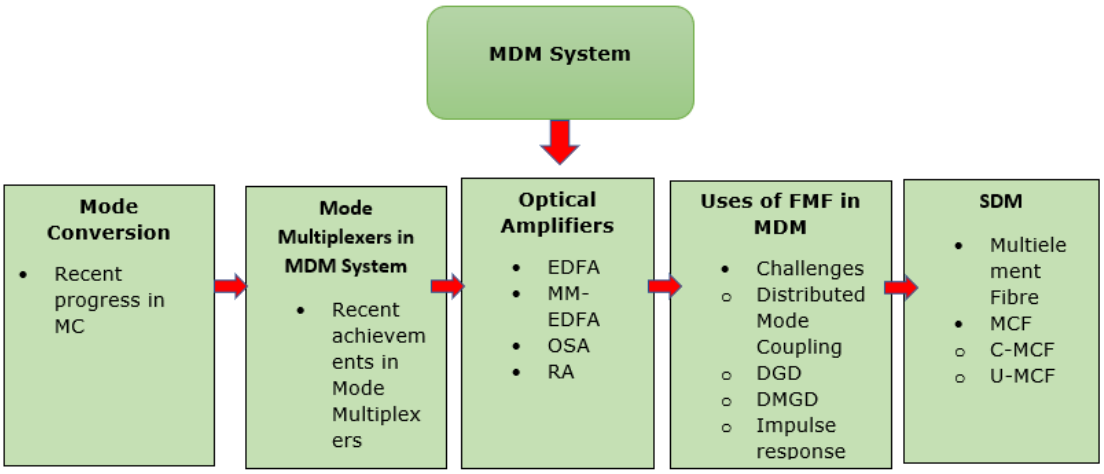


Fig. 2-13: Chapter summary

Chapter 3 Device Mathematical Model

3.1 Introduction

In multi-mode photonic (MMP) information of the high order modes in optical communication devices provide means of increasing channel count for data transmission [126]. It also provides flexibility of device modeling and design. However, the design of MMP devices is different from the conventional SMF that involves only a single mode.

This chapter presents a different mathematical model that serves as the basis of the algorithms implemented in the modeling and analysis of the proposed devices. The formulations for the converter devices include 2D FDTD equations, the TE wave equation, light source model, spectral response model, and power model. An FDTD [159] technique is employed for developing the simulation framework of the two proposed conversion devices. This is due to the capability of the FDTD to concurrently model light propagation, diffraction, scattering, reflection and polarisation effects. Moreover, it has the ability to model material anisotropy and dispersion without making prior assumptions in respect of a field behaviour, which includes slowly varying envelope approximation. This makes the FDTD approach a perfect domain for photonic device modeling. Employing this technique can allow analysing sub-micron optical photonic devices with very good structural details, which signifies a high level of light confinement [160].

On the other hand, an LP-MMM is employed to model two novel high dispersion fibres (CH and CL-fibres) for the MDM system applications [161]. It was achieved by using a matrix to describe the layers, which are written as a 4×4 matrix for the vector modes and a 2×2 matrix for the LP-modes. Details of the mathematical formulations are presented in section 3.4.

3.2 FDTD Formulation

In this section, the mathematical formulations used for the modelling of different conversion tools are presented.

3.2.1 Two Dimensional (2D) FDTD Equations

The FDTD method employs direct mathematical evaluation of the time-dependent Maxwell's curl relations. The following expressions define the lossless and source free relations [162].

$$\frac{\partial \boldsymbol{H}_x}{\partial t} = \frac{1}{\mu_0}\left[\frac{\partial \boldsymbol{E}_y}{\partial z} - \frac{\partial \boldsymbol{E}_z}{\partial y}\right] \quad \text{Eq (3.1)}$$

$$\frac{\partial \boldsymbol{H}_y}{\partial t} = \frac{1}{\mu_0}\left[\frac{\partial \boldsymbol{E}_z}{\partial x} - \frac{\partial \boldsymbol{E}_x}{\partial z}\right] \quad \text{Eq (3.2)}$$

$$\frac{\partial \boldsymbol{H}_z}{\partial t} = \frac{1}{\mu_0}\left[\frac{\partial \boldsymbol{E}_x}{\partial y} - \frac{\partial \boldsymbol{E}_y}{\partial x}\right] \quad \text{Eq (3.3)}$$

$$\frac{\partial \boldsymbol{E}_x}{\partial t} = -\frac{1}{\varepsilon}\left[\frac{\partial \boldsymbol{H}_y}{\partial z} - \frac{\partial \boldsymbol{H}_z}{\partial y}\right] \quad \text{Eq (3.4)}$$

$$\frac{\partial \boldsymbol{E}_y}{\partial t} = -\frac{1}{\varepsilon}\left[\frac{\partial \boldsymbol{H}_z}{\partial x} - \frac{\partial \boldsymbol{H}_x}{\partial z}\right] \quad \text{Eq (3.5)}$$

$$\frac{\partial \boldsymbol{E}_z}{\partial t} = -\frac{1}{\varepsilon}\left[\frac{\partial \boldsymbol{H}_x}{\partial y} - \frac{\partial \boldsymbol{H}_y}{\partial x}\right] \quad \text{Eq (3.6)}$$

where ε is the dielectric permittivity and μ_0 is the permeability. By employing FDTD, the proposed device is placed in the XZ plane with the propagation along the Z direction and the structure is assumed infinite on the Y-axis. As the model is infinite along the Y-axis, it eliminates any term comprising a spatial derivative in the Y direction from Maxwell's relations. Thus, the six expressions in Eqs (3.1) to Eq (3.6) are converted to partially uncoupled relations and are grouped into two: $(\boldsymbol{E}_y, \boldsymbol{H}_x, \boldsymbol{H}_z)$ and $(\boldsymbol{H}_y, \boldsymbol{E}_x, \boldsymbol{E}_z)$. The two field groups illustrate **TE** and **TM** modes respectively; nevertheless, different conversions are adopted with regards to which group of fields changed to which group. Here in our case, we adopt the **TE** designation. The numerical software uses conventional standard based on waveguides that look at the solutions to the field components which results in a given wave equation, comprising of $\boldsymbol{E}_y$ and $\boldsymbol{H}_y$. In this case, the **TE** designation moves to the group with the electric wave equation on the axis perpendicular to the Z-axis (direction of propagation of the fields) that is $(\boldsymbol{E}_y, \boldsymbol{H}_x, \text{and } \boldsymbol{H}_z)$. However, the **TM** designation moves to the group with the magnetic wave relation on the Y-axis $(\boldsymbol{H}_y, \boldsymbol{E}_x, \text{and } \boldsymbol{E}_z)$.

3.2.2 Transverse Electric (TE) Wave

As already highlighted, the 2D scenario evaluates the relations for $\boldsymbol{E}_y, \boldsymbol{H}_x$ and $\boldsymbol{H}_z$ by setting the remaining components to zero, which yields

$$\frac{\partial \boldsymbol{E}_y}{\partial t} = \frac{1}{\varepsilon}\left(\frac{\partial \boldsymbol{H}_x}{\partial z} - \frac{\partial \boldsymbol{H}_z}{\partial z}\right) \qquad \text{Eq (3.7)}$$

$$\frac{\partial \boldsymbol{H}_x}{\partial t} = \frac{1}{\mu_0}\frac{\partial \boldsymbol{E}_y}{\partial z} \qquad \text{Eq (3.8)}$$

$$\frac{\partial \boldsymbol{H}_z}{\partial t} = -\frac{1}{\mu_0}\frac{\partial \boldsymbol{E}_y}{\partial x} \qquad \text{Eq (3.9)}$$

where

$\varepsilon = \epsilon_0 \epsilon_r$ defines the material, ϵ_0 =8.854185 × 10^{-12} $C^2/(N\ m^2)$ and ϵ_r= 3.7 to 10 (for glass), μ_0 defines a free-space magnetic permeability, and the material refractive index, *n* is determined by :

$$n = (\epsilon_r)^{1/2} \qquad \text{Eq (3.10)}$$

To evaluate a given designation accurately, each field is characterised by a 2D array: $\boldsymbol{E}_y(i,k), \boldsymbol{H}_x(i,k)$ and $\boldsymbol{H}_z(i,k)$. The two indices, which are denoted by i and k quantify for the actual number of space steps in both the X and Z axis, respectively. For the **TE** designation, the field's location in the mesh is illustrated in Fig. 3-1. As can be seen, the separation of the **TE** fields is evaluated based on the concept of the 2D Yee Cell [162]. Each spatial cell is allocated to a given field, for example, the ***Ey*** field is assigned to the centre of the FDTD cell which is illustrated by the dashed lines.

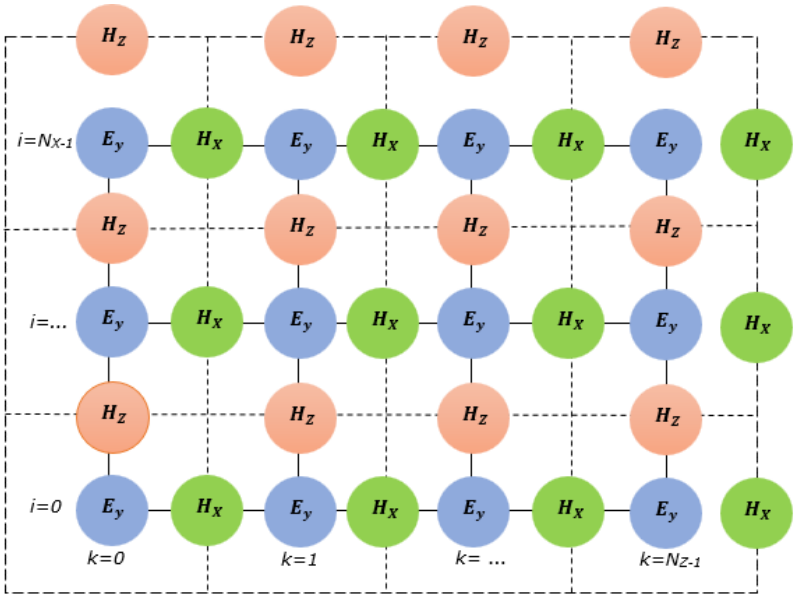


Fig. 3-1: Location of a transverse electric field (**TE**) in the computational layout.

$\boldsymbol{H}_X$ and $\boldsymbol{H}_z$ are the magnetic fields related to the cell edge. The offset fields signify that the derivatives within Maxwell's equations are to be discretised and expressed by employing finite differences, this ensures second-order accuracy in space and time. It is also important to mention that:

- $\boldsymbol{E}_y$ field is related with the indices *i* and *k;*
- $\boldsymbol{H}_x$ field is related with the integer value *i* and (k+1/2); and
- $\boldsymbol{H}_z$ field is related to the integer value indices (*i*+1/2)

The following relations defined the discretisation of Maxwell's equations along the grid [163].

$$\boldsymbol{E}_y^n(i,k) = \boldsymbol{E}_y^{n-1}(i,k) + \frac{\Delta t}{\varepsilon \Delta z}\left[\boldsymbol{H}_x^{n-\frac{1}{2}}\left(i,k+\frac{1}{2}\right) - \boldsymbol{H}_x^{n-\frac{1}{2}}\left(i,k-\frac{1}{2}\right)\right] - \frac{\Delta t}{\varepsilon \Delta x}\left[\boldsymbol{H}_z^{n-\frac{1}{2}}\left(i+\frac{1}{2},k\right) - \boldsymbol{H}_z^{n-\frac{1}{2}}\left(i-\frac{1}{2},k\right)\right] \quad \text{Eq (3.11)}$$

$$\boldsymbol{H}_x^{n+\frac{1}{2}}\left(i,k+\frac{1}{2}\right) = \boldsymbol{H}_x^{n-\frac{1}{2}}\left(i,k+\frac{1}{2}\right) + \frac{\Delta t}{\mu_0 \Delta z}\left[\boldsymbol{E}_y^n(i,k+1) - \boldsymbol{E}_y^n(i,k)\right] \quad \text{Eq (3.12)}$$

$$\boldsymbol{H}_z^{n+\frac{1}{2}}\left(i+\frac{1}{2},k\right)=\boldsymbol{H}_z^{n-\frac{1}{2}}\left(i+\frac{1}{2},k\right)+\frac{\Delta t}{\mu_0\Delta x}\left[\boldsymbol{E}_y^n(i+1,k)-\boldsymbol{E}_y^n(i,k)\right] \quad \text{Eq (3.13)}$$

where *n* is the DTS (discretised time step); *Δx* is the size in real units of a space step (RUSS) along the direction of *Δz* in the Z-direction and *Δt* is the size in real units of the time step.

In order to ensure the accuracy of the source representation, the spatial step size is set between the range of 10 to 20 steps per wavelength [164]. Moreover, to guarantee numerical steadiness of the algorithm, the sampling in time is chosen by the Courant condition. Thus, the time step is evaluated by:

$$\Delta t \leq \frac{1}{c\left(\frac{1}{(\Delta x)^2}+\frac{1}{(\Delta z)^2}\right)} \quad \text{Eq (3.14)}$$

As defined in the 2D formulations, the FDTD algorithm evaluates the fields within the time layout. The output data at each position of the computational domain for a time t are of the form

$$\boldsymbol{E}(x,y,z)=A.G(x,y,z)\sin(\omega t+\Phi_i) \quad \text{Eq (3.15)}$$

where A donates the field amplitude at a specified location, *G* is the wave envelope or profile, and Φ_i represents the corresponding phase.

To obtain the full amplitude wave information as the function of frequencies during simulation, the stationary complex field corresponding to the waveform of Eq (3.15) must be obtained. Thus, the complex field is finally evaluated by performing a DFT on the time domain results of the FDTD simulation. In addition, the final complex wave fields are computed at the particular planes and can be visualised as depicted in Fig. 3-2. The information being sought (amplitude) determines the appropriate position of the output planes.

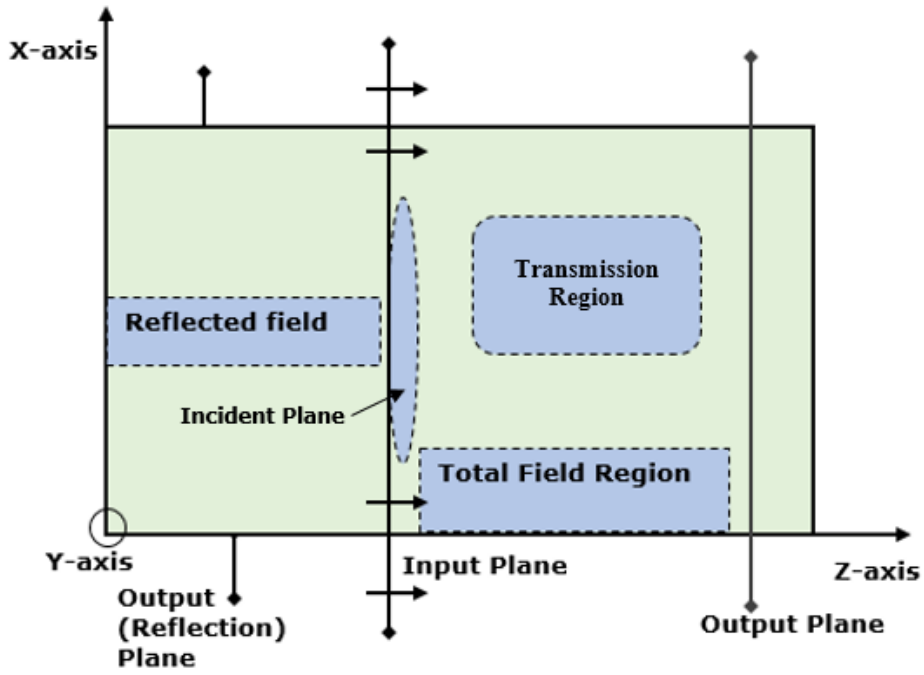


Fig. 3-2: Total field technique for the input plane.

The section in the transmission region for the plane consists of the total field area and the information recorded contains propagation properties of the space that is modelled. By putting the observation line at a position of interest or along the transmission region, a power or any quantity can be determined.

3.2.3 Light Source Model

A light source is considered as the main source that injects energy for the mode excitations in the simulation domain. It can be achieved by either employing an input plane or a point source. Here, in the work carried out, an input plane is employed as the means of injecting energy to the simulation layout. This is due to the ability of the input plane to propagate in a specified direction with the intensity distribution along the incidence plane. The numerical method adopting FDTD produces the solution based on the initial value problem in which on the first time step on numerical evaluation, the entire fields are set to zero.

As shown in Fig. 3-1, the algorithm needs the initial mode excitation to propagate in the computational domain. Because of the 2D implementation here, the propagation is along the z-direction. It is also important to mention that a continuous wave (CW) excitation is adopted. Thus, the incident field is assumed of a single frequency sinusoidal function that provides field amplitude modification. The incident $\boldsymbol{E}_y$ field can be determined using the following expression [159]:

$$\boldsymbol{E}_y^i(x, Z_i) = \boldsymbol{A}.\boldsymbol{F}(x, Z_i)\bullet\left[1 - e^{-t/t_r}\right]\bullet\mathrm{Sin}(\omega t + \theta_i) \qquad \text{Eq (3.16)}$$

Here,

- $\boldsymbol{A}$ denotes field amplitude;
- $\boldsymbol{A}.\boldsymbol{F}(x, Z_i)$ denotes the transverse field profile at the Z_i;
- θ_i is the initial phase offset, this defines the phase difference points along the incidence plane, the offset is used to define the direction of the incident field;
- ω represents an angular frequency of the input field; and
- t_r denotes a constant given by λ/c, this expresses the rise time coefficient of the exponential term employed to ramp the continuous wave signal to full amplitude. When CW source is used, the optical wave propagates until it covers the entire computational domain.

3.2.4 Spectral Response Model

In the FDTD, a single simulation contains a broadband spectral response, this is due to the fact that FDTD is a time domain numerical technique. Fourier transform is employed to determine the spectral response. The solution is computed through the DFT, which is of the form:

$$S(\omega) = \int_0^t S(t)\, e^{-j\omega t} dt \qquad \text{Eq (3.17)}$$

$$= \sum_{n=0}^{N} S(n)\, e^{-j\omega \Delta t} \Delta t \qquad \text{Eq (3.18)}$$

where $S(n)$ defines the DTDS sampled in given steps of Δt, N represents the number of samples in time, and the angular frequency is denoted by ω. Here for the work carried out, the FFT algorithm through which a level of accuracy is attached to the computational speed is adopted. Moreover, in the FFT algorithm employed, the spectral response that was determined is within the frequency range between 0 and f_s $[0, f_s]$, where f_s denote the sampling frequency depending on the step size in time while taking the Nyquist condition into consideration:

$$f_s = \frac{1}{2\Delta t} \qquad \text{Eq (3.19)}$$

Thus, the frequency domain sampling step size is determined by:

$$\Delta f_s = \frac{f_s}{N} \quad \text{Eq (3.20)}$$

$$\Delta f_s = \frac{1}{2N\Delta t} \quad \text{Eq (3.21)}$$

Therefore, based on the defined values, the observation line is computed to determine the power at a given region.

3.2.5 Power Model Based on the FDTD Method

The power at a given region is evaluated using an observation line that is mainly applicable to the 2D computations. An electromagnetic power for the propagating waves depends on both the intensity and the area over a given surface. This intensity is defined as the time-average of the Poynting vector. The Poynting vector ***S*** is expressed as:

$$\boldsymbol{S} = \boldsymbol{E} \times \boldsymbol{H} \quad \text{Eq (3.22)}$$

where, $\boldsymbol{E}$ and $\boldsymbol{H}$ are denoting the complex vector fields, which are defined through the following expressions:

$$\boldsymbol{E} = \boldsymbol{E}_0 e^{j(\omega t - \boldsymbol{k}.\boldsymbol{r})} \quad \text{Eq (3.23)}$$

$$\boldsymbol{H} = \boldsymbol{H}_0 e^{j(\omega t - \boldsymbol{k}.\boldsymbol{r})} \quad \text{Eq (3.24)}$$

where ω denotes the angular frequency, the wave vector is represented by **k** and the position vector by **r**. The two symbols $\boldsymbol{E}_0$ and $\boldsymbol{H}_0$ are representing the complex field amplitudes. Thus, the time-average of the Poynting vector $< S >$ is evaluated by substituting the complex quantities

$$\langle \boldsymbol{S} \rangle = \frac{1}{2} Re(\boldsymbol{E_0} \times \boldsymbol{H_0^*}) \quad \text{Eq (3.25)}$$

$$\begin{aligned} \langle \boldsymbol{S} \rangle = {} & \frac{1}{2} Re\left(\boldsymbol{E}_{y0}\boldsymbol{H}^*_{\boldsymbol{x0}} - \boldsymbol{E}_{x0}\boldsymbol{H}^*_{\boldsymbol{y0}}\right)\hat{x} \\ & + \frac{1}{2} Re(\boldsymbol{E}_{z0}\boldsymbol{H}^*_{\boldsymbol{x0}} - \boldsymbol{E}_{x0}\boldsymbol{H}^*_{\boldsymbol{z0}})\hat{y} \\ & + \frac{1}{2} Re\left(\boldsymbol{E}_{x0}\boldsymbol{H}^*_{\boldsymbol{y0}} - \boldsymbol{E}_{y0}\boldsymbol{H}^*_{\boldsymbol{x0}}\right)\hat{z} \end{aligned} \quad \text{Eq (3.26)}$$

Note that the complex quantities are transformed into amplitude in the computational domain.

Furthermore, the intensity of the electromagnetic field is expressed in terms of the time-average of the Poynting vector while the power as an intensity surface integral. Here, the power over XY-plane is needed, therefore, in this case, the z-component of the Poynting vector is employed, thus, the power is determined as

$$\boldsymbol{P}_Z = I_Z A_{xy} \qquad \text{Eq (3.27)}$$

$$\boldsymbol{P}_Z = \langle \boldsymbol{S_Z} \rangle \, A_{xy} \qquad \text{Eq (3.28)}$$

$$\boldsymbol{P}_Z = \frac{1}{2} Re\left(\boldsymbol{E_{x0}} \boldsymbol{H^*_{y0}} - \boldsymbol{E_{y0}} \boldsymbol{H^*_{x0}}\right) A_{xy}$$

$$= \frac{1}{2} \iint_S Re\left(\boldsymbol{E_{x0}} \boldsymbol{H^*_{y0}} - \boldsymbol{E_{y0}} \boldsymbol{H^*_{x0}}\right) dxdy \qquad \text{Eq (3.29)}$$

This expression provides means for the power to be interpreted as two quantities: $\boldsymbol{P}_Z$ is expressly based on the $\boldsymbol{E}_x$ component, which is denoted by $\boldsymbol{P}_{Z-x}$ and $\boldsymbol{P}_Z$ that is expressed based on the $\boldsymbol{E}_y$ component denoted by $\boldsymbol{P}_{Z-y}$.

Thus,

$$\boldsymbol{P} = \boldsymbol{P}_{Z-x} + \boldsymbol{P}_{Z-y} \qquad \text{Eq (3.30)}$$

where

$$\boldsymbol{P}_{Z-x} = \frac{1}{2} \iint_S Re\left(\boldsymbol{E_x} \boldsymbol{H^*_y} dxdy\right) \qquad \text{Eq (3.31)}$$

$$\boldsymbol{P}_{Z-y} = \frac{1}{2} \iint_S Re\left(\boldsymbol{E_y} \boldsymbol{H^*_x} dxdy\right) \qquad \text{Eq (3.32)}$$

3.2.6 Mode Converters Design Workflow

Fig. 3-3 illustrates the FDTD simulation design procedure, which involves the following steps:

(i) Define the simulation domain

(ii) Select and define the materials and profiles to be implemented

(iii) Create a model by selecting
   (a) Appropriate light source
   (b) Detectors

(iv) Run the simulation

(v) Analyse the results

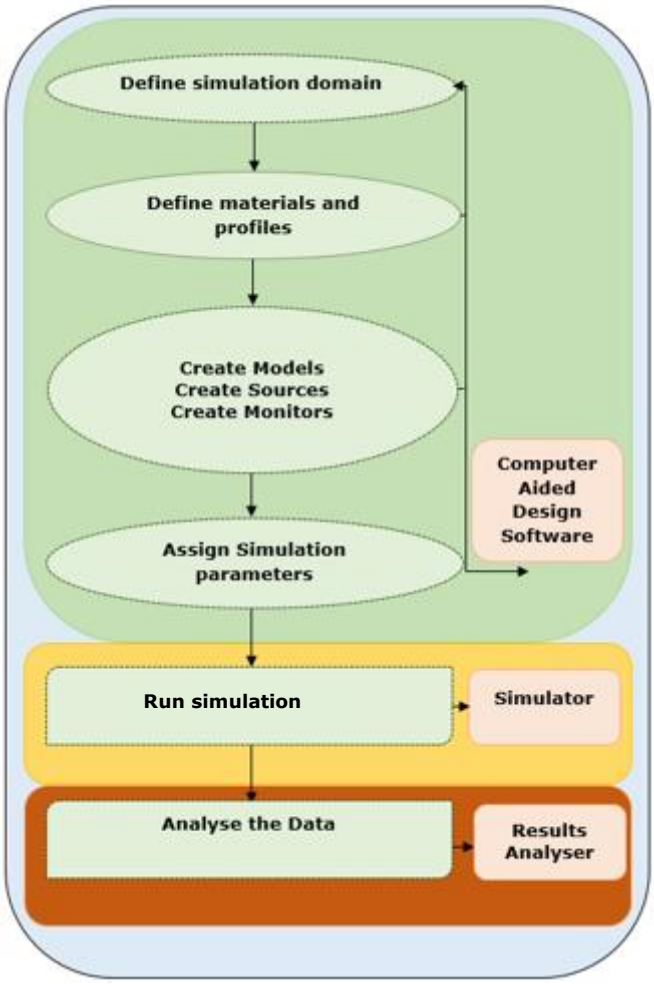


Fig. 3-3: Design workflow for the proposed different mode converters.

3.3 LP_{11}-LP_{01} MC Design Parameters

3.3.1 Multi-Ring Core Fibre (M-RCF)

Fibres with multi-step index profile (MSP) configuration have extensively been studied because of their advantages over conventional step index fibre (CSIF) due to their ability in mode confirenments and control in a core. It is attributed to the presence of MSP, which prevents the desire modes to get propagated in the cladding and operates in a similar way as graded index core (GIC). The index profile is radially decrease from the core centeral axis to the core-cladding interface. Another advantage is the simplicity in manufacturing the MSP during fabrication process. Avoiding the challenges being experienced in fabricating a GIC index with an optimum index profile that is expected to remain stable for a long period. The desired characteristics can be easily achieved using MSP. The core is

made to consist of MSP that performs a similar function as a parabolic curve in a series of steps, merging these steps is easier during the drawing process. As illustrated in Fig 3-4 (a), the light in M-RCF does not propagate along continually curved paths as in the GIC but on the multiple diffracted ray path. Fig 3-4 (b) shows the schematic of the CSIF consisting of a single layer core and a cladding.

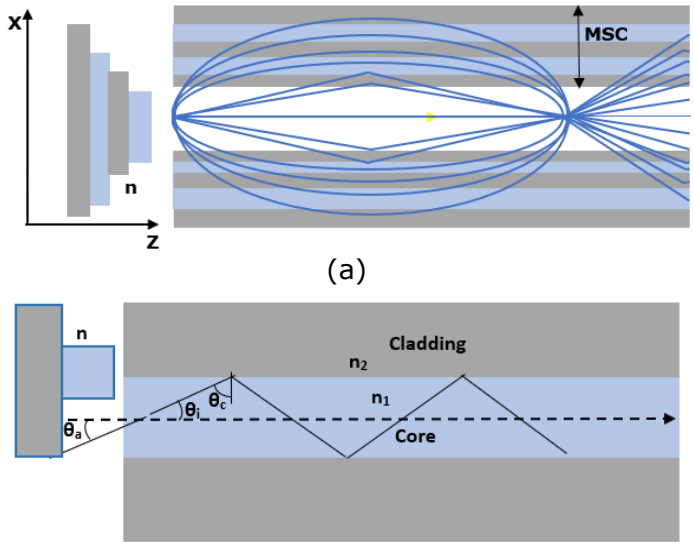


Fig. 3-4: (a) Schematic cut of the M-RCF; and (b) CSIF schematic as the light propagates along the fibre in 2D (xz-plane); MSC stands for the multi-step core.

Fig. 3-5 depicts an index profile of the M-RCF. The fibre comprises a central core having radius r_1 starting from the central axis and a refractive index n_1.

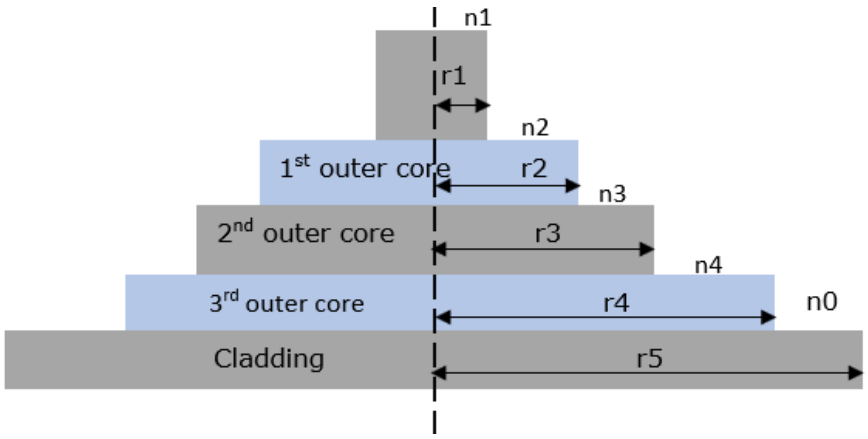


Fig. 3-5: M-RCF core profile, comprising the central layer, three outer cores, and a cladding, each with different refractive index; a central core layer is having the highest refractive index value.

The first outer core (1st outer core) is of radius 'r2' with the refractive index 'n2' lower than 'n1' that surrounds the central core. The second outer core (2nd outer core) consist of the radius 'r3' and refractive index 'n3' smaller than 'n2' and surrounds the 1st outer core. Next is the third outer core (3rd outer core) ring comprising a radius 'r4' and the refractive index 'n4' that is lower than 'n3'. And finally, a cladding surrounding the third outer ring having radius 'r5' and refractive index 'n0'. The refractive index of the first, second and third core ring is calculated using Eq (3.33). The relation can apply to any distribution of a refractive index profile [165].

$$n(\rho) = n_{cr}\left(1 - \Delta\left(\frac{\rho}{r}\right)\right)^{\alpha} \qquad \text{Eq (3.33)}$$

$$\Delta = (n_{cr}^2 - n_{cl}^2)/2n_{cr} \qquad \text{Eq (3.34)}$$

where ρ is the total core radius, r is the central core radius, α is the index profile parameter, n_{cr} is the centre core index, and n_{cl} is the refractive index of the cladding. Eq (3.34) can be approximated to $\Delta = (n_{cr} - n_{cl})/n_{cr}$, when $n_{cr} - n_{cl}$ is very small. The index parameter (α) determine the shape of the profile. When it is equal to 1, a triangular or cone-shaped index distribution is obtained. If α =2, an index profile with parabolic or hill shape is produced. Moreover, when α is equal to infinity (∞) a stepped index distribution is obtained. Table 3-1 summarises the design parameters calculated using Eqn (3.33); it consists of the three-core outer ring radius and an outer refractive index.

Table 3-1: Fibre design parameters for the outer rings.

Outer Rings Radius (μm)			Outer Rings Refractive Indices		
r2	**r3**	**r4**	**n2**	**n3**	**n4**
4	6	8	1.4497	1.4467	1.4445

The two-mode fibre parameters in Table 3-1 were used to define the outer rings refractive indices and material properties in the device setup.

3.3.2 Modeling of the M-RCF and CSIF converters

The commercial software named OPTI-FDTD 12.0 has been used to model the two converters. Fig. 3-6 shows the geometry of two identical fibres that can support two modes used for the modeling.

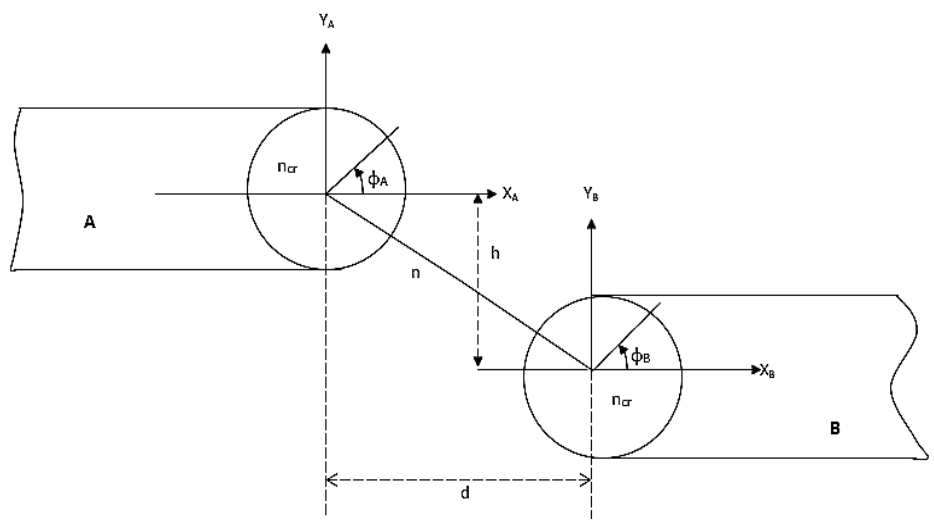


Fig. 3-6: Geometry of the two identical fibres that can support two modes separated by distance d between centres of the two fibres and a lateral displacement h.

3.3.3 Design of MC-MMF

This section presents the design parameters of the converter model based on multilayer core tilt fibre assisted by DAW.

3.3.4 MC-MMF Parameter Evaluation

The first parameter calculated to control the four-mode operation of the fibre is the V_p that was evaluated using Eq (2.1).

Fig. 3-7 depicts the graph of the core radial index profile distributions of the MC-MMF, the fibre is designed to operate at 1550 nm wavelength, this makes it easier to manufacture and reproduce. It comprises the fibre central core (FCC) having radius 'r1' starting from the central axis and a refractive index 'n1'. Next is the first outer core (FOC) layer of radius 'r2' with the refractive index 'n2' lower than 'n1' surrounding the central core; the second outer core (SOC) layer consisting of radius 'r3' and refractive index 'n3' smaller than 'n2' surrounding the first outer layer. The third outer core (TOC) layer comprising a radius 'r4' and refractive index 'n4' that is lower than 'n3'. The layer close to the cladding is the last outer core (LOC), with radius 'r5' and refractive index 'n5' lower than 'n4'. Finally, a cladding surrounds the last outer core layer having radius "r6" and refractive index "n0".

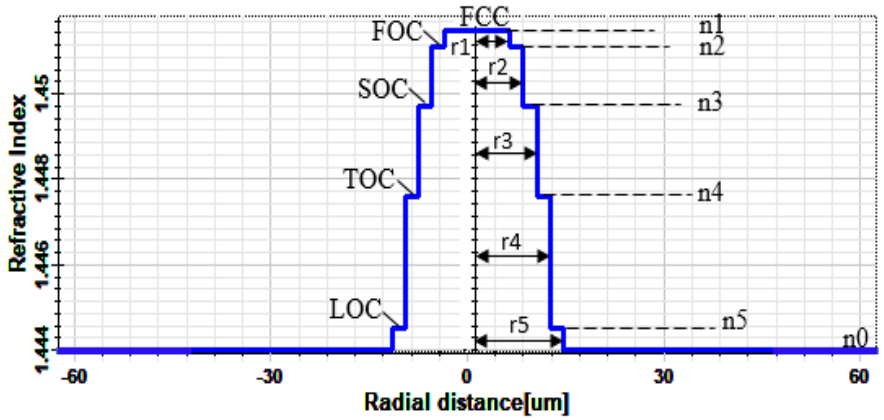


Fig. 3-7: Refractive index profiles of the four outer layers of the MC-MMF.

The V_p is optimised to 5.378 by determining the core radius at a fixed wavelength of 1550 nm, with the cladding index of 1.4409 and a numerical aperture of 0.147.

In order to model a fibre with the low loss [165], less pulse dispersion, large information capacity and low sensitivity to index variation [166], an MC-MMF is considered here. Fig. 3-8 illustrates the basic ray theory that governs the MC-MMF with *M+1* layer. The light passes through *M* internal layers while the outer layer represents the cladding. If only the meridional rays are assumed present and skew rays having a negligible light power after propagating a sufficient length of a fibre, then the ray will be confined in the core layers satisfying Eq (3.35) [166]:

$$cos\theta_1 \geq cos\theta_{1c} = n_{M+1}/n_1 \qquad \text{Eq (3.35)}$$

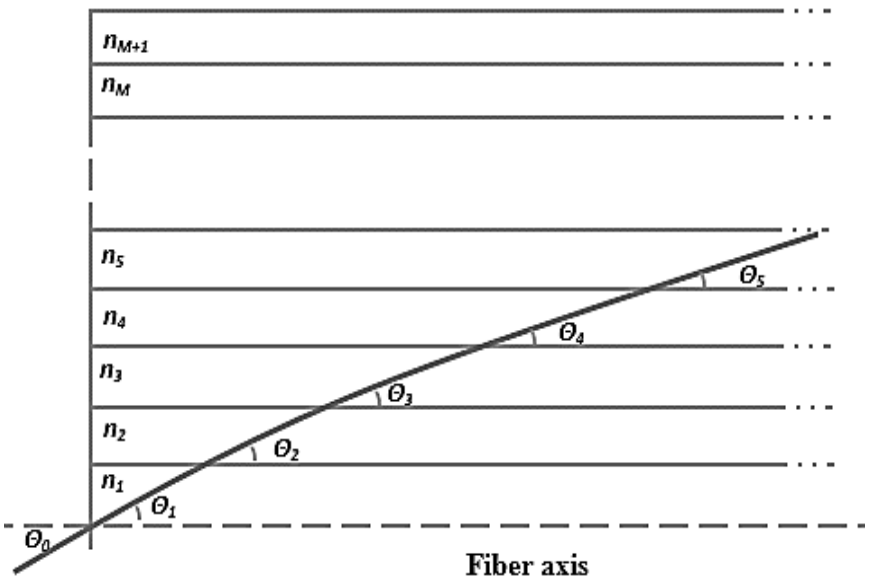


Fig. 3-8: A longitudinal cut of MC-MMF with M core layers.

where, θ_1 represents the angle between the ray and the fibre axis. As illustrated in Fig. 3-8, n_i is the i-th layer refractive index. Assuming that the outermost radius of the *i-th* layer is $r_i = iC$ where *C* is a constant, then the index of the i-th layer can be determined by [166]:

$$n_i = \left[1 - \Delta\left(\frac{i-1}{M}\right)^{\alpha}\right] \qquad \text{Eq (3.36)}$$

where, Δ represents the overall index contrast between a middle core and the cladding, and α denotes a core index profile parameter.

Fig. 3-9 illustrates the calculated ratio of the width of a fibre constituted by *M* number of layers and fibre with a conventional core (M=2), a variation of σ_M/σ_1 (pulse broadening) with α. This was achieved by assuming an index contrast (Δ) of 0.01 (typical practical value of the step index fibre) [166]. The depicted curves are for M= 2, 3, 4, and 8. From the graph, the pulse dispersion is significantly minimised as the number of layers increases. This justifies that the minimum of the curves appears broad, which means variations of the layer indices around the optimal value would not bring significant pulse broadening. Hence, a conclusion can be drawn that MC-MMF can enhance information capacity, a bit rate higher than a C-SIF [166].

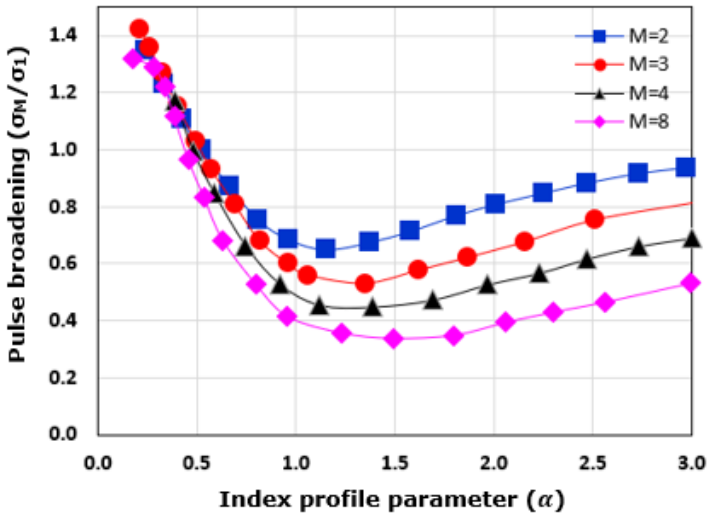


Fig. 3-9: Pulse broadening (σ_M/σ_1) decrease with increase in the core layer [166].

The behaviour of the MC-MMF depends on the parameters such as refractive indices, core thickness, A_{eff}, and λ. The optimisation can be achieved by considering the attributes of these parameters.

Fig. 3-10 illustrates the role of the third layer radius r_3 on the A_{eff} that determines the bending effect [37]. The A_{eff} for each mode was determined by varying the thickness of the third layer (r_3). As shown in Fig. 3-10, the effective areas increase with an increase in the thickness r_3. The values of the A_{eff} were chosen at r_3=7 μm because it corresponds with the thickness of the arc bend.

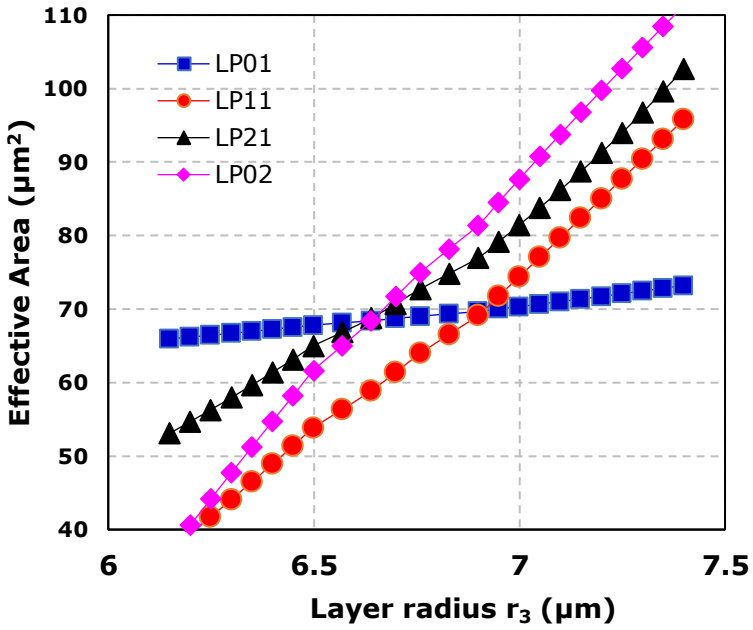
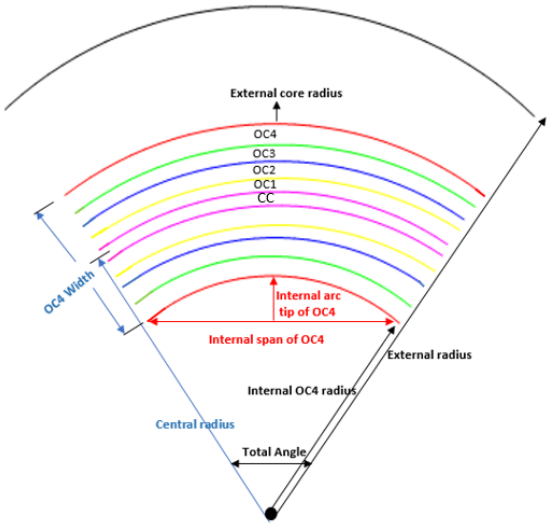


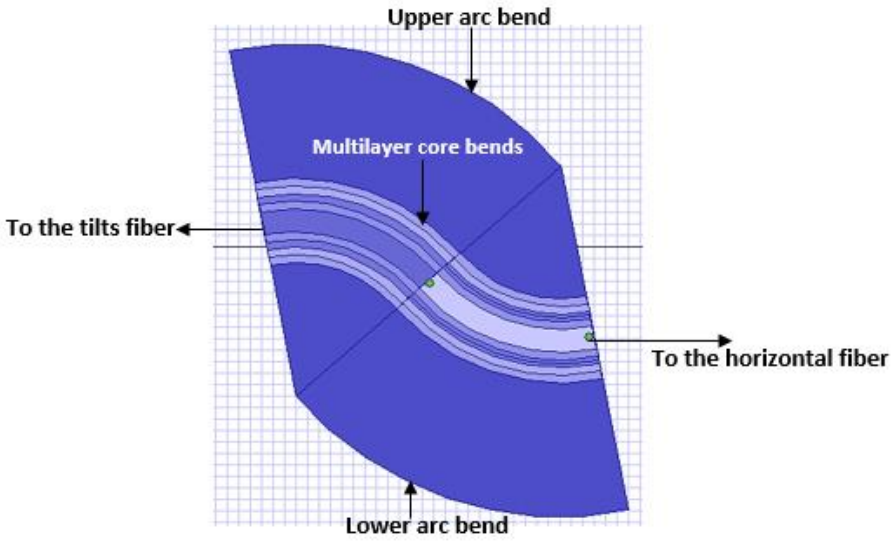
Fig. 3-10: Variation of the effective area with a change in the layer radius (r_3).

3.3.5 Principle and Model of the Arc Waveguide

An arc waveguide is chosen other than using a hard corner to minimise loss between the tilted and collecting fibres interfaces. As illustrated in Fig. 3-11 (a-b), the arc waveguide consists of four outer cores; outer core 1 (OC1), outer core 2 (OC2), outer core 3 (OC3), and outer core 4 (OC4) with radius r_2, r_3, r_4, and r_5, respectively. It retains the same values as the straight fibres (MC-MMF). The central core (CC), which is the innermost core of the arc waveguide has the same diameter and refractive index as the FCC in the tilted (input) and horizontal (output) fibres.



(a)



(b)

Fig. 3-11: (a) Cut off of the core layers in the multistep arc waveguide; and (b) Layout of the arc bends in the simulation domain.

The arc fibre is modelled based on the multilayer core configuration due to two reasons. One is due to the low loss [165] and the second is the decrease in pulse broadening (Fig. 3-9) and less sensitivity to refractive index variation [166]. As illustrated in Fig. 3-12, when an $LP_{l,\ m}$ mode polarised beam is launched into the input fibre with a bend region, the mode degenerates are assumed nearly equally excited. The mode conversion occurs as the mode propagates along the arc

waveguides due to the coupling at the bending region [167]. When a given mode is incident on an inhomogeneous region such as arc bend, a fraction of the mode power is converted to a radiation loss and some part to a guided mode. This makes the mode to lose some of its power and the original pulse is distorted. It is also important to note that radiation loss due to transitions from the straight fibre to the arc bend as depicted in Fig. 3-12 (a) is much higher than that due to a uniform bend when large R is used [167]. Assuming a smooth fibre bend at the junctions between ϕ= 0 (straight region) and the curve portion (L region), the reflected waves are neglected.

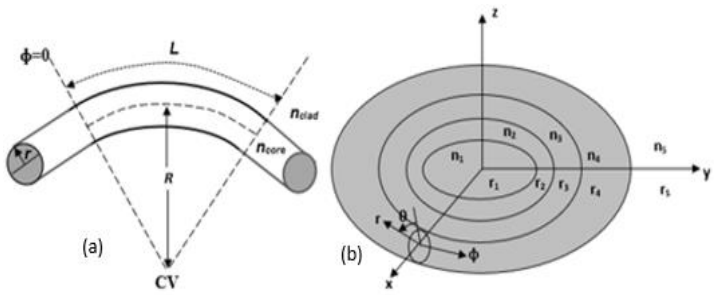


Fig. 3-12: (a) Connection of straight and bend (arc) fibres with core radius r, where R is the bending radius, n_{core} represents the refractive index of the core, and n_{clad} denotes that of the cladding, CV is the centre of curvature and (b) Illustration of a bend round MC-MMF with radial core indices of n_1, n_2, n_3, and n_4. The refractive index n_5 is for the cladding.

Table 3-2 summarises the parameters used to model the arc bends.

Table 3-2 Summary of parameters of the arc waveguides, these parameters corresponds to that of the core layers in the tilted and horizontal fibres.

Layer Radius (μm)				Layer Refractive Indices			
OC1	OC2	OC3	OC4	n_2	n_3	n_4	n_5
3	5	7	9	1.4514	1.4496	1.4476	1.4445

3.4 High Dispersion Fibre Model

This section presents a formulation of the high dispersion fibres equalisation model. The model can be applicable to both a vector and the LP-mode, this research adopts the linearly polarized mode matrix method (LP-MMM) due to the fact that the proposed fibre is assumed weakly guided.

3.4.1 LP-MMM Model

Different types of optical fibres can be modelled by employing various method. Here, the SI fibres that are constituted by the concentric layers of loss-less dielectric material are proposed. The aim is to develop a novel model for high dispersion fibres with the reduced MD. For fibre structures with a small index contrast, it is appropriate to employ a scalar wave equation to determine the LP modes [168]. Nevertheless, when the index difference becomes larger, the LP-mode approximation turns out to be inaccurate, thus, a full vector method is necessary [168]. In this approach, within each layer, the field components (FCs) are considered the linear combinations of both the ordinary and modified Bessel functions (MBFs). The solution is based on matching the tangential FCs of the adjacent layers that lead to the solution of a linear system. Different options can be adopted while arranging a linear system [169]. For a complete computation to be achieved, the efficient method for a general, fast algorithm is implemented [170]. The technique can be described as one that has an intuitive application in its similarity to the transfer matrix employed in the planar waveguides analysis [171]. Both the approaches adopt the matrix technique to express the wave fields in one layer and give their values at the other layer. Thus, the overall fibre structure is finally characterised by cascading the layers using matrix multiplication. For the vector modes, the two tangential field components (electric and magnetic) are included, as there is no specific approach of separating into **TE** and **TM** polarisation. Hence, instead of a 2×2 matrix at the layer boundary, a total of the 4×4 matrix is observed in the fibre because of the four transverse components (vector modes).

3.4.2 Dispersion Model Using LP-MMM

To determine the **EM** field in the fibre structure, the cylindrical coordinates (*r, θ*, *z*) is adopted and combined with the Debye potential (DP), which is in parallel with the rotation axis, $\hat{\boldsymbol{z}}$ [169]**:**

$$\boldsymbol{E} = \nabla \times (\hat{\boldsymbol{z}}\Psi) + \frac{1}{k\varepsilon}\nabla \times (\hat{\boldsymbol{z}}\varphi) \qquad \text{Eq (3.37)}$$

$$\boldsymbol{h} = \nabla \times (\varphi\hat{\boldsymbol{z}}) + \frac{1}{k}\nabla \times (\hat{\boldsymbol{z}}\Psi) \qquad \text{Eq (3.38)}$$

The solution is obtained by using boundary conditions that are applied by a physical consideration on Eq (3.37 and 3.38). The modes are supposed to form

from the potential expressed in Eqn (3.40), in which a solution of the variable separation is needed.

$$\Psi(r,\theta,z) = \Psi_v(r)\mathbf{exp}[j(v\theta - \beta z)] \qquad \text{Eq (3.39)}$$

where Ψ is the potential and β, is the propagation constant. If the same term is applied to DP, ϕ, and by expanding Eq (3.40) (Helmholtz equation) in the cylindrical coordinates and substitute into Eq (3.39), then

$$\nabla^2\Psi + k^2\varepsilon\Psi = 0 \qquad \text{Eq (3.40)}$$

If the region is assumed to have a constant permittivity (ε), then the relations follow the Modified Bessel functions (MBFs). In this case, the solution will be a linear sum of the Bessel functions (BFs) with an integer order represented by *v*, therefore, in any specific layer

$$\phi_v(r) = AJ_v(ur) + BY_v(ur)$$

$$\Psi_v(r) = CI_v(ur) + DK_v(ur) \qquad \text{Eq (3.41)}$$

where, $u = (k^2\varepsilon - \beta^2)^{1/2}$; *J* and *Y* are BFs; I and *K* are modified BFs; A, B, C, and D, are the coefficients. In the layers where a square of the propagation constant (β^2) is greater than $k^2\varepsilon$, then, BFs, *J* and *Y* are substituted by MBFs I and *K* respectively, giving:

$$\Phi_v(r) = AI(wr) + BK_v(ur)$$

$$\Psi_v(r) = CI_v(ur) + DK_v(ur) \qquad \text{Eq (3.42)}$$

where $w = (\beta^2 - k^2\varepsilon)^{1/2}$. Thus, Eq (3.39), (3.41), and (3.42) are inserted into the Eq (3.37) and (3.38), to determine the EM fields in which the tangential components *θ* and *z* are required; this is because the tangential components of ***E*** and ***h*** fields are needed to match at the layer boundary. These EM field components of the Eq (3.37 and 3.38) are expressed in relation to A, B, C, and D; which are the coefficients represented in the following 4×4 matrix:

$$\mathsf{F} = \begin{bmatrix} E_z \\ h_\theta \\ h_z \\ E_\theta \end{bmatrix} = \begin{bmatrix} u^2J_v(ur)/k\varepsilon & u^2Y_v(ur)/k\varepsilon & 0 & 0 \\ -uJ_v(ur) & -uY_v(ur) & nvJ_v(ur)/r & nvY_v(ur)/r \\ 0 & 0 & u^2J_v(ur)/k & u^2Y_v(ur)/k \\ nvJ_v(ur)/\varepsilon r & nvY_v(ur)/\varepsilon r & -uJ_v(ur) & -uY_v(ur) \end{bmatrix} \begin{bmatrix} A \\ B \\ C \\ D \end{bmatrix} \qquad \text{Eq (3.43)}$$

The components order within the vector ($_{\mathrm{f}}$) are selected to assist factor the matrix in Eq (3.45), into two matrices expresses by $\mathbf{F}_{\mathrm{f}} = \boldsymbol{Dc}$, $\boldsymbol{c}$ represents the coefficients [A, B, C, and D].

$$\nabla[\nabla \cdot (\hat{\boldsymbol{z}}\Psi)] - \nabla^2(\hat{\boldsymbol{z}}\Psi) - k^2\varepsilon\hat{\boldsymbol{z}}\Psi = \nabla\frac{\partial\Psi}{\partial z} \qquad \text{Eq (3.44)}$$

Which is true for any Ψ that satisfy Eq (3.44) in a constant permittivity region. Therefore,

$$\boldsymbol{F} = \begin{bmatrix} \varepsilon & 0 & 0 & 0 \\ 0 & -1 & nvk/ru^2 & 0 \\ 0 & 0 & 1 & 0 \\ nvk/ru^2 & 0 & 0 & -1 \end{bmatrix} \qquad \text{Eq (3.45)}$$

And

$$\boldsymbol{D} = \begin{bmatrix} u^2J_v/k & u^2Y_v/k & 0 & 0 \\ uJ_v & uY_v & 0 & 0 \\ 0 & 0 & u^2J_v/k & u^2Y_v/k \\ 0 & 0 & uJ_v & uY_v \end{bmatrix} \qquad \text{Eq (3.46)}$$

$k = \omega\sqrt{\mu_0\varepsilon_0}$, where k is the wave number. Note that factoring here simplifies the process of determining an expression for the two inverses. $\mathbf{F}^{-1}$ is obtained by two row reductions and $\mathbf{D}^{-1}$ through matrix inversion of 2×2 (block diagonal). Moreover, such matrices are needed to determine the succeeding layer coefficient, in which $\mathbf{c}_{\mathrm{m}}$ represents the *m-th* layers coefficients. Thus, the coefficient in the succeeding layer is calculated by the matrix multiplication:

$$\boldsymbol{c}_{m+1} = \boldsymbol{D}_{m+1}^{-1}(r_m)\boldsymbol{F}_{m+1}(r_m)\boldsymbol{F}_m^{-1}(r_m)\boldsymbol{D}_m(r_m)\boldsymbol{c}_m \qquad \text{Eq (3.47)}$$

Using the factorised matrix indicates that crossing the boundary requires four matrix multiplications (not two) to avoid the task of determining the inverse matrix. The matrix method employed in the multilayer is expressed as a 4×4 matrix [170], which is the multiple effects of all layers, an expression of a single layer represented in Eq (3.47). The equation that calculates dispersions is constituted when the determinant of this 4×4 matrix product is set to zero. Fibres with low Δ may demonstrate similar modal indices, making them difficult to trace by numerical means.

In addressing this issue, a rectangular matrix is implemented at the initial and final layers. In the initial layer that includes r=0, the two coefficients $\mathbf{B}_{\mathrm{o}}$ and $\mathbf{D}_{\mathrm{o}}$ must be set to 0 so that the first matrix, $\mathbf{D}_{\mathrm{o}}$, will be 4×2 which contain the first

column of the **D** matrix in Eq (3.46). Likewise, in the last layer, the two coefficients $\mathbf{A}_M$ and $\mathbf{C}_M$ will now be set to 0 as illustrated in Eq (3.42), this is because such matrix contains solutions $\mathbf{I_v}$ that has no physical growth. Therefore, a final $\mathbf{D}_M^{-1}$ will be constituted by the size of 2 x 4 that includes the initial and third rows of $\mathbf{D}^{-1}$. The combinations of all the matrices will contain the size of 2×2, [171] which is referred here **S**(n), (where n indicates explicitly the dependence on the modal index). A mode is calculated at a specify n value for a non-trivial solution expressed in Eq (3.48),

$$\mathbf{0} = \boldsymbol{S}(n)\begin{bmatrix}\boldsymbol{A}_0\\ \boldsymbol{C}_0\end{bmatrix} \qquad \text{Eq (3.48)}$$

The condition that the determinant det(**S**) set to zero is enough for a non-trivial situation.

3.4.3 Linearly Polarised Model (LP-Model)

LP-Modes can be determined with the same method described in section 3.4.2, by employing a transfer matrix method of the multilayer fibres. On adopting LP analysis, the initial excitation is presumed to have a linear polarisation, here, a study that supports only one field is adopted. This method is assumed to be a good approximation with low Δ. Considering the wave Eq (3.49) and using the vector identity in Eq (3.50), then, Eq (3.51) can be obtained without using DP.

$$\nabla \times \nabla \times \mathbf{E} - \mathrm{k}^2\varepsilon\boldsymbol{E} = 0 \qquad \text{Eq (3.49)}$$

$$\nabla(\nabla.) - \nabla^2 = \nabla \times \nabla \qquad \text{Eq (3.50)}$$

$$\nabla^2\mathbf{E} - \nabla(\nabla.\boldsymbol{E})\boldsymbol{E} + \mathrm{k}^2\varepsilon\boldsymbol{E} = \mathbf{0} \qquad \text{Eq (3.51)}$$

substituting the divergence Eq (3.52) into Eq (3.51)

$$\nabla.(\varepsilon\boldsymbol{E}) = \mathbf{0}, \qquad \nabla.\boldsymbol{H} = \mathbf{0} \qquad \text{Eq (3.52)}$$

yields

$$\mathbf{0} = \nabla.(\varepsilon\boldsymbol{E}) = \boldsymbol{E}.\nabla\varepsilon + \varepsilon(\nabla.\boldsymbol{E}) \qquad \text{Eq (3.53)}$$

Thus,

$$\nabla^2\mathbf{E} + \mathrm{k}^2\varepsilon\boldsymbol{E} + \nabla\left(\boldsymbol{E}.\frac{\nabla\varepsilon}{\varepsilon}\right) = \mathbf{0} \qquad \text{Eq (3.54)}$$

It is important to note that most of the practical fibres have a low Δ, hence, the last term in Eq (3.54) is very small and can be neglected. This last term is the only

one contributing coupling between the electric field components. Being ignored, the proposed model will preserve polarisation. For an LP-excitation parallel to the X-direction, the model is simplified further by taking only the X component. This illustrates that for an LP-model, the equation that determines the field is the Helmholtz Eq (3.40) that applies to the $\mathbf{E}_x$ field.

LP mode solution is constructed in the same way as the vector mode. Construction of $\mathbf{E}_x$ field in each layer is achieved based on the linear combination of BFs Eq (3.42) and Eq (3.43). Here, only two coefficients are required, and the continuity of the $\mathbf{E}_x$ and boundary condition is applied. The two conditions are associated with the two coefficients A and B by the 2×2 matrix. The modes are determined by setting up an evaluation that considers A_1, B_1=1,0, respectively, for the innermost layer, after which the coefficient in each of the coming layer is calculated through matrix manipulations. The final layer has to satisfy the condition that the A_M of the Bessel function I_V is set to zero, this is because the BF is not bounded at infinity. The modes are bounded by determining the zero of the coefficient $A_M\ (n)$.

3.5 Summary

Different mathematical formulations for the device modeling that includes the FDTD and TE-wave equations were presented. In addition, the light source model, the spectral response model, and the power models based on the FDTD are also explored. In Section 3.2.6, a brief description of the simulation workflow was illustrated. Moreover, in Section 3.3, LP_{11} to LP_{01} design parameters were determined, and section 3.3.4 examined the converter parameters based on the tilts MC-MMF. Theory and principle of an arc waveguide were discussed in section 3.3.5. Section 3.4 presents an LP-MMM model used for the modeling of the high dispersion fibres.

Chapter 4 Mode Conversion for MDM System

4.1 Introduction

This chapter presents the research work carried out on two models of the MC devices employing the FDTD formulations presented in Chapter 3. In section 4.2, mode conversion based on the lateral misalignment between two M-RCFs and CSIF is discussed. The main aim here is to model a device that can convert an LP_{11} to LP_{01} mode. Section 4.3 discusses a model with improved performance compared to the initial model. Here, mode conversions of LP_{11} to LP_{01}, LP_{02} to $LP_{11,}$ and LP_{21} to LP_{01} were demonstrated based on a tilted fibre assisted by the DAW. The fibre employed for modelling an MC device based on the DAW is the MC-MMF supporting four spatial modes.

Mode conversion from one LP mode to another is a crucial aspect of multiplexing in the MDM system. Mode conversion can be achieved using different approaches as highlighted in several reports [67][63][172-176]. The realisation of an MDM system depends largely on the mode multiplexing, which can be enhanced significantly through mode conversions. MCs can also play a key role during mode separation so that each mode can be transmitted as an independent signal channel [77].

4.2 LP_{11} to LP_{01} MC Using M-RCF and CSIF

In this Section two new LP_{11} mode converters are reported and compared, one employing two-mode conventional step index fibre (CSIF) and the other using M-RCF. In each case, the two fibres constituting the proposed devices were laterally misaligned. With the appropriate adjustments of the lateral displacements, 'h' and separation distance 'd' between the axis of the identical CSIF and M-RCF, an MCs with the CE of 69% and 94% were achieved, respectively. The performance of the two devices is compared in terms of the CE and mode purity (MP) at the outputs. The results based on the coupling power indicates that M-RCF-based device offers higher CE and MP than the CSIF-converter, which is due to the presence of multi-ring core. An MP of 84% and 58.8% were respectively determined for the M-RCF and CSIF converters. Fig. 4-1 illustrates how an LP mode is coupled into the input of the CSIF. The fibre comprises a cladding with a single layer core having a high refractive index.

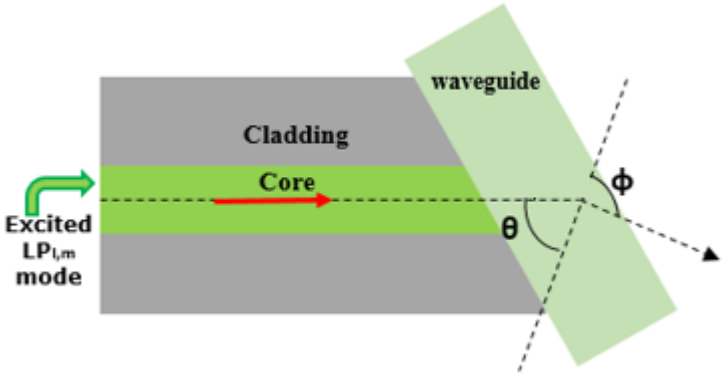


Fig. 4-1: Illustration of the light coupling into the angled-cleaved CSIF

Fig. 4-2 shows the model schematic used for the simulations of the proposed CSIF and M-RCF mode converters. It is important to mention that the multilayer-core is shown, but in CSIF converter, only a single layer core was used. Both the converters consist of two parts (A and B): The M-RCF-based converter comprises of two identical M-RCF with cleaved-angle at the end of the input fibre (Fig. 4-2-part A) and was employed to investigate cleaving effects at different angles. Similarly, the CSIF-based converter comprises of two identical CSIF, adopting similar configurations.

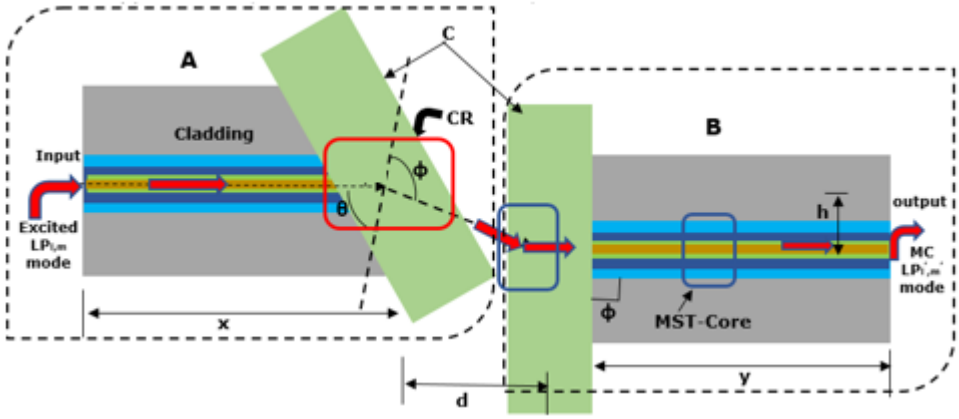


Fig. 4-2: Model of the proposed mode converter; CR is the coupling region; MST: multistep core. A similar model was used to simulate the CSIF with a single layer core.

The cleaving angle 'θ' in the two converters models (M-RCF and CSIF) was adjusted by changing the coordinates of the waveguide. The 'θ' can be defined as the angle between the normal at cleave point of the fibre A and the central axes, it can also be considered as the beam incident angle that propagates onto the CR [35]. Similarly, ϕ represents the angle between the normal of angled-cleave and the beam propagation axis (refracted angle). As illustrated in Fig. 4-2, the input fibre A (M-RCF and CSIF) having length 'x', was excited with an LP_{11}. The end face angle was cleaved at 42^0 (the same angle was maintained for the two models). This is because of the high coupling demonstrated by the two converters at this angle, it is due to the closeness of this angle (42°) to the critical angle (43°). The beam in fibre A was collected by fibre B of length 'y' having similar properties but longer than A (to properly observe the output beam). The fibre B of each model was positioned at a distance 'd' away from fibre A. It is important to note that the input of fibre B of the two converters was fixed at 0°, this is due to the observations made when the two converters were excited with an LP_{01} at 0°, no effect was seen. Thus, angle 0^0 is taken as reference for the two models at the input of collecting fibre. A lot of efforts were made before making the light beam to get confined into the collecting core of each model. This was achieved by varying 'd' that separates the centres of the two identical fibres in the two models. The light from the input fibres of each model was made to couple into the collecting fibre by carefully varying the 'h', the vertical offset between the central axes of the two models.

The parameters presented in Table 4-1 were used for the simulations of the two converter models. This is to make a proper comparison between the device's performance. The table includes the lengths of the fibres used, in which the same fibre lengths were maintained for the two simulations setup (M-RCF and CSIF converters). The distance of separation 'd' of CSIF-converter was reduced by 1 μm in order to achieve a maximum CE. The same length and width of the wafer are maintained in the two design layouts. There was a slight variation in the vertical height 'h' for the two models and the operating wavelength 'λ' was fixed the same.

Table 4-1: Design parameters of the M-RCF and CSIF mode converters.

Properties	M-RCF-Converter				CSIF-Converter			
Fibres	*A*	*B*	-	-	*A*	*B*	-	-
Measurements (µm)	x	y	*d*	*h*	x	y	*d*	*h*
Length (µm)	87	100	83	20.50	87	100	82	22.2
Wafer length (µm)	450	450	-	-	450	450	-	-
Wafer width (µm)	300	300	-	-	300	300	-	-

4.2.1 Mode Orientation

Another critical aspect is the mode orientation. As shown in Fig. 4-3, the fibre is assumed to have weak guiding characteristics with the less core rotation of fibre B. Here, an LP_{11} mode, which consists of two lobes (LP_{11x} and LP_{11y}) is excited at the input of fibre A.

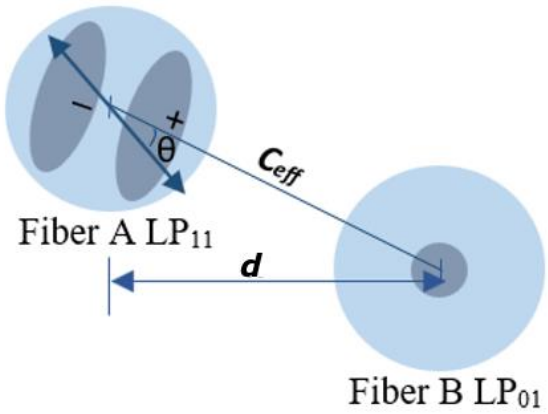


Fig. 4-3: Two M-RCF (ring cores are not shown) each supporting two LP modes. An LP_{11} is excited at the input of fibre A and LP_{01} is collected in fibre B.

The LP_{01} is collected at the core of the fibre B. As illustrated in Fig. 4-3, the field orientation of an LP_{11} mode depends on the angle θ, which is defined as the angle between the normal and the central axes of fibre A. It is also equivalent to an incident angle of the propagating beam onto the cleaved-angled fibre end. When $\theta=0^0$, the

coupling $C_{11x\text{-}11y}$ between LP_{11x} and LP_{11y} modes (degenerates) is negligible. Along the propagation axis (z-axis), a periodic variation in θ leads to a change in the coupling coefficient. The results of this effect are shown in section 4.3, Fig. (4-6) through Fig. (4-13). It is worth mentioning that an LP mode demonstrates an intrinsic rotation even in a perfectly homogeneous fibre. Here, the coupling between LP_{11x} and LP_{11y} is assumed to be as results of the cleaving effect at the end facet of the fibre A. When the two modes of the LP_{11} are considered phase matched (with the same propagation constant β), the forward modes coupled relation are determined by [177]:

$$\frac{d\boldsymbol{D}_{11x}(z)}{dz} = -j\beta\boldsymbol{D}_{11x}(z) - jE_0\cos(\theta)\boldsymbol{D}_{01}(z) \qquad \text{Eq (4.1)}$$

$$\frac{d\boldsymbol{D}_{11y}(z)}{dz} = -j\beta\boldsymbol{D}_{11y}(z) - jE_0\sin(\theta)\boldsymbol{D}_{01}(z) \qquad \text{Eq (4.2)}$$

And for the LP_{01} in the fibre B

$$\frac{d\boldsymbol{D}_{01}(z)}{dz} = -j\beta\boldsymbol{D}_{01}(z) - jE_0\cos(\theta)\boldsymbol{D}_{11x}(z) - jE_0\sin(\theta)\boldsymbol{D}_{01}(z) \qquad \text{Eq (4.3)}$$

where $\mathbf{D}_{11x}(z)$ and $\mathbf{D}_{11y}(z)$ are the electric fields of the two modes (LP_{11x} and LP_{11y}) in fibre A. $\mathbf{D}_{01}(z)$ denotes the electric field of the fundamental mode in fibre B and E_0 is the mode initial amplitude.

If coupling between the cores of fibre A and fibre B depends on the fibre and source parameters then, the radial dependence of the coupling coefficient can be determined by [178]:

$$C_r = (-1)^l \frac{2\sqrt{2k}\rho_2\Delta_2 u_1 u_2 (n_{cr,2})^{2/3}}{\rho_1 v_1 v_2^3 (n_{cr,1})^{1/2}} \times \frac{K_l\,(w_1 d/\rho_1)}{K_1(w_1)\sqrt{K_{l-1}(w_2)K_{l+1}(w_2)}} \qquad \text{Eq (4.4)}$$

where ρ_i represents the core radius, Δ_i is the core-cladding index difference, u_i and w_i denotes the core and cladding indices, respectively. The core index is represented by $n_{cr,i}$ and d is the separation between the centres of fibre A and B. The Ks (K_l, K_{l-1}, and K_{l+1}) represents the MBFs, v_i is the normalised frequency and the subscripts represent the fibre mode order. A circle-core fibre has a continuous rotational symmetry; therefore, the mode lobes pair are considered degenerates.

4.2.2 Simulation Setup

The simulation was run in the 2D domain under TE type with wafer dimension of length 450 μm and width 300 μm and the wafer material is air. The cells size was fixed at 100 nm; in order to achive good convergence, the step size was set to auto in oder to allow runing up to 4000 time steps (maximum runing time) to have a complete trip from input to the output. This process was ensured during the simulation of the two converters. Furthermore, the layout region was run in the XZ-plane, where X and Z represent vertical and horizontal components respectively. A dielectric material (glass) was used for the fibre profile in both converters. The modal light distribution was used with the plane positioned in the Z-direction. The fundemental requirement to setup a simulation domain is the energy or power source to provide (inject) modal field into the simulation region. It can be achieved using an input plane, which was employed to produce the modal field. Fig. 4-4 (a-b) illustrates the M-RCF and CSIF-converters simulation layout of fiber A. The main difference in the two setups is the core structure, the CSIF is of single layer core. This is to investigate the effect of different cleaved-angles for both converters. The position of the light source was mantained at the input of each model, by varying coordinates of the waveguide, the angle of interest is calculated.

The main reason for choosing the input plane is because of its ability to propagate in a spacific direction with the intensity distribution across the plane of incidence. A vertical input field was positioned at the input plane, which is perpendicular to the Z-aix and comprises of four input fields properties: modal field, Guassian field, rectangular, and user defined field. Here, the modal field is used to calculate the number of modes supported by the fibres, and any desired mode can be chosen to excite the fibre.

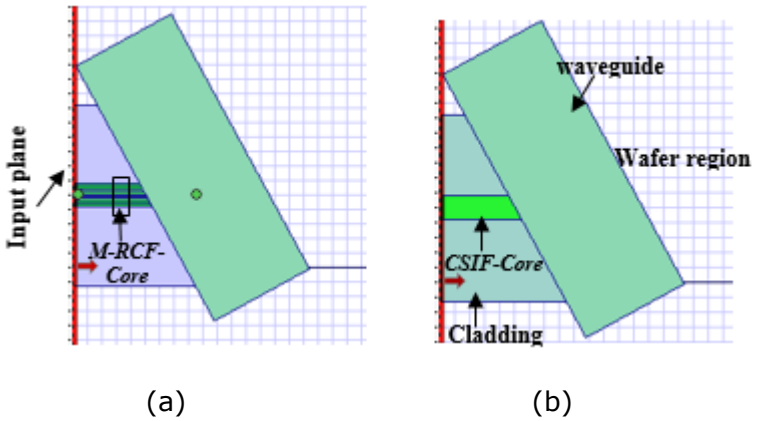
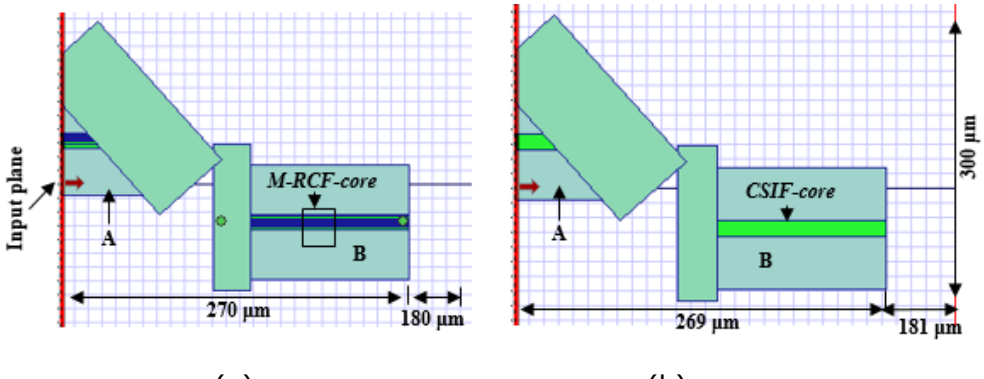


Fig. 4-4: The 2D-layout setting of the: (a) M-RCF (fiber A) to determine the effects of cleaving fibre end facet and (b) CSIF setup with a single layer core.

Both the LP_{01} and LP_{11} modes are independently excited to examine the cleaved-angle effect on each of them (the results are presented in section 4-3, Fig. 4-7 to Fig. 4-13. It is crucial to remember that modes of similar or identical propagation constants are expected to share power due to coupling effect.

Fig. 4-5 (a-b) represents the simulation layout of the M-RCF and CSIF converters, consisting of the fibre cleaved at 42°. The refracted beam from A was collected at B, by determining a proper coupling point at the input of B. The overall length of the M-RCF-converter is 270 μm, and that of the CSIF-converter is 269 μm. The 1 μm difference in the device length is due to the variation in the distance of separation.



(a) (b)

Fig. 4-5: 2D simulation layout of: (a) M-RCF-converter and (b) CSIF-converter, each consists of fibre A and fibre B. An LP_{11} mode is launched at the input side of fibre A.

Fibre B is used to collect the refracted beam from A and is achieved by adjusting B to a proper coupling point. The entire length of the proposed device is 270 µm, this includes the distance of separation between the two fibres.

4.3 Results and Discussions

Fig. 4-6 depicts the simulated profile of the LP_{01} and LP_{11} at different angles (23°, 39°, 42°, 60°, 70°, 80° and 0°). The calculated results were determined using the CSIF model of Fig. 4-1, the one lobe in the LP_{01} and two lobes of the LP_{11} are shown.

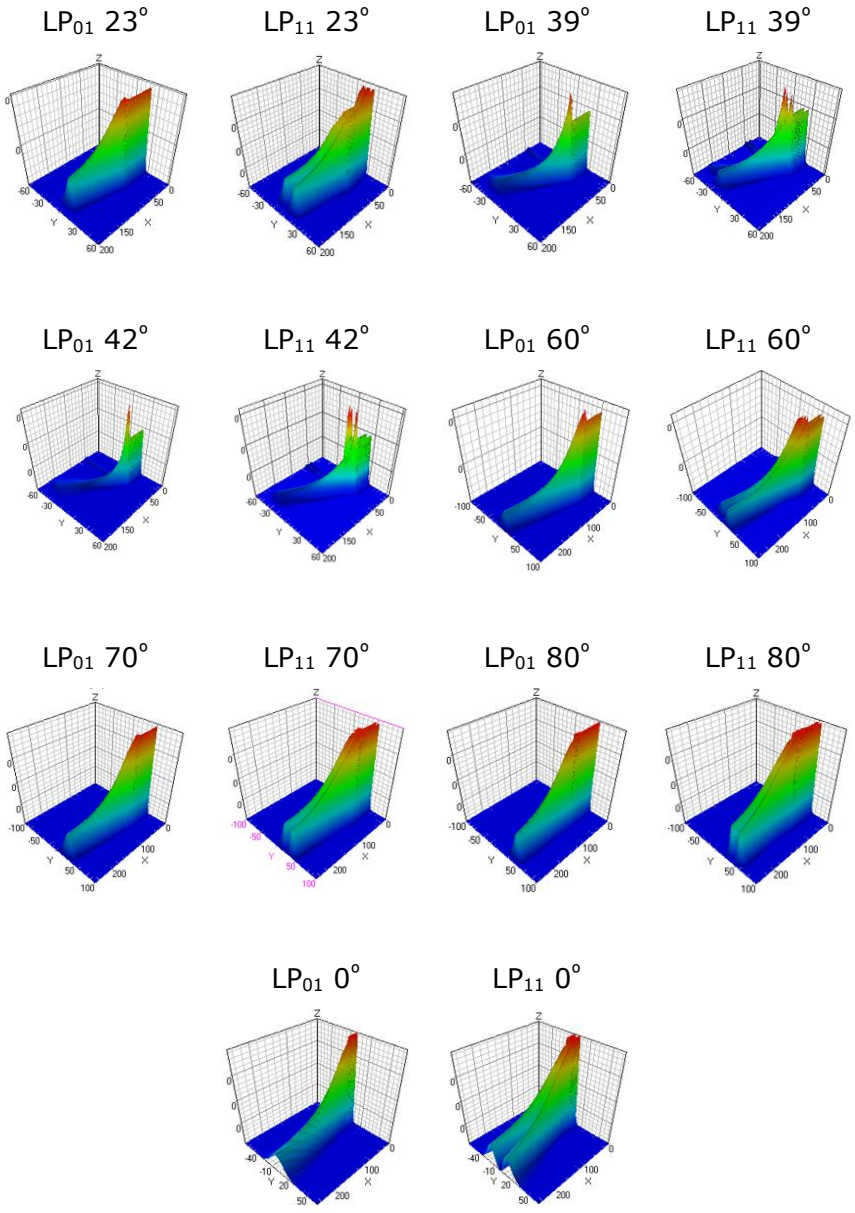


Fig. 4-6: Mode profiles of the CSIF at different cleaving angles.

Fig. 4-7 to Fig. 4-13 is the simulation results of the effects of an angled-cleave (Fig. 4-5 A) excitations of both LP_{01} and LP_{11} modes for the M-RCF. The investigation was carried out at various angles (23°, 39°, 42°, 60°, 70°, 80° and 0°). As can be seen from Fig. 4-7 to Fig. 4-13, at these angles, an LP_{01} has one lobe and LP_{11} has two lobes except at 42°. In this angle (42°) only one lobe is dominant for the LP_{11}. This may be due to its closeness to the critical angle (43°). The graph at the right of each

modal excitation at all the angles corresponds to their amplitudes. For LP_{01}, a single amplitude is observed while for the LP_{11} double amplitudes are observed. This shows that each amplitude represents one lobe except for the 42°, which indicates the existence of coupling between the two lobes of an LP_{11} at this angle.

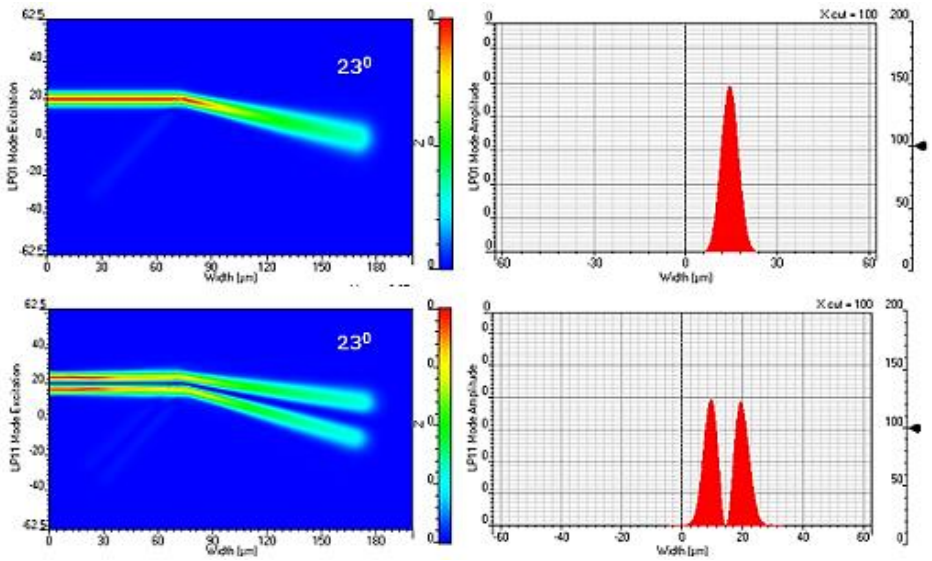


Fig. 4-7: Mode excitation for LP_{01} and LP_{11} at angled-cleave 23°.

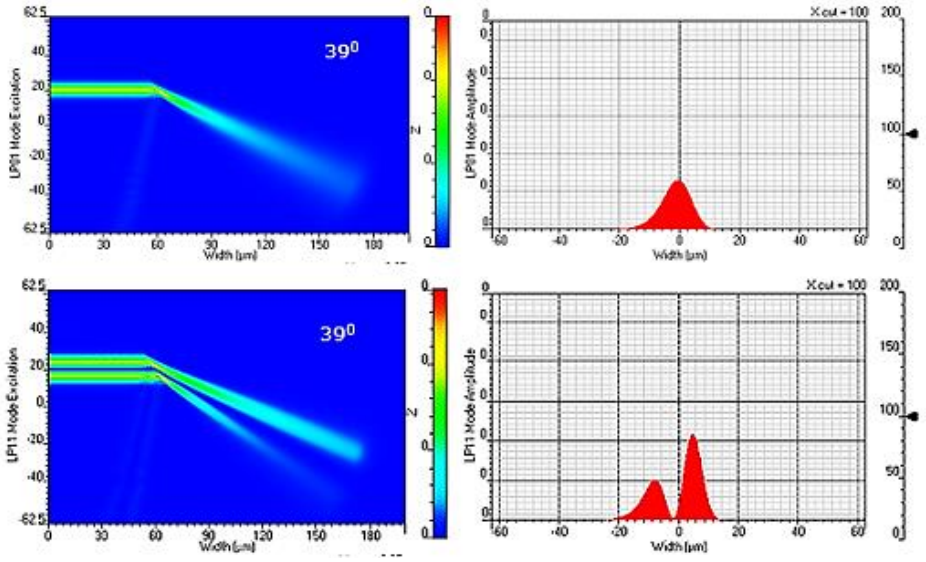


Fig. 4-8: Mode excitation for LP_{01} and LP_{11} at angled-cleave 39°.

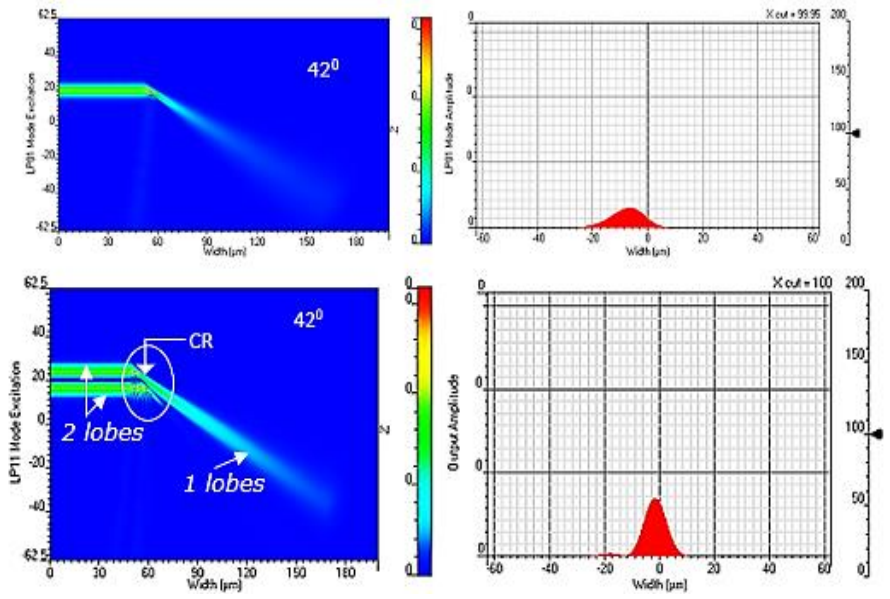


Fig. 4-9: Mode excitation for LP_{01} and LP_{11} at angled-cleave 42°.

.

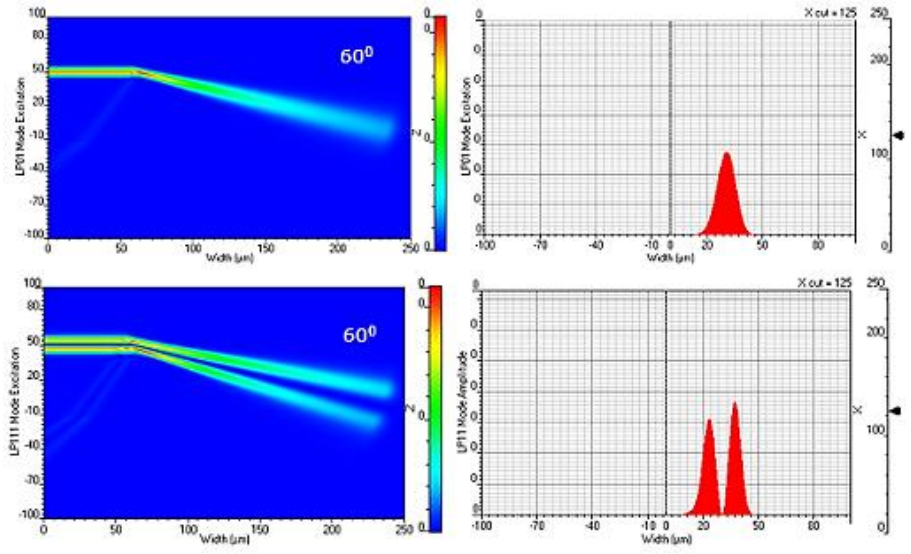


Fig. 4-10: Mode excitation for LP_{01} and LP_{11} at angled-cleave 60°.

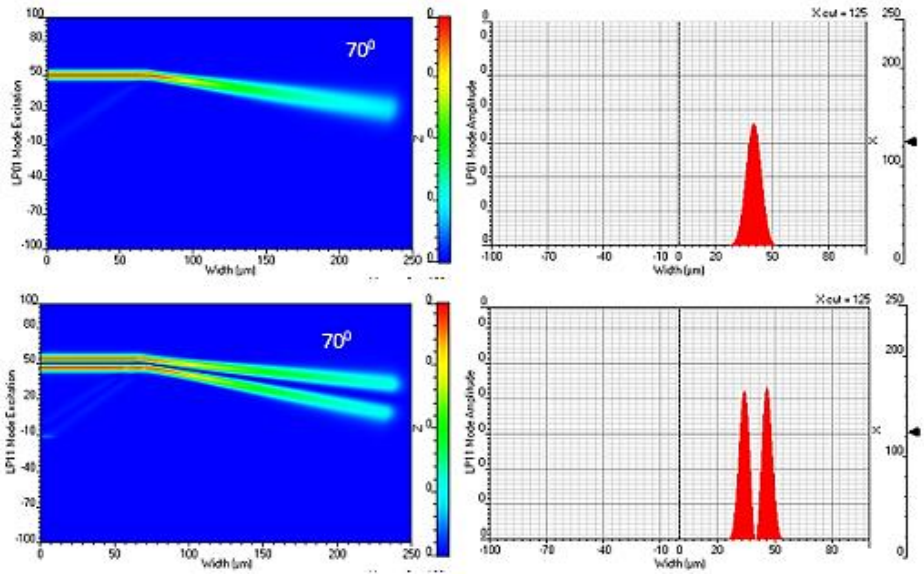


Fig. 4-11: Mode excitation for LP_{01} and LP_{11} at angled-cleave 70°.

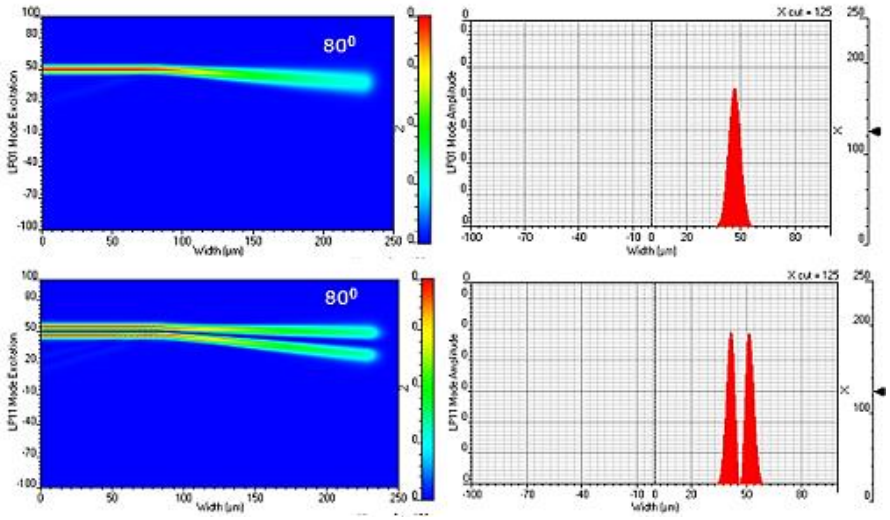


Fig. 4-12: Mode excitation for LP_{01} and LP_{11} at angled-cleave 80°.

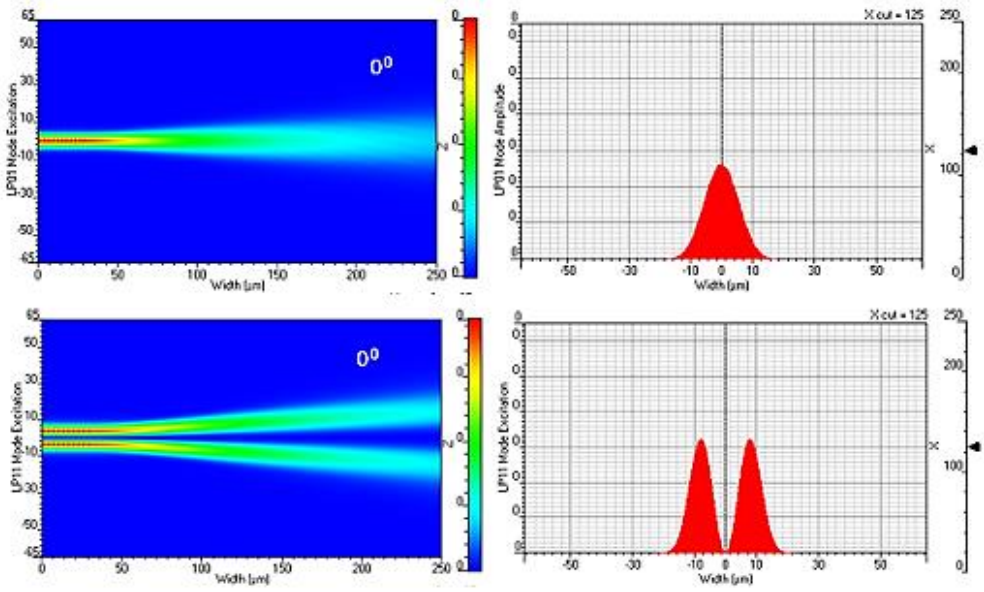


Fig. 4-13: Mode excitation for LP_{01} and LP_{11} at angled-cleave 90°.

Fig. 4-14 shows an M-RCF-converter 3D diagram, which was proposed in Fig. 4-5; the letters A, B, and C stands for the input fibre under excitation, fibre at the output (collecting fibre), and the waveguides employed to vary the coordinates while calculating the angles, respectively. A similar diagram can be shown for the CSIF-converter.

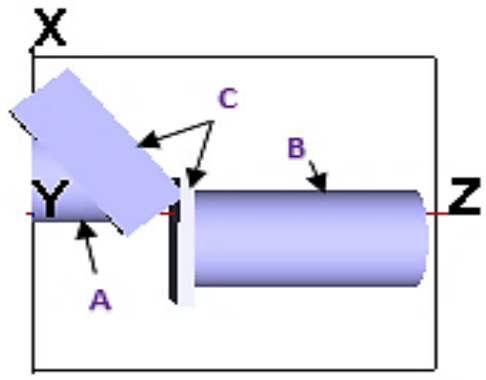


Fig. 4-14: M-RCF-converter 3D-model, a similar diagram can be obtained for the CSIF-converter.

The two waveguides, which are of air index profiles, were used to set up the coordinates used to determine the cleaved-angle.

Fig. 4-15 is the 2D index distributions of the two proposed converters, Fig. 4-15 (a) is the M-RCF-convert distribution and Fig. 4-15 (b), the CSIF-converter index distribution. In each case, the two fibres (A and B) are clearly shown. The major difference between the two is the core structure, in which the M-RCF has multiring core configuration, and the CSIF has a core with a single layer. The two index distributions can be used to evaluate accuracy in setting the simulation layout of the devices.

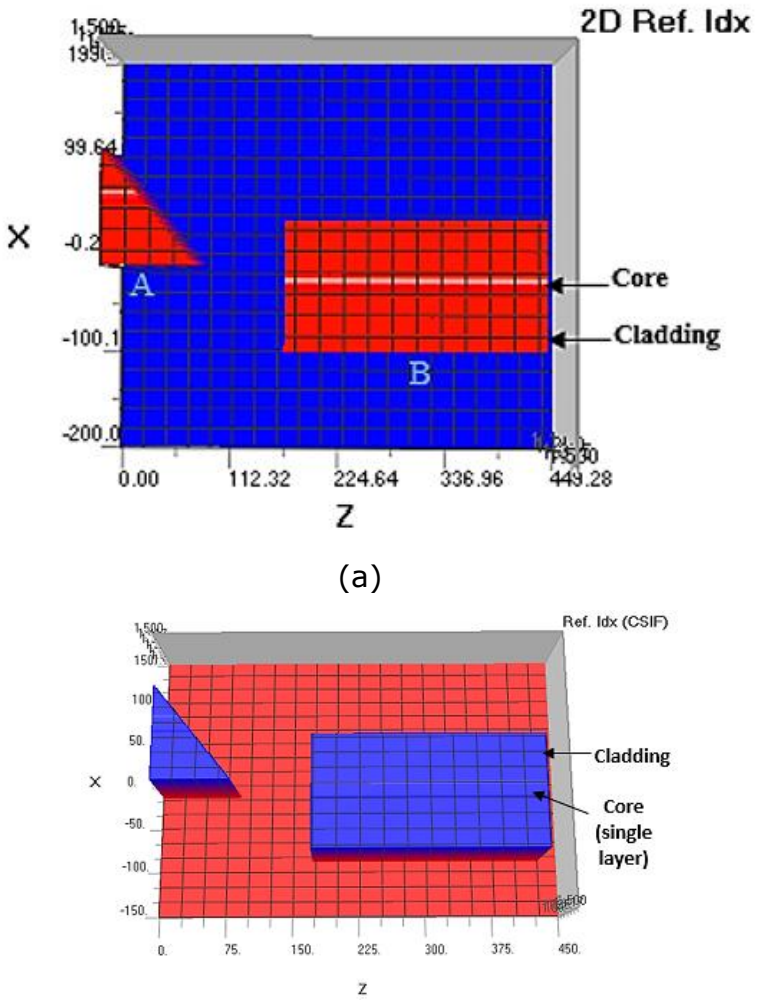


Fig. 4-15: (a) M-RCF-converter index distribution and (b) CSIF-converter index distribution during simulations.

The performance parameter of the M-RCF and CSIF that was initially evaluated for this study is the refraction angle. Fig. 4-16 shows the plot of the angle of refraction versus the incident cleaving angles. The results for the M-RCF-converter was deduced from Fig. 4-7 to Fig. 4-13, and that of the CSIF-converter can be determined using a similar procedure, this is due to the fact that the figures in the two cases look similar. The refracted angle of an LP_{01} and the degenerates of LP_{11} (LP_{11a} and LP_{11b}) of both devices increases with variation in θ.

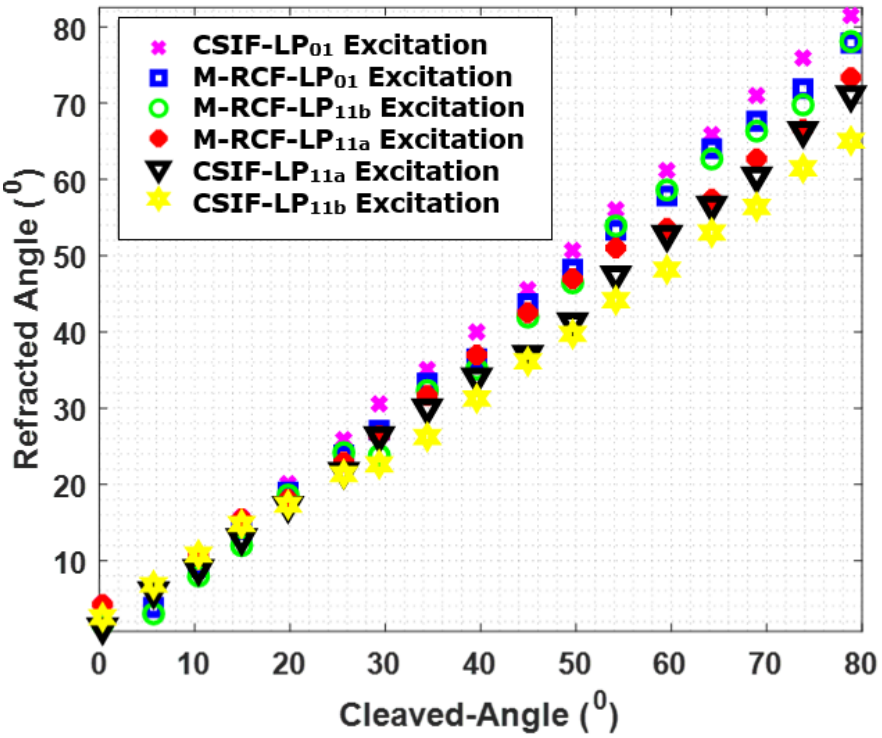


Fig. 4-16: Plot of the M-RCF- and CSIF-converter Refracted angle versus incident cleaved-angles. The blue, red, and green markers illustrate the graphs of the LP_{01}, LP_{11a}, and LP_{11b} for the M-RCF-converter, respectively. Similarly, the magenta, black, and yellow, colour markers represent the mode excitations of the LP_{01}, LP_{11a}, and LP_{11b} for the CSIF-converter, respectively.

Fig. 4-17 illustrates the behaviour of CE with variation in lateral misalignment 'h'. The red curve represents the CE of the M-RCF, and the blue curve represents the CE of the CSIF converter. In the absence of Fresnel losses/reflection and other constraints such as forward and back scattering, a CE close to 100% can be achieved. In both converters, the CE decreases with the increase in misalignment between centres of the two fibres. Shifting away from the coupling point can immediately lower the efficiency. For example, at 20.5 µm and 22.2 µm, which are the coupling points of the M-RCF and CSIF converters, respectively, the efficiency of the M-RCF is 94% while at 23 µm it dropped to 49% (0.49). Similarly, the CE of the CSIF device is 69% at the coupling point (22.2 µm). It must ensure that the final coupling point determined is not

displaced as slight variation can lead to excessive power loss, particularly at the interface of fibre B.

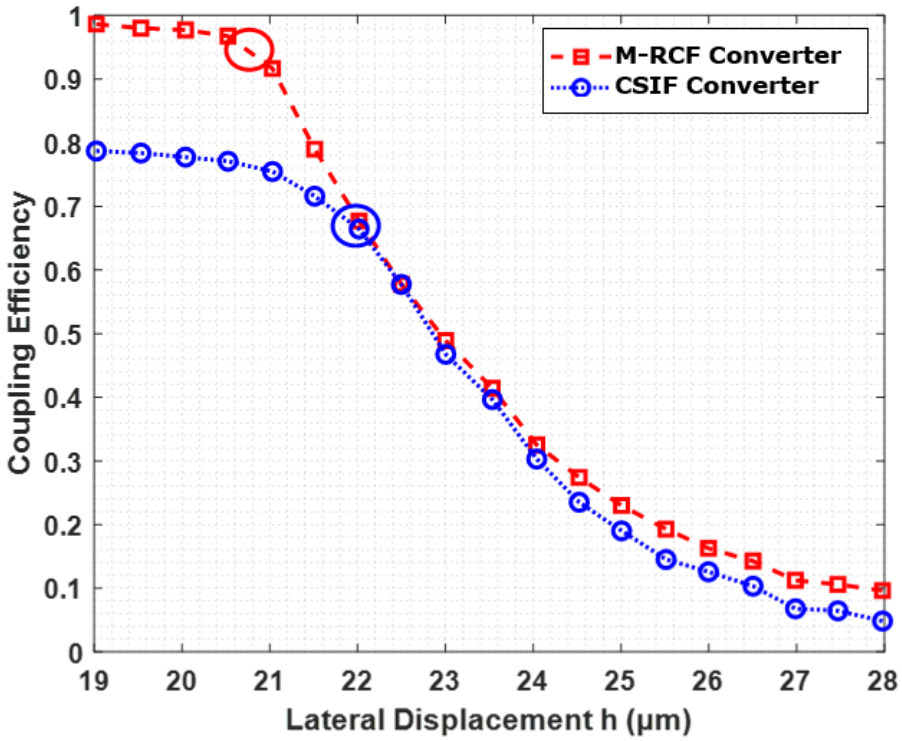


Fig. 4-17: Effect of 'h' on CE (a) of the M-RCF (red curve) (b) CSIF (blue curve). The coupling point of the M-RCF and CSIF (red and blue circles) is 20.5 μm and 22.2 μm, respectively.

Another important design parameter in this study is the distance of separation 'd' between the two fibres. Fig. 4-18 depicts the effect of coupling length variation with the separation distance 'd' between the two fibres in the M-RCF and CSIF converters at the operating wavelength (λ=1550 nm). In each case, the position of fibre B varied at fixed fibre A position. As shown in Fig. 4-18, both converters demonstrate similar behaviour of the exponential increase in coupling length with the increase in 'd' (between the centre of the two-fibres), mainly due to model interaction and power exchange. This explains the fact that coupled-power can be improved by bringing the two fibres closer. The two curves indicate similar behaviour of the two devices in terms of the coupling length relations with 'd'.

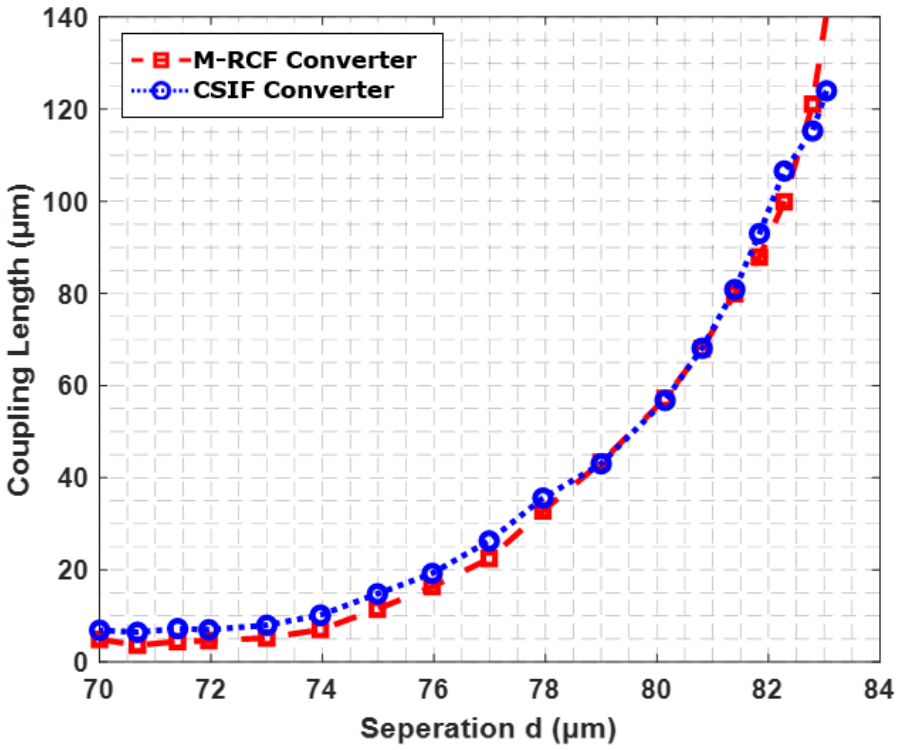
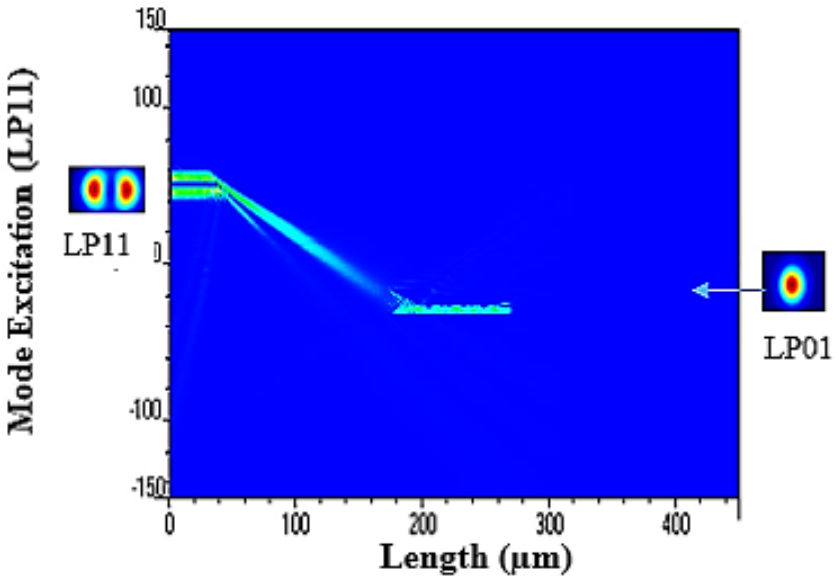
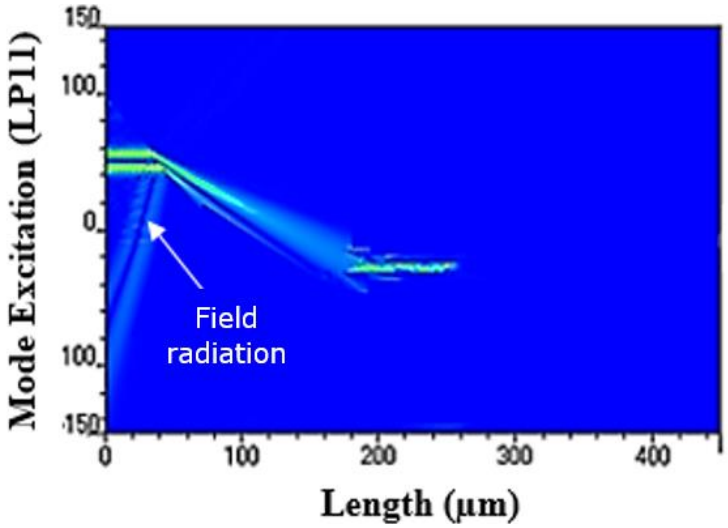


Fig. 4-18: Coupling length variation with the separation distance. The red curve is for the M-RCF and the blue curve for the CSIF converter.

Fig. 4-19 (a) is the overall conversion of LP_{11} to LP_{01} of the M-RCF -converter, it can be observed that the converter demonstrates low power loss (Fig. 4-24) and high CE (Fig. 4-17) compared to the CSIF converter in Fig. 4-19 (b), which indicates significant field radiations at the coupling point. The high CE demonstrated by the M-RCF may be attributed to the core multi-ring nature.



(a)



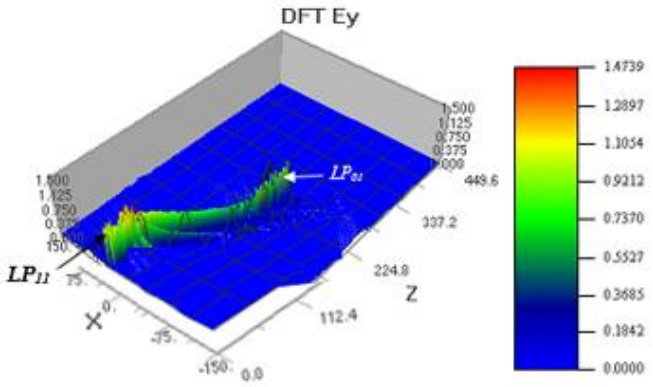
(b)

Fig. 4-19: Mode profiles of the proposed mode converters (Fig 4-2) and simulated using the layout in Fig. 4-5: (a) M-RCF and (b) CSIF

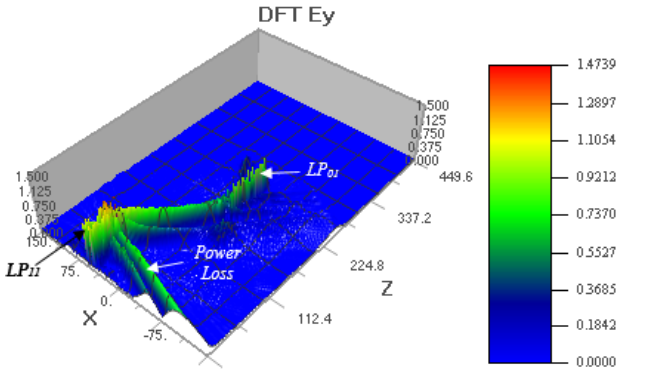
It is crucial to mention that the entire dark blue region shown in Fig. 4-19 (a-b) represents the wafer region of dimensions 450 μm×300 μm. As already presented in Table 4-1, the length of M-RCF is 87 μm and 100 μm for the fibre A and fibre B respectively, with the 'd' having a value of 83 μm. Furthermore, the CSIFs maintained the same lengths with 'd' of 1 μm less than the M-RCF converter. Thus, the total length of the M-RCF and CSIF converter device is found to be 270 μm and 269 μm

respectively. The dark region past the mode profile on the right of the collecting fibre is the wafer offset of 180 μm for the M-RCF and 181 μm for the CSIF converters as shown in Fig. 4-19 (a-b). It can be observed from Fig. 4-19 (a-b) that the profile distributions demonstrated by the two devices do not exactly match an LP_{01}. This may be attributed to the power loss at various transition points (P_{AC}, P_{L1}, and P_{L2}). To address this challenge, an alternative design model is proposed in section 4.4. For example, by coupling the two fibres without any separation, which can be achieved by tilting the input fibre A to a small angle and connecting it with fibre B with the help of DAW to minimise power loss at the corner. This can significantly improve device performance in terms of the exactness of energy distribution and power efficiency. The proposed design may also provide means of accommodating higher order modes.

Fig. 4-20 (a) and Fig. 4-20 (b) shows the discrete Fourier transform (DFT **E**y) fields of the M-RCF and CSIF converters, respectively. From the two field profiles, it can be seen that the power loss in the CSIF is clearly visible, justifying Fig. 4-19 (b).



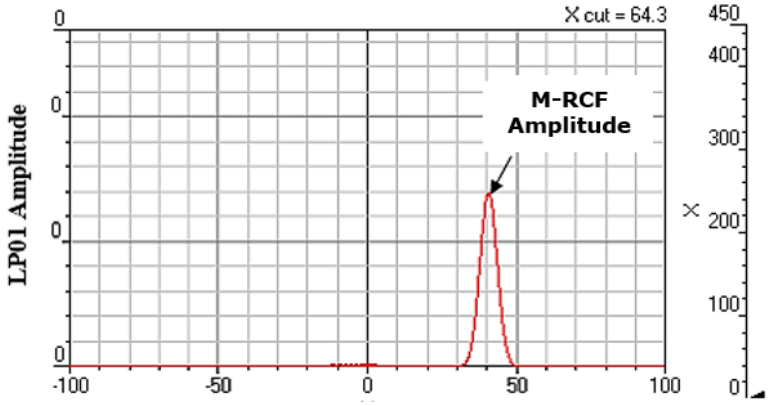
(a)



(b)

Fig. 4-20: (a)Discrete Fourier transform field of the M-RCF mode converter and (b) Discrete Fourier transform field of the CSIF mode converter.

Fig. 4-21 (a) represents the amplitudes at the output of the M-RCF and Fig. 4-21 (b) the amplitude of CSIF converters. The amplitude of the CSIF seems to be distorted probably because of the mode instability as it propagates in the core, which is contrary to that of the M-RCF, the mode amplitude appeared to be stable and may be linked to the mode confinement nature of the M-RCF.



(a)

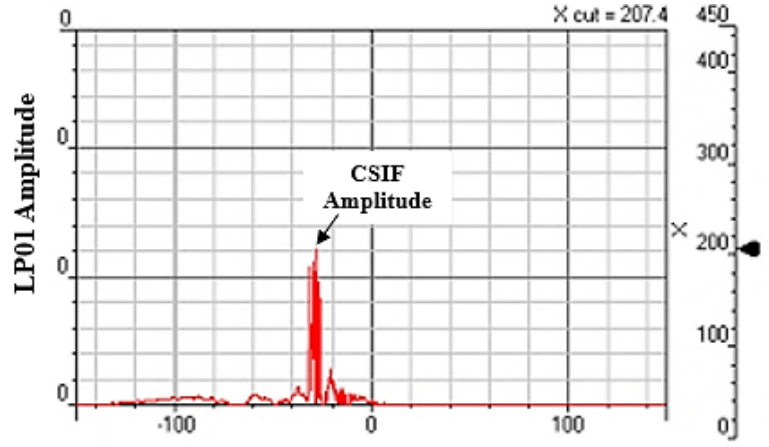


Fig. 4-21: (a) LP_{01} mode amplitude of the M-RCF device (b) LP_{01} mode amplitude of the CSIF device.

Another important performance parameter is the mode impurity, which occurs due to various factors that will cause the LP mode being distorted when propagates in a fibre. Therefore, it is important to quantify the distortion level to detect the purity of the mode. Fig. 4-22 evaluates the wavelength dependence of the proposed converters. It was achieved by positioning an input plane at the device input to inject modal energy at the range of wavelength from 1.480 μm to 1.610 μm. The mode purity of each mode converter was measured (using detector/observation point) at a different wavelength. As illustrated in Fig 4-22, the bandwidth of 85% for the M-RCF and 58.8% for the CSIF falls within the devices operating wavelength (1550 nm) and degrades as the operating wavelength shifted away from this wavelength. The wavelength dependence may be attributed to the phase mismatch at different wavelength in the angled-cleave CR.

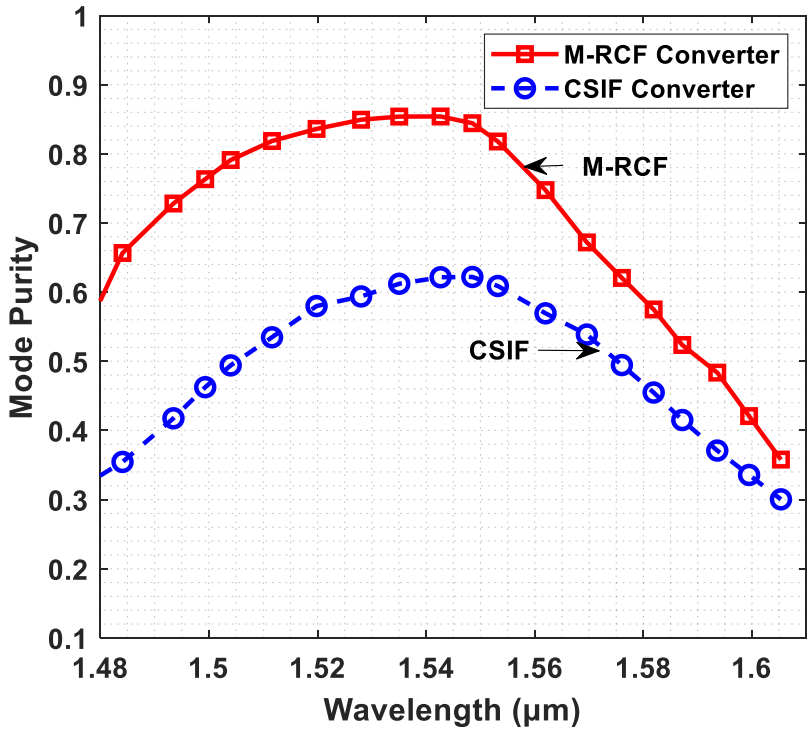


Fig. 4-22: LP_{01} mode purity of the injected model field as a function of wavelength.

Fig. 4-23 illustrates mode evaluation and stability process by calculating the mode purity as the function of lateral height 'h' between centres of the two fibres that modelled both the M-RCF and CSIF devices. The 'h' of each proposed converter was varied between 19 μm and 28 μm (the coupling point that provided the higher efficiency falls within this range). It can be seen that the mode purity of the M-RCF converter (red curve) increases from approximately 62% to 85% and stabilized at the range of 'h' value between 20.5 μm to 21.8 μm, which means the best LP_{01} modal purity (85%) is determined within this range. A similar analysis for the CSIF converter shows that mode purity increases from approximately 15% to around 58.8% between the range of 'h' from 19.5 μm to around 22.4 μm, then start degrading a bit. It is important to mention that the mode purity in each case was determined by placing an observation point (detector) at the relevant positions along the fibre.

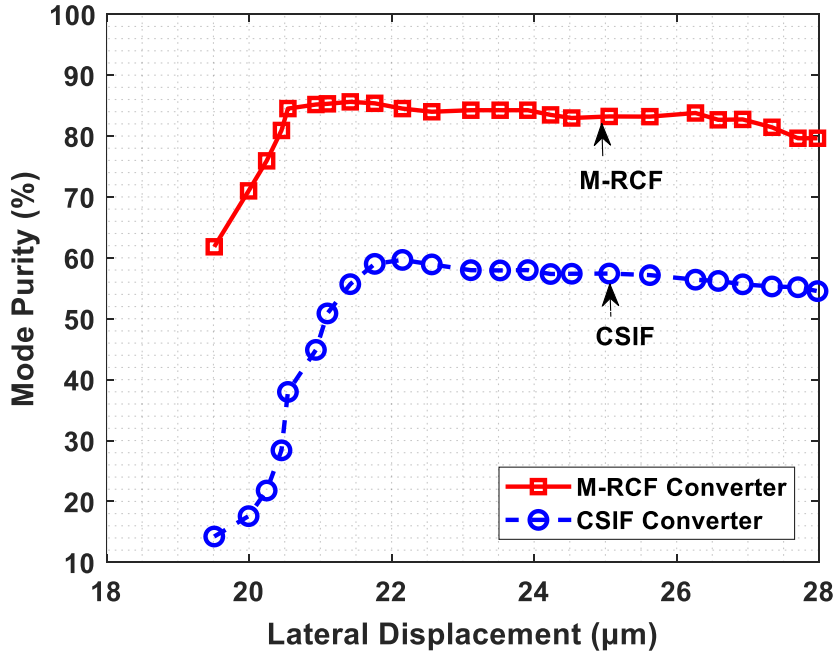


Fig. 4-23: LP_{01} mode purity as a function of the lateral height of the two converters.

Fig. 4-24 illustrated the wavelength dependence of the M-RCF converter. The blue curve is the LP_{11} power before the conversion and the red curve is the LP_{11}-LP_{01} converted output power. In order to analyse the dependence of the converter on wavelength. The measured power was determined using the observation line (OL), which was placed in the two positions. The power before the conversion was evaluated to be $5x10^{-9}$ W/m, and the power after the conversion was calculated to be around 4.7×10^{-9} W/m as shown in Fig. 4-24 (at 1550 nm).

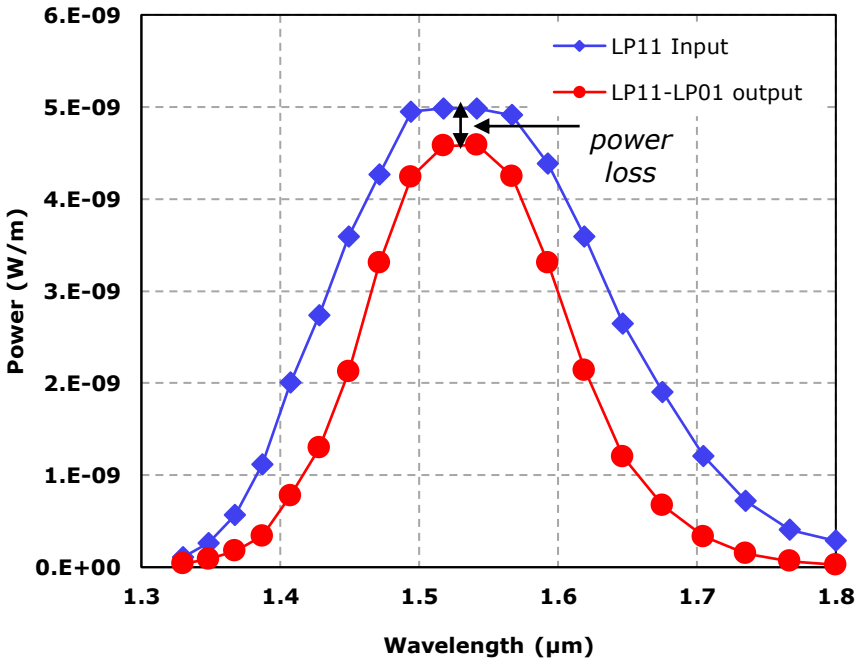


Fig. 4-24: Converter wavelength dependence.

The coupled power of the two devices was determined by placing the OL at the point of interest. The OL centre can be defined horizontally along the Z-axis or vertically along the X-axis. Note that in order to compute correct power results, it is necessary to align the OL with wafer orientation. It is defined as a function that consists of the intensity over a specified surface (time average of the Poynting vector). The power in the two models was calculated by positioning the OL at three different points: at the cleaved region to determine the power at cleaved-angle (P_{AC}), which is then coupled to fibre B; the next is to evaluate the coupled power at the input of B (P_{IB}). The last is coupled power (P_{OC}) at the fibre B output. The difference in P_{AC} and P_{IN} (input power) determines the coupling loss at angled-cleave (P_{L1}).

$$P_{L1} = P_{IN} - P_{AC} \qquad \text{Eq (4.5)}$$

Similarly, the difference between P_{IB} and P_{AC} defines the loss in the transmitted power along the 'd' as it couples at the input of fibre B (P_{L2}).

$$P_{L2} = P_{AC} - P_{IB} \quad \text{Eq (4.6)}$$

A summary of the calculated power of the M-RCF and CSIF converters at different positions are presented in Table 4-2. This includes P_{IN} fibre A, P_{AC}, and the P_{IB}, also presented are the P_{OC}, P_{L1}, and $P_{L\,2}$.

Table 4-2 Calculated power of the M-RCF and CSIF devices at 'h' value of 20.5 μm, for M-RCF and 22.2 μm for the CSIF-converter. The approximate output power of 94 % and 69 % for the M-RCF and CSIF converters were received at fibre B output.

Power (W/m)	P_{IN} A	P_{AC}	P_{IB}	P_{L1}	$P_{L\,2}$	P_{OC}
M-RCF-Converter	2.054×10^{-8}	2.009×10^{-8}	1.891×10^{-8}	4.45×10^{-10}	$5.6731.89\times10^{-12}$	1.89×10^{-8}
CSIF-Converter	2.054×10^{-8}	1.54×10^{-8}	1.438×10^{-8}	5.14×10^{-9}	1.025×10^{-9}	1.42×10^{-8}

4.4 Mode conversion Based on Tilts MC-MMF

In this section, mode conversion based on the MC-MMF assisted by the DAW is presented. The MC-MMF is used to model the device due to their low bending loss, high precession in mode confinement and ease of fabrication during manufacturing. In order to improve the performance of the device investigated in section 4.2, a new model is presented. Here, the proposed configuration consists of a 12°-tilted MC-MMF (optimised angle) at the device input. A horizontal fibre of the same properties at the output is connected with the help of the DAW to form a corner. This was achieved by making proper alignment between the core layers of the two fibres and the arc bends. Mode conversions of LP_{11} to LP_{01}, LP_{02} to LP_{11}, and LP_{21} to LP_{01} were achieved with the CE of 89.6%, 91.2%, and 94.34%, respectively.

4.4.1 Optimisation of the tilts input MC-FMF

In order to optimise a suitable angle at which the input fibre to be inclined, a range of values (10°-45°) are considered. The effect of tilting the fibre at various angles was examined. This was achieved by varying the tilted angle using the layout depicted in Fig. 4-25.

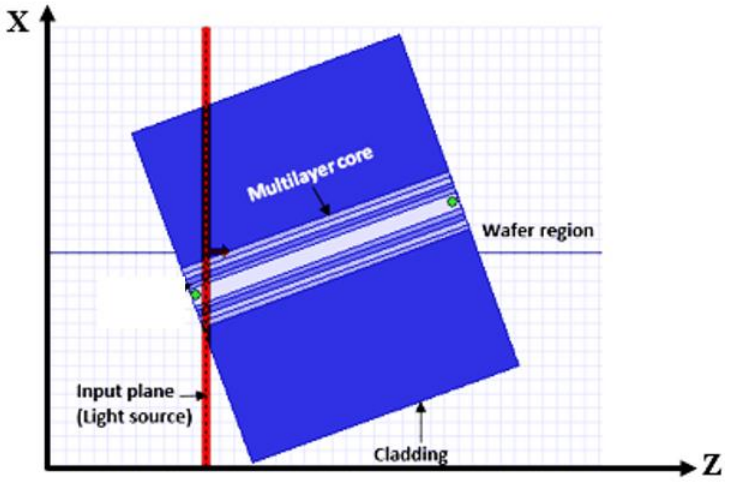


Fig.4-25: 2D Simulation layout of the tilted fibre, the modes are excited from the left using an input plane as the energy source.

It was found that increasing the tilted angle beyond the critical angle value (43°) could lead to amplitude decay and distortion. This is because as the tilted angle increased the effects of radiation also increases.

Fig. 4-26 (a-c) illustrates such effects at θ_t=45°. The amplitude of each mode decreases as it propagates through the tilted fibre at this angle. Fig. 4-27 (a-c) depicts the mode amplitude at the tilted angle of 12°. Fig 4-27 (a) is the LP_{11} with two lobes clearly visible. Fig 4-27 (b) represents LP_{02} mode amplitude, the three lobes are visible and clearly represented. Fig 4-27 (c) depicts an LP_{21} mode amplitude, the four lobes are visible, compared to Fig. 4-26 (c) where the lobes are almost disappeared at 45°. Because of the proper mode amplitude displayed by 12°, it was chosen to model the device input.

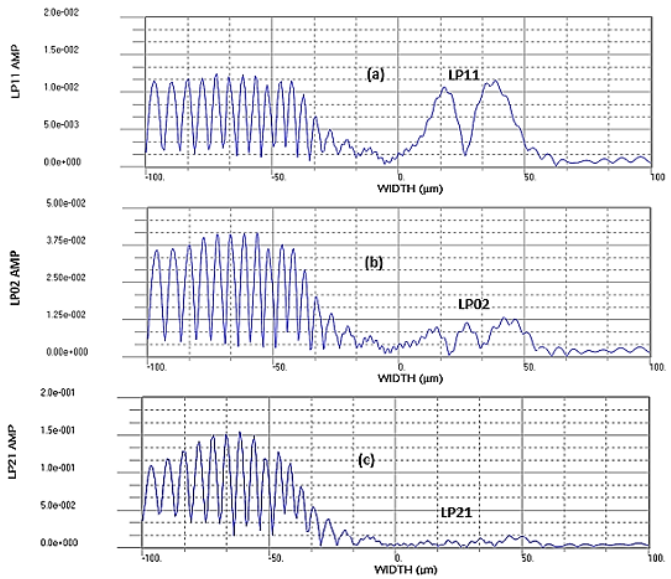


Fig. 4-26: LP mode amplitudes decay at a 45°-tilted angle as it propagates along the fibre: (a) LP_{11} mode; (b) LP_{02} mode amplitude; and (c) LP_{21} mode. The lobes are gradually disappearing as the order of the modes get higher.

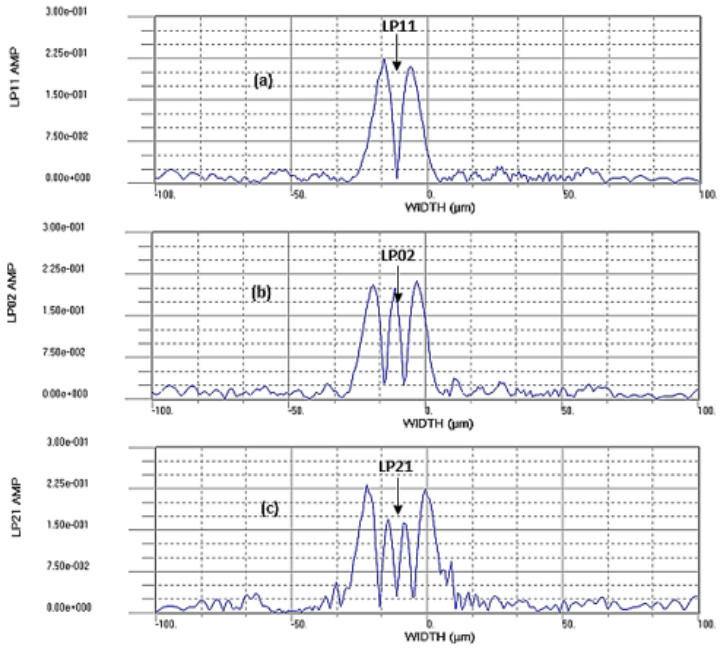


Fig. 4-27: Mode amplitudes at 12°-tilted angle: (a) LP_{11} mode; (b) LP_{02} mode; and (c) LP_{21} mode.

4.4.2 Device Setup

As presented in Section 3.3.3, the design parameters were evaluated based on the FDTD analysis. The simulation was run in the 2D domain under the TE type. A wafer dimension was set to 300 μm×200 μm (length× width) and the wafer material index is air. The cells used are of 100 nm size and 2700-time step. Thus, the time step size is set to auto to ensure good convergence of the solutions. This is run for 2700 time steps in order to have enough trip from the input of the tiled fibre through the DAW to the horizontal fibre. The transverse input field (light source) was positioned at the device input in Z-direction. Here, the modal field is used to calculate the number of modes supported by the MC-MMF. Each of the modes (LP_{01}, LP_{11}, LP_{02}, and LP_{21}) is separately excited to study the behavior of each independently. Table 4-3 presents the parameters used in the simulation domain at the operating wavelength of 1.55 μm.

Table 4-3 Converter design parameters.

Fiber/WG	Length (μm)	Layer Diameter (μm)				TA
		FOC/OC1	SOC/OC2	TOC/OC3	LOC/OC4	
Tilted fibre	37.5	6	10	14	18	12^0
H. Fibre	40	6	10	14	18	-
DAW	20	6	10	14	18	-
Wafer	300/200	-	-	-	-	-

4.4.3 Conversion Design and Analysis

Fig. 4-28 depicts the model of the proposed device that consists of three sections. The input section (I-Section), conversion region (C_R), and the output section (O-Section). If a field is incident from the left (I-Section), theoretically on reaching the C_R, it will be scattered into four distinct components. The components include back radiation, reflected propagation, propagation modes, and forward radiation field. To mitigate the effect of the reflected field and backward radiation, the core-cladding index contrast was made small and the fibre diameter made large. Moreover, the radiation field is cause mainly by mode propagation near cut-off. Therefore, by making the tilt angle small, radiation field can be made negligible [179].

In order to achieve an efficient conversion, the device FOM (figure-of-merit) design parameters that determine its performance were linked to the CE. Thus, it is defined as [180-181]

$$CE_{(LP11-LP01)} = \frac{P_{01}}{P_{11}} \qquad \text{Eq (4.7)}$$

$$CE_{(LP02-LP11)} = \frac{P_{11}}{P_{02}} \qquad \text{Eq (4.8)}$$

$$CE_{(LP21-LP01)} = \frac{P_{01}}{P_{21}} \qquad \text{Eq (4.9)}$$

where, P_{01}, P_{11}, P_{21}, and P_{02} denotes the output power of the converter in the LP_{01}, LP_{11}, LP_{21} and LP_{02} modes, respectively.

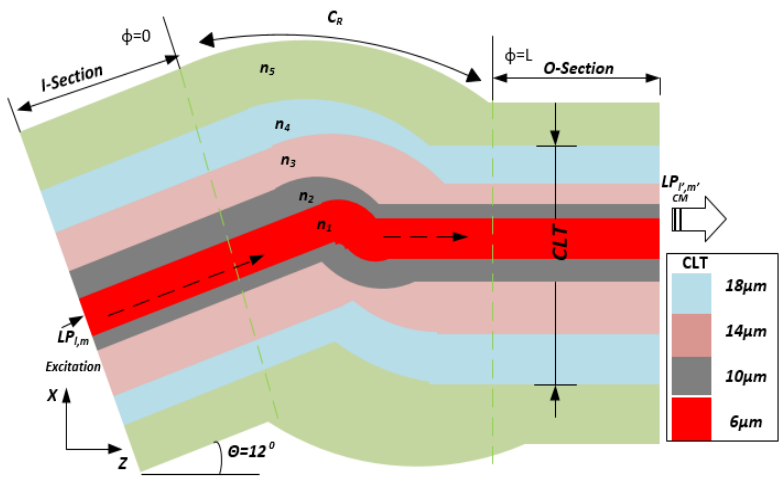


Fig. 4-28: Schematic of the proposed conversion device consists of three sections that include an input section (I-Section), conversion region (C_R), and the output section (O-Section).

Fig. 4-29 illustrates the device evaluated IL as a function of the layer offset in the profile steps at the conversion length of 20 μm. The bending loss can be evaluated by computing the mismatch in the field distributions of the arc bends and the straight fibre [182].

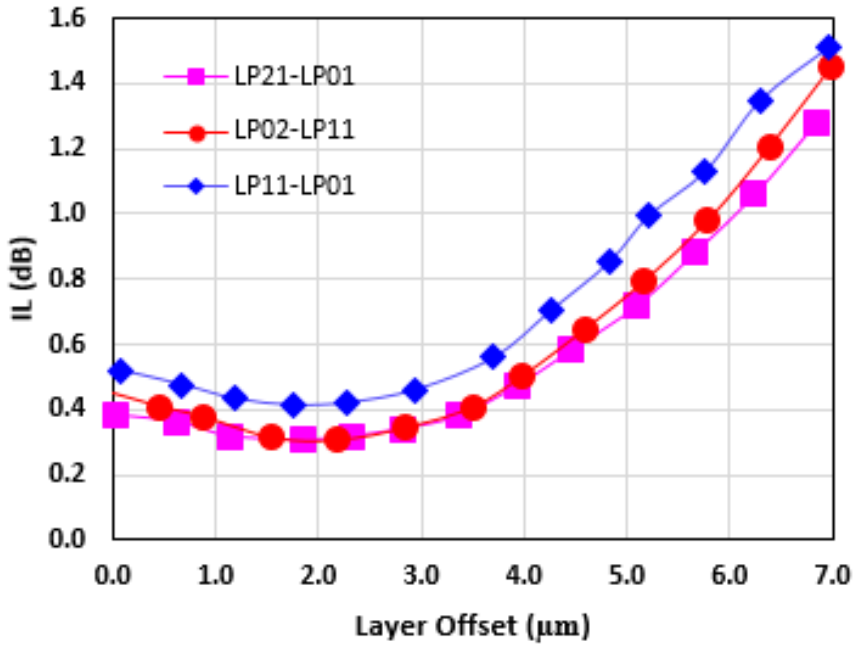


Fig. 4-29: Effect of varying the layer offset as a function of IL.

The minimum value of IL is obtained when the offset is 2 µm for the LP_{21} to LP_{01}, LP_{02} to LP_{11}, and LP_{11} to LP_{01} mode conversions. It can also be seen that when the positions deviate from 2 µm point, the IL tends to increase to a higher value**.**

4.5 Results and Discussions

Fig. 4-30 to Fig. 4-32 illustrates the results of the mode energy distributions achieved on the excitations of LP_{11}, $LP_{02,}$ and LP_{21}, at 12^{o} tilts angle.

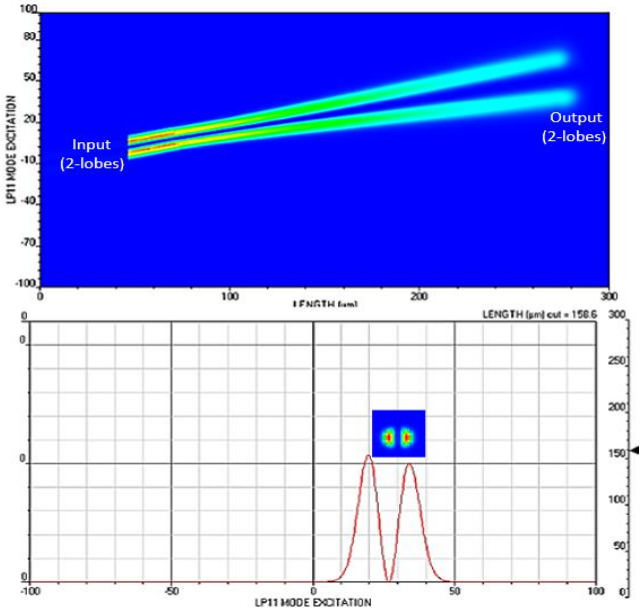


Fig. 4-30 LP_{11} mode excitation at the input of the tilted fibre with the two lobes visibly seen at the input and the output.

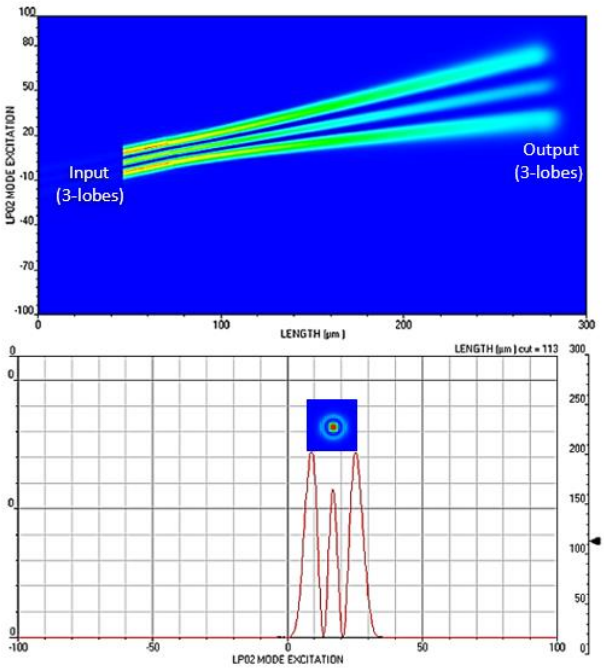


Fig. 4-31: LP_{02} mode excitation at the input of the tilted fibre with the three lobes visible at the input and output.

The results in Fig. (4-30 to 4-32) justified the results shown in Fig. 4-27, in which all the mode lobes were clearly visible. Therefore, the two results are in good agreement with the theory mentioned earlier. Hence, it can be concluded that the radiation loss is negligible at this angle (12^0).

Similar behavior was observed with LP_{02} and LP_{21} when each was excited, all the lobes are clearly seen at the output as depicted in Fig 4-31 and Fig. 4-32, respectively.

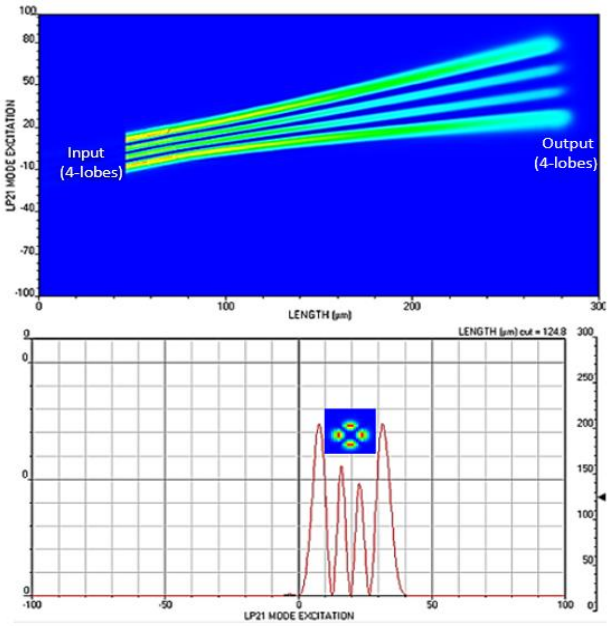


Fig. 4-32: LP_{21} mode excitation at the input of the tilted fibre with the four lobes visibly seen at the input and output.

Fig. 4-33 illustrates the relationship between the mode amplitudes and the tilt angles. The amplitude of the propagating LP_{01} mode decreases close to zero at 43° (critical angle), then increases a bit to a small peak. Moreover, the higher order modes (LP_{11}, LP_{02}, and LP_{21}) demonstrate similar behavior, starting with a tilt angle equal to zero (0°). When the tilt angle is greater than the critical angle an approximate equal distribution is observed.

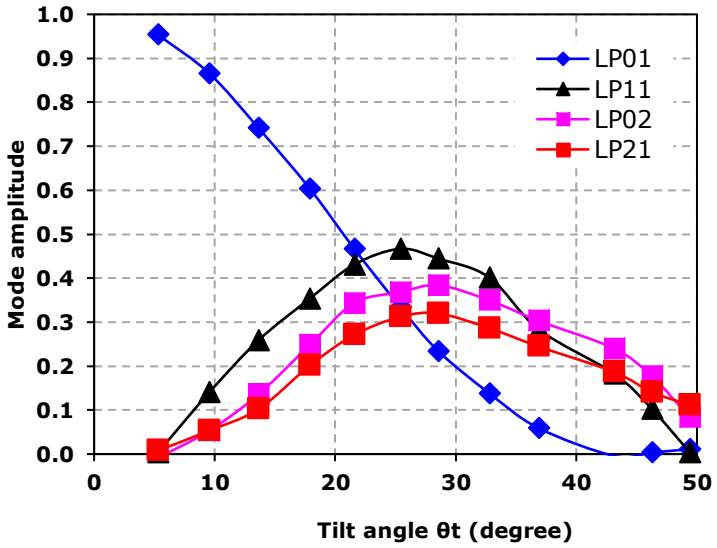


Fig. 4-33: Modes amplitude as a function of tilt angles.

Fig. 4-34 is the 3D layout of the converter comprising of the tilted fibre, dual arc, and the horizontal fibre.

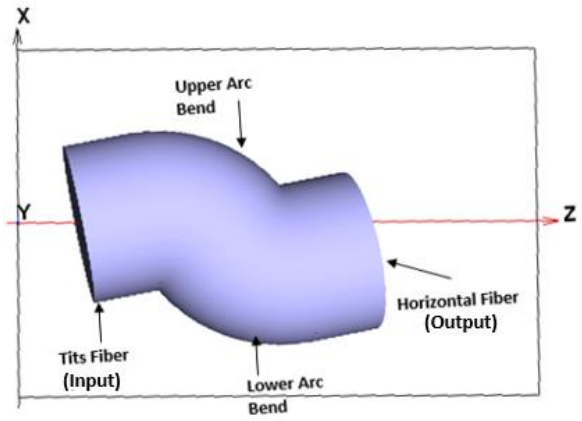


Fig. 4-34: 3D layout of the device displayed during simulations. The components that constituted the device were well aligned to give the overall device architecture.

Fig. 4-35 illustrates the 2D refractive index distribution of the the proposed device at the simulation point. It comprises a multilayer core, a cladding and the wafer (blue region), which housed the device setup. From Fig. 4-35, it can be seen that both the

cladding and multilayer core of the tilted fibre, DAW, and the horizontal fibre are well joined to avoid power leakages. The index distribution is a very important aspect in running successful simulation. Because only at this point one is able to check the connectivity of all the components (tilted fibre, DAW, and the horizontal fibre) involved in the design.

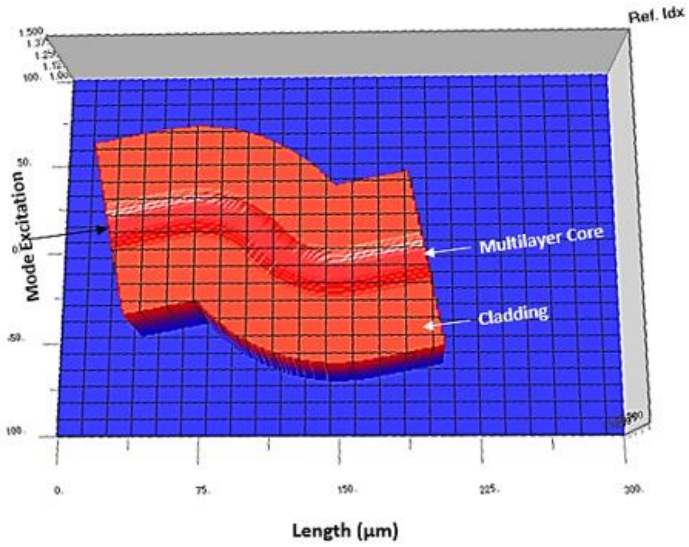


Fig. 4-35: 2D Refractive index distribution of the proposed model.

Next is the results of the overall device. The proposed model depicted in Fig. 4-28 was simulated by exciting one mode at a time to the input of the tilted fibre. The results were shown in Fig. 4-36 to Fig.4-38. Fig. 4-36 depicts the conversion of an LP_{11} to LP_{01} mode, the two lobes of the LP_{11} can be seen at the input. After propagating through the C_R, only one lobe appeared at the output. This indicates that conversion has taken place due to the coupling between the two lobes (degenerates) of the LP_{11} because of the bend. The lobe appears at the output fibre assumed to be an LP_{01}. This is because it is the only mode having one lobe supported by the fibres.

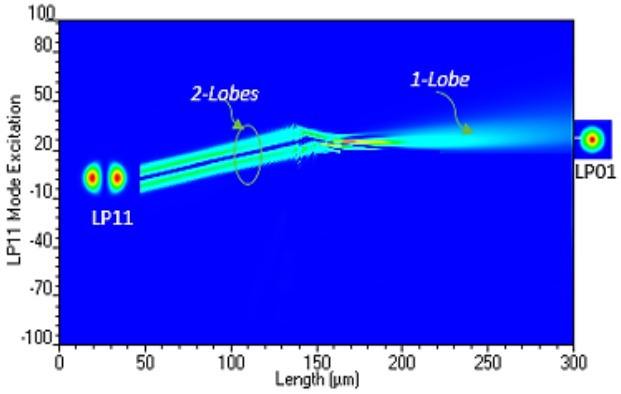


Fig. 4-36: LP_{11} to LP_{01} Mode conversion. An LP_{11} mode was excited at the input of the tilted fibre. After propagating through the bend, an LP_{01} mode is observed.

The entire dark blue region is the wafer which is of 300 µm (length) and 200 µm (width). Fig 4-37 illustrates the result of the conversion of an LP_{02} to LP_{11}. An LP_{02} was excited at the input of the tilted fibre (Fig 4-28). In this case, three lobes are clearly observed in the entire length of the tilted fibre (input fibre). On propagating through the C_R, two lobes are dominant at the output of the horizontal fibre due to coupling. This indicates the presence of an LP_{11}, as it is the only mode having two lobes supported by the fibres. The inset of the mode distribution is for a better understanding.

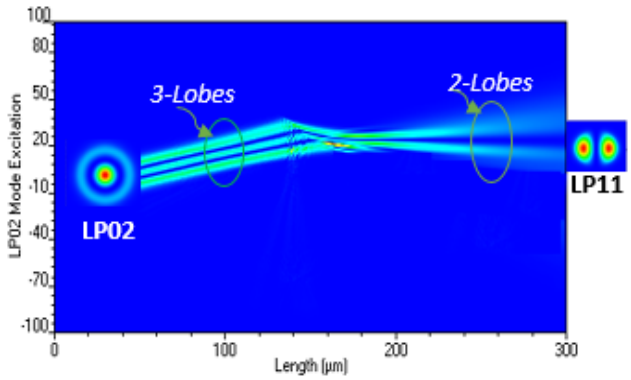


Fig. 4-37: LP_{02} to LP_{11} Mode conversion. An LP_{02} mode was excited at the input of the tilted fibre. After propagating through the bend, an LP_{11} mode is observed at the output of the horizontal fibre.

Fig. 4-38 is the conversion result of an LP_{21} to LP_{01} mode. At the input of the tilted fibre, an LP_{21} was excited. Four lobes are clearly visible at the entire length of the input fibre. On passing the bend (C_R), only one lobe is observed at the output of the horizontal fibre. This indicates a conversion of LP_{21} to LP_{01}. The other lobes are believed to be affected by coupling at the C_R.

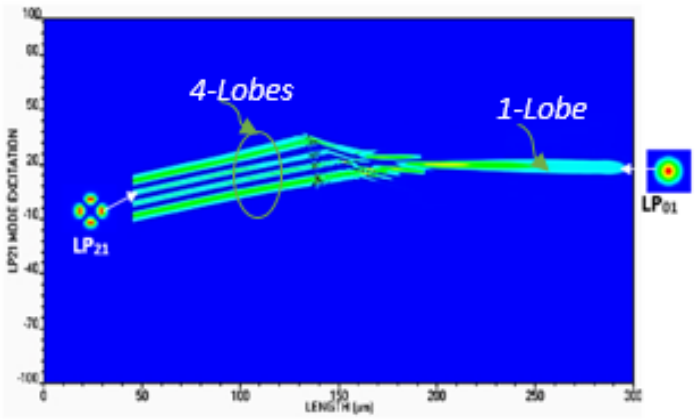


Fig. 4-38: LP_{21} to LP_{01} Mode conversion, LP_{21} mode was excited at the input of the tilted fibre. After propagating through the bend, an LP_{01} mode is observed at the output of the horizontal fibre.

Fig. 4-39 depicts the calculated absolute power spectrum at the output of the proposed device. The pick of the spectrum is within the range of C-band, which is the operating wavelength of the device. As illustrated in Fig. 4-39, the absolute power spectrum of the conversions of an LP_{02} to LP_{11} (Red curve) and LP_{11} to LP_{01} (blue curve) is the wavelength dependence. It can also be observed that the peak of the spectrum in both cases falls within the operating wavelength.

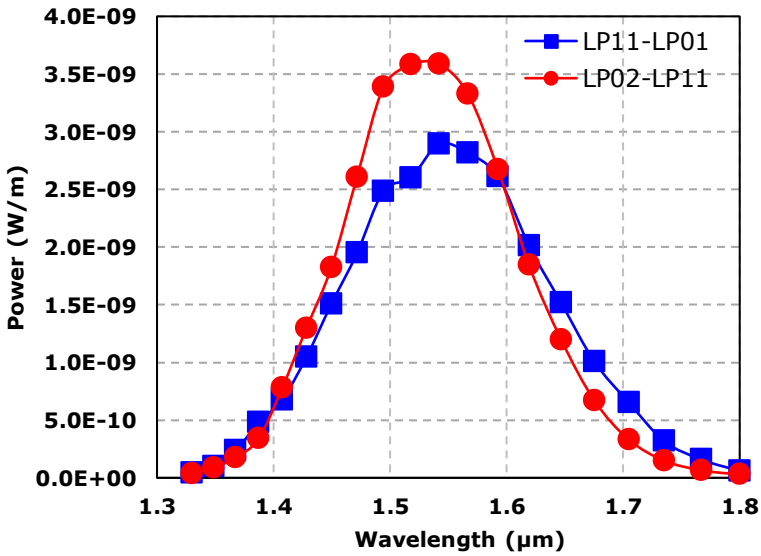


Fig. 4-39: Output absolute power of LP_{02} to LP_{11} and LP_{11} to LP_{01} mode conversions.

The device CE was evaluated using Eqn (4.7) through Eqn (4.9). It was calculated by determining the power at the output of the tilted fibre (interface between the tilted, the input of the arc bend and the power at the output of the bend (interface between the bend output and the horizontal fibre input). This is due to the conversion taken

place within the DAW. The CE of the LP_{11} to LP_{01}, LP_{02} to LP_{11}, and LP_{21} to LP_{01} were found to be 89.6%, 91.2%, and 94.34%, respectively. Similar fabrication procedure proposed by [165][183][184] can be upgraded and implemented for the proposed devices. Finally, on comparing the proposed devices presented in this Chapter with the one reported in Table 2-1, one can see that most of the work in Table 2-1 targeted the conversion of fundamental mode to higher order modes whilst the work reported here is the reverse. Another important point is the simplicity in our approach, in which all the proposed devices are fibre-based.

4.6 Summary

In section 4.2-4.3, two different mode converters are modeled to convert an LP_{11} to LP_{01} mode. The first converter employs CSIF, and the second converter employs M-RCF. In both cases, the distance of separation 'd' between the two fibres and their lateral misalignment 'h' were varied to determine the maximum coupled power. Each of the two fibres were used independently to study mode conversion on LP_{11}. The performance of the two converters were evaluated and compared. It was found that the M-RCF -based converter demonstrates high CE, high MP, and low loss at the coupling region. By cleaving the fibre under excitation (fibre A) in both CSIF and M-RCF at angle 42°, the CE of the two converters at the output fibres were found to be 69% and 94% with the MP of 58.8% and 85%, respectively.

Section 4.4 presented the conversion of multiple high order modes. In this case, a numerical demonstration of higher order mode conversion is investigated and achieved using MC-MMF assisted by the DAW. The radiation loss was suppressed by tilting the fibre at 12^0. It was shown that tilting the fibre at an angle greater than the critical angle could lead to amplitude distortion/decay due to the field radiation. Another relationship investigated is the variation of mode amplitude on tilt angles by exciting different LP modes from the input of the tilted fibre. The amplitude of the propagating LP_{01} mode decrease close to zero at 43^0, then increases a bit to a small peak. Moreover, the higher order modes (LP_{11}, LP_{02}, and LP_{21}) demonstrate similar behavior, starting with a tilt angle equal to zero (0^0). It was found that when the tilt angle is greater than the critical angle, an approximate equal amplitude distribution is observed. Finally, an LP_{11} to LP_{01}, LP_{02} to LP_{11}, and LP_{21} to LP_{01} mode conversions were achieved. The CEs of the LP_{11}-LP_{01}, LP_{02}-LP_{11}, and LP_{21}-LP_{01} were found to be 89.6%, 91.2%, and 94.34%, respectively.

Based on the calculated results the device can be a good potential for mode conversion in mode multiplexing for MDM systems due to their low loss.

Chapter 5 Novel High Dispersion Fibres for MDM System

5.1 Introduction

For the successful realisation of an MDM communication network, it is essential to investigate the MD [40], and MDL [185] of a fibre. Relevant research dealing with this concept has already been published, in which the idea of PSP has been extended to the FMF/MMF [186]. The statistics of the comparable (GD) group delays and crucial remarks on the dynamics of the MDL were also reported [187]. Nevertheless, a thorough investigation of the true nature of these scenarios can highly benefit the overall idea of the analytical tool that is indispensable to the study of polarisation.

Linearly polarised (LP) modes can be used to describe light transmission in a fibre under the weakly guiding approximation [16]. Thus, a group of 2-4 (quasi) degenerate hybrid modes constitutes each of the LP modes. Therefore, the MD of a fibre originates from two viewpoints. The one that leads to the inter-modal dispersion (I-MD) arises due to the dissimilarity in the propagation constants of the LP modes having distinct order. Moreover, the other comes from the dissimilarity in the propagation constants of the hybrid modes constituting each LP group of the degenerate modes. This describes intra-modal dispersion. In FM/MMF, the effects of I-MD is superior over the intra-modal one. It can be mitigated or eliminated completely if the LP groups are degenerating modes (can be strongly coupled) [188]. One of the adopted techniques in MDM is to mitigate coupling effects between the LP modes. This can allow each group of a quasi-degenerate mode to be employed as an independent transmission channel, which can minimise complexity or eliminate using MIMO equaliser at the receiver [40][126]. In such case, I-MD has a smaller effect. Moreover, principal modes (PMs) were also engaged for MMFs as the generalisation of PSP in SMF to overcome MD [186][189][40]. The temporal distortions can be minimised using complex MIMO technique but can increase system cost. An MMF in a long-distance transmission was initially deserted due to the MD between the transporting modes. It is only available when distinct signal mode channels transmission occurs in the MMF/FMF. In the SMF, there is no MD as there is only one exciting mode and the total signal power remains in the LP_{01} mode. In addition, an OFDM has been adopted to provide high dispersion tolerance in MMF [190]. An OFDM method can be employed in the MMF optical network regardless of the number of the mode count [23]. Here, the signal has to be coherently detected, which increases receiver complexity as well as overall system cost.

5.1.1 Modal Dispersion Equalisation

Several techniques on MD equalisation were reported regarding the FMF. For example, by employing equivalent planar waveguide [39]. The technique developed a numerical method to determine the propagation constants in the fields and group velocities of an arbitrary mode in a weakly guiding symmetric fibre. The employed program confirmed the dispersion equalisation in a known index profile solution and can also be applied to optimise other profiles. Here the work only restricted to three spatial modes. In another report [191], an index profile capable of supporting four LP-modes propagating with the same group velocity was investigated. A numerical technique was proposed for computing the GD of the LP modes involved (LP_{01}, LP_{11}, LP_{02}, and LP_{21}). The index profile that employs a power-law for the index variation was constituted using multiple index exponent in the fibre over distinct radial distances along the axis. In this case, the fibre propagates four modes, which are I-MD free. However, adopting multiple exponents makes this approach more difficult.

Large mode area fibre can be used to mitigate I-MD. The main challenges are their incompatibility with standard mode fibre components, and most of the available fibre-optic components still maintain the standard modal size. Therefore, fusing spliced can bring a large mismatch in the mode area, which can lead to excessive power loss at the fibre joint [192]. Moreover, controlling the A_{eff} can minimise mismatch at the expenses of a nonlinearity [193], also one important point to note is that lowering the A_{eff} can increase dispersion [194]. Enlarging the A_{eff} is achieved by decreasing a core-cladding contrast (which decreases the numerical aperture). However, this can initiate some other limitations [195], such as weakening the guiding capability of fibre and significant losses can surface due to a small imperfection of the optical fibre (bend loss) [196]. Thus, there should be a limit on how small the numerical aperture values can be reduced. It has been reported that the value should not be below 0.06, however, in an ultimate case, a value close to 0.04 has been adopted [197].

The magnitude of an MD can also be accessed from the level of the DMGD (differential mode group delay). It relays tightly on the index profile of the optical fibre (in or around the core) [198]. It can be observed in fibre with SI profile that the higher-order LP modes possess a lower group velocity. This leads to a DGD (close to 10 ps/m) and can make it very difficult for such fibres to achieve high-speed data capacity rates of multiple Gbit/s in an optical transmission link even for a kilometer length [199]. In a fibre-based link employing MMF, the MD severely reduces the achievable bit rate. Therefore, to deal with signal mode distortion, it is extremely crucial to set the pulses to maintain equitable temporal overlapping components from the distinct modes. The perfect means of eliminating MD is to use SMF-based fibre transmission links; however, using MMF with a parabolic index profile

also serves as an alternative way of reducing MD [200] at the expenses of employing complex MIMO DSP. Swens Zlong *et al.* [201], reported a novel multiple-ring core single-mode large A_{eff} fibre, composing of a periodic alternating CH, and CL index profile and demonstrating large area fibre with low bending loss. The fibre targeted high-power applications. However, the work restricts to a single mode operation.

As opposed to the previous approaches, the proposed model here was extended to a four-mode fibre supporting LP_{01}, LP_{11}, LP_{02}, and LP_{21}. Using the two different refractive index profiles (CH and CL), an optimised thickness (OPT) value was determined by adjusting each of their core-ring radii. At 1550 nm wavelength, these values were used to model the two fibres to achieve an equalised MD. The main difference between the proposed model and the principle mode model is that our model intends to work in the weakly coupled regime. In this case, each mode is transmitted separately as an individual signal channel, without using a complex MIMO technique. While the principle mode approach provides an effective method to reduce the temporal distortions particularly in the strong coupling regime, in such a case, MIMO digital signal processing is inevitable. The complexity of the MIMO scaled up as the number of spatial mode increases, thus, increasing the system cost.

In this chapter, a novel dispersion equalisation technique employing MC-MMF using LP-MMM approach is presented. Each of the core ring radii of the alternating CH and CL index profile was optimized to a specific thickness value. The core ring radius varied in each case to determine the OPT for the dispersion equalisation.

5.2 Multilayer-Core Design Property

Fig. 5-1 depicted a schematic of the core-ring cross-sections of the proposed four modes (4MF) fibres. The core structures composed of an alternating CH and CL-refractive-index layers. The yellow-green and grey colors are representing high and low index region respectively.

As illustrated in Fig 5-1 (a-b) two types of fibre core cross-section structures are presented. The structure schematic with a center ring having high-index value (Fig. 5-1a) is referred here the CH-ICF. The structure schematic with a center-ring having low-index value (Fig. 5-1b) is referred here as CL-ICF. Raising the high index can be achieved by adding erbium/aluminum as proposed in [201]. Similarly, the low index regions can be doped with fluorine. The cladding material is assumed to be pure silica with a diameter of 125 μm, and a refractive index of 1.444.

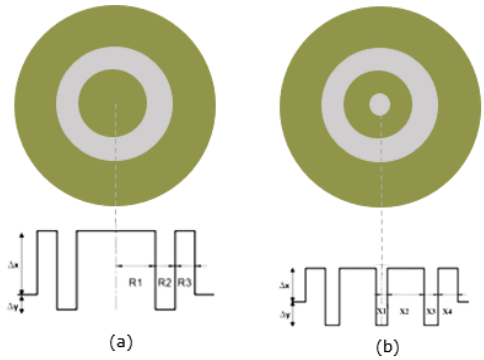


Fig. 5-1: (a) Cross section of the proposed CH-ICF. R1, R2, and R3 are the layer thicknesses and (b) Cross section of the CL-ICF with the X1, X2, X3, and X4 as the thickness of the rings.

The two core structures consist of the following parameters. The core rings thicknesses of the CH-ICF structure are R_1 (high index centre layer), R_2 (low index ring second layer), and R_3 (high index ring third layer). Similarly, for the CL-ICF; X_1 (low- index rings thickness at the centre layer). X_2 (high index ring thickness, second layer), X_3 (low index ring thickness, third layer). And X_4 (high index ring thickness, fourth layer). The difference in index between the high index ring and the cladding defines by $\Delta_x=n_h-n_{clad}$, where n_h is the refraction index of the higher index, n_{clad} represents the cladding index. In addition, the index contrast between the cladding and a low index ring defines by $\Delta_y= n_{clad}-n_L$. The fibre wavelength was fixed at 1550 nm for the entire operations. To ensure the four-mode operation at this wavelength, the *Vp* was determined to be 5.378 using Eq (2.1). The relations between A_{eff} and thickness of the lower index regions are investigated. It is observed that mode confinement in the core reduces as the diameter of the lower core region increased, which results in the A_{eff} increase. Therefore, the ring thickness R_2 of the high-index core was optimised such that the mode confinement is not affected. The A_{eff} of each of the modes in relation to the structural parameters of both CH-ICF and CL-ICF was also investigated. The remaining parameters used in the core-cladding design are $\Delta_x=0.017$, $\Delta_y=0.007$, $R_1=4.25$ µm, $R_2=2.6$ µm, and $R_3=2.3$ µm. Also, $X_1=2$ µm, $X_2=3$ µm $X_3=4.2$ µm, and $X_4=1.6$ µm.

Fig. 5-2 depicts the field distributions and intensities of the four modes displayed by the CH-ICF. The LP modes can be determined using a transfer matrix analysis of the multiple layer fibres. By employing an LP-analysis, a modal excitation with the linear polarisation is

assumed, thus, a modal analysis supporting a single field was employed. For a fibre with low index difference (practical optical fibres), a solution of the given LP-modes is constituted almost in the same way as the vector modes. The Field pattern seems to distribute in the core layers of the fibre as shown in Fig. 5-2. In addition, the CL-ICF demonstrates similar field distributions.

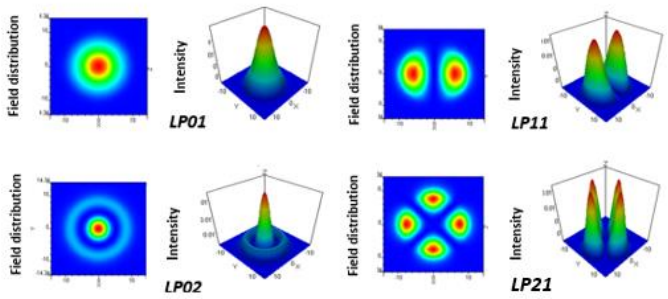


Fig. 5-2: Simulated modal distributions and field intensity of the multilayer-core CH-ICF.

5.3 Optimisation of the Design Parameters

A commercial OptiFibre numerical software package was used to investigate the effect of varying the core rings thickness on MDs. An LP-MMM was chosen for the calculations of the dispersion because of its accuracy over the finite difference method. Details of this method were presented in chapter 3, section 3.4.1. The choice of the number of rings for a given fibre design plays an important role in the equalisations. The overall core radius was held fixed to maintain the intended number of mode count by the fibres. The optimisation was achieved in two stages. In the first stage, the thicknesses RI, R2, and R3 of the CH-ICF and XI, X2, X3, and X4 of the CL-ICF were adjusted until the MDs are equalised. In the second stage, the effects of varying thickness of the lower index rings on the A_{eff} of the four modes in each core were investigated.

5.3.1 Inter-Modal Dispersion Optimisation

In an MMF/FMF, the signal pulse broadening is caused by combining the effects of the following three circumstances. (1) the group dispersion, which is because of the dielectric characteristics in fibre material. (2) because of the dispersion effect in a waveguide, and (3) due to the group velocities (GV) variation between the individual modes. The third one has

been assumed the major cause of the signal broadening. In an SMF, the group dispersion can be reduced by nonlinear variation of the dielectric constant in an optical wavelength greater than 1300 nm (anomalous dispersion) [202]. However, in MMF, the dominant dispersive effect is due to the variation in the GV of the modes propagated by a fibre. Therefore, the same approach is not applicable [160]. Different techniques can be employed to achieve both relatively large A_{eff} and negligible I-MD at a wavelength of 1550 nm. For example, in the case of a core with the GI profile [199], MD can be reduced by minimising spread in the group velocities. Moreover, dispersion impairments can also be tackled through a complex MIMO-DSP implementation at the receiver side [21]. This brings more complication to the system due to a strong MCP in the fibre. To avoid such MIMO complexities, new and simple fibre models are proposed in this work, which has been published in [114].

5.3.2 Modal dispersion Optimisation in the CH-ICF

An MD is equalised by varying the dimensional parameters of the core index profiles. The optimisation was achieved by varying the core layer thicknesses (core-ring radius) to a specified OPT value. These values would coincide with the one used in optimising the A_{eff} (for the case of R2 and X3 in the low index region of the two fibres). The target here is to match the dispersion of the individual modes to a specific reference value of 17 ps/(km.nm). This is because most of the practical glassy fibres operate around this value. Moreover, equalising the dispersion close to this value can allow a mode signal to transmit and receive without using the complex DSP module for the dispersion equalisation [203]. Note that the overall core radius was kept fixed throughout the optimisation process to sustain the four-mode operation. The thickness varying must occur simultaneously to achieve equalisation (this means R1, R2, and R3 were varied concurrently to achieve equalisation at λ= 1550 nm).

The best thickness value of each ring at which dispersions of the four modes converges is referred here as the OPT value. Fig. 5-3 to Fig. 5-5 depicts the effect of varying the core rings thickness (R) on the dispersion of the CH-ICF. As shown in Fig. 5-3, the convergence in the dispersion of the four-LP modes started from R_1 = 4 μm to 4.5 μm. However, the dispersion of LP_{01} rises slightly from R1 =4.3 μm, where the dispersions of LP_{11}, LP_{21}, and LP_{02} remained converged.

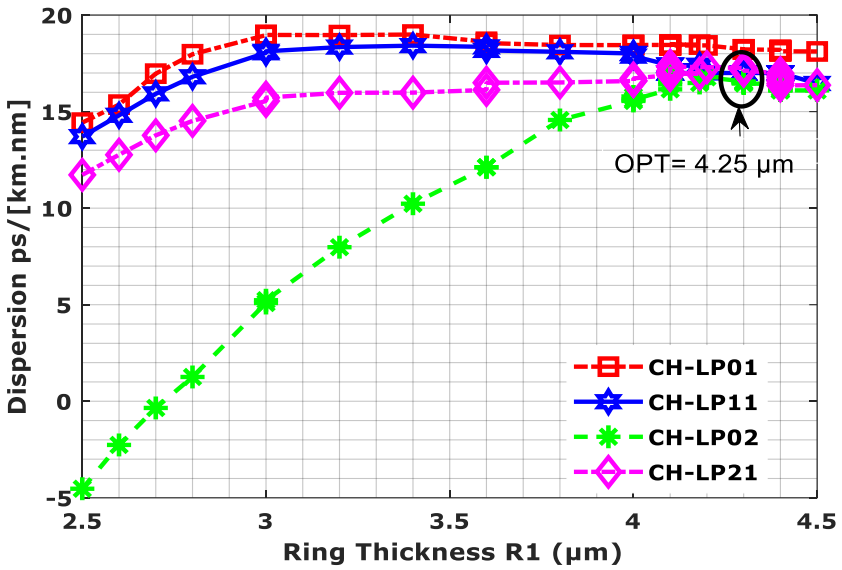


Fig. 5-3: The effect of R1 on the dispersion of the CH-ICF.

Fig. 5-4 illustrates the change in the dispersion as a function of the lower ring thickness (R2). Convergence in the dispersion of the four modes was observed from R_2 = 2.3 μm to 2.7 μm, after which there is a little divergence of LP_{01} and LP_{11}, while an LP_{21} and LP_{02} still remain converged. Therefore, the 2.6 μm is chosen as an OPT because both the dispersion convergence and an optimised value of the A_{eff} coincide at this point. Note that the criteria for choosing the optimum values are to make sure that each value coincides in the two optimisations (dispersions equalisation and the A_{eff}). The measured dispersions for the corresponding core ring thickness variations are presented in Appendix A. It is also important to mention that the index contrast was made fixed during the dispersion optimisation.

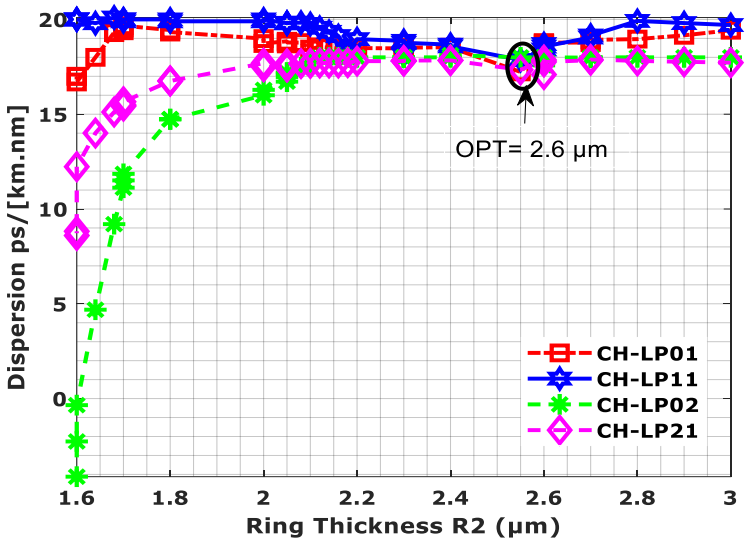


Fig. 5-4: Graph of R2 on versus dispersion CH-ICF.

Fig. 5-5 depicts the effect of varying the outer core ring thickness (R3) on dispersions. Here the convergence in the dispersion of the four modes occurred in three different points (R3=1.6 μm, 1.75 μm, and 2.3 μm).

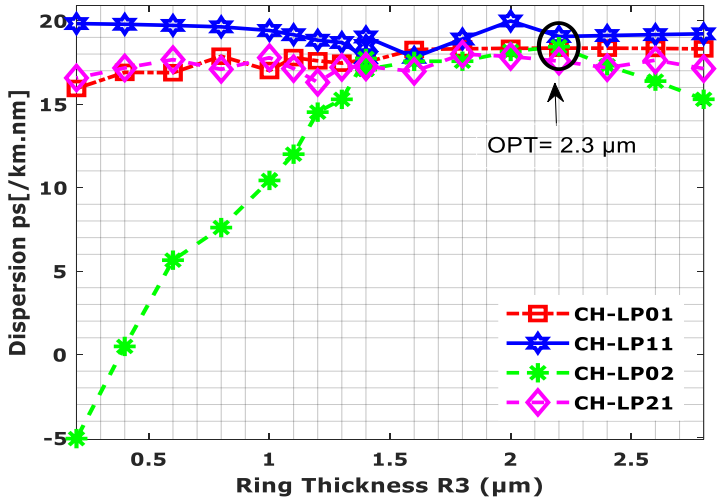


Fig. 5-5: Graph of the effect of R3 on dispersion CH-ICF.

To choose an appropriate OPT other factors must be taken into consideration. For example, being the outer ring, its thickness must not go below or beyond a value that will decrease or increase the overall core radius. Therefore, to satisfy this requirement an OPT of 2.3 μm is chosen to maintain the four-mode operation. Thus, the OPT values of R1, R2, and R3 that constitute the three rings of the CH-ICF were found to be 4.25 μm, 2.6 μm, and 2.3 μm respectively. Hence, the sum of these thicknesses gives an overall core radius of 9.15 μm (18.3 μm in diameter). Note that convergence in dispersions at a given thickness indicates equalisation in the dispersion at that point.

5.3.3 Modal dispersion Optimisation in CL-ICF

The optimisation of the CL-ICF was carried out in a similar way as CH-ICF, Fig. 5-6, Fig. 5-8, Fig. 5-9, and Fig. 5-10 depict the graphs of the measured dispersions against variation in the core rings thicknesses of the CL-ICF.

Fig. 5-6 illustrates a variation in the dispersion as a function of X1 (centre ring with the low index). Convergence in the dispersions occur at several points (for example, at X1=1.6 μm, 1.85 μm, and 2 μm). An OPT of 2 μm was chosen because the modes are more confined to the core centre at this thickness.

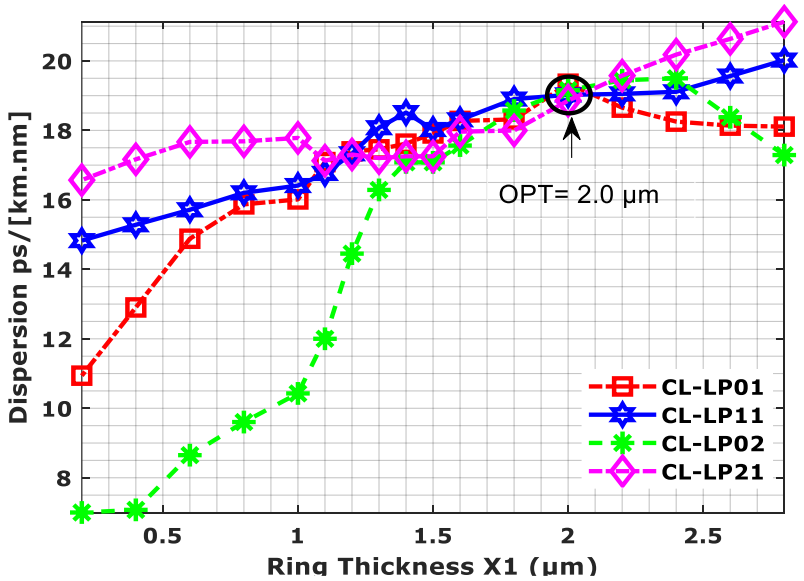


Fig. 5-6: Graph of change in X1 versus dispersion CL-ICF.

Fig. 5-7 (a-d) illustrates the modes confinement demonstrated by the CL-profile fibre at the specified thickness of (2 μm). It can be observed that the modes are

confined toward the centre for all the spatial modes. In each of the figures, the mode consists of the mode field, confinement graph, and the field distributions. It is crucial to mention that mode confinement at the core centre minimises power loss as the mode propagates through the fibre.

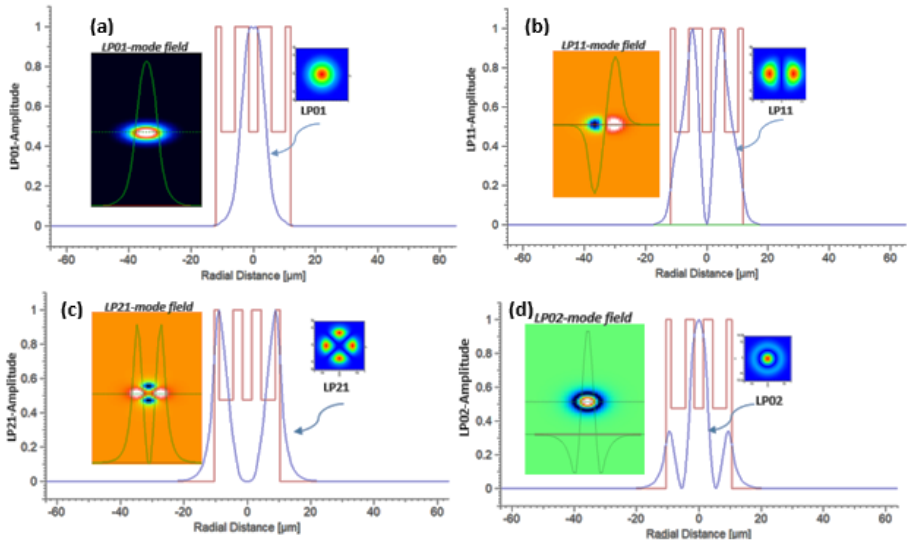


Fig. 5-7: (a) CL- profile of the LP_{01} mode confinement (b) CL- profile of the LP_{02} mode confinement (c) CL- profile of the LP_{21} mode confinement and (d) CL- profile of the LP_{02} mode confinement.

Fig. 5-8 illustrates the variation in MD as a function of the change in the second ring radius X2 (high index layer). As can be seen, the best OPT value is when X2 is 3.0 µm. This is because the dispersions at this thickness are closer to the reference value (17 ps/[km. nm]).

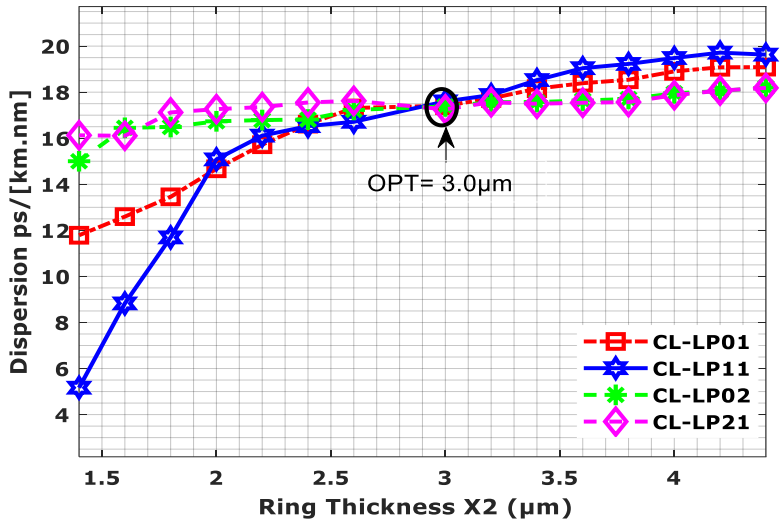


Fig. 5-8: Graph of change in thickness X2 against dispersion CL-ICF.

Fig. 5-9 depicts the effect of increasing the thickness X3 (third layer with low index) to MD. The requirement for choosing an OPT here is not only limited to the convergence in dispersions

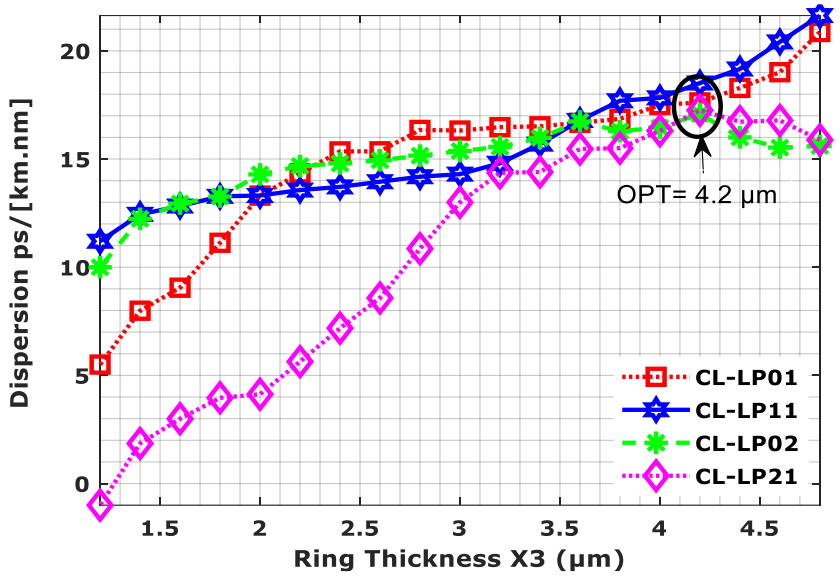


Fig. 5-9: Graph of the effect of varying thickness X3 on dispersion CL-ICF.

but also requires optimision to a thickness that can suite the A_{eff} simultaneously. Therefore, the best OPT that satisfies both conditions in this ring is when X3 is equal to 4.2 μm as shown in Fig. 5-9.

Fig. 5-10 illustrates variation of dispersion as a function of the thickness of the fourth layer (X4). At the outermost ring, the optimisation here should not decrease or increase the initial overall value of the core radius. Therefore, the OPT is chosen to be 1.6 μm. Thus, the overall core radius constituted by the sum of the individual ring thicknesses. Hence, on combining the optimised values X1, X2, X3, and X4 equal to 2 μm, 3 μm, 4.2 μm, and 1.6 μm respectively, the overall core radius is 10.8 μm (21.6 μm in diameter).

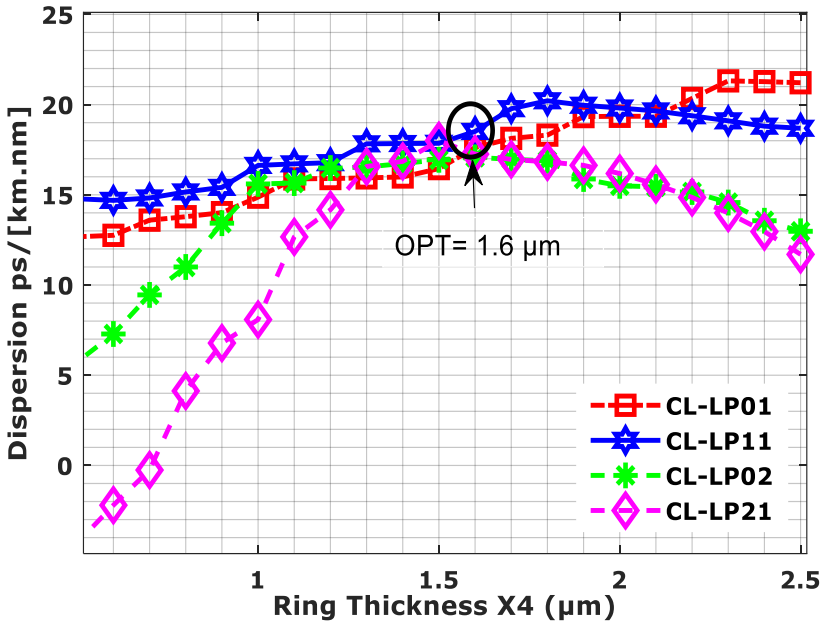


Fig. 5-10: Graph of measured dispersions against change in the thickness (X4) CL-ICF.

To justify the OPT calculated values, a plot of dispersions of the four modes at a various wavelength of both the CH and CL -ICF were plotted in Fig. 5-11 and Fig. 5-12 respectively. From these graphs, the dispersions of the four LP modes were converged at the operating wavelength (λ=1550 nm) of the two fibres. This demonstrates tolerance in dispersions of the two fibres at the specified wavelength. The inset values are the achieved dispersions of the four modes at the converging wavelength.

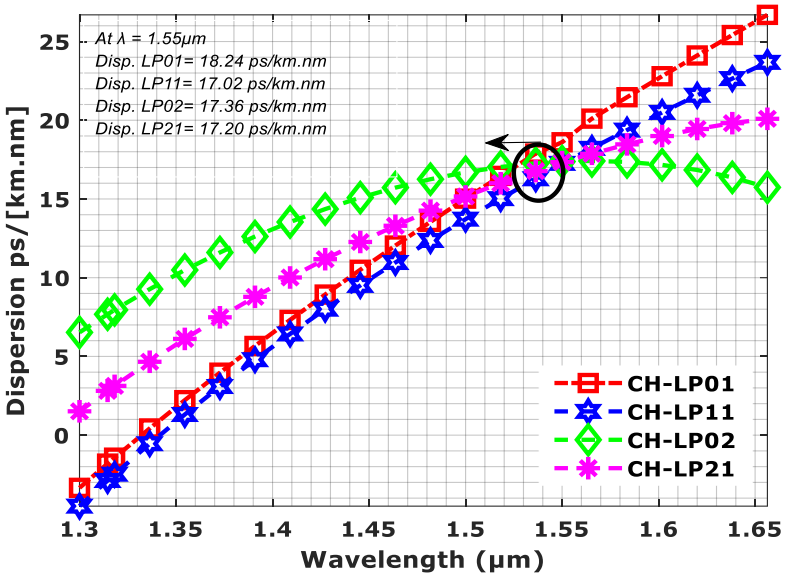


Fig. 5-11: Dispersion against change in wavelength of LP_{01}, LP_{11}, LP_{02}, and LP_{21} of the CH-ICF at λ=1.55 μm.

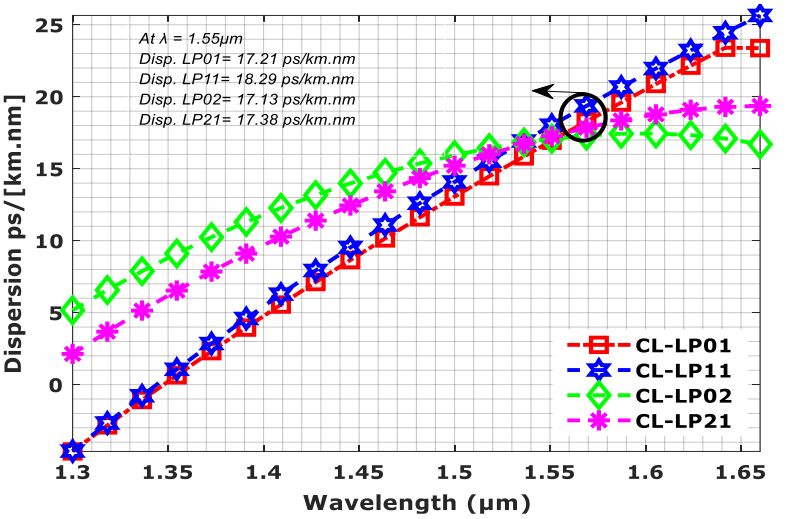


Fig. 5-12: Dispersions against change in the wavelength of LP_{01}, LP_{11}, LP_{02}, and LP_{21} of the CL-ICF at λ=1.55 μm.

5.3.4 CH-ICF and CL-ICF A_{eff} Optimisations

To optimise the A_{eff} of the CH-ICF, the central ring thickness is fixed to a value corresponding to the OPT of the dispersion equalisation. The thickness of the low index ring R2 varied to examine the effect on the A_{eff} of each mode in the fibre. It is observed that as the thickness of the low index ring increases the A_{eff} also increased. In addition, decreasing the index of this portion brings a benefit of increasing the A_{eff}, which moves away the dispersion from 1.55 µm. The cladding indices or its dimensions can be adjusted to restore the dispersion to 1.55 µm. The challenge here is that the extent of modifying the indices and the dimensions depends on other factors such as the size and index of the lower index region. Therefore, the radius or thickness of the lower region can be varied to 2.6 µm to optimise the A_{eff}.

Fig. 5-13 illustrates the relation of the thickness of the low index region (R2) of the CH-ICF and the A_{eff}. At the thickness of 2.6 µm, the values of the A_{eff} of the LP_{01}, LP_{11}, LP_{21}, and LP_{02} are found to be 72.03 µm^2, 81.72 µm^2, 89.23 µm^2, and 94.82 µm^2 respectively.

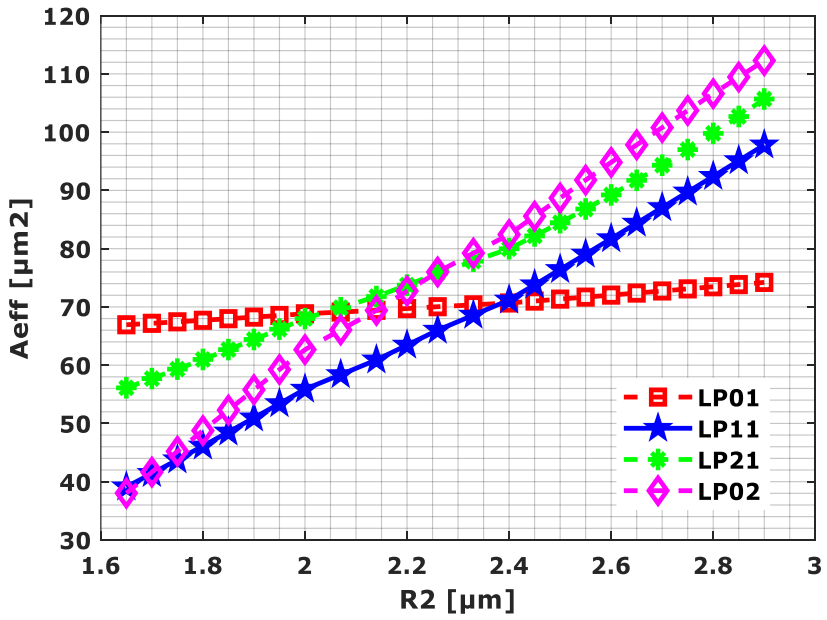


Fig. 5-13: Relation of the thickness of the low index region (R_2) of the CH-ICF and the A_{eff}.

These values are chosen at 2.6 µm thickness because it coincides with the thickness at which the dispersion is optimised (Fig. 5-4). Thus, shifting it away from this thickness (R2=2.6 µm) could move the dispersion equalised point away from the OPT.

Similarly, Fig 5-14 illustrates the relationship of the A_{eff} as a function of the thickness of the lower index region of the CL-ICF. Here, two low index regions exist in the core (Fig 5-1b), one at the core centre and another in the third ring (X3). The low index at the core centre (X1) was held fixed for the same reason stated in the CH-ICF. The lower index region of the third core layer X3 (Fig 5-1b) was adjusted to optimise the A_{eff}.

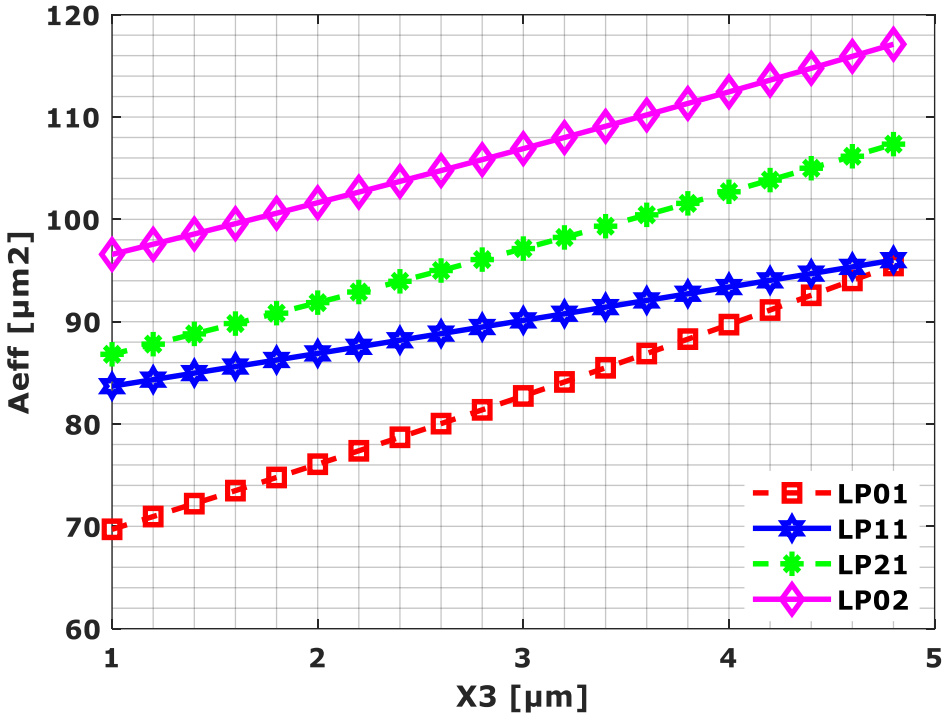


Fig. 5-14: Relationship of the A_{eff} as a function of the thickness (X3) of the lower index region of the CL-ICF.

The optimisation was achieved when the thickness X3 reach an OPT value of 4.2 µm. This thickness is chosen as it coincides with the thickness in the dispersion optimisation. Fig 5-15 and Fig. 5-16 depict the relation between A_{eff} as a function of the wavelength. As can be seen from these figures in both cases, the A_{eff} of CH-ICF and CL-ICF increases as the wavelength moves from 1.3 µm to 1.6 µm.

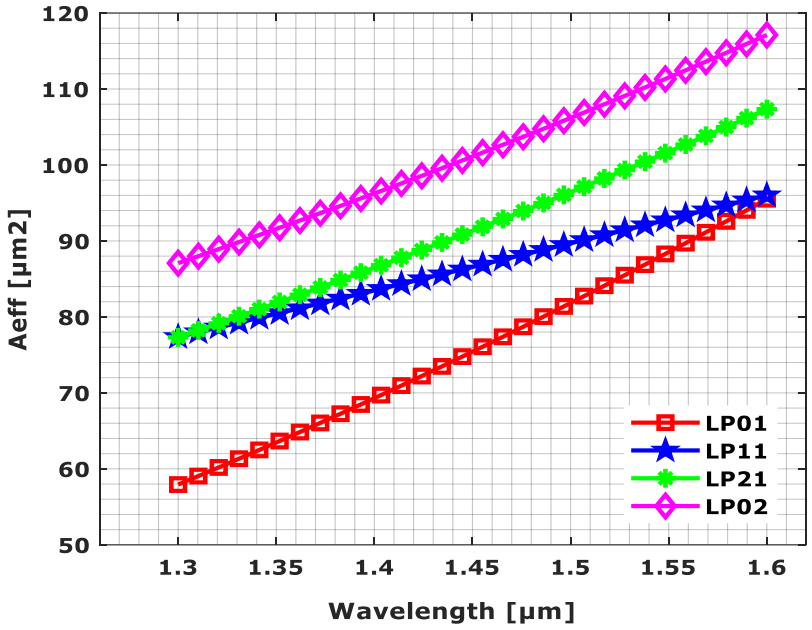


Fig. 5-15: Effective area of CH-ICF as a function of wavelength.

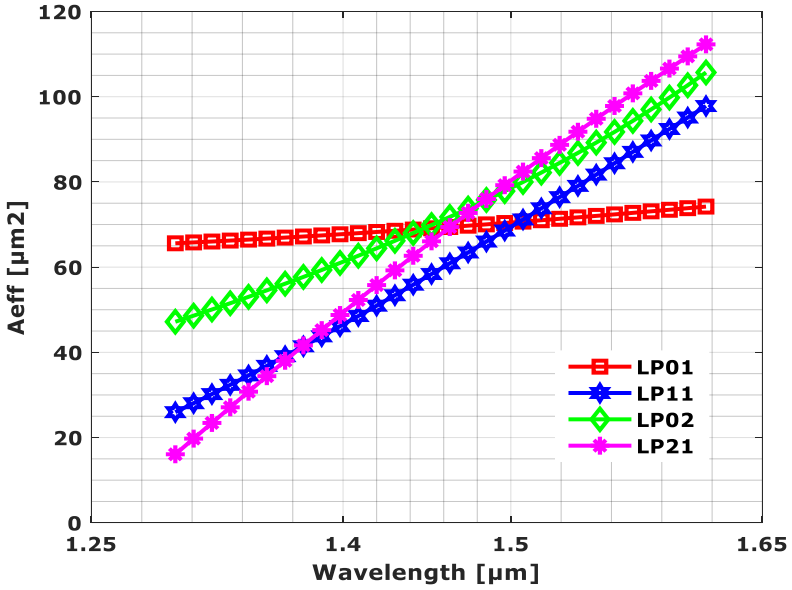


Fig. 5-16: Effective mode area of the CL-ICF as a function of wavelength.

Fig. 5-17 depicts relations between the core-cladding index contrast (Δx) and the A_{eff}. As the core-cladding index difference increases, the A_{eff} decreases exponentially. In addition, the parametric characteristics observed in relation to the cladding-low index ring difference illustrated in Fig. 5-18. The increase in index difference Δy of low-index rings increases the A_{eff}, which may be because of the increase in R2 or X3 in a CH-ICF and CL-ICF respectively. However, this can trigger the decrease of the core index; thus, bring in the decreases of the effective indices, which finally can attribute to a mode coupling. It is important to mention that care must be taken during fabrications to avoid varying the radius of the ring by more than ±1%. It can shift the equalisation value away from the operating wavelength (1550 nm) [201] [204].

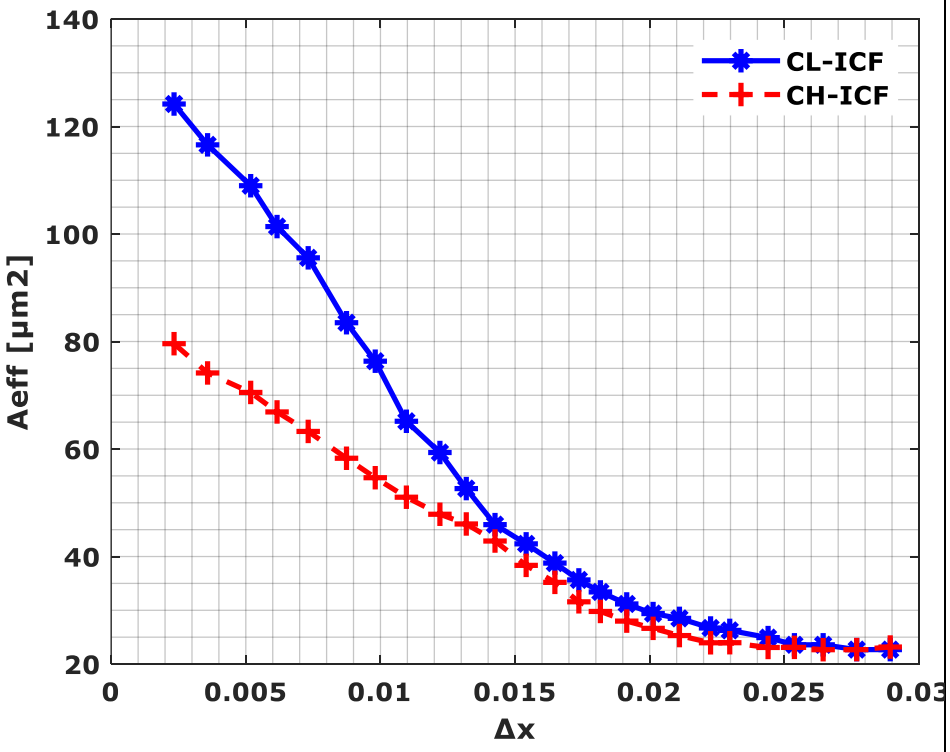


Fig. 5-17: Relation between the core-cladding index contrast (Δx) and $A_{eff.}$

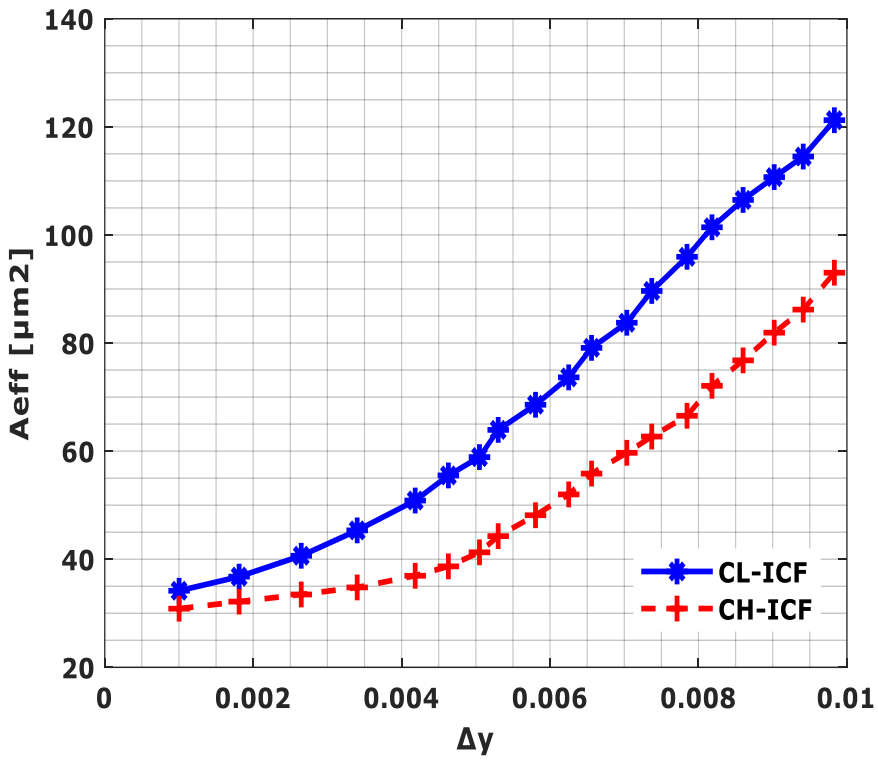


Fig. 5-18: Relation between the cladding-low index contrast (Δy).

Table 5-1 summarises the optical properties of the two fibres.

Table 5-1: Summary of the optical properties of the two fibres (CH-, CL- ICF at 1.55 μm). It includes A_{eff}, dispersion (Disp.) of the four LP modes, and the OPT.

FIBER TYPE	CH-/CL - ICF A_{eff} (μm^2)				CH-/CL – ICF Disp.ps/ (km. nm)				CH-/CL – ICF OPT (μm)			
	LP01	LP11	LP21	LP02	LP01	LP11	LP21	LP02	R1/X1	R2/X2	R3/X3	X4
CH-ICF	72.73	81.72	89.23	94.82	18.24	17.02	17.36	17.23	4.25	2.6	2.3	-
CL-ICF	88.29	92.73	102.56	111.33	17.21	18.29	17.13	17.38	2.0	3.0	4.2	1.6

5.4 Summary

An LP mode matrix method was numerically used to investigate the effect of core structural parameters variation with the modal dispersion of different modes. The dispersion equalisation of the modes was demonstrated, and their effective areas were optimised at the same values. A new and simple approach was proposed and presented, where the modal dispersions are equalised by varying the dimensional parameters of the core index profiles. The optimisation was achieved by varying the core layer thicknesses (core-ring radius) to a specified OPT value. These values would coincide with the one used in optimising the A_{eff} (for the case of R2 and X3 in the low index region of the two fibres). The thickness of the low index ring (R2) of the CH-ICF and that of the CL-ICF (X3) were varied to examine the effect on the A_{eff} of the fibres. It is observed that as the thickness of the low index ring increases (R2 and X3) the A_{eff} also increased. In addition, decreasing the index of this portion brings a benefit of increasing the A_{eff}, this moves away the dispersion from 1.55 μm regions. The relations between the cladding-low index contrast (Δy) and the A_{eff} was also investigated. As the cladding-low index difference increases, the A_{eff} decreases exponentially. It can be concluded that if more properties of the proposed structures can be investigated, the FMF can be a good potential medium for MDM systems, due to the high dispersion tolerance.

Chapter 6 High-Speed MDM Transmission

6.1 Introduction

This chapter investigate the transmission performance of a high-speed short distance MDM system. The communication network model was examined in two models. The first one presented in section 6-3 transmits two spatial signal mode channels (LP_{01} and LP_{11}) as signal carriers. In this proposed structure, an NRZ and RZ-OOK modulation formats were adopted in order to carry out the investigations. The two-mode channels were recovered by DD. This was achieved by a spatial receiver at the two aggregated bit rate of 20 Gb/s and 40 Gb/s optical link operating at 1550 nm. The performance of the system was successfully optimised to extend the transmission distance by varying the bias voltages of the DP-DD-MZ modulator. Thus, extending the transmission reach compared to that of the C-MZM by 8 km and 7 km, at the bit rate of 10 Gb/s and 20 Gb/s respectively. Each of the LP-mode carriers was examined in terms of the receiver sensitivity, OSNR, and the maximum transmission distance. It is important to mention that the DP-DD-MZ modulator operates based on the quantum confined stark effect and was employed to enhance the system reach at the two bit rates. The optimisation was realised by controlling the amplitude of each of the mode channel eye level. This requirement was achieved by employing a DP-DD-MZM, consisting of the dual ports-dual arms (DP-DA). Where its input side is having a Y-branch splitter, while at the output, a Y-branch combiner configuration is attached. Thus, both the attenuation as well as the optical pulse phase constants pass through the waveguide. Moreover, this depends on the bias voltage that is applied to each of the dual arms of the device. Hence, by varying the bias voltages the eye opening can be improved. It is suggested that this technique offers the optimal amplitude distribution that enhanced the eye-opening of both the LP_{01} and LP_{11} signal at the targeted BER of 10^{-9}.

Furthermore, in section 6-5, an MDM transmission supporting four non-degenerative spatial modes at 10Gb/s was examined. The analysis adopts the NRZ modulation format to evaluate the system performance in terms of the P_N and P_{TH} for each mode at the BER of 10^{-9}. The receiver sensitivity, the ONSR, and the maximum transmission distance were also investigated using the DD at 10Gb/s bit rate. By properly analyzing the MM-EDFA, the system performance can significantly be enhanced. This is because the Er-doped fibre can support multiple modes at the pump, ASE, or signal wavelength. An EDFA with the step index profile was considered to carry out the investigations. The fibre supports four spatial non-

degenerative modes with the EDFA core radius larger than the Erbium-doped core size.

6.1.1 Optical Transmission System

Due to the high cost and complexity in a short reach optical communication system such as metro and data centres (DCNs), system deployment has been inclined more toward the intensity modulation (IM) and DD [205]. Currently, optical transceivers of high bandwidth are available [206], including a spatial transceiver. Thus, a simple binary RZ/NRZ and possibly a partial response modulation technique can be used. The electric duobinary (EDB) can also be employed, which is promising for high-speed short reach system [207] [208]. Furthermore, advanced modulation formats that include 4-level PAM4 [209] and discrete multitoned (DMT) were reported. The two formats support a single lane high-speed transmission, which was achieved with a relaxing requirement on the system bandwidth. In addition, a short reach system, which requires a few kilometers is recently investigated. This was achieved when an advanced modulation transmission (employing a high data rate) with a single mode (about 1.5 μm) when VCSEL [210] was used. It has shown an interesting result to match the important requirement that comprises footprint, cost, and energy/power consumption. This indicates the potential for a smooth and continuous extension to a long-term mode multiplicity facilitated by the SDM approach.

6.2 System Theory

6.2.1 MDM System

Fig. 6-1 depicts the schematic of the basic principle and mode of operation of an MDM network using MMF. At the system input, a spatial laser source that is divided into N number of modulators was used as spatial transmitters. Each encodes a separate signal mode $k_i(x)$ on the optical carrier that modulates the optical signal $g_i(t)$. The field distribution is matched to a linearly polarised-mode in the S-Mux and transported via MMF that support N number of modes. At the system output (receiver end), the modes are separated using S-deMux and are detected using N corresponding photodiodes or R_x. The spatial mode data signals are finally recovered at the data recovery units.

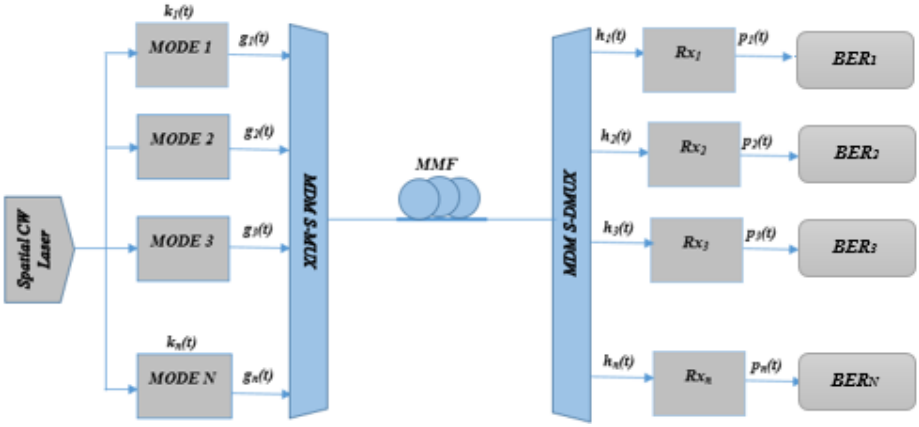


Fig. 6-1: Mode of operation of the MDM system. R_x: spatial receiver.

Moreover, an MDM system can be modelled in a form of spatial super-channels so that the spatial paths can originate and terminate at the same transponder. This technique was used in the MIMO wireless communication (long-term evolution or LTE) systems [24]. The spatial super channel provide means for further optoelectronic integration, which can improve system capacity beyond what can be achieved using parallel WDM channels. For a successful implementation of an MDM-WDM hybrid, operation of the MDM must be independent of wavelength [211]. This is explained by the fact that any attempt to allow multiple distinct wavelengths through spatial modulation over a single transmitting fibre can cause channels overlapping. In addition, this can create signal crosstalk among the transmitting modes. Moreover, if the MDM output does not depend on the wavelength of the input, one can guide the individual signal modes into the MMF. Thus, in an MDM-WDM hybrid structure [212], the signals can be separated using the conventional WDM de-multiplexing procedure or a using S-deMux. On the other hand, if MDM signals are wavelength dependent, the signal mode of the distinct wavelength may be difficult to route to the intended fibre for subsequent transportation over a given distance link.

6.2.2 Two-Mode Fibre

Fibre with the SI profile is adopted here because of its simplicity in the fabrication process. It consists of a core of high refractive index region (n_{pk}), sandwiched in a cladding layer having a lower refractive index (n_{clad}) and an infinite radius (*a)* for a given *M* number of LP-modes. The highest achievable value of V_p is chosen in order to allow for the first *M* number of LP modes to propagate and cutting-off the next undesired modes. By adopting this procedure, the *M* number of modes would have

the normalised propagation constant (B) given by $B = \left(n_{eff}^2 - n_{clad}^2\right)/\left(n_{pk}^2 - n_{clad}^2\right)$. Here, n_{eff} represents the effective index of the modes close to their highest achievable values. Thus, making it less vulnerable to bending effects [37]. Once the value of V_p is set, the core radius (a) is optimised to maintain its value. Thus, the difference in the core-cladding index (n_{pk}–n_{clad}), being subsequently determined from the V_p relation. Fig. 6-2 schematically illustrates a fibre cut of section along the *xy*-plane.

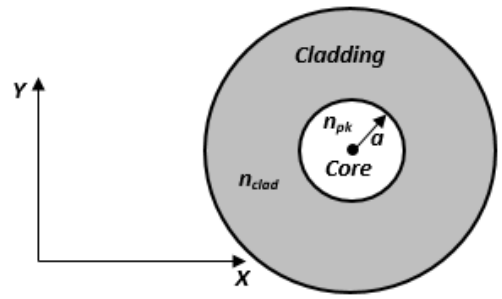


Fig. 6-2: Section cut of a step index MMF.

To model the two-mode fibre component using Optisystem software, a general purpose measured index multimode fibre (MI-MMF) was used because it allows the refractive index profile to be defined. The SI profile is constituted from the core refractive index peak, index cladding, core radius and cladding thickness values using the following relations.

$$n(r) = n_{pk}\left(1 - \Delta \cdot \left[\frac{r}{a}\right]^{\alpha}\right) \quad \text{For r<a} \qquad \text{Eq (6.1)}$$

$$n(r) = n_{pk} \cdot (1 - \Delta) = n_{clad} \quad \text{For r ≥a} \qquad \text{Eq (6.2)}$$

where a represents the core radius, n_{clad}, the refractive index of the cladding, α, the alpha profile. n_{pk} is the peak core refractive index, and Δ, the index contrast. Alternatively, the cladding index can be defined based on the parameters of Δ or numerical aperture (NA), in such case, the index of the cladding is calculated using the following relation

$$n(r) = n_{pk}\left(1 - \Delta \cdot \left[\frac{r}{a}\right]^{\alpha}\right) \quad \text{For r<a} \qquad \text{Eq (6.3)}$$

$$n_{clad} = \sqrt{\left|\left(n_{pk} - NA\right)^2\right|} \qquad \text{Eq (6.4)}$$

Note that the main results of the fibre computation target the following three parameters: spatial profiles, coupling coefficients and the time delay for each fibre modes. Therefore, the final solution for the output field, which is the combined

effects of the temporal and spatial characteristics of the fibre for an arbitrary number of modes, is calculated as

$$E_{out}(r, \emptyset, t) = \sum_{i=1}^{N} [C_i E_{in}(t - \tau_i)] E_i(r, \emptyset) \qquad \text{Eq (6.5)}$$

where E_{in} is the field that denotes the input signal, C_i represents the coupling coefficient among the fibre supporting modes and its spatial profile. E_i is the fibre field for each given index i. Thus, when the power of (C_i E_{in}) is below a certain value (*Min. signal power*), the signal i is discarded. Fig. 6-3 (a-e) depicts the simulated field distribution of an LP_{01}, LP_{11} mode signal channels.

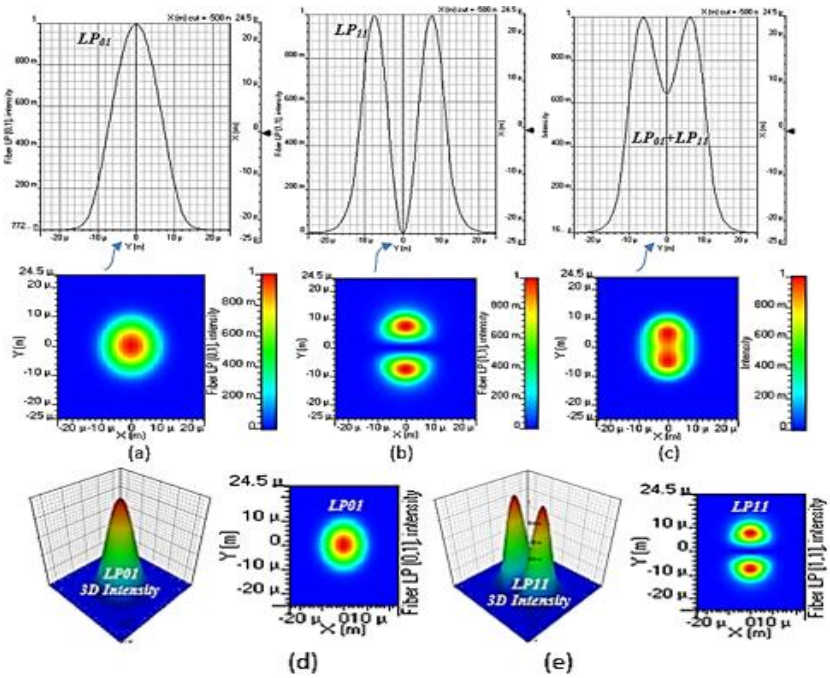


Fig. 6-3: Spatial mode profile distributions and 2D intensities of the fibre signal modes: (a) LP_{01}, before multiplexing (b), LP_{11} before multiplexing (c) LP_{01}+LP_{11} (after multiplexing) (d) LP_{01} 3D intensity and profile distribution after separation using spatial de-multiplexers and (e) LP_{11} 3D intensity and profile distribution after demultiplexing.

The fields calculations were made using a spatial visualiser component.

6.2.3 DP-DDMZ Modulator

As depicted in Fig. 6-4, the DP-DDMZ is made to consist of an input with the dual waveguide arms. It is constituted by a Y-branch configuration so that the input launched light E_{in} (t) is made to split and pass through the dual waveguide arms. These arms are constituted with a separately applied voltage V_i (t), driven the electrodes to provide $\Delta\beta i$ (phase difference) and then recombined at the output

end with the help of a Y-branch combiner, generating E_{out} *(t)* as a modulated optical signal.

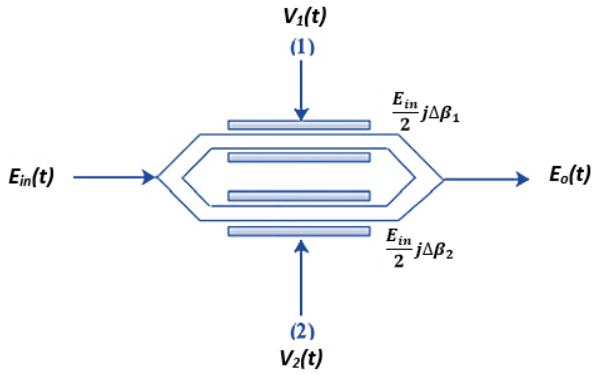


Fig. 6-4: DP-DD-Modulator layout.

The output signal of the modulator which is in the form of an electrical field can be determined by [213]:

$$E_o(V_1, V_2) = E_{in}(t) cos\left(L\frac{\Delta\beta_1 - \Delta\beta_2}{2}\right) exp\left(jL\frac{\Delta\beta_1 - \Delta\beta_2}{2}\right) \qquad \text{Eq (6.6)}$$

Here, the first term, *cos (L ((Δβ2 − Δβ1)/2))* represents the IM, and the other term, *exp (jL((Δβ2 −Δβ1)/2))* represents the phase modulation.

6.2.4 Signal Pulse of NRZ and RZ Modulation format

Pulses in modulation formats can be described in the form of NRZ and RZ. The extra optical modulator is needed for the RZ format to generate the 1 NRZ to RZ as illustrated in Fig. 6-6. The main function of the additional modulator is to interchange position with each other without affecting pulse generation. The extra modulator is considered as pulse carver. It is important to note that the bandwidth provided by the modulators regulates the rise and fall time of the edges of the pulse.

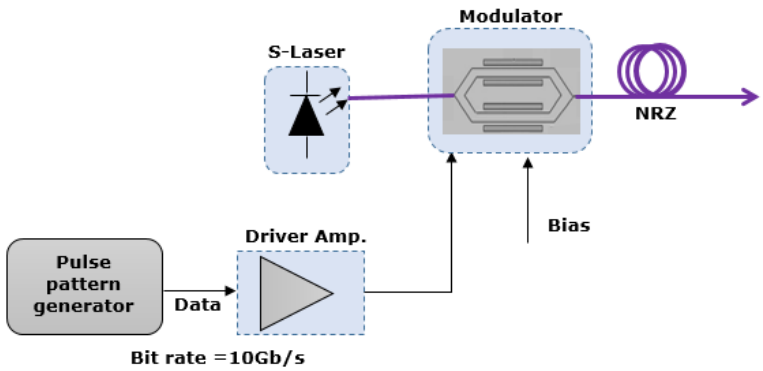


Fig. 6-5: Illustration of how optical signals of format NRZ are generated using an external modulator.

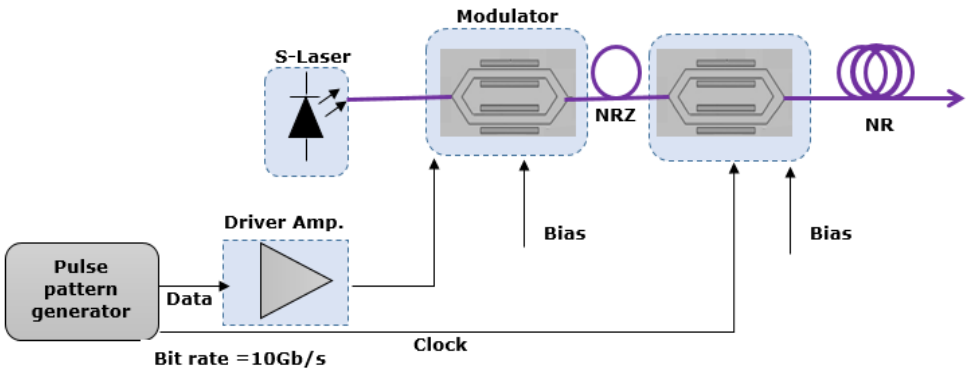


Fig. 6-6 Illustrations of how optical signals of format RZ are generated.

Once the laser source is switched on, its lightwave is modulated through electro-optic modulator by employing the concept of interferometric interference (constructive and destructive) to represent the ON/OFF states of the wave. The RZ is similarly generated by adding an optical modulator so as to generate periodic pulses of width half of that of the bit period. The phase and frequency of the modulated signals are generated through electro-optic modulation. It is achieved by biasing and controlling the signal amplitude of the pulses.

6.3 Two Channels MDM System Model

In order to design an efficient MDM system, it is important to employ an accurate simulation model for the multiple mode channels-based transmission. The model would not only be restricted to the accuracy of the individual components. Nevertheless, can allow combining them to examine and optimise their contributions to the overall system performance. In addition, it requires a simple

model based on MMF and OOK with a transmitter based on spatial CW Laser [214]. This can substantially reduce system cost. An Optisystem 15.20 commercial communication package was used in order to model and study the system performance. The analysis was conducted in two phases. Fig. 6-7 (a-b) illustrates the MDM setup for the two cases. In the first stage Fig. 6-7(a), the setup in the dashed rectangle consists of a spatial transmitter comprising a transverse mode profile in its optical output. It is a unit in the system build by employing a WDM transmitter optical and the MM-Generator. This allows adding a given transverse LP mode profile (LP_{01} and LP_{11}) in the optical signal by using spatial transmitter, which assign a given mode by specifying its azimuthal and radial number.

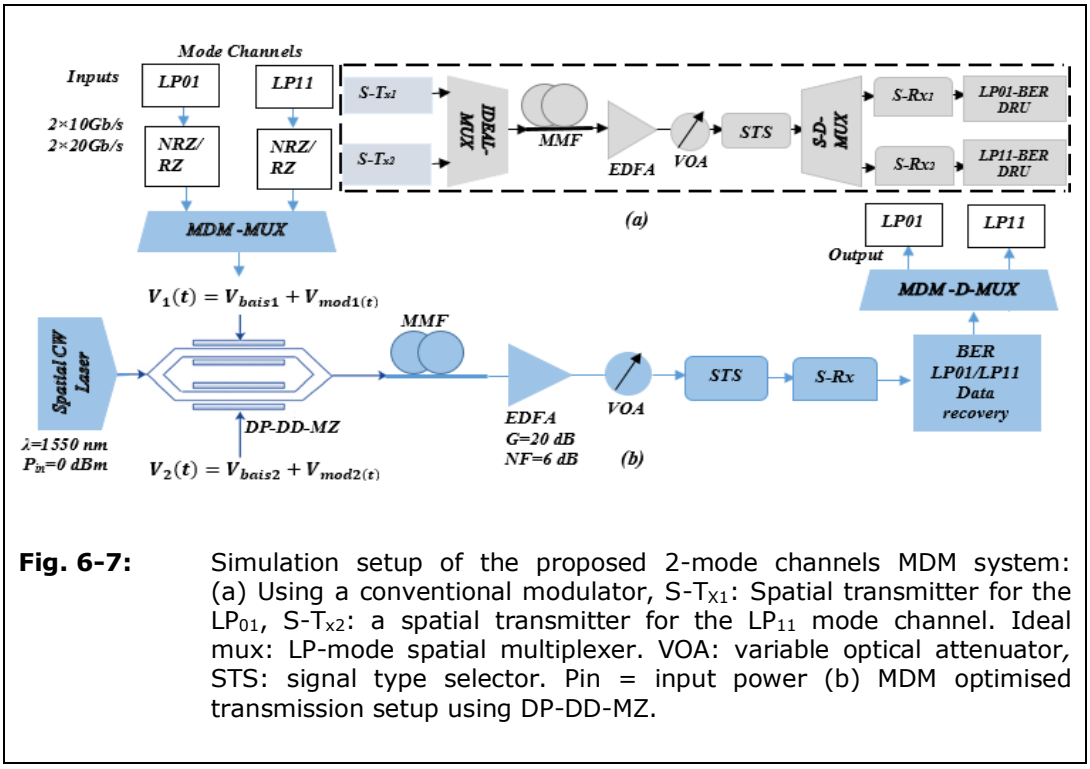


Fig. 6-7: Simulation setup of the proposed 2-mode channels MDM system: (a) Using a conventional modulator, S-T_{X1}: Spatial transmitter for the LP_{01}, S-T_{x2}: a spatial transmitter for the LP_{11} mode channel. Ideal mux: LP-mode spatial multiplexer. VOA: variable optical attenuator, STS: signal type selector. Pin = input power (b) MDM optimised transmission setup using DP-DD-MZ.

The MDM signals were modulated using NRZ and RZ-OOK data format and a spatial CW-Laser at 1550 nm. To avoid signal mode channel overlapping, the launch power is set to a low value of 0 dBm. Initially, the signal of 10 Gb/s and then 20Gb/s with the pseudo-random sequence are generated with the 10 dB ER, 0-chirp factor, and a linewidth of 10 MHz. The modulated signal of both LP_{01} and LP_{11} was combined using ideal multiplexer with the user-defined number of inputs WDM signal channels. Two input ports were chosen, each allocated to one of the two LP-mode channels. To confirm the presence of the two modes, a spatial visualiser was used to measure the LP-mode profile distribution. Fig. 6-3(a-e) depicted the profile at both input and the output of each of the spatial transmitter and receiver. The

entire modulated mode signals were fed into the MMF. The fibre was modeled using Eqn 6.1 through Eqn 6.3. To maintain the two mode operation, the V_p was determined using Eq (2.1) to be 3.0 [126]. With the core radius a=10.4 μm and the core, cladding refractive indices of 1.462 and 1.46, respectively. The reference frequency of the fibre was set at 1550 nm and attenuation of 1.4 dB/km. An EDFA with the fixed gain of 20 dB and *NF*=6 dB was used to boost the signal from the two modes. In order to separate the LP-modes, an S-deMux was employed. The multiplexer is user defined with the number of WDM spatial channels. We maintained the default value of 10 GHz for the 3 dB filter bandwidth. The maximum attenuation for the filter (depth) was set to 100 dB. Because of the presence of the two-mode channels, the Gaussian filter order was assigned to be 2 so that each signal mode will have a dedicated port. Also, the default value of 193.1 THz for the filter centre frequency was maintained throughout. And the additional loss (ripple) of the filter for both the two channels were set to 0 dB, after which the spatial mode associated with each channel is separated. The level of crosstalk associated with both multiplexer and demultiplexer components was determined by three factors: bandwidth, ripple, and depth of the filter. Here, the filter depth was considered the most crucial parameter, as it is the determining factor in accessing the power level associated with the neighboring channels. A PIN photodetector with a Bessel filter and 3R regenerator constituted the spatial optical receiver component. The circular aperture having a width diameter of 10.4μm with a gain of 3 dB was adopted and a photodetector responsivity of 1 A/W. For the low-pass filter, the 3-dB cutoff frequency of 0.7*Bit rate for the NRZ which optimised to 2×times for the RZ format was adopted. The IL was fixed at zero and the 100 dB maximum attenuation value of the filter was retained. The receiver was centred at the maximum power; all the noise sources are included in the calculations: amplified spontaneous emission (ASE) noise, short noise as well as the thermal noise). For the 3R generator, the two-reference bit rates (10 Gb/s and 20 Gb/s) were used. This is for the decision instant evaluation and 0.5 bit for the bit sequence recovery.

Similarly, in the second stage (Fig 6-7b), which was the optimised version of Fig. 6-7 (a), the setup was modeled by replacing the C-MZM in the spatial transmitter with DP-DD-MZ. This component allows for adjusting the applied bias voltages so that the amplitude of the eye level of the two signal modes can be varied. The MDM signals are employed to modulate th SCW-Laser at 1550 nm and the data from the 2-mode channels for the total aggregated bit rate of 20 Gb/s and 40 Gb/s were treated separately. In order to achieve the maximum ER, the splitting ratio was set to 1 and modulating voltage (V_{mod}) at 1.2 V. The optical MDM

signal is boosted with an EDFA and the *NF* was fixed at the same value with the previous setup. It is also useful to mention that the signal type selector (STS) component was used in the two setups to filter signal types from the input. These signal types will then reach the individual spatial receivers (S-R_X) dedicated to the two modes.

6.4 Results and Discussions

6.4.1 NRZ and RZ MDM performance at 10 Gb/s

The system performance using NRZ and RZ modulation formats with the C-MZM was first examined. Fig. 6-8 depicts the bit-error-rate (BER) of the LP_{01} and LP_{11} signal channels for the back-to-back (B2B) and at different distance link configurations. For the B2B link, the LP_{01} and LP_{11} receiver sensitivity of NRZ at BER of 10^{-9} is about -15.5 dBm and -11 dBm, respectively. This introduces a power penalty of about 4.5 dB between the two-mode channels. Similarly, for the RZ B2B configuration, the LP_{01} and LP_{11} receiver sensitivity at BER of 10^{-9} is -16 dBm and -11.5 dBm respectively.

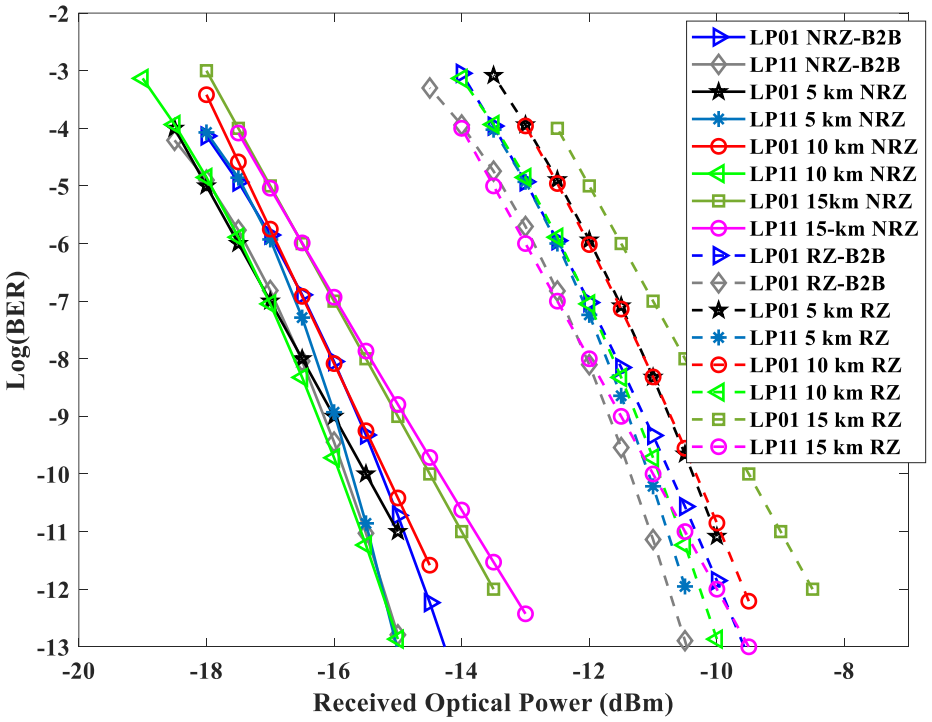


Fig. 6-8: NRZ and RZ performance for various distance link at 10Gb/s

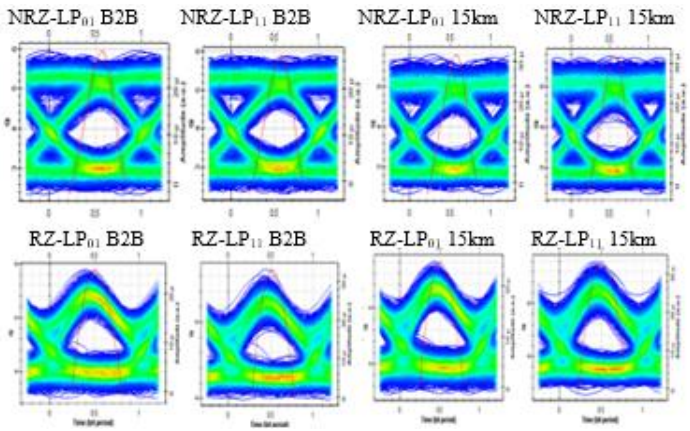


Fig. 6-9: Eye diagrams for NRZ-LP_{01} B2B, LP_{11}-B2B, LP_{01}-15 km, and LP_{11} -15 km. Similarly, for the RZ format LP_{01}-B2B, LP_{11}-B2B, LP_{01} -15 km and LP_{11} -15 km at BER of 10^{-9}.

results to the power penalty of 4.5 dB. For the NRZ at various distance links, a penalty between the LP_{01} and LP_{11} of about 4.74 dB over a 5 km, 5 dB over a 10 km, and 5.2 dB over a 15 km distance links were respectively observed. Similar comparisons for the RZ format for the distance link over 5 km, 10 km, and 15 km leads to a penalty of 4.5 dB, 5 dB, and 5 dB between the two modes respectively, indicating a similar performance at both 10 km and 15 km. In this case, both the NRZ and RZ demonstrates similar performance at the 15 km distance link. The power sensitivity difference between the LP_{01} and LP_{11} modes is because of the difference in gain between the individual mode channels. Fig. 6-9 illustrates the calculated eye diagrams for both the NRZ and RZ LP_{01} B2B, LP_{11} B2B, LP_{01} 15 km and LP_{11} 15 km.

The B2B, 5 km, 10 km, and 15 km BER results at 10Gb/s of the two-mode channels as a function of the optical signal-to-noise ratio were shown in Fig. 6-10. Using the NRZ format, the B2B OSNR at the BER of 10^{-9} was calculated to be 29 dB and 30 dB for the LP_{01} and LP_{11} channels, respectively. Similarly, for the 5 km, 10 km, and 15 km distance links, the OSNR at BER of 10^{-9} was also evaluated. For the 5 km distance link at the same BER, an OSNR of 28 dB and 29.5 dB for the LP_{01} and LP_{11} was achieved. This results in a power penalty of 1.5 dB, which is 0.5 dB higher than that of the B2B (no fibre). Table 6-1 summarises the OSNR and power penalty between the LP_{01} and LP_{11} at 10 Gb/s and 20 Gb/s bit rate.

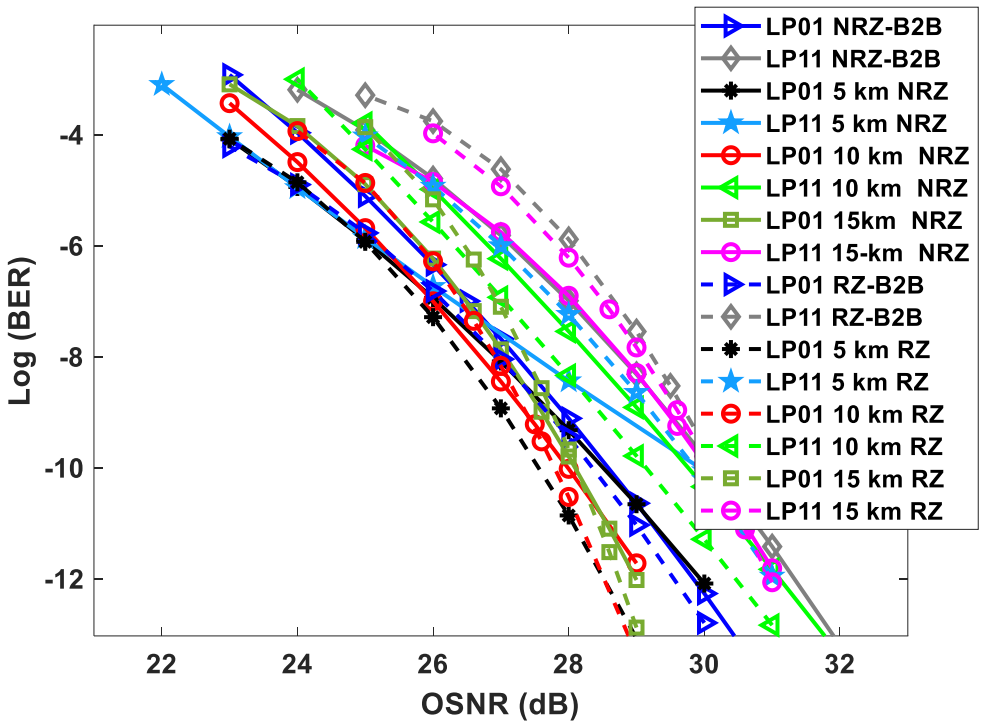


Fig. 6-10: BER as a function of the OSNR at 10 Gb/s; the results of the B2B, 5 km, 10 km, and 15 km for both the NRZ and RZ modulation formats are plotted.

Table 6-1: Summary of the LP_{01} / LP_{11} signal to noise ratio and the receive power penalty at a bit rate of 10 Gb/s and 20 Gb/s. in each case, the penalty is determined by evaluating the difference in power between the two modes.

Bit Rate (Gb/s)	Distance (km)	LP_{01} / LP_{11} NRZ-OSNR (dB)	LP_{01} /LP_{11} RZ-OSNR (dB)	LP_{01} /LP_{11} NRZ-Penalty (dB)	LP_{01} /LP_{11} RZ-Penalty (dB)
10	0	1	0	4.5	4.50
	5	1.5	2	4.75	4.50
	10	2.6	2	5.00	5.00
	15	3	2.5	52	5.00
20	0	-	-	0.5	2.5
	5	-	-	0.5	2
	10	-	-	1	2.5
	15	-	-	1.1	2.6

On carrying similar evaluation for the 10 km and 15 km distance link, a penalty of 2.6 dB and 3 dB were observed, respectively between the LP_{01} and LP_{11} channels. A similar effect was also observed while adopting the RZ format. In this case, the power penalty between the LP_{01} and LP_{11} for the B2B, 5 km, 10 km, and 15 km, was calculated to be 0 dB, 2 dB, 2 dB, and 2.5 dB, respectively. The penalty between the two-mode channels may be attributed to a low pass filtering.

Another parameter that was investigated is the effect of misalignment between the Tx and a spatial Rx for the two channels at B2B and over 15 km. This was determined using the spatial connector component to calculate the Q-factor variation with change in the X-shift parameter. The applied longitudinal shift (X-shift) rotates and translates the optical field that propagates the signal. The transmitter misalignment (Tx-misalignment) illustrated in Fig. 6-11 shows a decrease in the Q-factor of the two mode channels at B2B and over the 15 km distance link. This is due to shifting the field outside the active area of the photodetector.

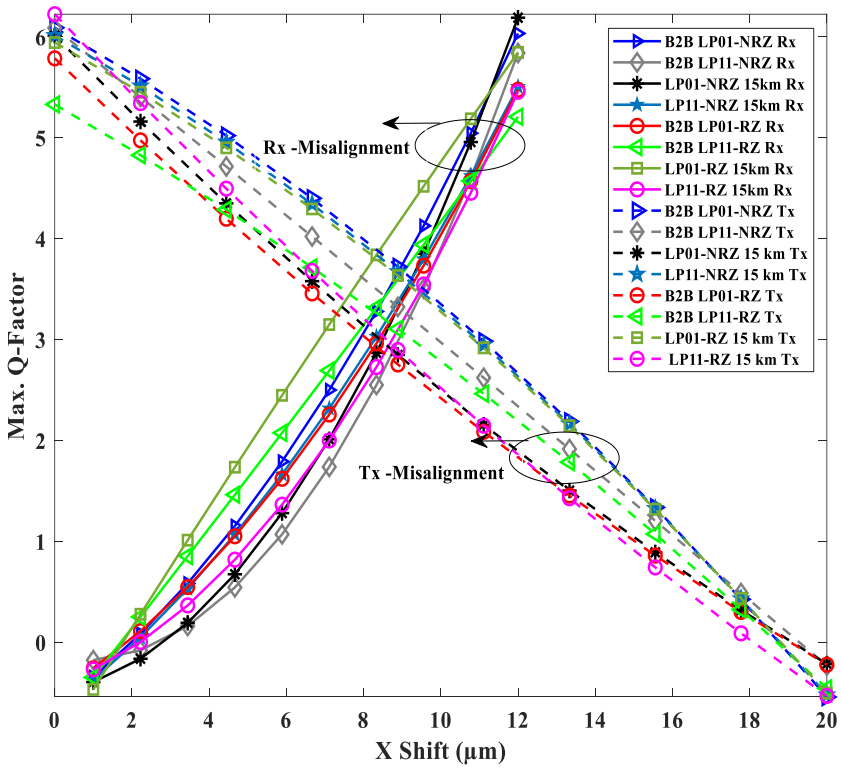


Fig. 6-11: Effects of misalignment between the transmitter and receiver, which was observed on plotting the value of maximum Q-Factor (Max. Q-Factor) against photodetector active area width (X shift) at B2B and 15 km for both LP_{01} and LP_{11} using the NRZ and RZ at 10Gb/*s.*

Similar results can be calculated by varying the width of the active area in addition to shifting of the field. Therefore, by varying the X-shift, the misalignment at the receiver (Rx-misalignment) demonstrates an increase in the Q-Factor with the increase in the active area of the photodetector. This effect was observed at B2B and over the 15 km distance link for both the two signal mode channels.

6.4.2 NRZ and RZ MDM performance at 20 Gb/s

Fig. 6-12 illustrates the distance link performance plots of NRZ and RZ at 20 Gb/s. The BER of the LP_{01} and LP_{11} signal channels for the B2B scenario and at different distance link configurations were determined. For the B2B link, the receiver sensitivity of LP_{01} and LP_{11} of the NRZ at 10^{-9} was about -27.5 dBm and -27 dBm, respectively.

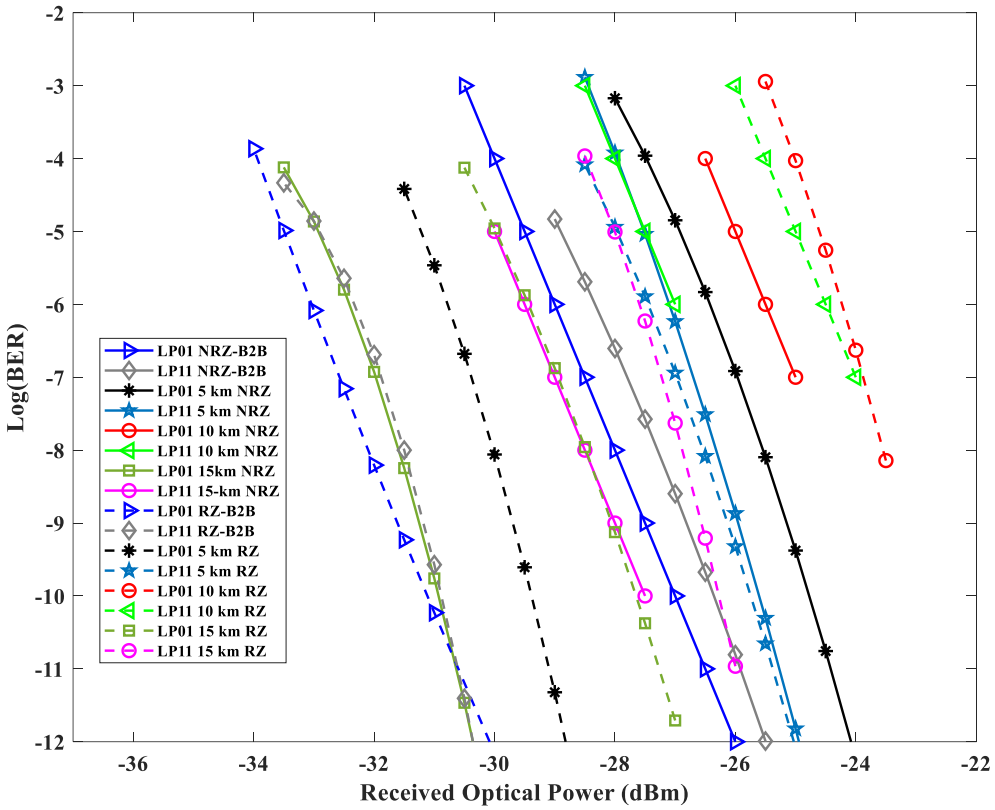


Fig. 6-12: NRZ and RZ performance for various distance links at 20 Gb/s for the 2-mode channels.

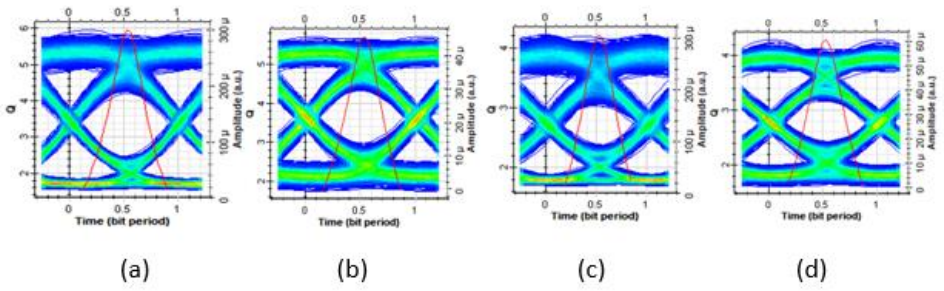


Fig. 6-13: Eye diagrams of the NRZ modulation format (a) B2B LP_{01} (b) B2B LP_{11} (c) 15 km LP_{01}. (d) 15 km LP_{11}. With the Q-Factor of 5.82, 5.72 for the LP_{01}, LP_{11}, B2B and 4.65, 4.58 for the LP_{01}, LP_{11} at 15 km were achieved at BER of 10^{-9} and 10^{-6} at 20 Gb/s bit rates, respectively.

This leads to a power penalty of about 0.5 dB between the two-mode channels. Similarly, for the RZ B2B scenario, the LP_{01} and LP_{11} receiver sensitivity at BER of 10^{-9} is -31 dBm and -28.5 dBm respectively, introducing a power penalty of 2.5 dB. At the distance link over the 5 km, a penalty of 0.5 dB was also noted between the LP_{01} and LP_{11} for the NRZ format. On extending the link distance to 10 km, the penalty is 1 dB at BER of 10^{-8} for the LP_{01} and LP_{11}, respectively. At the distance link of 15 km, a penalty of 1.1 dB was observed at BER of 10^{-6}. It is significant to mention that these BER values were the closest achieved values of the targeted BER of 10^{-9}. In addition, by carrying a similar analysis for the RZ format at 5 km, 10 km, and 15 km distance links. A power penalty of 2 dB, 2.5 dB, and 2.6 dB were respectively, calculated between the two-mode channels. Comparing the power penalties at 10 Gb/s and 20 Gb/s of both NRZ and RZ modulation formats, the performance at 20 Gb/s demonstrates less penalty. This is at the expenses of shorter distance link and a BER that is greater than 10^{-9} for the two-mode channels as depicted in Fig. 6-13. For example, at 10 km and 15 km, BER of 10^{-8} and 10^{-6} were achieved, respectively. In order to enhance the eye-opening at 10 km, 15 km, and beyond, an optimisation of the eye level is required.

6.4.3 MDM Optimisation Using DP-DDMZ at 10 Gb/s

For the transmission at 10 Gb/s over a 20 km distance, the highest achieved *Q*-Factor using the NRZ format with the C-MZM for the LP_{01} and LP_{11} channels were 4.63 and 4.57, respectively. This provides a BER of 10^{-6} for the NRZ as depicted in Fig. 6-14 (a to b). In the case of RZ, Fig. 6-14 (c to d), the highest achievable *Q*-Factor was around 2.55 for the LP_{01} and almost completely closed for the LP_{11} channel. This may be attributed to the nonlinear transfer function of the C-MZM,

and the MD effect in the system. To enhance the performance of the system, the eye-opening was improved by replacing C-MZM with the DP-DDMZ. The value of the targeted *Q* was enhenced, achieving a value close to *Q*=6 at BER of 10^{-9} over a given distance link. This was achieved by varying or increasing the eye-opening level over a distance link of interest.

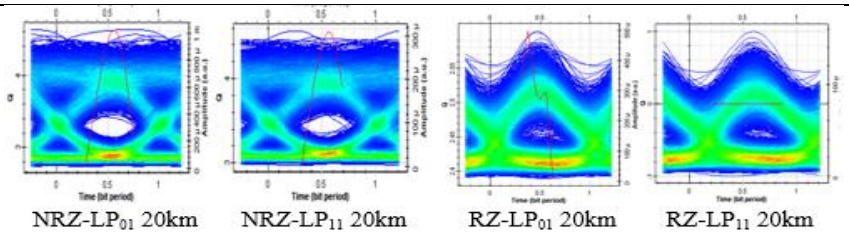


Fig. 6-14: Eye opening of (a) LP_{01} NRZ and (b) LP_{11} NRZ (c) LP_{01} RZ (d) LP_{11} RZ over 15 km at 10 Gb/s.

Details about the working principle of the DP-DDMZ was described in section 6.2.3. It is employed here to increase the eye height in each of the LP mode channels eye diagram shown in Fig. 6-13 and Fig. 6-14. To achieve this, the dual arm bias voltages *Vb1* and *Vb2* in the DP-DDMZ are adjusted to optimise the eye height. The optimisation was achieved in two ways; either by keeping *Vb1* fixed while varying *Vb2* or the other way. Fig. 6-15 depicts the *Q-factor* of the two LP mode channels eyes at the distance link of 23 km. The optimisation was achieved by varying the value of *Vb1* at the fixed received power of −13.75 dBm and keeping the bias voltage in the second arm (*Vb2*) fixed to −2 V.

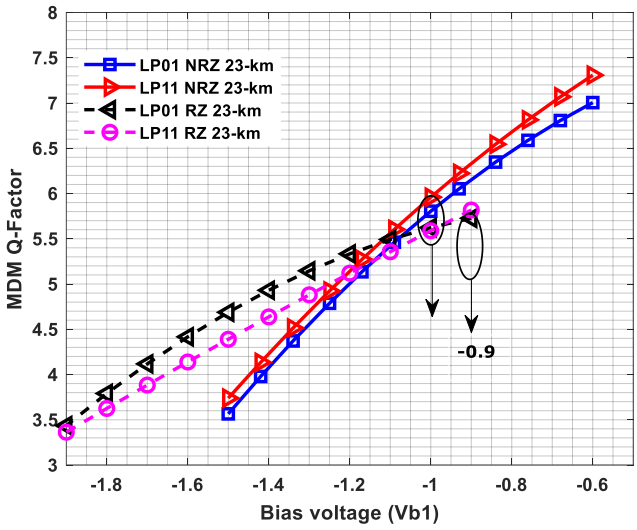


Fig. 6-15: MDM-Q factors over a 23 km distance link at the fixed receiver power of −13.75 dBm as a function of the Bias voltage Vb1.

It can be observed that the optimised value of *Vb1* is around −1.0 V for LP_{01} and LP_{11} adopting NRZ format. Similarly, for the RZ when *Vb2* fixed to -2V, an optimised *Vb1* of -0.9V is achieved as shown in Fig. 6-15. Fig. 6-16 illustrates the variation of the Q-factor when *Vb1* fixed to -1V (circular region) at a fixed received power of -13.75 dBm. By adjusting the bias voltage *Vb2* as illustrated in Fig. 6-16, an optimised value of -2 V for the closest value of *Q-factor* of both the LP_{01} and LP_{11} was achieved using NRZ. For the RZ format, the optimised value of *Vb2* equal to -2.9 V was found when *Vb1* was fixed at -1.1 V.

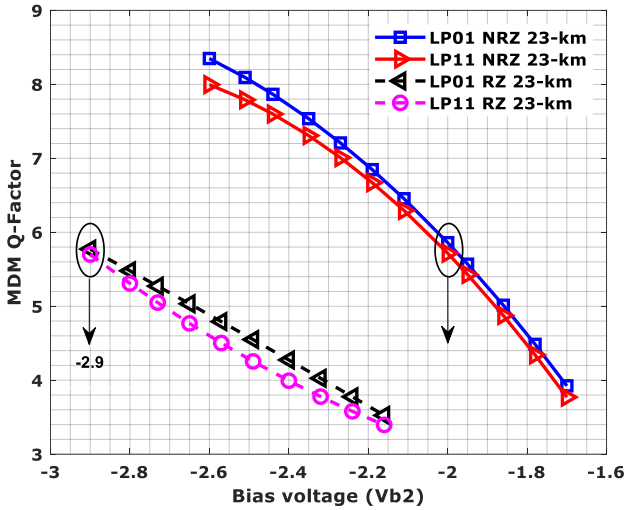


Fig. 6-16: Variation of MDM-Q factor bias voltage (Vb2) over a 23 km distance link at a bit rate of 10 Gb/s.

6.4.4 Optimision Using DP-DDMZ at 20 Gb/s

The MDM system performance at the bit rate of 20 Gb/s cannot reach even 15 km at the BER of 10^{-9}. This can be justified from Fig. 6-13. The eye closure narrows down as the transmission distance was extended, even at 10 km, the BER cannot go below 10^{-8}. To address this issue, the same optimisation techniques as in the 10 Gb/s bit rate (section 6.4.3) was employed. The overall transmission distance here was extended to cover 22 km compared to that of the C-MZM (10 km at BER 10^{-9}).

Fig. 6-17 and 6-18 show the highest achieved system performance at 20 Gb/s in terms of the transmission distance. The optimised bias voltages (*Vb1* and *Vb2*) that can give a closer *Q-factor* value of 6 over a 22 km distance link were determined. In Fig. 6-17, at -0.7V fixed bias voltage *Vb2,* the NRZ optimised *Vb1*

at the fixed receiver power of -29.75 dBm is -1.7 V and -2.59 V for the RZ format at -2V fixed value of *Vb2.* Similar results were obtained in Fig. 6-18 when the bias voltage *Vb1* was fixed at -2.6 V. The optimised *Vb2* for the NRZ and RZ formats are -2.4 V and -2 V, respectively. This value for the RZ format was when the *Vb1* was fixed at -2.68 V.

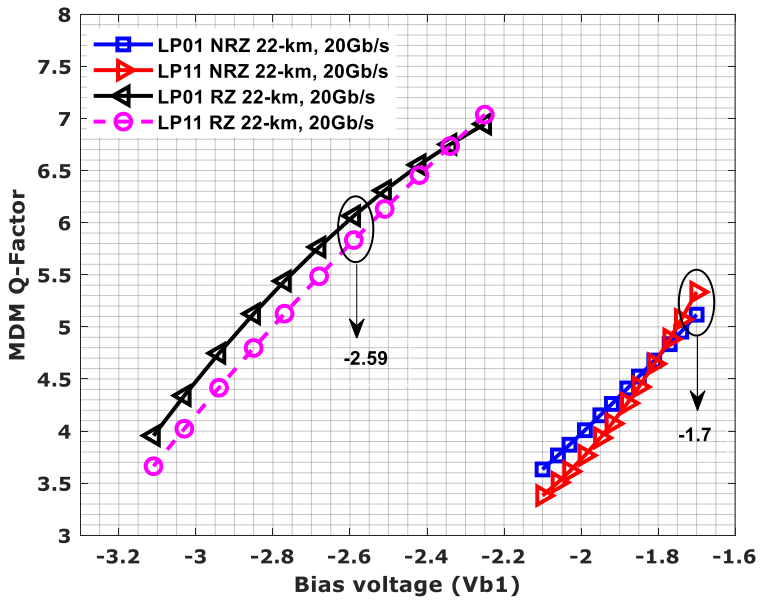


Fig. 6-17: MDM-Q factors over 22 km distance link at a fixed power of −29.75 dBm as a function of Bias voltage Vb1

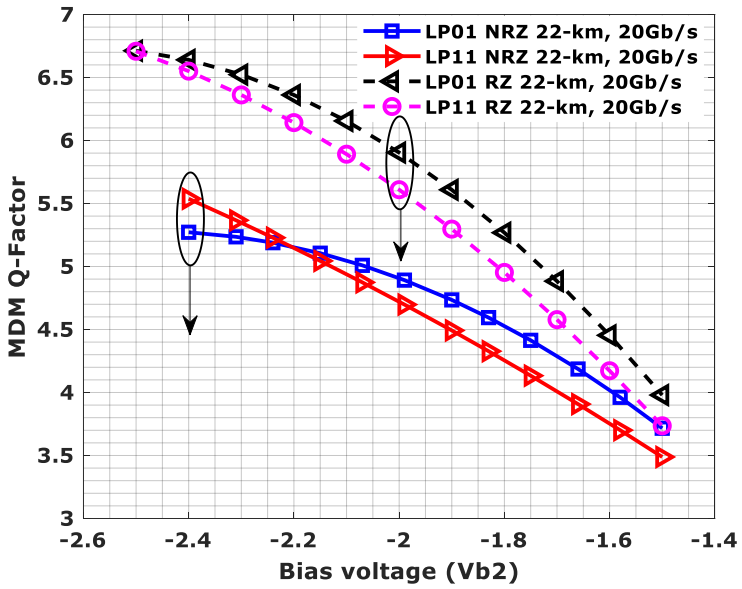


Fig. 6-18: Variations of MDM-Q factor as a function of Bias voltage Vb2 at 20 Gb/s bit rate.

Fig. 6-19 illustrates the eye diagram at different distance links after optimisation using the DP-DD-MZ modulator, which was evaluated at the BER of 10^{-9} (telecommunication limit). The improved eye diagrams were obtained by optimising the bias voltages (*V1* and *V2*) of the modulator at 10 Gb/s over 23 km as illustrated in Fig. 6-15 and Fig 6-16. When compared with Fig. 6-14, an increment of 8 km is achieved. Similarly, Fig. 6-20 shows the optimised eye diagrams at 20 Gb/s over a distance of 20 km and 22 km. When the C-MZM was replaced with DP-DD-MZ modulator as shown in Fig. 6-17 and Fig. 6-18, the transmission distance was extended by 7 km. It is worth mentioning that at the same bit rate (10 Gb/s) when the C-MZM was used, the BER achieved over a 15 km distance link was 10^{-6}. Table 6-2 provides summary of the optimised parameters at different distance link. It can be observed that most of the BER have reached the required value of 10^{-9}, except for the distance link over 22 km at 20 Gb/s, in which the BER of LP_{01} and LP_{11} is 10^{-8}.

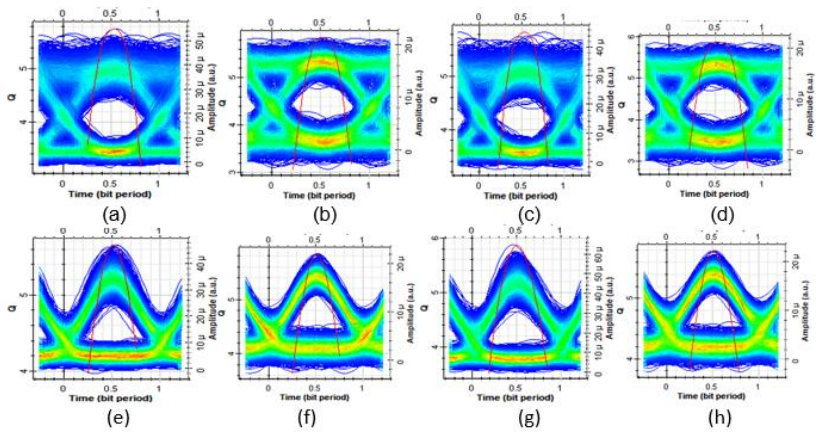


Fig. 6-19: Optimised eye diagram at 10 Gb/s using NRZ and RZ modulation format over 20 km and 23 km distance links: (a) LP_{01}-NRZ over 20 km (b) LP_{11}-NRZ over 20 km (c) LP_{01}-NRZ over 23 km (d) LP_{11}-NRZ over 23 km (e) LP_{01}-RZ over 20 km (f) LP_{11}-RZ over 20 km (g) LP_{01}-RZ over 23 km and (h) LP_{11}-RZ over 23 km.

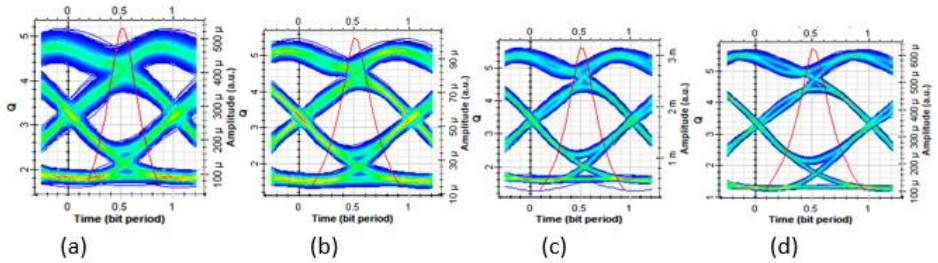


Fig. 6-20: Optimised eye diagram at 20 Gb/s using NRZ modulation format over 20 km and 22 km distance links: (a) LP01-NRZ-20 km (b) LP11-NRZ-20 km (c) LP01-NRZ- 22 km and (d) LP11-NRZ- 22 km.

Table 6-2: Performance optimisations at 10 Gb/s and 20 Gb/s bit rates, which includes all the optimised bias voltages (Vb1, Vb2), and their corresponding BER and Q-factors. The distance links were extended to 20 km, 22 km, and 23 km. Note that at 20 Gb/s bit rate, the distance can only be extended to 22 km.

Distance Link (km)	Optimised Values	Performance Optimisation at 10 Gb/s				Performance Optimisation at 20 Gb/s			
	LP-modes/ Modulation	LP_{01}-NRZ	LP_{01}-NRZ	LP_{01}-RZ	LP_{11}-RZ	LP_{01}-NRZ	LP_{11}-NRZ	LP_{01}-RZ	LP_{11}-RZ
20	Vb1 (V)	-0.75	-0.75	-0.92	-0.92	-1.2	-1.2	-1.2	-1.2
	Vb2 (V)	-1.06	-1.06	-1.61	-1.61	-1.95	-1.95	-2.14	-2.14
	BERb1,2	10^{-9}	10^{-9}	10^{-9}	10^{-9}	10^{-9}	10^{-9}	10^{-9}	10^{-9}
	Qb1	5.9	5.72	5.6	5.6	5.87	5.68	5.7	5.62
	Qb2	5.9	5.81	5.9	5.82	5.91	5.83	5.89	5.83
	Vb1(V)	-	-	-	-	-1.7	-1.7	-2.59	-2.59
	Vb2(V)	-	-	-	-	-2.4	-2.4	-2	-2
22	BERb1,2	-	-	-	-	10^{-8}	10^{-8}	10^{-9}	10^{-9}
	Qb1	-	-	-	-	5.1	5.3	6	5.8
	Qb2	-	-	-	-	5.3	5.5	5.9	5.6
	Vb1(V)	-1	-1	-0.9	-0.9	-	-	-	-
23	Vb2(V)	-2	-2	-2.9	-2.9	-	-	-	-
	BER b1,2)	10^{-9}	10^{-9}	10^{-9}	10^{-9}	-	-	-	-
	Qb1	5.81	5.9						

6.5 Four Channels MDM System Model

In this section, the transmission system supporting four non-degenerative spatial modes at 10 Gb/s was analysed. The analysis adopts only the NRZ modulation format to evaluate the system performance in terms of the P_N and the P_{TH} at a BER of 10^{-9}. The receiver sensitivity, the OSNR, and the maximum transmission distance were investigated using the DD. By properly analysing the MM-EDFA, the system performance can be enhanced. Fig. 6-21 depicts the system setup; all the components retain their usual meaning as defined in section 6.3, except that here an MM-EDFA is introduced because of the increase in the number of mode channels. Moreover, the fibre length in this case is 40 km.

We adopt similar MSI-MMF used in section 6.2.2 with a core radius of 16.44 μm, a numerical aperture of 0.24 and index contrast (Δ=0.013). This results in a fibre with the V of 5.3 at 1550 nm and supports four spatial nondegenerate modes (LP_{01}, LP_{11}, LP_{21}, and LP_{02}). Furthermore, the simulation was carried out based on the assumption that each of the LP-mode carries a single wavelength. A single pump power of 400 mW (26 dBm) was injected for the four mode channels. The short distance MDM transmission was modelled at a 5 km interval in order to determine the maximum distance. System performance at each interval was evaluated.

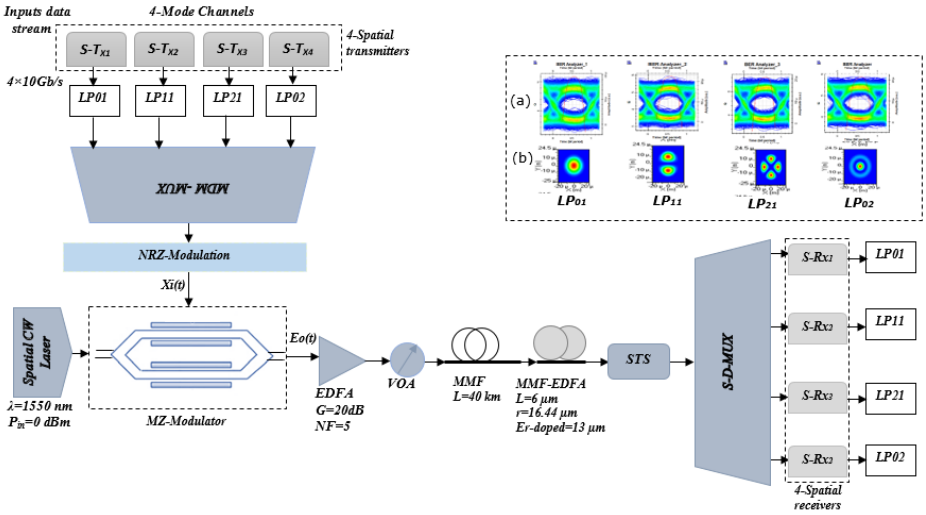


Fig. 6-21: 4-Mode channel MDM transmission system setup (a) LP modes eye diagram at BER of 10^{-9}. (b) output field distribution of the four modes.

6.5.1 MDM Transmission using MM-EDFA

The performance of a four mode channels system using an MM-EDFA was examined. This is because the Er-doped fibre can support more than one mode at the pump, ASE, or signal wavelength. An EDFA fibre with the SI profile was considered to carry out the investigations. Table 6-3 summarises the simulation parameters of the MM-EDFA employed for analysis of the 4-mode channels. The core radius (16.44 μm) of the amplifier was made the same as that of the transmission fibre to avoid conflict.

Table 6-3 MM-EDFA Simulation parameters

Parameter	Unit	Value	Parameter	Unit	Value
r_{core}	μm	16.44	Pump ref. wavelength [λ]	nm	1310
$r_{Er\text{-}doped}$	μm	13	Noise cent. Freq.	nm	850
NA	-	0.24	Pump frequency	nm	980
Ion density	m^{-3}	$10e^{+24}$	Pump Power	mW	400 (4 modes)

The fibre in the MM-EDFA supports four spatial nondegenerate modes with the core radius larger than the Erbium-doped core size. It is worth to mention that the fibre used for the MM-EDFA is an SI that is weakly guided, thus, all the modes were approximated by the LP modes.

Fig. 6-22 illustrates the mode intensities profile and its view along the x-axis. It can be seen that all the non-degenerate spatial modes demonstrate a single polarisation. The normalised intensity profile is determined through modal analysis

of the fibre. The intensity distributions of the mode signal, the pump as well as ASE can be expressed as:

$$I_S(r,\emptyset,Z) = P_S(Z).\, i_S(r,\emptyset) \qquad \text{Eq (6.7)}$$

$$I_P(r,\emptyset,Z) = P_P(Z).\, i_P(r,\emptyset) \qquad \text{Eq (6.8)}$$

$$I_{ASE}(r,\emptyset,Z) = P_{ASE}(Z).\, i_{ASE}(r,\emptyset) \qquad \text{Eq (6.9)}$$

The power ratio allocates to the input spatial field is defined by the coupling coefficients based on the following relation

$$C_i = \int_0^{2\pi} \int_0^{\infty} E_{in}(r,\emptyset)\, E_i^*(r,\emptyset) r dr d\emptyset \qquad \text{Eq (6.10)}$$

where E_i denotes modes spatial profile and E_{in} represents mode spatial input.

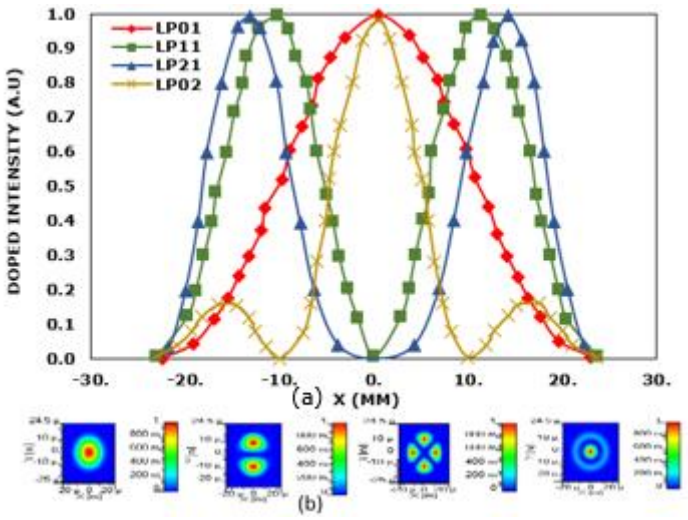


Fig. 6-22: (a) Doped intensity profile of the four pump non-degenerate modes (LP_{01}, LP_{11}, LP_{21}, and LP_{02}) (b) normalized intensity of the four spatial modes profile.

Fig. 6-23 depicts the effects of the change in the core size of the MM-EDFA. It has shown that varying the core size away from the optimised value can affect the BER performance.

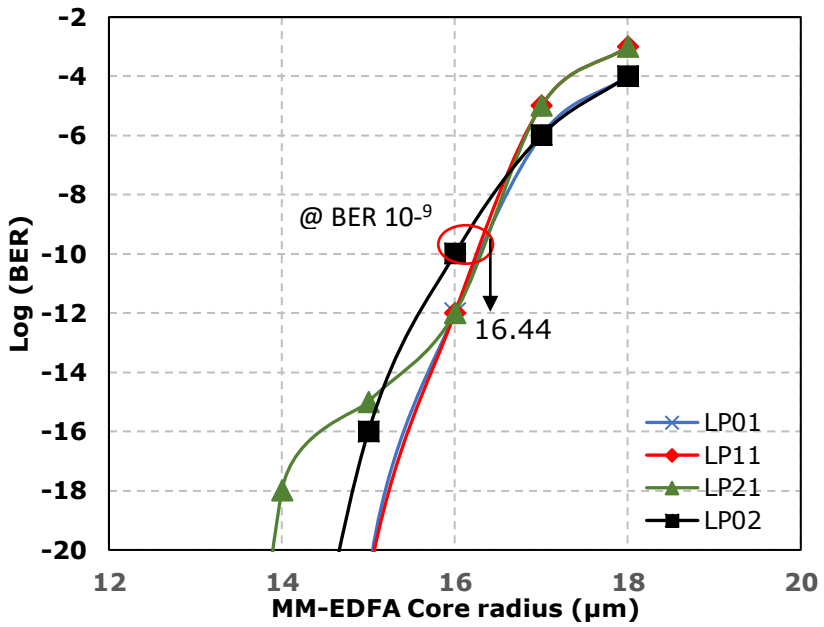


Fig. 6-23: BER Performance of the multimode EDFA with the variation in the EDFA core radius.

The optimised core radius is 16.44 μm. This value corresponds to the core size of the transmission fibre. As shown, reducing this value can degrade BER performance. All the four mode channels demonstrate similar behaviour. Fig. 6-24 illustrates the variation of the Er-doped radius with the mode power distributions. The power distribution per mode changes as the Er-doped size is varied. Therefore, an optimisation is also required to determine the appropriate doped radius for a given number of modes.

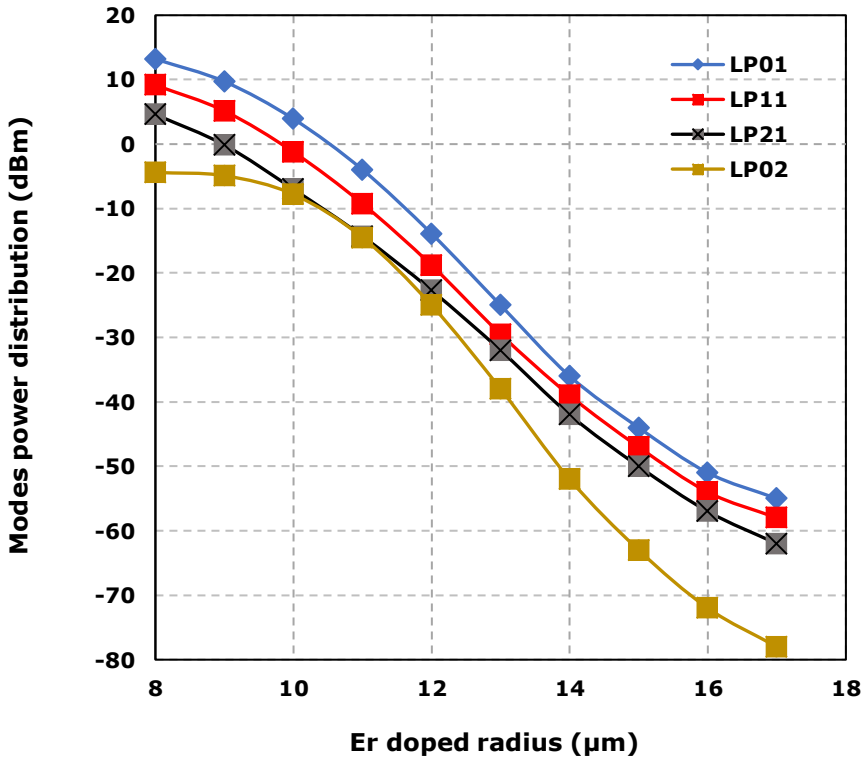


Fig. 6-24: Variation of the erbium-doped radius with the power distribution per mode channel.

Fig. 6-25 depicts the variation of the MM-EDFA core radius with pump power per signal mode. As can be seen, the power distribution among the modes also depends on the core radius of the MM-EDFA.

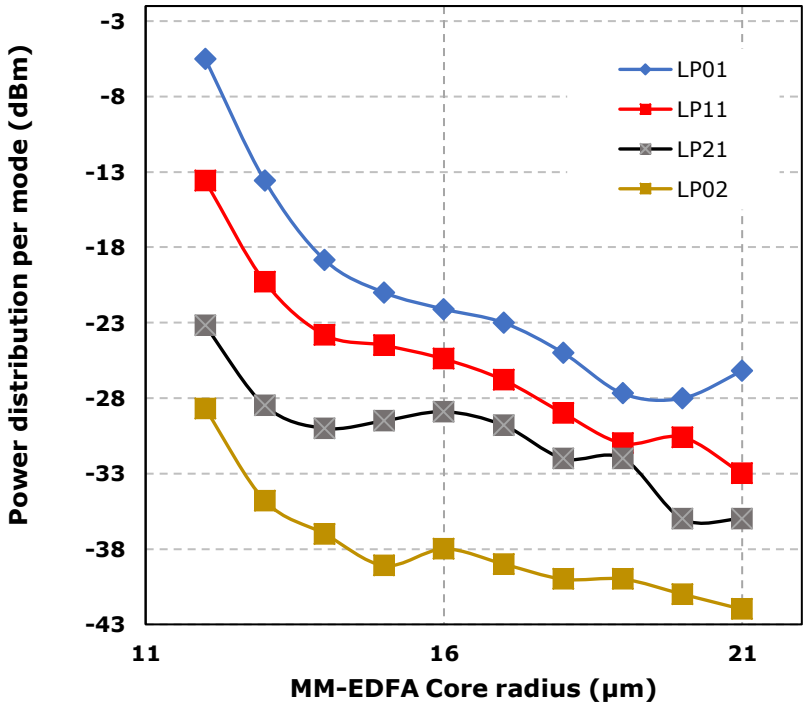


Fig. 6-25: Variation of MM-EDFA core radius with the power distribution per modes.

Fig. 6-26 illustrates the calculated BER of the MM-EDFA variation with the input signal power per mode (P_{in}) at a fixed single pump power (P_P) of 26 dBm (400 mW). It can be observed that the BER performance of all the spatial modes depends on the P_{in} in which too low P_{in} results in a rapid degradation in the BER of the mode channels. This may be attributed to the increasing level of ASE, which can reduce OSNR.

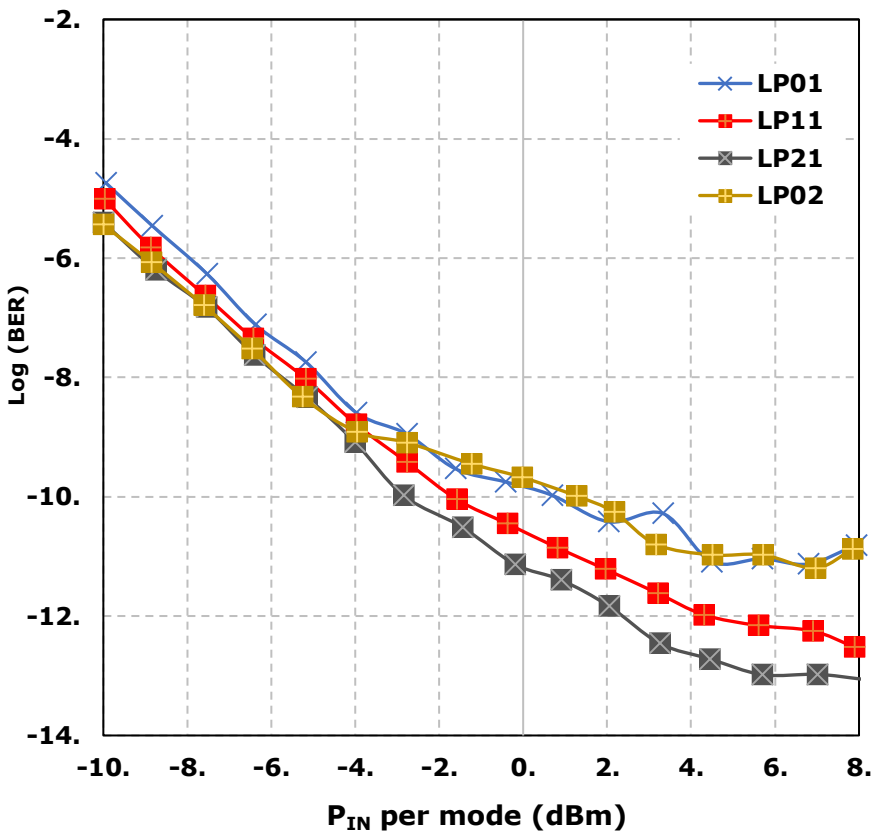


Fig. 6-26: Performance of the multimode EDFA in terms of BER as a function of the input power per spatial mode.

Fig. 6-27 shows the BER performance of the amplifier at various values of the P_P at a fixed input power of 0 dBm per mode channel. The calculated BER curve illustrating that an optimum P_P occurs, which gives the best BER performance for a given P_{in}. when the population inversion gets higher, the amplifier NF gets lower. Therefore, at a value of P_P lower than 26 dBm, the BER performance can be enhanced by increasing the P_P, which is as a result of the increase in the population inversion. Nevertheless, at P_P value greater than 26 dBm the BER performance starts degrading because of the increase in ASE from the MM-EDFA.

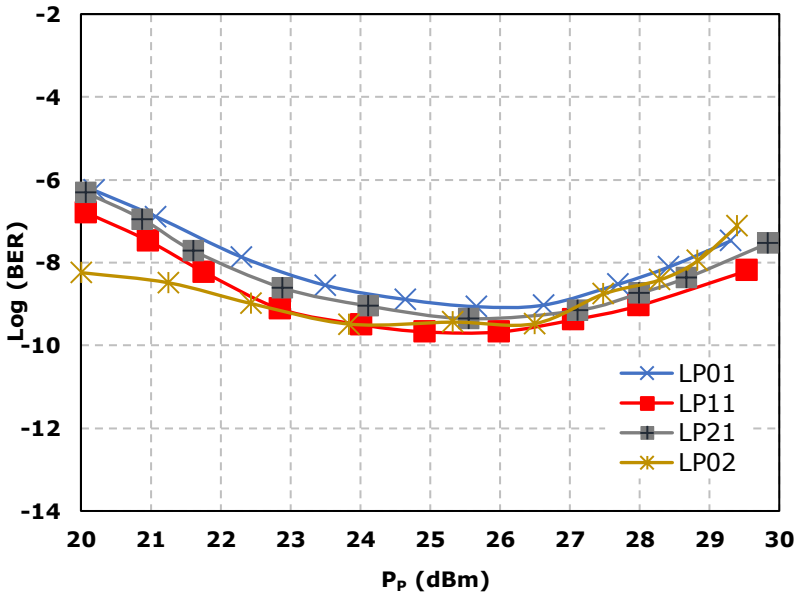


Fig. 6-27: Performance of the multimode EDFA in terms launched pump power.

6.5.2 4-Channel Transmission Performance at 10 Gb/s

The simulation results of the four LP modes MDM transmission over 40 km using DD is presented. Table 6-4 summarise the fibre properties operating at 1550 nm (default values). The system BER performance after transmission over 40 km at 5 km interval was measured. The P_N and P_{TH} at BER of 10^{-9} (optical communication limit) are investigated for the MDM system using the four mode channels.

Table 6-4: Fibre parameters at 1550 nm.

Parameters	Unit	LP01	LP11	LP21	LP02
Attenuation	dB/km	1.4	1.4	1.4	1.4
A_{eff}	μm^2	91	174.2	183	192.4
γ-(intra-modal)	W^{-1}/km	0.4	0.52	0.45	0.36
γ-(inter-modal)	W^{-1}/km	0.3	0.3	0.3	0.3
Dispersion slope	$Ps/(nm^2.m)$	0.05	0.05	0.05	0.05

6.5.1 Intermodal Nonlinearity

The intermodal nonlinear characteristics of an optical fibre have been studied both for long-haul and short distance telecommunication networks [215]. Theoretically, small variations in the fibre refractive-index profile lead to nonlinear effects that relate to the third-order susceptibility. This is based on the optical waveguide theory, in which MMF/FMF can support several transverse modes. Each of the

modes propagates with a different characteristic group velocity [216]. It is important to mention that the effective nonlinear coefficients of the MMF depend on the nonlinear indices and waveguide characteristics. It includes mode shapes and their level of confinement in the core. Thus, the effective nonlinear coefficient (n_E) can be expressed as [217]:

$$n_E = n_E(\omega, Pol., M, P)$$
$$= \frac{\iint_{-\infty}^{+\infty} n_2(x,y) \cdot |F(x,y)|^4 dxdy}{\iint_{-\infty}^{+\infty} |F(x,y)|^2 dxdy} \quad \text{Eq (6.11)}$$

where n_E is the effective nonlinear coefficient, P stands for the power, Pol. Represents state of polarisation, and ω denotes the wavelength. $n_2(x,y)$ represents the nonlinear refractive index and $F(x,y)$ denotes a normalised mode field pattern. Eqn 6.11 illustrates the dependence of the fibre effective index on frequency, signal power, modes, and polarisation. The linear effects that include PMD, DMGD, and chromatic dispersion originated from the first three terms. Similarly, the nonlinearity in the fibre consisting of the self-phase modulation (SPM), cross-phase modulation (XPM), and four wave mixing (FWM), etc. initiated from the variation of power. The nonlinear coefficient between four modes (γ_{lmuv}) is assumed related to the overlap integral (f_{lmuv}) of the distribution of the mode in fibre and can be defined as [123]:

$$\gamma_{lmuv} = \frac{n_2 v_0}{C} f_{lmuv} \quad \text{Eq (6.12)}$$

Where n_2 denotes the nonlinear index coefficient and v_0 reparents a centre frequency of the wave. Based on the third order susceptibility, the real part of Eqn (6.12) leads to a Kerr-effect that results in the nonlinearity such as SPM, XPM, and FWM. On the other hand, the imaginary parts bring about effects such as stimulated Brillouin scattering (SBS) and stimulated Raman scattering (SRS) [218]. The IM-XPM and IM-FWM have recently being investigated [219]. The IM-FWM was successfully phase matched despite the presence of the chromatic dispersion in the spatial modes [220]. Thus, pump wavelength may not necessarily be matching with zero dispersion wavelength and no need to reduce chromatic dispersion. The power transfer spectrum of the I-XPM which is frequency dependent can be processed as a super Gaussian function (SGF) of frequency v defined by:

$$G(v) = exp\{-[(v - v_0)/\Delta v]^{2m}\} \quad \text{Eq (6.13)}$$

where Δv denotes a filter spectral bandwidth and m signifies super Gaussian order.

Other nonlinearity effects include the SBS and SRS. Details of the SRS theory and observations are discussed in [221]. Generally, SRS effectiveness depends on the Stokes modes characteristics under distinct pump and excitations and is weighted via the overlap using the electric field of the pump and signal. Thus the frequency shift v_R is expressed as:

$$v_R = \omega_P - \omega_S \qquad \text{Eq (6.14)}$$

where ω_S denotes the downshifted Stoke frequency, ω_P represents a pump frequency, v_R is evaluated by the modes vibration of the transmission fibre [222]. Fig. 6-28 demonstrates the Log (BER) over the distance link of 40 km as a function of the launch power per mode channels at the BER of E10^{-9}. It demonstrates the effects of the XPM on the NRZ modulation format as a result of varying the lunch power between the four LP modes. The performance of the system gets worst after increasing the power beyond 0 dBm. It may be attributed to the variations of the GVD in the fibre [216].

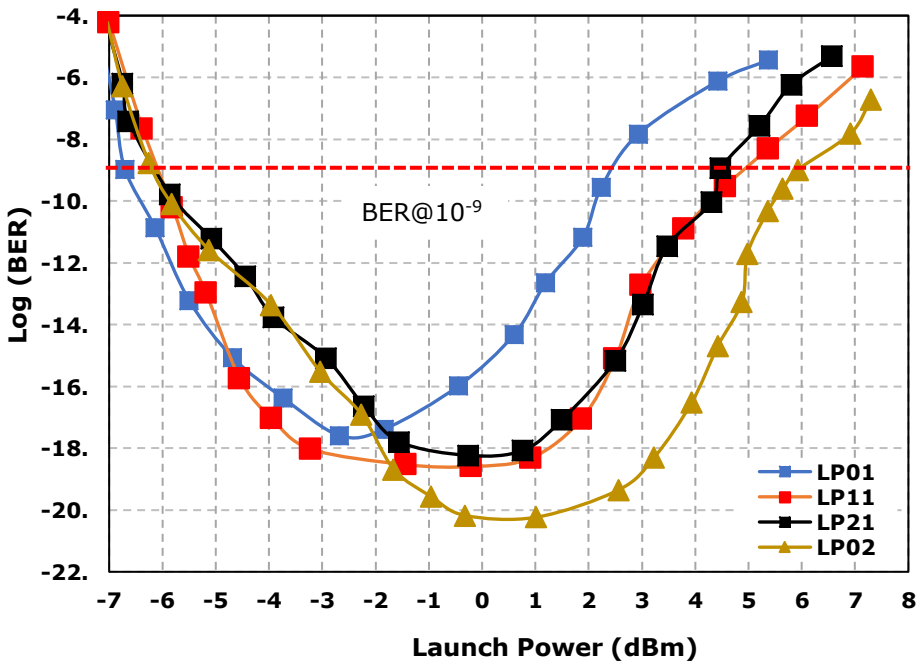


Fig. 6-28: Log (BER) for an MDM transmission over 40km of a four-mode fibre as a function of launch power.

Another factor that might contribute to the power fluctuation between the modes is the coupling between them, reducing the mode coupling can improve the level of the penalty. This can be achieved by increasing the effective area of the fibre modes. In addition, the transmission reach can be extended by reducing the linear crosstalk that is not compensated as the system employed the DD technique. Table 6-5 depict a summary of the minimum and threshold power required by each mode.

Table 6-5: Minimum and threshold power for the four LP modes at the BER of 10^{-9}.

LP-modes	Min. Power P_m (dBm)	Threshold power P_{thu} (dBm)
LP_{01}	-6.7	2.2
LP_{11}	-6.2	4.2
LP_{21}	-6.5	4.2
LP_{02}	-6.2	6.0

Fig. 6-29 illustrates the BER of the transmitting four spatial modes for the B2B and over a 40 km as function of the OSNR. The bit streams are transmitted at 10 Gb/s on the four distinct modes. The power penalty in the transmission modes is reduced compared to the results in Fig 6-10. It may be attributed to the optimisation of different parameters of the MM-EDFA. For example, the OSNR penalty between B2B and the distance link over 40 km of the four modes is between the range of 0.75 dB and 1.86 dB.

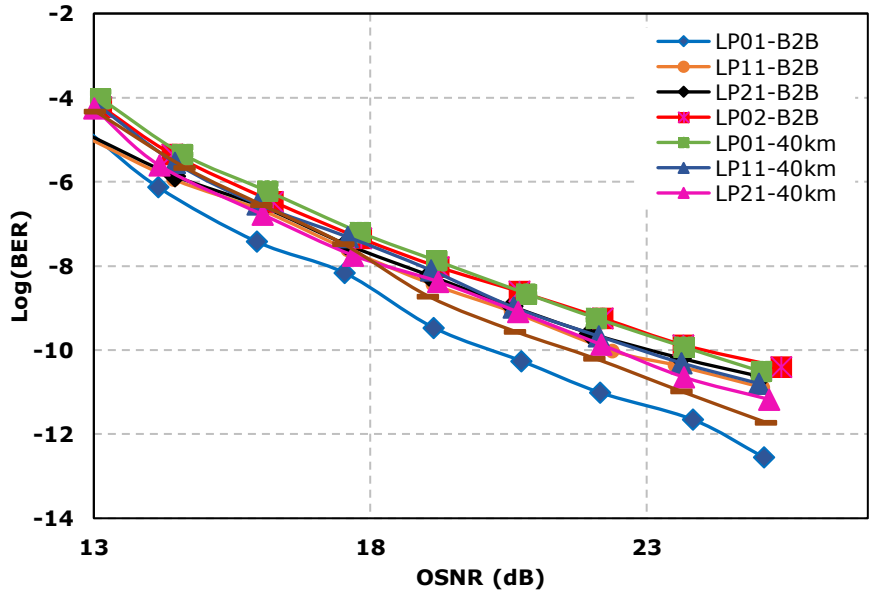


Fig. 6-29: Comparison of the BER performance versus OSNR of the four signal modes at B2B and over 40km distance link.

Fig. 6-30 is the variation of the BER performance with the receiver sensitivity at the distance interval over 5 km, 15 km, and 30 km.

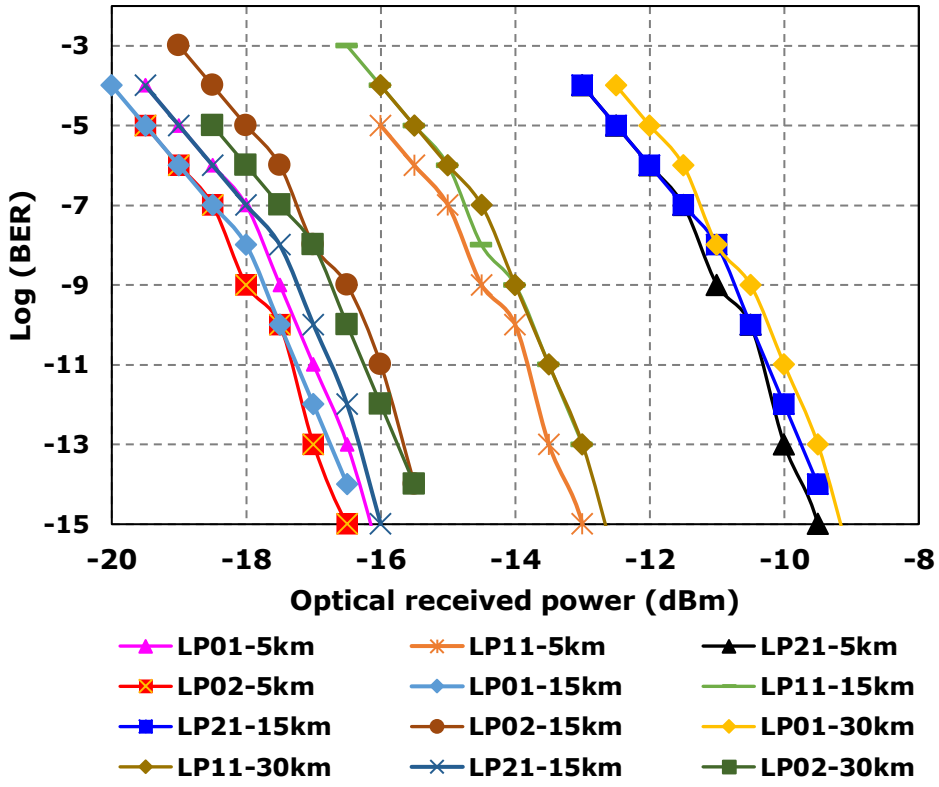


Fig. 6-30: BER performance with the variation of the received optical power over the 5km, 15km, and 30km distance links.

The fixed received optical power of the LP_{01} is -16 dBm, -15.7 dBm and -9 dBm and that of the LP_{11} are fixed at -14.5 dBm, -13.5 dBm and -13 dBm over the distance link of 5 km, 15 km and 30 km. Therefore, the power penalty between the two modes are found to be 1.5 dB, 2.2 dB, and 4 dB respectively. Similarly, the power penalty between the LP_{21} and LP_{02} over the distance link of 5 km, 15 km and 30 km were found to be 3.4 dB, 4.6 dB and 4.8 dB respectively. The improve in the power penalty in the four mode channels may be as result of optimising the MM-EDFA.

Finally, Fig. 6-31 illustrates the corresponding eye diagrams at the BER of 10^{-9} for the back-back and over 40 km distance link. It can be observed that the eye opening is similar in both cases.

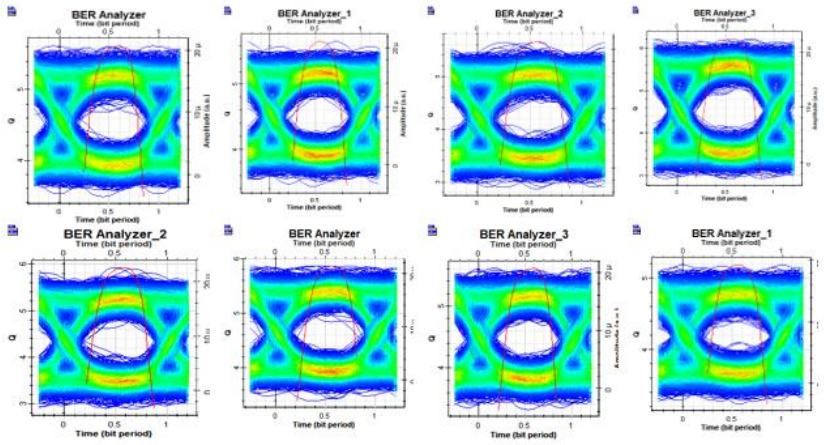


Fig. 6-31: Eye diagrams of the LP_{01}, LP_{11}, LP_{21}, and LP_{02} at BER of 10^{-9} respectively. The first row is for the B2B, and the second row is the eye diagrams over 40 km.

6.6 Summary

The Chapter discusses the transmission performance of the high-speed mode division multiplexing (MDM) system for interconnect and metro applications. The network link is modelled to transmit two spatial signal mode channels (LP_{01} and LP_{11}) as signal carriers. A binary non-return-to-zero (NRZ) and return-to-zero (RZ)-OOK modulation formats were adopted in order to carry out the investigations. The two-mode channels were recovered by direct detection (DD). This was achieved by a spatial receiver at the two aggregated bit rate of 2×10 Gb/s and 2×20 Gb/s at 1550 nm. By optimizing the bias voltages of a dual port dual derive Mach Zehnder modulator (DP-DD-MZ) the performance of the system was optimized in order to extend the transmission distance. Thus, extending the transmission reach compared to that of the conventional Mach Zehnder (C-MZM) modulator by 8 km and 7 km, at 10 Gb/s and 20 Gb/s respectively. The proposed system can be used as an alternative candidate for a data center and metro communication network, due to its potentiality for enhancing the capacity of an optical communication system.

Similarly, the performance of an MDM transmission supporting four non-degenerate spatial modes was also examined at the bit rate of 10 Gb/s. In this case, the NRZ modulation format was adopted to evaluate the system performance in terms of

the P_N and the P_{TH} at a BER of 10^{-9}. The receiver sensitivity, the optical signal to noise ratio and the maximum transmission distance also investigated using direct detection. It was found that the system performance depends largely on the optimisation of the MM-EDFA for the NRZ modulation format.

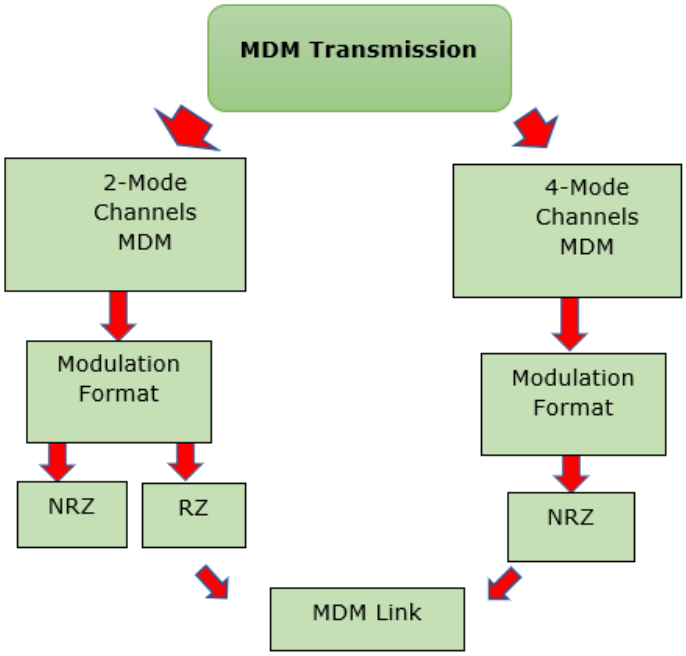


Fig. 6-32: Chapter summary

Chapter 7 General Conclusion and Future Work

7.1 Conclusion and Summary

Novel multiplexing techniques are essential in order to meet up with future multiplicative bandwidth demands in the next generation optical networking system. MDM was investigated as a viable option to increase optical communication bandwidth based on spatial domain multiplexing. In this thesis, we have proposed some of the essential devices that can play an important role in the future MDM communication system.

A general review on the current progress in optical devices for SDM systems was presented. The state-of-the-art includes the recent achievements in the optical fibre devices, which are paramount to the successful realisation of an MDM system. Section 2.2.2 described different mode conversion techniques. It was observed that more effort is needed for the investigation of higher order mode conversions as most of the work recently reported were centred on the LP_{01} to high order mode conversions. This is due to the importance of the conversion during mode multiplexing. The recent finding in mode multiplexing schemes was discussed in section 2.2.2. It includes the one exhibiting the highest demonstrated LP-mode selectivity in the ten-mode multiplexing, with the average crosstalk of -26 dB, reporting higher coupling efficiency (low IL <4 dB when coupled to the MMF) and very low MDL (average 1.2 dB), over the entire C and L band. In addition, the recent advancement of various schemes in minimising differential mode gains in FM-EDFAs and MC-FM-EDFAs were examined in section 2.2.3. Thus, highlighting the advantages of Raman amplifiers over EDFA and SOA, which includes achieving distributed amplification and reducing noise generation. It is suggested that combining the two technologies (EDFA and RA) can allow extending transmission distance more than when only EDFA is adopted. Finally, in section 2.2.7, a recent highlight on the SDM system is given, it is crucial to have unanimity between the individual spatial signal channels to minimise the required space needed for the SDM system. This can reduce the overall cost for both system operation and deployment. The unanimity anticipated across the system include along the entire fibre length, optical amplifiers, and transceivers.

The mathematical formulations for the MDM device modeling were also presented. This includes the FDTD and **TE**-wave equations that were presented in section 3.2.2 and 3.2.3, respectively. In addition, the light source model, the spectral response model, and the power model based on the FDTD were also explored in section 3.3.4, 3.2.5, and 3.2.7, respectively. In section 3.2.8, a brief

description of the simulation workflow was illustrated. Section 3.3 determines the LP_{11} to LP_{01} design parameters were determined by considering M-RCF as the proper fibre (section 3.3.1). Section 3.3.2 examined the converter parameters based on the tilts MC-MMF. The theory and principle of an arc waveguide were discussed in section 3.3.4. Finally, section 3.4 presented an LP-MMM model technique used for modeling the high dispersion fibres. In this case, both the vector modes (section 3.4.2) and LP modes matrix relations (section 3.4.3) were derived and discussed.

Two new proposed LP_{11} mode converters with a lateral misalignment are reported. In this study, the theory of the M-RCF and CSIF were discussed and the effects of literal misalignments on coupling power were examined. Two novel mode converters based on M-RCF and CSIF are compared in terms of their performance parameters. Both the two devices were modeled by laterally misaligning the two identical fibres that constituted each device. Different effects such as that of the literal misalignments as a function of CE, separation distance d variation with coupling length L_c, were examined too. Lastly, an M-RCF and CSIF based LP_{11} to LP_{01} mode conversion devices demonstrating 94% and 69% CE, with MP of 85% and 58.8% were achieved, respectively. Based on the performance parameters demonstrated by the M-RCF based model, it may find applications in mode conversion in mode division multiplexing system.

In addition, section 4.3 presents the conversion of multiple higher order modes. In this study, a numerical demonstration of higher order mode conversion was explored and achieved using MC-MMF assisted by the DAW. The input fibre was tilted at a small angle to suppressed radiation loss. The optimised tilted angle of the input fibre was determined to be 12^{o}. The investigations also show that tilting the fibre at an angle greater than the critical angle could lead to amplitude distortion/decay due to the field radiation. Another relationship investigated is the variation of the mode amplitude on tilt angles by exciting different LP modes from the input of the tilted fibre. The amplitude of the propagating LP_{01} mode decrease close to zero at 43^{0} (critical angle), then increases a bit to a small peak. Besides, the higher order modes (LP_{11}, LP_{02}, and LP_{21}) demonstrates similar behavior, starting with a tilt angle equal to zero (0^{o}). It was found that when the tilt angle is greater than the critical angle, an approximate equal power distribution is observed. Finally, an LP_{11} to LP_{01}, LP_{02} to LP_{11}, and LP_{21} to LP_{01} mode conversions were achieved. The conversion efficiencies were found to be 89.6%, 91.2%, and 94.34% respectively. Based on the calculated results, this technique can potentially be good for mode conversion in mode multiplexing for an MDM system due to their low loss.

Furthermore, two novel high dispersion fibres using LP mode matrix method were reported. A numerical technique was employed to investigate the effect of core structural parameters variation on modal dispersion of different modes. The dispersion equalisation of two different four-mode fibres was demonstrated, and their effective areas were optimised at the same thickness values. A new and simple approach was proposed and presented, in which modal dispersions of four linearly polarised modes were equalised by varying the dimensional parameters of the core index profiles. The optimisation was achieved by varying the core layer thicknesses (core-ring radius) to a specified OPT value. These values would coincide with the one adopted in optimising the A_{eff} (for the case of R2 and X3 in the low index region of the two fibres). The thickness of the low index ring (R2) of the centre high index fibre (CH-ICF) and that of the centre low index core fibre (CL-ICF) X3 were varied to examine the effect on A_{eff} on the fibres. It was observed that as the thickness of the low index ring (R2 and X3) increases the A_{eff} also increased. In addition, decreasing the index of this portion bring a benefit of increasing the A_{eff}, this moves the dispersion away from 1550 nm (operating wavelength) regions. The relations (Fig. 5-13) between the cladding-low index contrast (Δy) and the A_{eff} was also examined. As the cladding-low index difference increases, the A_{eff} decreases exponentially. It can be concluded that if more properties of the proposed structures can be investigated, the FMF can be a good potential medium for MDM systems, due to the high dispersion tolerance.

Finally, the transmission performance of a 2-channel MDM system for metro and interconnect application was evaluated. Performance of the system using Conventional MZM (C-MZM) at 10 Gb/s and 20 Gb/s bit rate was initially considered to examine the power penalty between the two mode channels. Moreover, the transmitter/receiver misalignment at 10 Gb/s was analyzed for the B2B and 15 km distance link. It was observed that the *Q*-factor of the two signal modes was decreased as the field outside the active area of the photodetector was shifted. At the receiver, the *Q*-Factor for both B2B and over the 15 km distance link increases with an increase in the active area of the photodetector for the two signal mode channels. The 15 km transmission distance was optimised by varying the bias voltage of the DP-DD-MZ modulator, which consequently extends the initial transmission distance of the C-MZM. Finally, it was found that the maximum transmission distance achieved by C-MZM could be extended by 8 km and 7 km at 10 Gb/s and 20 Gb/s bit rates, respectively. Similarly, the performance of an MDM transmission supporting four non-degenerate spatial modes was examined at the bit rate of 10 Gb/s. In this case, the NRZ modulation format was adopted to evaluate the system performance in terms of the minimum power needed (P_N) and the nonlinear threshold power (P_{TH}) at a BER of 10^{-9}. It demonstrates the effects of

the XPM on the NRZ modulation format as a result of varying the lunch power between the four LP modes. The performance of the system gets worst after increasing the power beyond 0 dBm. This may be attributed to the variations of the GVD in the fibre. The receiver sensitivity, the OSNR, and the maximum transmission distance were also investigated using the DD at 10 Gb/s bit rate. It was found that the system performance depends largely on the optimisation of an MM-EDFA.

7.2 Future Work

Mode conversion is an integral part of mode multiplexing in MDM communication system. Two new mode converter devices have been proposed, the first one is limited to converting LP_{11} to LP_{01} mode only. By modeling the M-RCF to accommodates high order, modes other than LP_{11}, such as LP_{21} can allow achieving similar objectives. Furthermore, the mode converter presented in chapter 4, section 4.3, can be expanded to convert up to twelve spatial modes. This can only be achieved if the conversion region (DAW) is carefully engineered to avoid radiation loss. Finally, the two high dispersion fibres proposed in chapter 5 can be modeled to equalise modal dispersion of a fibre that can support six, eight, or even twelve modes. The modal dispersion equalisation technique reported here can be applied to index profiles of a shape other than the centre high and centre low refractive index profiles. Other issues such as sensitivity to parametric variation, sensitivity to bending loss, splice loss, and polarisation mode dispersion can also be explored. This can significantly improve the bandwidth of a future optical communication system.

Reference

[1] R.-J. Essiambre, G. Kramer, P. J. Winzer, G. J. Foschini, and B. Goebel, "Capacity Limits of Optical Fiber Networks," *J. Light. Technol.*, vol. 28, no. 4, pp. 662–701, Feb. 2010.

[2] D. J. Richardson, J. M. Fini, and L. E. Nelson, "Space-division multiplexing in optical fibres," *Nat. Photonics*, vol. 7, no. 5, pp. 354–362, May 2013.

[3] F. F. Al Quayed and S. S. Zaghloul, "Analysis and evaluation of Internet Protocol Television (IPTV)," *2014 3rd Int. Conf. e-Technologies Networks Dev. ICeND 2014*, pp. 162–164, 2014.

[4] X. Tian, C. Zhao, H. Liu, and J. Xu, "Video On-Demand Service via Wireless Broadcasting," *IEEE Trans. Mob. Comput.*, vol. 16, no. 10, pp. 2970–2982, Oct. 2017.

[5] E. N. Pencheva, "Multimedia broadcasting in multi-access edge computing," in *2017 13th International Conference on Advanced Technologies, Systems and Services in Telecommunications (TELSIKS)*, 2017, pp. 57–60.

[6] M. Ye, Y. Yu, G. Chen, Y. Luo, and X. Zhang, "On-chip WDM mode-division multiplexing interconnection with optional demodulation function," *Opt. Express*, vol. 23, no. 25, p. 32130, 2015.

[7] M. S. Faruk and S. J. Savory, "Digital Signal Processing for Coherent Transceivers Employing Multilevel Formats," *J. Light. Technol.*, vol. 35, no. 5, pp. 1125–1141, Mar. 2017.

[8] P. J. Winzer, "Spatial multiplexing in fiber optics: The scaling of metro/core capacities," *Bell Labs Tech. J.*, vol. 19, pp. 22–30, 2014.

[9] A. Gatto, P. Parolari, and P. Boffi, "Frequency division multiplexing for very high capacity transmission in bandwidth-limited systems," in *Optical Fiber Communication Conference*, 2017, p. W1K.1.

[10] T. A. Eriksson, E. Agrell, and M. Karlsson, "Multidimensional modulation formats for coherent optical communications," *Proc. of SPIE* , vol. 977403, no. February 2016, p. 977403.

[11] P. J. Winzer, "Energy-Efficient Optical Transport Capacity Scaling Through Spatial Multiplexing," *IEEE Photonics Technol. Lett.*, vol. 23, no. 13, pp. 851–853, Jul. 2011.

[12] "Cisco Visual Networking Index: Global Mobile Data The Cisco ® Visual Networking Index (VNI) Global Mobile Data Traffic," 2017.

[13] K. I. Kitayama *et al.*, "Mode division multiplexing network: A deployment scenario in metro area network," *2014 IEEE Glob. Commun. Conf. GLOBECOM 2014*, pp. 2154–2159, 2014.

[14] Cisco, "Web." 2017.

[15] Cisco, "Web." 2017.

[16] A. M. Ortiz and R. L. Sáez, "Multi-Core Optical Fibers: Theory, Applications and Opportunities," in *Selected Topics on Optical Fiber Technologies and Applications*, InTech, 2018.

[17] R. G. H. van Uden *et al.*, "8.96Tb/s (32×28GBaud×32QAM) Transmission over 0.95 km 19 cell Hollow-Core Photonic Bandgap Fiber," in *Optical Fiber Communication Conference*, 2014, p. W4J.3.

[18] R. Nejabati *et al.*, "First Demonstration of Software Defined Networking (SDN) over Space Division Multiplexing (SDM) Optical Networks," in *39th European Conference and Exhibition on Optical Communication (ECOC 2013)*, 2013, pp. 1263–1265.

[19] L. E. Nelson *et al.*, "Spatial Superchannel Routing in a Two-Span ROADM System for Space Division Multiplexing," *J. Light. Technol.*, vol. 32, no. 4, pp. 783–789, Feb. 2014.

[20] J. Sakaguchi *et al.*, "SDM-WDM hybrid reconfigurable add-drop nodes for self-homodyne photonic networks," in *2013 IEEE Photonics Society Summer Topical Meeting Series*, 2013, pp. 117–118.

[21] G. M. Saridis, D. Alexandropoulos, G. Zervas, and D. Simeonidou, "Survey and Evaluation of Space Division Multiplexing: From Technologies to Optical Networks," *IEEE Commun. Surv. Tutorials*, vol. 17, no. 4, pp. 2136–2156, 2015.

[22] R. Hays and H. Frasier, "40G Ethernet Market Potential IEEE 802.3 HSSG Interim Meeting," *IEEE 802.3 HSSG Intrime Meeting* 2007.

[23] S. Yan *et al.*, "Archon: A Function Programmable Optical Interconnect Architecture for Transparent Intra and Inter Data Center SDM/TDM/WDM Networking," *J. Light. Technol.*, vol. 33, no. 8, pp. 1586–1595, Apr. 2015.

[24] S. Jain, V. J. F. Rancano, T. C. May-Smith, P. Petropoulos, J. K. Sahu, and D. J. Richardson, "Multi-element Fiber for space-division multiplexed optical communication system," *Int. Conf. Transparent Opt. Networks*, pp. 6–9, 2014.

[25] B. J. Puttnam *et al.*, "Investigating Self-Homodyne Coherent Detection in a 19-core Spatial-Division-multiplexed Transmission Link," *Eur. Conf. Exhib. Opt. Commun.*, vol. 21, no. 2, p. Tu.3.C.3, 2012.

[26] T. Mori, T. Sakamoto, M. Wada, T. Yamamoto, and K. Nakajima, "Few-mode fiber technology for mode division multiplexing," *Opt. Fiber Technol.*, vol. 35, pp. 37–45, Feb. 2017.

[27] T. Sakamoto, T. Mori, M. Wada, T. Yamamoto, F. Yamamoto, and K.

Nakajima, "Strongly-coupled multi-core fiber and its optical characteristics for MIMO transmission systems," *Opt. Fiber Technol.*, vol. 35, pp. 8–18, 2017.

[28] Y. Sasaki, Y. Amma, K. Takenaga, S. Matsuo, K. Saitoh, and M. Koshiba, "Few-Mode Multicore Fiber With 36 Spatial Modes (Three Modes (LP01,LP11a,LP11b) × 12 Cores)," *J. Light. Technol.*, vol. 33, no. 5, pp. 964–970, Mar. 2015.

[29] K. Igarashi *et al.*, "114 Space-Division-Multiplexed Transmission over 9.8-km Weakly-Coupled-6-Mode Uncoupled-19-Core Fibers," in *Optical Fiber Communication Conference Post Deadline Papers*, 2015, p. Th5C.4.

[30] Y. Sasaki, K. Takenaga, S. Matsuo, K. Aikawa, and K. Saitoh, "Few-mode multicore fibers for long-haul transmission line," *Opt. Fiber Technol.*, vol. 35, pp. 19–27, Feb. 2017.

[31] R. G. H. van Uden *et al.*, "Ultra-high-density spatial division multiplexing with a few-mode multicore fibre," *Nat. Photonics*, vol. 8, no. 11, pp. 865–870, 2014.

[32] Nokia Siemens Networks, "Space Division Multiplexing: A new milestone in the evolution of fiber optic communication," *WHITE Pap.,* 2013.

[33] A. J. Lowery and L. B. Du, "Optical orthogonal division multiplexing for long haul optical communications: A review of the first five years," *Opt. Fiber Technol.*, vol. 17, no. 5, pp. 421–438, 2011.

[34] J.-W. Goossens, M. I. Yousefi, Y. Jaouën, and H. Hafermann, "Polarization-division multiplexing based on the nonlinear Fourier transform," *Opt. Express*, vol. 25, no. 22, p. 26437, Oct. 2017.

[35] J. M. Fini, T. F. Taunay, B. Zhu, and M. F. Yan, "Low Cross-Talk Design of Multi-core Fibers," in *Conference on Lasers and Electro-Optics 2010*, 2010, p. CTuAA3.

[36] A. Gaur and V. Rastogi, "Gain equilization of six mode groups using trench-assisted annular core EDFA," in *2015 Workshop on Recent Advances in Photonics (WRAP)*, 2015, pp. 1–4.

[37] J. Han, G. Gao, Y. Zhao, and S. Hou, "Bend Performance Analysis of Few-Mode Fibers With High Modal Multiplicity Factors," *J. Light. Technol.*, vol. 35, no. 13, pp. 2526–2534, Jul. 2017.

[38] Y. Sasaki, Y. Amma, K. Takenaga, S. Matsuo, K. Saitoh, and M. Koshiba, "Investigation of Crosstalk Dependencies on Bending Radius of Heterogeneous Multicore Fiber," *Opt. Fiber Commun. Conf. Fiber Opt. Eng. Conf. 2013*, vol. 2, p. OTh3K.3, 2013.

[39] N. Riesen and J. D. Love, "Dispersion equalisation in few-mode fibres," *Opt.*

Quantum Electron., vol. 42, no. 9–10, pp. 577–585, 2011.

[40] C. Antonelli, A. Mecozzi, M. Shtaif, and P. J. Winzer, "Stokes-space analysis of modal dispersion in fibers with multiple mode transmission," *Opt. Express*, vol. 20, no. 11, p. 11718, May 2012.

[41] J. M. Kahn, K. Ho, and M. Bagher Shemirani, "Mode coupling effects in multi-mode fibers," in *Optical Fiber Communication Conference*, 2012, p. OW3D.3.

[42] J. van Weerdenburg *et al.*, "10 Spatial mode transmission using low differential mode delay 6-LP fiber using all-fiber photonic lanterns," *Opt. Express*, vol. 23, no. 19, p. 24759, 2015.

[43] N. K. Fontaine *et al.*, "30×30 MIMO Transmission over 15 Spatial Modes," in *Optical Fiber Communication Conference Post Deadline Papers*, 2015, p. Th5C.1.

[44] K.-P. Ho and J. M. Kahn, "Linear Propagation Effects in Mode-Division Multiplexing Systems," *J. Light. Technol.*, vol. 32, no. 4, pp. 614–628, Feb. 2014.

[45] A. Lobato *et al.*, "On the mode-dependent loss compensation for mode-division multiplexed systems," in *2013 15th International Conference on Transparent Optical Networks (ICTON)*, 2013, pp. 1–4.

[46] C. M. Serpa-Imbett, J. Marin-Alfonso, C. Gomez-Santamaria, L. Betancur, and F. Amaya-Fernandez, "Performance of spatially multiplexed systems based on numerical simulations of OFDM-MIMO in a two-core fiber with low coupling, and a few mode fiber with high DGD," *SBMO/IEEE MTT-S Int. Microw. Optoelectron. Conf. Proc.*, pp. 0–3, 2013.

[47] G. Lopez-Galmiche *et al.*, "Few-mode erbium-doped fiber amplifier with photonic lantern for pump spatial mode control," *Opt. Lett.*, vol. 41, no. 11, p. 2588, Jun. 2016.

[48] C. Shuai, C. Gao, Y. Nie, H. Hu, and S. Peng, "Microstructure analysis in the coupling region of fiber coupler with a novel electrical micro-heater," *Opt. Fiber Technol.*, vol. 17, no. 6, pp. 541–545, 2011.

[49] H. Sakata, H. Sano, and T. Harada, "Optical Fiber Technology Tunable mode converter using electromagnet-induced long-period grating in two-mode fiber," *Opt. Fiber Technol.*, vol. 20, no. 3, pp. 224–227, 2014.

[50] T. Uematsu *et al.*, "PLC-type LP11 mode rotator with single-trench waveguide for mode-division multiplexing transmission," in *Optical Fiber Communication Conference*, 2014, p. Th2A.52.

[51] R. I. Sabitu and A. Malekmohammadi, "Mode Conversion Based on Lateral Misalignment between Two Multi-Ring Core Fibers for MDM System," *J. Opt. Commun.*, pp. 1–10, Jan. 2019.

[52] M. Salsi *et al.*, "Mode-division multiplexing of 2 × 100 Gb/s channels using an LCOS-based spatial modulator," *J. Light. Technol.*, vol. 30, no. 4, pp. 618–623, 2012.

[53] R. Ryf *et al.*, "Mode-division multiplexing over 96 km of few-mode fiber using coherent 6×6 MIMO processing," *J. Light. Technol.*, vol. 30, no. 4, pp. 521–531, 2012.

[54] Y. Zhao *et al.*, "All-fiber mode converter based on long-period fiber gratings written in few-mode fiber," *Opt. Lett.*, vol. 42, no. 22, p. 4708, Nov. 2017.

[55] Y. Cao *et al.*, "Mode conversion-based crosstalk-aware routing, spectrum and mode assignment in space-division multiplexing elastic optical networks," in *2017 16th International Conference on Optical Communications and Networks (ICOCN)*, 2017, vol. 4, no. 1, pp. 1–3.

[56] M. Lan *et al.*, "An arbitrary mode converter with high precision for mode division multiplexing in optical fibers," *J. Mod. Opt.*, vol. 62, no. 5, pp. 348–352, 2015.

[57] D. Garcia-Rodriguez, J. L. Corral, and R. Llorente, "Mode Conversion for Mode Division Multiplexing at 850 nm in Standard SMF," *IEEE Photonics Technol. Lett.*, vol. 29, no. 11, pp. 929–932, 2017.

[58] H. Mellah, X. Zhang, and D. Shen, "Analysis of optical fiber-based LP_01 ↔ LP_02 mode converters for the O-, S-, and C-Band," *Appl. Opt.*, vol. 54, no. 17, p. 5568, Jun. 2015.

[59] Z. Wu *et al.*, "Fundamental-mode MMF transmission enabled by mode conversion," *Opt. Commun.*, vol. 410, no. August 2017, pp. 112–116, 2018.

[60] H. Mellah, J.-P. Bérubé, R. Vallée, and X. Zhang, "Fabrication of a LP 01 to LP 02 mode converter embedded in bulk glass using femtosecond direct inscription," *Opt. Commun.*, vol. 410, pp. 475–478, Mar. 2018.

[61] D. Shen, C. Ma, C. Wan, H. Yuan, and X. Zhang, "A new all-fiber LP<inf>01</inf>]]>/LP<![CDATA[<inf>02</inf> mode converter in mode division multiplexing," in *2017 16th International Conference on Optical Communications and Networks (ICOCN)*, 2017, vol. 78, pp. 1–3.

[62] D. Pérez-Galacho, C. Alonso-Ramos, D. Marris-Morini, V. Vakarin, X. Le Roux, and L. Vivien, "Mode converters based on periodically perturbed waveguides for mode division multiplexing," *Silicon Photonics: From Fundamental Research to Manufacturing*, 2018, vol. 10686, p. 26.

[63] Y. Gao, J. Sun, G. Chen, and C. Sima, "Demonstration of simultaneous mode conversion and demultiplexing for mode and wavelength division multiplexing systems based on tilted few-mode fiber Bragg gratings," *Opt. Express*, vol. 23, no. 8, p. 9959, 2015.

[64] K. Igarashi *et al.*, "114 Space-Division-Multiplexed Transmission over 9.8-km Weakly-Coupled-6-Mode Uncoupled-19-Core Fibers," in *Optical Fiber Communication Conference Post Deadline Papers*, 2015, p. Th5C.4.

[65] R. Ryf *et al.*, "Mode-Multiplexed Transmission over Conventional Graded-Index Multimode Fibers," *Opt. Express* vol. 10, no. 2011, 2014.

[66] P. Genevaux *et al.*, "6-mode Spatial Multiplexer with Low Loss and High Selectivity for Transmission over Few Mode Fiber," *Opt. Fiber Commun. Conf.*, no. 1, p. W1A.5, 2015.

[67] K. Igarashi, D. Souma, T. Tsuritani, and I. Morita, "Performance evaluation of selective mode conversion based on phase plates for a 10-mode fiber," *Opt. Express*, vol. 22, no. 17, p. 20881, Aug. 2014.

[68] G. Labroille, P. Jian, N. Barre, B. Denolle, and J.-F. Morizur, "Recent progress in mode multiplexing devices using Multi-Plane Light Conversion," *2016 21st Optoelectron. Commun. Conf. OECC 2016 - Held Jointly with 2016 Int. Conf. Photonics Switch. PS 2016*, vol. 2, pp. 1–3, 2016.

[69] Y. Han and G. Hu, "A novel MUX/DEMUX based on few-mode FBG for mode division multiplexing system," *Opt. Commun.*, vol. 367, pp. 161–166, May 2016.

[70] R. Ismaeel and G. Brambilla, "Removing the directional degeneracy of LP11mode in a fused-type mode selective coupler," *J. Light. Technol.*, vol. 34, no. 4, pp. 1242–1246, 2016.

[71] S. Yerolatsitis, I. Gris-Sánchez, and T. A. Birks, "Adiabatically-tapered fiber mode multiplexers," *Opt. Express*, vol. 22, no. 1, p. 608, 2014.

[72] A. M. Velazquez-Benitez *et al.*, "Six mode selective fiber optic spatial multiplexer," *Opt. Lett.*, vol. 40, no. 8, p. 1663, 2015.

[73] K. Saitoh *et al.*, "PLC-based mode multi/demultiplexers for mode division multiplexing," *Opt. Fiber Technol.*, vol. 35, pp. 80–92, Feb. 2017.

[74] K. Igarashi, K. J. Park, T. Tsuritani, I. Morita, and B. Y. Kim, "All-fiber-based selective mode multiplexer and demultiplexer for weakly-coupled mode-division multiplexed systems," *Opt. Commun.*, vol. 408, no. May 2017, pp. 58–62, 2018.

[75] T. Fujisawa *et al.*, "Scrambling-Type Three-Mode PLC Multiplexer Based on Cascaded Y-Branch Waveguide With Integrated Mode Rotator," *J. Light. Technol.*, vol. 36, no. 10, pp. 1985–1992, May 2018.

[76] D. Melati, A. Alippi, and A. Melloni, "Reconfigurable photonic integrated mode (de)multiplexer for SDM fiber transmission," *Opt. Express*, vol. 24, no. 12, p. 12625, Jun. 2016.

[77] J. Li *et al.*, "Recent progress in mode-division multiplexed passive optical

networks with low modal crosstalk," *Opt. Fiber Technol.*, vol. 35, pp. 28–36, Feb. 2017.

[78] W. K. Zhao, K. X. Chen, J. Y. Wu, and K. S. Chiang, "Horizontal Directional Coupler Formed With Waveguides of Different Heights for Mode-Division Multiplexing," *IEEE Photonics J.*, vol. 9, no. 5, pp. 1–9, Oct. 2017.

[79] G. Labroille *et al.*, "Characterization and applications of spatial mode multiplexers based on Multi-Plane Light Conversion," *Opt. Fiber Technol.*, vol. 35, pp. 93–99, Feb. 2017.

[80] M. Y. Chen, G. D. Cao, L. Yang, Y. Q. Tong, and J. Q. Yao, "Design of mode conversion waveguides based on adiabatical mode evolution for mode division multiplexing," *Appl. Phys. B Lasers Opt.*, vol. 123, no. 10, pp. 1–9, 2017.

[81] K. Chen, Z. Nong, J. Zhang, X. Cai, S. He, and L. Liu, "Multimode 3 dB Coupler Based on Symmetrically Coupled Waveguides for On-Chipbrk Mode Division Multiplexing," *J. Light. Technol.*, vol. 35, no. 19, pp. 4260–4267, Oct. 2017.

[82] Jiangli Dong, Kin Seng Chiang, and Wei Jin, "Compact Three-Dimensional Polymer Waveguide Mode Multiplexer," *J. Light. Technol.*, vol. 33, no. 22, pp. 4580–4588, Nov. 2015.

[83] H. Huang *et al.*, "Mode division multiplexing using an orbital angular momentum mode sorter and MIMO-DSP over a graded-index few-mode optical fibre," *Sci. Rep.*, vol. 5, no. May, p. 14931, Oct. 2015.

[84] N. Hanzawa *et al.*, "PLC-based four-mode multi/demultiplexer with LP11 mode rotator on one chip," *J. Light. Technol.*, vol. 33, no. 6, pp. 1161–1165, 2015.

[85] B. Bouzid, "Analysis and review of Erbium doped fiber amplifier," *2013 Saudi Int. Electron. Commun. Photonics Conf.*, pp. 1–5, 2013.

[86] C. H. Henry, "Theory of Spontaneous Emission Noise in Open Resonators and its Application to Lasers and Optical Amplifiers," *J. Light. Technol.*, vol. 4, no. 3, pp. 288–297, 1986.

[87] L. Bigot, G. Le Cocq, and Y. Quiquempois, "Few-Mode Erbium-Doped Fiber Amplifiers: A Review," *J. Light. Technol.*, vol. 33, no. 3, pp. 588–596, Feb. 2015.

[88] N. Bai, E. Ip, T. Wang, and G. Li, "Multimode fiber amplifier with tunable modal gain using a reconfigurable multimode pump," *IEEE Photonic Soc. 24th Annu. Meet. PHO 2011*, vol. 3, pp. 589–590, 2011.

[89] R. Nasiri Mahalati, D. Askarov, and J. M. Kahn, "Adaptive modal gain equalization techniques in multi-mode erbium-doped fiber amplifiers," *J.*

Light. Technol., vol. 32, no. 11, pp. 2133–2143, 2014.

[90] N. Bai *et al.*, "Mode-division multiplexed transmission with inline few-mode fiber amplifier," *Opt. Express*, vol. 20, no. 3, p. 2668, Jan. 2012.

[91] M. Wada, T. Sakamoto, T. Mori, N. Hanzawa, T. Yamamoto, and F. Yamamoto, "Modal Gain Controllable All-fiber Type Multimode Fiber Amplifier," *Optoelectron. Commun. Conf. Photonics Switch. 2013*, pp. 14–15, 2013.

[92] Q. Kang, E. L. Lim, Y. Jung, F. Poletti, S. Alam, and D. J. Richardson, "Design of Four-Mode Erbium Doped Fiber Amplifier with Low Differential Modal Gain for Modal Division Multiplexed Transmissions," in *Optical Fiber Communication Conference/National Fiber Optic Engineers Conference 2013*, 2013, p. OTu3G.3.

[93] P. Genevaux *et al.*, "A Five-Mode Erbium-Doped Fiber Amplifier for Mode-Division Multiplexing Transmission," *J. Light. Technol.*, vol. 34, no. 2, pp. 456–462, 2016.

[94] G. Le Cocq *et al.*, "Few mode Er^3+-doped fiber with micro-structured core for mode division multiplexing in the C-band," *Opt. Express*, vol. 21, no. 25, p. 31646, Dec. 2013.

[95] Yongmin Jung *et al.*, "Reconfigurable Modal Gain Control of a Few-Mode EDFA Supporting Six Spatial Modes," *IEEE Photonics Technol. Lett.*, vol. 26, no. 11, pp. 1100–1103, Jun. 2014.

[96] S. Wittek *et al.*, "Mode-selective amplification in a large mode area Yb-doped fiber using a photonic lantern," *Opt. Lett.*, vol. 41, no. 10, p. 2157, May 2016.

[97] G. Lopez-Galmiche *et al.*, "Gain-controlled erbium-doped fiber amplifier using mode-selective photonic lantern," 2016, vol. 9774, p. 97740P.

[98] S. Matsuo, H. Ono, K. Ichii, M. Yamada, and T. Hosokawa, "Improvement of differential modal gain in few-mode fibre amplifier by employing ring-core erbium-doped fibre," *Electron. Lett.*, vol. 51, no. 2, pp. 172–173, 2015.

[99] H. Chen *et al.*, "Integrated cladding-pumped multicore few-mode erbium-doped fibre amplifier for space-division-multiplexed communications," *Nat. Photonics*, vol. 10, no. 8, pp. 529–533, Aug. 2016.

[100] H. Ono, Y. Amma, T. Hosokawa, and M. Yamada, "Recent progress on few-mode fiber amplifier," in *2016 IEEE Photonics Society Summer Topical Meeting Series (SUM)*, 2016, vol. 1, pp. 74–75.

[101] H. Ono, T. Hosokawa, K. Ichii, S. Matsuo, H. Nasu, and M. Yamada, "2-LP mode few-mode fiber amplifier employing ring-core erbium-doped fiber," *Opt. Express*, vol. 23, no. 21, p. 27405, Oct. 2015.

[102] A. F. Herbster and M. A. Romero, "Rigorous and optimized few-mode erbium-doped fiber amplifier design by using topology optimization and genetic algorithms," *Opt. Eng.*, vol. 56, no. 4, p. 046102, Apr. 2017.

[103] J.-B. Trinel, G. Le Cocq, Y. Quiquempois, E. R. Andresen, O. Vanvincq, and L. Bigot, "Theoretical study of gain-induced mode coupling and mode beating in few-mode optical fiber amplifiers," *Opt. Express*, vol. 25, no. 3, p. 2377, 2017.

[104] J. Li, J. Du, L. Ma, M.-J. Li, K. Xu, and Z. He, "Second-order few-mode Raman amplifier for mode-division multiplexed optical communication systems," *Opt. Express*, vol. 25, no. 2, p. 810, Jan. 2017.

[105] J.-B. Trinel *et al.*, "Amplification sharing of non-degenerate modes in an elliptical-core few-mode erbium-doped fiber," *Opt. Express*, vol. 24, no. 5, p. 4654, 2016.

[106] E. L. Lim *et al.*, "First demonstration of cladding pumped few-moded EDFA for mode division multiplexed transmission," *Conf. Opt. Fiber Commun. Tech. Dig. Ser.*, vol. 22, no. 23, pp. 29008–29013, 2014.

[107] Y. Jung *et al.*, "Few-mode TDFA for mode division multiplexing at 2μm," *Proc. - 2014 Summer Top. Meet. Ser. SUM 2014*, vol. 22, no. 9, pp. 152–153, 2014.

[108] A. W. Setiawan Putra, M. Yamada, S. Ambran, and T. Maruyama, "Theoretical Comparison of Noise Characteristics in Semiconductor and Fiber Optical Amplifiers," *IEEE Photonics Technol. Lett.*, vol. 30, no. 8, pp. 756–759, Apr. 2018.

[109] K. Rottwitt, S. M. M. Friis, M. A. U. Castaneda, E. N. Christensen, and J. G. Kofoed, "Higher order mode optical fiber Raman amplifiers," in *2016 18th International Conference on Transparent Optical Networks (ICTON)*, 2016, pp. 1–4.

[110] Z. Feng *et al.*, "Significant intensity noise suppression of single-frequency fiber laser via cascading semiconductor optical amplifier," *Laser Phys. Lett.*, vol. 12, no. 9, p. 095101, Sep. 2015.

[111] M. Yamada, "Analysis of intensity and frequency noises in semiconductor optical amplifier," *IEEE J. Quantum Electron.*, vol. 48, no. 8, pp. 980–990, 2012.

[112] A. W. Setiawan Putra, M. Yamada, H. Tsuda, and S. Ambran, "Theoretical Analysis of Noise in Erbium Doped Fiber Amplifier," *IEEE J. Quantum Electron.*, vol. 53, no. 4, pp. 1–8, Aug. 2017.

[113] H. Wen, Y. Alahmadi, P. LiKamWa, C. Xia, C. Carboni, and G. Li, "Invited Article: Four-mode semiconductor optical amplifier," *APL Photonics*, vol. 1,

no. 7, p. 070801, Oct. 2016.

[114] R. I. Sabitu, N. Dong-Nhat, and A. Malekmohammadi, "High dispersion four-mode fiber for mode-division multiplexing systems," *Optik (Stuttg).*, vol. 181, no. September 2018, pp. 1–12, Mar. 2019.

[115] G. Rademacher *et al.*, "Long-Haul Transmission Over Few-Mode Fibers With Space-Division Multiplexing," *J. Light. Technol.*, vol. 36, no. 6, pp. 1382–1388, Mar. 2018.

[116] M. Bigot-Astruc, D. Boivin, and P. Sillard, "Design and fabrication of weakly-coupled few-modes fibers," *2012 IEEE Photonics Soc. Summer Top. Meet. Ser. PSST 2012*, vol. 1, no. 978, pp. 189–190, 2012.

[117] S. Ö. Arik, D. Askarov, and J. M. Kahn, "Effect of mode coupling on signal processing complexity in mode-division multiplexing," *J. Light. Technol.*, vol. 31, no. 3, pp. 423–431, 2013.

[118] S. Chebaane, H. Seleem, H. Fathallah, and M. Machhout, "Design tradeoffs of few-mode step index fiber for next generation mode division multiplexing optical networks," *2015 Int. Conf. Inf. Commun. Technol. Res. ICTRC 2015*, no. October, pp. 262–265, 2015.

[119] C. R. Doerr and H. Kogelnik, "Dielectric Waveguide Theory," *J. Light. Technol.*, vol. 26, no. 9, pp. 1176–1187, May 2008.

[120] "Theory of Dielectric Optical Waveguides, Second Edition: Dietrich Marcuse: 9780123941855: Amazon.com: Books." .

[121] R. Ryf *et al.*, "MIMO-based crosstalk suppression in spatially multiplexed 3 ?? 56-Gb/s PDM-QPSK signals for strongly coupled three-core fiber," *IEEE Photonics Technol. Lett.*, vol. 23, no. 20, pp. 1469–1471, 2011.

[122] D. Rafique, S. Sygletos, and A. D. Ellis, "Impact of power allocation strategies in long-haul few-mode fiber transmission systems," *Opt. Express*, vol. 21, no. 9, p. 10801, May 2013.

[123] S. Mumtaz, R.-J. Essiambre, and G. P. Agrawal, "Nonlinear Propagation in Multimode and Multicore Fibers: Generalization of the Manakov Equations," *J. Light. Technol.*, vol. 31, no. 3, pp. 398–406, Feb. 2013.

[124] P. Sillard *et al.*, "Micro-Bend-Resistant Low-Differential-Mode-Group-Delay Few-Mode Fibers," *J. Light. Technol.*, vol. 8724, no. c, pp. 1–1, 2016.

[125] S. Randel *et al.*, "6×56-Gb/s mode-division multiplexed transmission over 33-km few-mode fiber enabled by 6×6 MIMO equalization," *Opt. Express*, vol. 19, no. 17, p. 16697, Aug. 2011.

[126] P. Sillard, "Scalability of few-mode fibers for mode-division-multiplexed systems," in *2014 IEEE Photonics Conference*, 2014, vol. 32, no. 16, pp. 520–521.

[127] F. M. Ferreira, D. Fonseca, and H. J. A. Da Silva, "Design of few-mode fibers with M-modes and low differential mode delay," *J. Light. Technol.*, vol. 32, no. 3, pp. 353–360, 2014.

[128] S. Nishimoto, T. Fujisawa, Y. Sasaki, H. Uemura, and K. Saitoh, "Theoretical Investigation of Six-Mode Multi/Demultiplexer Based on Fused-Type Multicore Fiber Coupler," *IEEE Photonics J.*, vol. 8, no. 3, pp. 1–8, Jun. 2016.

[129] R. Asif, "Advanced and flexible multi-carrier receiver architecture for high-count multi-core fiber based space division multiplexed applications," *Sci. Rep.*, vol. 6, no. November 2015, p. 27465, 2016.

[130] C. Xia, M. Ajgaonkar, and W. Rosenkranz, "Combination of optical and electrical compensation of differential mode delay in MMF links for 10-gigabit ethernet," in *Optical Transmission, Switching, and Subsystems II*, 2005, vol. 5625, p. 77.

[131] W. Shieh, A. Li, A. Al Amin, and X. Chen, "Space division multiplexing : MIMO and multimode fiber communications," *IEEE Photonics Society Newsletter* vol. 26, no. 5, 2012.

[132] G. Milione, E. Ip, M.-J. Li, J. Stone, G. Peng, and T. Wang, "Spatial Mode Analysis of an Elliptical-core, Few-mode, Optical Fiber for MIMO-less Space-division-multiplexing," *Opt. Fiber Commun. Conf.*, no. March, p. W1F.3, 2016.

[133] S. Ö. Arik, J. M. Kahn, and K. P. Ho, "MIMO signal processing for mode-division multiplexing: An overview of channel models and signal processing architectures," *IEEE Signal Process. Mag.*, vol. 31, no. 2, pp. 25–34, 2014.

[134] B. Yang, J. Duan, Z. Xie, and H. Xiao, "Evaluation of Mode Field Diameter of Step-Index Fibers and Comparison Analysis," *Res. J. Appl. Sci. Eng. Technol.*, vol. 6, no. 3, pp. 382–386, Jun. 2013.

[135] R. Olshansky, "Leaky modes in graded index optical fibers.," *Appl. Opt.*, vol. 15, no. 11, pp. 2773–2777, 1976.

[136] T. Sakamoto, T. Mori, T. Yamamoto, and S. Tomita, "Differential Mode Delay Managed Transmission Line for WDM-MIMO System Using Multi-Step Index Fiber," *J. Light. Technol.*, vol. 30, no. 17, pp. 2783–2787, 2012.

[137] R. Maruyama, N. Kuwaki, S. Matsuo, and M. Ohashi, "Relationship between Mode Coupling and Fiber Characteristics in Few-Mode Fibers Analyzed Using Impulse Response Measurements Technique," *J. Light. Technol.*, vol. 35, no. 4, pp. 650–657, 2017.

[138] M. J. Adams, "Linewidth of a single mode in a multimode injection laser," *Electron. Lett.*, vol. 19, no. 17, p. 652, 1983.

[139] D. W. Peckham, Y. Sun, A. McCurdy, and R. Lingle, "Few-Mode Fiber

Technology for Spatial Multiplexing," in *Optical Fiber Telecommunications*, Elsevier, 2013, pp. 283–319.

[140] I. Transactions, O. N. Microwave, and T. Techniques, "{ J," vol. M, no. 1, pp. 121–122, 1975.

[141] K.-P. Ho and J. M. Kahn, "Statistics of Group Delays in Multimode Fiber With Strong Mode Coupling," *J. Light. Technol.*, vol. 29, no. 21, 2011.

[142] M.-J. L. John Abbott, Scott Bickham, Paulo Dainese, "Optical Fiber Telecommunications VIA: Chapter 7. Fibers for Short-Distance ... - John Abbott, Scott Bickham, Paulo Dainese, Ming-Jun Li - Google Books," in *Fibers for Short-Distance Applications*, Elsevier Inc. Chapters, 2013, p. 794.

[143] P. J. Winzer and G. J. Foschini, "MIMO capacities and outage probabilities in spatially multiplexed optical transport systems," *IEEE Commun. Mag. J. Light. Technol. Opt. EXPRESS*, vol. 5, no. 17, pp. 320–339, 2006.

[144] A. Technologies, "Avago Technologies Safe Harbor Statement," 2015. .

[145] K. Sakaime, R. Nagase, K. Watanabe, and T. Saito, "Connection characteristics of multicore fiber connector," *2013 18th Optoelectron. Commun. Conf. Held Jointly with 2013 Int. Conf. Photonics Switch. OECC/PS 2013*, vol. 3, pp. 76–77, 2013.

[146] "'Avago Technologies.' [Online]. Available: http://www.avagotech.com/. - Google Search." [Online]. Available: https://www.google.com/search?q="Avago+Technologies."+%5BOnline%5D.+Available%3A+http%3A%2F%2Fwww.avagotech.com%2F.&oq="Avago+Technologies."+%5BOnline%5D.+Available%3A++http%3A%2F%2Fwww.avagotech.com%2F.&aqs=chrome..69i57&s. [Accessed: 20-Jun-2018].

[147] P. Mitchell, G. Brown, R. R. Thomson, N. Psaila, and A. Kar, "57 Channel (19x3) Spatial Multiplexer Fabricated using Direct Laser Inscription," in *Optical Fiber Communication Conference*, 2014, p. M3K.5.

[148] H. Ono, K. Shikama, T. Takahashi, S. Yanagi, and Y. Abe, "Fan-in/fan-out device employing v-groove substrate for multicore fibre," *Electron. Lett.*, vol. 51, no. 17, pp. 1347–1348, Aug. 2015.

[149] H. Uemura, K. Omichi, K. Takenaga, S. Matsuo, K. Saitoh, and M. Koshiba, "Fused taper type fan-in/fan-out device for 12 core multi-core fiber," *2014 Optoelectron. Commun. Conf. OECC 2014 Aust. Conf. Opt. Fibre Technol. ACOFT 2014*, no. July, pp. 49–50, 2014.

[150] K. Igarashi *et al.*, "Ultra-dense spatial-division-multiplexed optical fiber transmission over 6-mode 19-core fibers," *Opt. Express*, vol. 24, no. 10, p. 10213, May 2016.

[151] K. Shikama, Y. Abe, H. Ono, and A. Aratake, "Low-Loss and Low-Mode-

Dependent-Loss Fan-In/Fan-Out Device for 6-Mode 19-Core Fiber," *J. Light. Technol.*, vol. 36, no. 2, pp. 302–308, Jan. 2018.

[152] Y. Sasaki, "Few-Mode Multicore Fiber With 36 Spatial Modes," *J. Light. Technol.*, vol. 33, no. 5, pp. 964–970, 2015.

[153] K. Igarashi *et al.*, "Ultra-dense spatial-division-multiplexed optical fiber transmission over 6-mode 19-core fibers," *Opt. Express*, vol. 24, no. 10, p. 10213, May 2016.

[154] R. Ryf *et al.*, "Coherent 1200-km 6 x 6 MIMO Mode-Multiplexed Transmission over 3-Core Microstructured Fiber," *37th Eur. Conf. Expo. Opt. Commun.*, p. Th.13.C.1, 2011.

[155] R. Ryf *et al.*, "Space-Division Multiplexed Transmission over 4200 km 3-Core Microstructured Fiber," in *National Fiber Optic Engineers Conference*, 2012, p. PDP5C.2.

[156] T. Hayashi, Y. Tamura, T. Hasegawa, and T. Taru, "Record-Low Spatial Mode Dispersion and Ultra-Low Loss Coupled Multi-Core Fiber for Ultra-Long-Haul Transmission," *J. Light. Technol.*, vol. 35, no. 3, pp. 450–457, 2017.

[157] M. Hirano *et al.*, "Record Low Loss, Record High FOM Optical Fiber with Manufacturable Process," *Opt. Fiber Commun. Conf. Fiber Opt. Eng. Conf. 2013*, p. PDP5A.7, 2013.

[158] R. Ryf *et al.*, "Long-Haul Transmission over Multi-Core Fibers with Coupled Cores," in *2017 European Conference on Optical Communication (ECOC)*, 2017, vol. 2017-Septe, no. 1, pp. 1–3.

[159] F. Costen, J.-P. Berenger, and A. K. Brown, "Comparison of FDTD Hard Source With FDTD Soft Source and Accuracy Assessment in Debye Media," *IEEE Trans. Antennas Propag.*, vol. 57, no. 7, pp. 2014–2022, Jul. 2009.

[160] A. Hasegawa, "Self-confinement of multimode optical pulse in a glass fiber," *Opt. Lett.*, vol. 5, no. 10, p. 416, 1980.

[161] R. I. Sabitu, N. Dong-Nhat, and A. Malekmohammadi, "High dispersion four-mode fiber for mode-division multiplexing systems," *Optik (Stuttg).*, vol. 181, pp. 1–12, Mar. 2019.

[162] Kane Yee, "Numerical solution of initial boundary value problems involving maxwell's equations in isotropic media," *IEEE Trans. Antennas Propag.*, vol. 14, no. 3, pp. 302–307, May 1966.

[163] S.-T. Chu and S. K. Chaudhuri, "A finite-difference time-domain method for the design and analysis of guided-wave optical structures," *J. Light. Technol.*, vol. 7, no. 12, pp. 2033–2038, 1989.

[164] M. J. Rycroft, "Computational electrodynamics, the finite-difference time-domain method," *J. Atmos. Terr. Phys.*, vol. 58, no. 15, pp. 1817–1818,

Nov. 1996.

[165] C. W. Hull, "Apparatus for production of three-dimensional objects by stereolithography," *US Pat. 4,575,330*, vol. 1, no. 12, pp. 1–16, 1986.

[166] R. Petrović, "Multilayer multimode optical fibre," *Electron. Lett.*, vol. 16, no. 14, p. 562, 1980.

[167] S. Kawakami, "Mode conversion losses of randomly bent, singly and doubly clad waveguides for single mode transmission.," *Appl. Opt.*, vol. 15, no. 11, pp. 2778–84, 1976.

[168] K. Okamoto, ''*Fundamentals of optical waveguides*.'' *2nd Edition, pp100-105,* 2005.

[169] C. Tsao, *Optical fibre waveguide analysis*. Oxford University Press, 1992.

[170] C. Yeh and G. Lindgren, "Computing the propagation characteristics of radially stratified fibers: an efficient method," *Appl. Opt.*, vol. 16, no. 2, pp. 483–493, 1977.

[171] J. Chilwell and I. Hodgkinson, "Thin-films field-transfer matrix theory of planar multilayer waveguides and reflection from prism-loaded waveguides," *J. Opt. Soc. Am. A*, vol. 1, no. 7, p. 742, 1984.

[172] D. Dai, "Silicon-based multi-channel mode (de)multiplexer for on-chip optical interconnects," in *Advanced Photonics for Communications*, 2014, p. IM2A.2.

[173] N. Bhatia, K. C. Rustagi, and J. John, "Single LP(0,n) mode excitation in multimode fibers.," *Opt. Express*, vol. 22, no. 14, pp. 16847–62, 2014.

[174] H. Mellah, X. Zhang, and D. Shen, "LP01 to LP0m mode converters using all-fiber two-stage tapers," *Opt. Commun.*, vol. 354, no. November 2015, pp. 148–153, Nov. 2015.

[175] Z. Li, D. Lu, L. Zhao, S. Liang, X. Zhou, and J. Pan, "An InP-based two-mode converter/(de)multiplexer with 100% mode conversion efficiency by using multimode interference couplers as the building blocks," in *Conference on Lasers and Electro-Optics*, 2016, p. JW2A.123.

[176] Y.-S. Lee, K.-S. Lim, M. K. A. Zaini, and H. Ahmad, "LP 11 –LP 01 Mode Conversion Based on an Angled-Facet Two-Mode Fiber," *IEEE Photonics Technol. Lett.*, vol. 29, no. 12, pp. 1007–1010, Jun. 2017.

[177] S. Jiang, L. Ma, and Z. He, "Orientation-insensitive azimuthally asymmetric mode rotator using chirally-coupled-core fiber," *Opt. Express*, vol. 26, no. 5, p. 5146, 2018.

[178] J. D. Love and N. Riesen, "Mode-selective couplers for few-mode optical fiber networks," *Opt. Lett.*, vol. 37, no. 19, p. 3990, 2012.

[179] P. L. Chu, "Mode conversion due to tilts in multimode optical fibre," *Electron. Lett.*, vol. 10, no. 22, p. 459, 1974.

[180] D. M. H. Leung, B. M. A. Rahman, and K. T. V. Grattan, "Numerical analysis of asymmetric silicon nanowire waveguide as compact polarization rotator," *IEEE Photonics J.*, vol. 3, no. 3, pp. 381–389, 2011.

[181] T. Cao, S. Chen, Y. Fei, L. Zhang, and Q.-Y. Xu, "Ultra-compact and fabrication-tolerant polarization rotator based on a bend asymmetric-slab waveguide," *Appl. Opt.*, vol. 52, no. 5, p. 990, 2013.

[182] H. Deng, D. O. Yevick, and S. K. Chaudhuri, "Bending characteristics of asymmetric SOI polarization rotators," *IEEE Photonics Technol. Lett.*, vol. 17, no. 10, pp. 2113–2115, 2005.

[183] K. Solehmainen, T. Aalto, J. Dekker, M. Kapulainen, M. Harjanne, and P. Heimala, "Development of multi-step processing in silicon-on-insulator for optical waveguide applications," *J. Opt. A Pure Appl. Opt.*, vol. 8, no. 7, 2006.

[184] R. K. Navalakhe, N. DasGupta, and B. K. Das, "Fabrication and characterization of straight and compact S-bend optical waveguides on a silicon-on-insulator platform," *Appl. Opt.*, vol. 48, no. 31, p. G125, 2009.

[185] C. Antonelli, A. Mecozzi, M. Shtaif, and P. J. Winzer, "Modeling and performance metrics of MIMO-SDM systems with different amplification schemes in the presence of mode-dependent loss," *Opt. Express*, vol. 23, no. 3, p. 2203, 2015.

[186] W. Xiong, P. Ambichl, Y. Bromberg, B. Redding, S. Rotter, and H. Cao, "Principal modes in multimode fibers: exploring the crossover from weak to strong mode coupling," *Opt. Express*, vol. 25, no. 3, p. 2709, Feb. 2017.

[187] K.-P. Ho and J. M. Kahn, "Mode-dependent loss and gain: statistics and effect on mode-division multiplexing," *Opt. Express*, vol. 19, no. 17, p. 16612, Aug. 2011.

[188] L. Palmieri and A. Galtarossa, "Intramodal Dispersion Properties of Step-Index Few-Mode Spun Fibers," *J. Light. Technol.*, vol. 34, no. 2, pp. 303–313, 2016.

[189] A. A. Juarez, C. A. Bunge, S. Warm, and K. Petermann, "Perspectives of principal mode transmission in mode-division-multiplex operation," *Opt. Express*, vol. 20, no. 13, p. 13810, 2012.

[190] M. Sung, H. Kim, J. Lee, and J. Jeong, "Improvement of the chromatic dispersion tolerance in coherent optical OFDM systems using shifted DFT windows for ultra-long-haul optical transmission systems," *Opt. Express*, vol. 22, no. 19, p. 23539, Sep. 2014.

[191] H. Sakata, H. Sano, and T. Harada, "Tunable mode converter using electromagnet-induced long-period grating in two-mode fiber," *Opt. Fiber*

Technol., vol. 20, no. 3, pp. 224–227, Jun. 2014.

[192] S. Warm and K. Petermann, "Splice loss requirements in multi-mode fiber mode-division-multiplex transmission links," *Opt. Express*, vol. 21, no. 1, p. 519, Jan. 2013.

[193] M. Suzuki, Y. Tamura, Y. Yamamoto, and T. Hasegawa, "Low-loss Splice of Large Effective Area Fiber Using Fluorine-doped Cladding Standard Effective Area Fiber," in *Optical Fiber Communication Conference*, 2017, p. M2F.4.

[194] G. Prabhakar, A. Peer, V. Rastogi, and A. Kumar, "Large-effective-area dispersion-compensating fiber design based on dual-core microstructure," *Appl. Opt.*, vol. 52, no. 19, p. 4505, 2013.

[195] M. Kasahara *et al.*, "Design of Few-Mode Fibers for Mode-Division Multiplexing Transmission," *IEEE Photonics J.*, vol. 5, no. 6, pp. 7201207–7201207, Dec. 2013.

[196] D. Jain, C. Baskiotis, and J. K. Sahu, "Bending performance of large mode area multi-trench fibers," *Opt. Express*, vol. 21, no. 22, p. 26663, Nov. 2013.

[197] F. Beier *et al.*, "Narrow linewidth, single mode 3 kW average power from a directly diode pumped ytterbium-doped low NA fiber amplifier," *Opt. Express*, vol. 24, no. 6, p. 6011, Mar. 2016.

[198] A. V Bourdine and V. A. Burdin, "DMGD Reducing in Few-mode Fiber Optic Links by Special Refractive Index Profile and Selective Mode Excitation Provided by Designed MDM Channels Placement Scheme over Fiber Core End," in *2017 Progress In Electromagnetics Research Symposium — Spring (PIERS), St Petersburg, Russia, 22–25 May D*, 2017, pp. 22–25.

[199] R. Ryf *et al.*, "Mode-multiplexed transmission over conventional graded-index multimode fibers," *Opt. Express*, vol. 23, no. 1, p. 235, Jan. 2015.

[200] T. Ma, A. Markov, L. Wang, and M. Skorobogatiy, "Graded index porous optical fibers – dispersion management in terahertz range," *Opt. Express*, vol. 23, no. 6, p. 7856, Mar. 2015.

[201] S. Zheng, G. Ren, Z. Lin, W. Jian, and S. Jian, "Design and analysis of novel multilayer-core fiber with large mode area and low bending loss," *Opt. Commun.*, vol. 315, pp. 317–323, 2014.

[202] D. Gloge and E. A. J. Marcatili, "Multimode Theory of Graded-Core Fibers," *Bell Syst. Tech. J.*, vol. 52, no. 9, pp. 1563–1578, 1973.

[203] F. Vaquero Caballero, F. Pittalà, G. Goeger, M. Wang, Y. Ye, and I. Tafur Monroy, "Novel Equalization Techniques for Space Division Multiplexing Based on Stokes Space Update Rule," *Photonics*, vol. 4, no. 1, p. 12, 2017.

[204] C. Brunet, B. Ung, L. Wang, Y. Messaddeq, S. LaRochelle, and L. A. Rusch,

"Design of a family of ring-core fibers for OAM transmission studies," *Opt. Express*, vol. 23, no. 8, p. 10553, 2015.

[205] R. Lin *et al.*, "Spatial division multiplexing for optical data center networks," *International Conference on Optical Network Design and Modeling (ONDM)*, 2018, pp. 239–241.

[206] M. Chacinski, U. Westergren, B. Stoltz, L. Thylen, R. Schatz, and S. Hammerfeldt, "Monolithically Integrated 100 GHz DFB-TWEAM," *J. Light. Technol.*, vol. 27, no. 16, pp. 3410–3415, Aug. 2009.

[207] N. Dong-Nhat, L. Nguyen, and A. Malekmohammadi, "Using duobinary with first- and second-order optical equalisers for extending transmission distance of optical access networks," *IET Optoelectron.*, vol. 12, no. 5, pp. 239–243, Oct. 2018.

[208] M. Verplaetse *et al.*, "Real-Time 100 Gb/s Transmission Using Three-Level Electrical Duobinary Modulation for Short-Reach Optical Interconnects," *J. Light. Technol.*, vol. 35, no. 7, pp. 1313–1319, 2017.

[209] J. Verbist *et al.*, "DAC-less and DSP-free PAM-4 Transmitter at 112 Gb/s with Two Parallel GeSi Electro-Absorption Modulators," *European Conference on Optical Communication (ECOC)*, 2017, no. 3, pp. 1–3.

[210] X. Pang *et al.*, "7×100 Gbps PAM-4 Transmission over 1-km and 10-km Single Mode 7-core Fiber using 1.5-μm SM-VCSEL," *Optical Fiber Communication Conference*, 2018, p. M1I.4.

[211] S. Murshid *et al.*, "Analysis of spatial domain multiplexing/space division multiplexing (SDM) based hybrid architectures operating in tandem with wavelength division multiplexing," in *Proc. of SPIE Vol. 9202 920214-2*, 2014, vol. 9202, p. 920214.

[212] L. Luo *et al.*, "Simultaneous Mode and Wavelength Division Multiplexing On-Chip," *ArXiv*, pp. 1–21, 2013.

[213] M. A. Elsherif and A. Malekmohammadi, "Performance enhancement of mapping multiplexing technique utilising dual-drive Mach–Zehnder modulator for metropolitan area networks," *IET Optoelectron.*, vol. 9, no. 2, pp. 108–115, Apr. 2015.

[214] N. Karelin *et al.*, "Modeling and design framework for SDM transmission systems," in *2015 17th International Conference on Transparent Optical Networks (ICTON)*, 2015, vol. 2015-Augus, no. October, pp. 1–4.

[215] C. Koebele, M. Salsi, G. Charlet, and S. Bigo, "Nonlinear Effects in Mode-Division-Multiplexed Transmission Over Few-Mode Optical Fiber," *IEEE Photonics Technol. Lett.*, vol. 23, no. 18, pp. 1316–1318, Sep. 2011.

[216] Z. Pan, Y. Weng, and J. Wang, "Investigation of nonlinear effects in few-

mode fibers," *Photonic Netw. Commun.*, vol. 31, no. 2, pp. 305–315, Apr. 2016.

[217] Z. Pan, Y. Weng, and J. Wang, "Investigation of nonlinear effects in few-mode fibers," *Photonic Netw. Commun.*, no. March, 2015.

[218] S. Mumtaz, R.-J. Essiambre, and G. P. Agrawal, "Nonlinear Propagation in Multimode and Multicore Fibers: Generalization of the Manakov Equations," *J. Light. Technol.*, vol. 31, no. 3, pp. 398–406, Feb. 2013.

[219] R.-J. Essiambre *et al.*, "Experimental Observation of Inter-Modal Cross-Phase Modulation in Few-Mode Fibers," *IEEE Photonics Technol. Lett.*, vol. 25, no. 6, pp. 535–538, Mar. 2013.

[220] R.-J. Essiambre *et al.*, "Experimental Investigation of Inter-Modal Four-Wave Mixing in Few-Mode Fibers," *IEEE Photonics Technol. Lett.*, vol. 25, no. 6, pp. 539–542, Mar. 2013.

[221] G. P. (Govind P. . Agrawal, *Nonlinear fiber optics*. Elsevier Science, 2013.

[222] R. W. Boyd, *Nonlinear optics*. Academic Press, 2008.

Appendix A:

The following tables represents the measured dispersions as a function of the core ring thickness obtained during optimisations of the two high dispersion fibers.

Table 9-1: CH-FMF ring thickness R1 and measured dispersion of LP_{01}, LP_{11}, LP_{02} and LP_{21}

Ring Thickness	**Dispersion (ps/km.nm)**			
CH-R1	**LP01**	**LP11**	**LP02**	**LP21**
2.5	19.43	19.704	-4.531	13.723
2.6	19.462	19.808	-2.262	13.764
2.7	19.461	19.921	-0.347	13.812
2.8	19.421	20.052	1.258	13.886
3	18.861	20.047	4.088	12.849
3.2	18.763	20.341	5.978	14.056
3.4	18.812	20.617	7.229	14.300
3.6	18.293	20.85	8.122	15.267
3.6	17.937	20.429	10.116	15.495
3.8	17.972	20.375	11.266	15.6027
4	18.729	20.69	12285	15.823
4.1	19.544	20.972	14.208	16.185
4.18	19.662	21.251	16.082	16.304
4.2	19.763	20.317	16.043	16.523
4.3	17.707	19.9064	17.364	17.013
4.4	18.466	19.841	18.053	17.124
4.5	17.2320	18.416	17.2612	17.3414

Table 9-2: CH-FMF ring thickness R2 and measured dispersion of LP_{01}, LP_{11}, LP_{02} and LP_{21}

Ring Thickness	**Dispersions (ps/km.nm**			
CH-R2	**LP01**	**LP11**	**LP02**	**LP21**
3.000	19.43	19.704	-4.531	13.723
2.900	19.462	19.808	-2.262	13.764
2.800	19.461	19.921	-0.347	13.812
2.700	19.421	20.052	5.258	13.886
2.700	18.861	20.047	8.088	14.849
2.600	17.6731	19.5704	10.984	15.757
2.600	17.757	19.702	12.116	15.09
2.600	17.806	19.416	13.733	16.3705
2.500	18.763	20.341	14.978	16.456
2.400	17.937	20.429	15.116	16.495
2.400	18.033	19.646	16.6095	17.158
2.300	18.2400	17.0200	17.3670	17.2027
2.200	18.4898	21.2957	18.995	18.3481
2.180	18.425	20.678	17.222	16.836
2.160	18.4681	20.687	16.982	16.749
2.140	18.511	20.697	16.748	16.6613
2.120	18.555	20.706	16.493	16.571
2.100	18.437	20.441	17.152	16.486
2.080	18.7776	21.3747	17.6751	17.972
2.050	18.7828	21.2755	16.1272	17.0672
2.000	18.988	21.424	16.6997	17.6899
1.800	19.439	21.543	15.848	16.855
1.700	19.668	21.582	14.154	16.3581
1.680	19.603	21.821	18.201	14.113
1.640	19.662	21.251	18.082	14.004
1.600	19.721	21.144	17.81	13.824

Table 9-3: CH-FMF ring thickness R3 and measured dispersion of LP_{01}, LP_{11}, LP_{02} and LP_{21}

Ring Thickness	**Dispersions (ps/km.nm)**			
CH-R3 (μm)	**LP01**	**LP11**	**LP02**	**LP21**
2.80	21.3095	22.2124	15.2897	21.1278
2.60	21.3367	22.1645	15.3776	20.634
2.40	21.3526	22.1112	16.4987	20.1813
2.20	21.3555	22.0513	16.4431	19.5758
2.00	21.344	21.9823	17.1564	18.8565
1.80	21.3162	21.9014	18.57182	17.9969
1.60	21.2728	21.8043	17.56367	16.9626
1.40	17.5123	18.025	17.0805	17.2538
1.40	17.61786	18.5124	17.0802	17.2533
1.40	18.6732	19.7823	16.7345	17.2635
1.30	19.4552	20.69177	14.2866	17.2036
1.20	19.596	20.8267	12.4516	16.3056
1.10	19.787	21.1603	10.001	17.1266
1.00	20.0127	21.4122	7.4278	17.1834
0.80	20.8704	21.6303	5.6038	17.0854
0.60	20.8808	21.7156	-0.668	17.211
0.40	20.9033	21.7827	-2.1673	17.012
0.20	16.4394	208265	-5.5688	16.978

Table 9-4: CL-FMF ring thickness R1 and measured dispersion of LP_{01}, LP_{11}, LP_{02}, and LP_{21}

Ring Thickness	**Dispersions (ps/km.nm**				
CL-R1	**LP01**	**LP11**	**LP02**	**LP21**	**LP01**
2.8	15.3095	20.024	17.2897	21.1278	15.3095
2.6	16.3367	19.5645	18.3776	20.634	16.3367
2.4	17.3526	19.1112	19.4987	20.1813	17.3526
2.2	18.3555	19.0513	19.4431	19.5758	18.3555
2.0	19.344	19.023	19.1564	18.8565	19.344
1.8	18.3162	18.9014	18.5718	17.9969	18.3162
1.6	18.2728	18.3043	17.5637	16.9626	18.2728
1.5	17.5123	18.025	17.0805	17.2538	17.5123
1.4	17.6179	18.5124	17.0802	17.2533	17.6179
1.3	17.4552	18.077	16.2866	17.2036	17.4552
1.2	17.396	17.3267	14.4516	16.3056	17.396
1.1	17.087	16.7603	10.001	17.1266	17.087
1.0	16.0127	16.4122	7.4278	17.7834	16.0127
0.8	15.8704	16.203	5.6038	17.6854	15.8704
0.6	14.8808	15.7156	4.6506	17.668	14.8808
0.4	12.9033	15.2827	4.0760	17.1673	12.9033
0.2	10.9394	14.8265	4.0000	16.5688	10.9394

Table 9-5: CL-FMF ring thickness R2 and measured dispersion of LP_{01}, LP11, LP_{02} and LP_{21}

Ring Thickness	Dispersions (ps/km.nm			
CL-R2	**LP01**	**LP11**	**LP02**	**LP21**
4.4	20.8704	21.6303	19.6038	21.0854
4.2	20.8808	21.7156	18.6506	20.668
4.0	20.9033	21.7827	17.4835	20.1673
3.8	20.9394	21.8265	16.041	19.5688
3.6	20.9894	21.8423	14.2366	18.8537
3.4	21.053	21.8262	11.9412	17.9961
3.2	21.1284	22.7752	8.96469	16.9628
2.8	21.3095	22.2124	15.2897	21.1278
2.6	20.0127	21.4122	15.4278	17.7834
2.4	17.5123	18.025	17.0805	17.2538
2.2	17.6179	18.5124	17.0802	17.2533
2.0	18.6732	19.7823	16.7345	17.2635
1.8	19.4552	20.6918	16.2866	17.2036
1.6	19.5960	20.8267	14.4516	16.3056
1.4	19.7870	21.1603	15.0010	17.1266

Table 9-6: CL-FMF ring thickness R3 and measured dispersion of LP_{01}, LP_{11}, LP_{02} and LP_{21}

Ring Thickness	Dispersions (ps/km.nm				
CL-R3	**LP01**	**LP11**	**LP02**	**LP21**	**LP01**
4.8	20.8704	21.6303	15.6038	15.8854	20.8704
4.6	19.0127	20.4122	15.5278	16.7834	19.0127
4.4	18.287	19.1603	16.001	16.7266	18.287
4.2	17.6179	18.5124	17.0802	17.2533	17.6179
4.0	17.496	17.8267	16.4516	16.3056	17.496
3.8	16.8552	17.6918	16.2866	15.5036	16.8552
3.6	16.6732	16.7823	16.7345	15.4635	16.6732
3.4	16.5131	15.6885	15.9782	14.4002	16.5131
3.2	16.4728	14.8043	15.5637	14.3626	16.4728
3.0	16.3162	14.3014	15.3718	12.9969	16.3162
2.8	16.344	14.1823	15.1564	10.8565	16.344
2.6	15.3555	13.9513	14.9431	8.5758	15.3555
2.4	15.3526	13.7112	14.7987	7.1813	15.3526
2.2	14.3367	13.5645	14.6776	5.634	14.3367
2.0	13.3095	13.3124	14.2897	4.1278	13.3095
1.8	11.1284	13.2752	13.2647	3.9628	11.1284
1.6	9.053	12.8262	12.9412	2.9961	9.053
1.4	7.9894	12.4423	12.2366	1.8537	7.9894
1.2	5.5000	11.2000	10.000	-1.000	5.5000

Table 9-7: CL-FMF ring thickness R4 and measured dispersion of LP_{01}, LP_{11}, LP_{02} and LP_{21}

Ring Thickness	Dispersions (ps/km.nm			
R4-CL	**LP01**	**LP11**	**LP02**	**LP21**
2.5	21.2131	18.6885	12.9782	11.7002
2.4	21.2728	18.8043	13.5637	12.9626
2.3	21.3162	19.1014	14.5718	13.9969
2.2	20.344	19.3823	15.1564	14.8565
2.1	19.3555	19.6513	15.4431	15.5758
2.0	19.3526	19.8112	15.4987	16.1813
1.9	19.3367	19.9645	15.8776	16.634
1.8	18.3095	20.2124	16.8897	16.8278
1.7	18.1284	19.7752	16.9647	16.9628
1.6	17.6179	18.5124	17.0802	17.2533
1.5	16.453	17.8562	16.9412	17.9961
1.4	15.9894	17.8423	16.7366	16.8537
1.3	15.9394	17.8265	16.541	16.5688
1.2	15.9033	16.7827	16.4835	14.1673
1.1	15.8808	16.7156	15.6506	12.668
1.0	14.8704	16.6303	15.6038	8.0854
0.9	14.0127	15.4122	13.4278	6.7834
0.8	13.787	15.1603	11.001	4.1266
0.7	13.596	14.8267	9.4516	-0.2560
0.6	12.7552	14.6918	7.2866	-2.2036
0.5	12.6732	14.7823	5.7345	-4.3000

Table 9-8: CH-FMF ring thickness R2 and measured effective index of LP_{01}, LP_{11}, LP_{02} and LP_{21}

Ring Thickness	Effective Index			
R2 (μm)	**LP01**	**LP11**	**LP02**	**LP21**
3.00	1.4480052	1.44669	1.444699	1.444886
3.00	1.4481512	1.4468306	1.4448682	1.445158
2.90	1.4482088	1.4468419	1.4449391	1.4451602
2.80	1.4482694	1.446857	1.445004	1.4451629
2.70	1.4483328	1.4468694	1.4450628	1.4451662
2.70	1.4483434	1.4467333	1.4451269	1.4450357
2.65	1.4489794	1.4467223	1.4454393	1.4449848
2.63	1.4489336	1.4468062	1.4458868	1.4453429
2.62	1.4490957	1.4468327	1.4455475	1.4450997
2.60	1.4491088	1.4469088	1.4456697	1.4452225
2.58	1.4490433	1.446991	1.4452848	1.4450754
2.55	1.449032	1.4468066	1.4455221	1.4450793
2.50	1.4490064	1.446805	1.4455049	1.4450723
2.50	1.4484898	1.446778	1.4451979	1.4450472
2.30	1.4487568	1.4466282	1.4451574	1.444803
2.20	1.4489093	1.4466038	1.4450667	1.4446915
2.20	1.4491362	1.4470256	1.4456254	1.4452652
2.10	1.4489098	1.4467257	1.4451655	1.4448374
2.10	1.4489098	1.4467257	1.4451655	1.4448374
1.60	1.4491664	1.4470721	1.4452818	1.4470721
1.64	1.4492161	1.4470743	1.4452534	1.4450716